DTU Mechanical Engineering
Department of Mechanical Engineering

Integrated micro product/process quality assurance in micro injection moulding production

Federico Baruffi

PhD Thesis

Ph.D. Thesis

Integrated micro product/process quality assurance in micro injection moulding production

Federico Baruffi

2019

Technical University of Denmark

"*E sognai così forte*
che mi uscì sangue dal naso."

—Fabrizio De André, Sand Creek

Preface

The present thesis was submitted as one of the requirements of the Ph.D. degree at the Technical University of Denmark. The related work has been carried out from May 2016 to February 2019 at the Technical University of Denmark (DTU), Kongens Lyngby, Denmark, at the Department of Mechanical Engineering (MEK) under the supervision of Associate Professor Guido Tosello and Researcher Matteo Calaon.

From February 2018 to March 2018, two months were spent at the University of Bradford, UK, at the Centre for Polymer Micro and Nano Technology (Polymer MNT) under the supervision of Professor Ben Whiteside.

This work was funded by the MICROMAN project ("Process Fingerprint for Zero-defect Net-shape MICROMANufacturing"). MICROMAN is a European Training Network supported by Horizon 2020, the EU Framework Programme for Research and Innovation (ID: 674801) and is greatly acknowledged for the financial support.

Kongens Lyngby
February 2019

Federico Baruffi

Abstract

The present thesis is dedicated to the advancement of the current state-of-the-art of process/product control of polymer micro components manufactured by micro injection moulding (µIM). The main focus was the achievement of in-line quality assurance and optimization in µIM by means of a combination of product micro/nano metrology and real-time process monitoring. To achieve this, the newest technologies available in the moulding scenario were employed. Multiple important aspects of µIM, as the use of unconventional materials, process simulations and indirect metrology for mould assessment were also investigated.

A thorough experimental investigation was carried out to study the behaviour of thermoplastic elastomers (TPEs) when moulding a commercial micro ring component having a mass of 2.2 mg. The quantification of part defects such as weld lines and air traps allowed drawing clear recommendations on how to set up the process window. The geometrical precision and accuracy of the produced parts were investigated using optical measurements over a broad range of process variables in order to characterize the impact of process variations on the final output. A novel shrinkage behaviour, most probably induced by residual stresses, was observed and studied. Finally, the produced parts were also functionally tested, allowing to define a clear relationship between process settings and functionality.

A novel method based on the definition of product and process fingerprints was applied to both a 3D micro component and a nano-structured one to define an in-line quality assurance strategy based on process monitoring. As for the 3D component, which was designed for medical applications and had a mass of 0.1 mg, geometrical focus variation measurements and in-line monitored pressure and velocity data were combined to determine the most suitable control strategy. It was found that the integral of the injection pressure during filling was the process indicator that was most correlated to the quality of the moulded part and to the size of its defects. Therefore, clear indications could be given on how to monitor the process in-line to obtain the most valuable information with respect to conformity to design specifications.

The nano-structured component was moulded by replicating a laser-structured surface having a texture composed by ripples with an average height of 50 nm and pitch of 900 nm. The replication behaviour was investigated over a wide range of process variables and the simultaneous use of two areal surface roughness parameters was identified as the best way to characterize the produced surfaces. High-speed infrared temperature data were obtained and considered as a tool for in-line quality monitoring.

The results showed that the in-cavity temperature during the initial heating of the cavity, which was caused by the entrance of the polymer melt, had a strong impact on the replication quality, being highly correlated to the variation of the surface roughness parameters. Clear recommendations were drawn on how to in-line monitor the nano scale replication by using the value of this temperature indicator.

The use of process simulations as a tool for dimensional quality prediction and virtual process optimization was investigated in this thesis. A commercially available injection moulding simulation software was employed to build models and run simulations for two of the case studies of the project, namely the TPE micro ring and the 3D micro component. Model calibration proved a task of primary importance in order to match experimental measurements with numerical data. In regard to the micro ring simulations, the calibrated model was capable of predicting the final dimensions of the moulded parts with a 1.6 µm accuracy. The effects of the µIM parameters on the part dimensions were also well forecasted, validating the model as a tool for virtual optimization. Process simulations were applied to the 3D micro component to predict the size of the flash that affected the part quality. The results showed that the model accurately captured the variations induced by the different process variables on the defect.

The use of replica technology as a method for indirect measurements of inaccessible micro milled features, which are often present in micro moulds, was assessed. Two benchmark samples were designed and micro milled in order to quantify the degree of fidelity of a commercial two-component silicone rubber when applied to the measurement of both surface texture and geometry. The comparison between direct and indirect measurements allowed defining the applicability of the method. The surface topography measurements showed that the indirect approach led to an overestimation of the real roughness because of the stretch of the replication media generated during its manual removal from the master. On the other hand, indirect measurements of geometry revealed that the silicone shrunk linearly with respect to the original dimension. The shrinkage factor was calculated to provide a method to extrapolate the mould dimensions in the industrial situation in which only indirect data are available.

Acknowledgements

I would like to express my deep gratitude to all the people that supported me during the time spent as Ph.D. student at DTU. This three-year journey has made me better as a person and has also substantially improved my working skills, by providing significant high-level experience in the field of research and advanced manufacturing.

Firstly, I would like to express my deepest gratitude to my supervisors for their contribution, encouragement and support. I would like to thank my main supervisor Guido Tosello who gave me the great opportunity to pursue a Ph.D. degree at the Technical University of Denmark. I also acknowledge the incredibly valuable insights, positive attitude and contribution he constantly provided through his supervision. My co-supervisor, Matteo Calaon, is also greatly thanked for the consistent support, fruitful discussion, priceless guidance as well as for the friendly relationship we share. It was a true pleasure to work with them.

René Elsborg, Daniel Piesiak and Christen H. Nielsen of Ortofon A/S are deeply acknowledged for their support and substantial help during the experiments and functional tests I carried out at their facilities and with their equipment.

Ben Whiteside, Mert Gülçür and all the team at the Polymer MNT of Bradford are deeply thanked for the opportunity of the external research stay, for their great hospitality and for the considerable contribution to my work regarding surface replication and flow visualization experiments.

My thanks also go to Martin Hirschenauer and Martin Philipp-Pichler of Wittmann-Battenfeld GmbH for their availability in hosting the experiments related to the 3D micro medical component. The profound insights they shared about the µIM machine were of substantial importance for my work. Wolfgang Wittner and Christian Bruckmüller of Ernst Wittner GmbH are also acknowledged for the realization of the mould.

Massimiliano Annoni, Paolo Parenti and Francesco Cacciatore of Politecnico di Milano are deeply thanked for their valuable collaboration related to the replica technology experiments.

I would like to thank all the past and present colleagues of building 427 for all the discussions, pieces of advice, friendly chats and laughs. They really succeeded

in making the office a friendly environment in which sitting at my desk for many consecutive hours has never been a burden.

The whole MICROMAN consortium is greatly acknowledged for the excellent collaboration and fruitful insights on micro manufacturing I received during the 9 project meetings we had all around Europe. Special thanks go to the 12 Early Stage Researchers for their kindness and availability.

My gratitude goes also to all the students I supervised during my work. Their projects represented a valuable contribution for the achievement of the results obtained during my research.

Filippo is particularly acknowledged, as his Master Thesis work represented an important input for chapter 5 and chapter 7:

- F. Degli Esposti. "Micro Injection Moulding Process Simulation for Quality Assurance". Master Thesis. Technical University of Denmark, 2017.

Frederik and Maros are also acknowledged since their Master Thesis projects were valuable resources for chapter 4 and chapter 7:

- F. B. Hasnæs. "Micro Injection Moulding Technology of Thermoplastic Elastomers". Master Thesis. Technical University of Denmark, 2014.
- M. Hluchy. "Micro Injection Moulding Process Validation for High Precision Thermoplastic Elastomer Components Manufacture". Master Thesis. Technical University of Denmark, 2016.

I would like to thank Nicolò, Federica, Emanuele, Tommaso, Alessandro, Riccardo and all the other friends I made in Denmark during this three-year period. They enriched my life and contributed to making this journey unforgettable.

Exceptional thanks go to my parents and family, whose support never failed to reach me, even though we were far apart.

Finally, the biggest thank goes to Ester: you make every day the best I could possibly ask for.

Contents

List of Figures

List of Tables

List of Mathematical Symbols

Symbol	Meaning	SI unit
Latin		
a_e	radial depth of cut	m
a_p	axial depth of cut	m
A_flash	flash area	m^2
$A_\mathrm{flash\text{-}exp}$	flash area as output of experiments	m^2
$A_\mathrm{flash\text{-}num}$	flash area as output of simulations	m^2
A_p	pixel area	m^2
b_1m	data-fitted constant	$\mathrm{m}^3\,\mathrm{kg}^{-1}$
b_2m	data-fitted constant	$\mathrm{m}^3\,\mathrm{kg}^{-1}\,\mathrm{K}^{-1}$
b_3m	data-fitted constant	Pa
b_4m	data-fitted constant	K^{-1}
b_1s	data-fitted constant	$\mathrm{m}^3\,\mathrm{kg}^{-1}$
b_2s	data-fitted constant	$\mathrm{m}^3\,\mathrm{kg}^{-1}\,\mathrm{K}^{-1}$
b_3s	data-fitted constant	Pa
b_4s	data-fitted constant	K^{-1}
b_5	data-fitted constant	K
b_6	data-fitted constant	$\mathrm{K\,Pa}^{-1}$
b_7	data-fitted constant	$\mathrm{m}^3\,\mathrm{kg}^{-1}$
b_8	data-fitted constant	K^{-1}
b_9	data-fitted constant	Pa^{-1}
$B(T)$	temperature-dependent function	Pa
C	constant	1
c_p	specific heat capacity at constant pressure	$\mathrm{J\,kg}^{-1}\,\mathrm{K}^{-1}$
C_1^0	constant	K^{-1}
C_2^0	constant	K^{-1}
d	constant decrement applied to $\mathrm{OD}_\mathrm{model}$	m
$\mathrm{d}\,T/\mathrm{d}t$	slope of T_max profile	$\mathrm{K\,s}^{-1}$
D	diameter	m
D_1	constant	Pa s
$\mathrm{D_C}$	mill diameter	m
$\mathrm{D_{mould}}$	diameter of mould cavity	m
$\mathrm{D_{polymer}}$	diameter of moulded part	m
$\mathrm{D_{ref}}$	reference diameter	m

Symbol	Meaning	SI unit
f_z	feed per tooth	m
$\boldsymbol{g}$	gravitational acceleration vector	$\mathrm{m\,s^{-2}}$
ID	inner diameter	m
IDb	inner bottom diameter	m
IDt	inner top diameter	m
I_p	integral of injection pressure	Pa s
$I_p/\Delta t$	integral mean of injection pressure	Pa
k	coverage factor	1
k	thermal conductivity	$\mathrm{W\,m^{-1}\,K^{-1}}$
L1	linear dimension	m
L2	linear dimension	m
L_{mark}	gate mark length	m
$\mathbf{M}$	vector of repeated dimensional measurements	m
n	power-law index	1
N_{p}	number of pixels	1
OD	outer diameter	m
ODb	outer bottom diameter	m
$\mathrm{OD_{exp}}$	outer diameter as output of experiments	m
$\mathrm{OD_{model}}$	outer diameter assigned to the numerical model	m
$\mathrm{OD_{mould}}$	outer diameter of the mould	m
$\mathrm{OD_{num}}$	outer diameter as output of simulations	m
ODt	outer top diameter	m
p	injection pressure	Pa
p_{hold}	holding pressure	Pa
p_{max}	maximum injection pressure	Pa
p_{mean}	average injection pressure	Pa
R	roundness indicator	m
Ra	arithmetic average of profile heights	m
s_W	shrinkage related to W measurement	1
$\boldsymbol{S}$	vector of repeated roughness measurements	m
Sa	arithmetic mean height of surface	m
Sa_{master}	arithmetic mean height of the master surface	m
Sa_{replica}	arithmetic mean height of the replica surface	m
Sdq	root mean square of the surface gradient	1
Sk	core height	m
Sku	kurtosis of the surface	1
Spk	reduced peak height	m
Sq	root mean square height of the surface	m
Svk	reduced dale height	m
t	time	s
T	temperature	K
T_{g}	glass transition temperature	K

Symbol	Meaning	SI unit
$T_{\max}$	maximum temperature for each time frame	K
T_{mean1}	average temperature in the initial phase of filling	K
T_{mean2}	average temperature during filling	K
T_{melt}	melt temperature	K
T_{mould}	mould temperature	K
T_{peak1}	temperature at the first $T_{\max}$ profile peak	K
T_{peak2}	temperature at the second $T_{\max}$ profile peak	K
T_{t}	transition temperature	K
u_{cal}	calibration uncertainty	m
u_{CONF}	uncertainty of the confocal microscope	m
u_{FV}	uncertainty of the focus variation microscope	m
u_{p}	uncertainty due to measurement procedure	m
u_{res}	resolution uncertainty	m
$u_{\text{res,CONF}}$	resolution uncertainty of the confocal microscope	m
$u_{\text{res,FV}}$	resolution uncertainty of the focus variation microscope	m
$u_{Sa,\text{mill}}$	uncertainty of Sa for milled samples	m
u_{w}	uncertainty due to manufacturing variations	m
$u_{W,\text{mill}}$	uncertainty of W for milled samples	m
U	expanded uncertainty	m
U_{Sa}	expanded uncertainty associated with Sa	m
U_{W}	expanded uncertainty associated with W	m
v	velocity of injection plunger	$\mathrm{m\,s^{-1}}$
$\boldsymbol{v}$	velocity vector	$\mathrm{m\,s^{-1}}$
v_{c}	cutting speed	$\mathrm{m\,s^{-1}}$
v_{inj}	injection speed	$\mathrm{m\,s^{-1}}$
v_{mean}	mean velocity	$\mathrm{m\,s^{-1}}$
v_{slope}	slope of velocity profile	$\mathrm{m\,s^{-2}}$
V	specific volume	$\mathrm{m^3\,kg^{-1}}$
$V_0(T)$	temperature-dependent function	$\mathrm{m^3\,kg^{-1}}$
$V_{\text{t}}(p,T)$	temperature-dependent function	$\mathrm{m^3\,kg^{-1}}$
V_{part}	volume of a part	$\mathrm{m^3}$
$W1$	width	m
$W2$	width	m
W_{master}	width of master	m
W_{replica}	width of replica	m

Symbol	Meaning	SI unit
Greek		
α	alignment angle	rad
β	coefficient of volumetric expansion	K^{-1}
$\dot{\gamma}$	shear rate	s^{-1}
$\dot{\boldsymbol{\gamma}}$	shear rate tensor	s^{-1}
Δ_{D}	shrinkage of diameter	1
Δ_{D}	replication of diameter	m
Δ_{ID}	inner diameter deviation	m
Δ_{IDb}	shrinkage of inner bottom diameter	1
Δ_{IDb}	replication of inner bottom diameter	m
Δ_{OD}	outer diameter deviation	m
Δ_{ODb}	replication of outer bottom diameter	m
Δ_{ODt}	shrinkage of outer top diameter	1
Δ_{ODt}	replication of outer top diameter	m
Δ_S	surface replication indicator	1
Δ_{Sa}	deviation of *Sa* indirect measurements	m
Δ_{Sq}	*Sq* replication indicator	1
Δ_{Sdq}	*Sdq* replication indicator	1
Δt	integration range	s
Δ_W	deviation of W indirect measurements	m
η	viscosity	Pa s
η_0	zero shear rate viscosity	Pa s
ρ	density	$\mathrm{kg\,m}^{-3}$
ρ	Pearson coefficient of correlation	1
$\boldsymbol{\sigma}$	stress tensor	Pa
τ	shear stress	Pa
$\boldsymbol{\tau}$	shear stress tensor	Pa
τ^*	critical shear stress	Pa

List of Acronyms

Abbreviation	Meaning
µEDM	micro electro-discharge-machining
µIM	micro injection moulding
ABS	acrylonitrile butadiene styrene
AFM	atomic force microscope
ANOVA	analysis of variance
ANN	artificial neural networks
CMM	coordinate measuring machine
COC	cyclic olefin copolymer
CT	computed tomography
DoE	Design of Experiments
DTU	Technical University of Denmark
ECM	electro-chemical machining
EDM	electro-discharge-machining
ESR	Early Stage Researcher
EU	European Union
FEA	finite element analysis
FEM	finite element method
HTC	heat transfer coefficient
ICM	injection compression moulding
IM	conventional injection moulding
IR	infrared
MRR	material removal rate
MVR	melt volume rate
OFAT	one factor at time
Ph.D.	Doctorate of Philosophy
PC	polycarbonate
PDMS	polydimethylsiloxane
PET	polyethylene terephthalaye
PIV	particle image velocimetry
PMMA	poly(methyl methacrylate)
POM	polyoxymethylene
PP	polypropylene
PS	polystyrene

Abbreviation	**Meaning**
PVS	polyvinylsiloxane
RHCM	rapid heat cycle moulding
SEBS	styrene-ethylene-butylene-styrene
SEM	scanning electron microscopy
SS	sum of square
TPE	thermoplastic elastomer

1 Introduction and objectives

1.1 Introduction

The recent decades revolutionised the industrial world, which nowadays relies heavily upon the availability of micro systems. The discipline of manufacturing engineering responded to this need by developing the so-called micro manufacturing technologies, with the aim of producing miniaturized components in high volumes and in a cost-effective way. As such, micro manufacturing plays a central role in numerous engineering sectors, with applications in microfluidic devices, connectors, micro engines, micro pumps, surgery tools, medical implants, smartphones, sensors for automotive industry and hearing aid systems [1, 2].

Micro manufacturing is a complex engineering field that involves multi-material interactions as well as process chains spanning across different dimensional scales. To face these challenges, new manufacturing processes were developed either by inventing new principles or by adapting well-established conventional technologies to the micro scale. Micro injection moulding (µIM) belongs to the second category, being the miniaturized counterpart of conventional injection moulding (IM), which is based on the replication of the geometry of a mould with a polymeric material. µIM is capable of successfully combining the high throughput rate and net-shape production of IM with replication capabilities at micro-scaled accuracy, standing out as preferable manufacturing process for the fabrication of micro plastic components having geometrical features below the millimetre range [3–5]. The know-how derived from the 150-year old IM process was transferred to µIM, setting the basis for an extremely repeatable and productive technology that is already widely employed in the current industrial scenario. Targets of µIM are miniaturized parts as well as macro-scaled parts having structured surfaces, thus covering a large variety of key-enabler applications, spanning from micro gears to microfluidic devices (see Figure 1.1). Nowadays, µIM research focuses primarily on statistical control, in-line process monitoring, modelling, tooling technologies and processing of new materials, with the aim of enhancing accuracy and precision as well as pushing the technology capabilities to lower and unexplored dimensional limits.

As critical dimensions are scaled down in micro-manufactured components, their complexity also increases. Moreover, tolerance ranges become much tighter than for macro-sized parts, posing big challenges with respect to process optimization and compliance verification when conventional measuring instruments, which are not designed

to deal with such a small scale, are employed. These and other fundamental issues opened the door for the design of new measurement principles and instrumentations that allow coping with the challenges of the micro scale [6]. Nowadays, instruments such as atomic force microscopes (AFMs), micro coordinate measuring machines (µCMMs), micro computed tomography (µCT) machines and high-resolution optical microscopes are available to deal with miniaturized components. However, a big room for improvement remains open in the field of quality assurance of micro parts. This is particularly true for high-throughput replication processes such as µIM. In fact, a moulding cycle time is typically in the order of 5-20 s, while a measurement performed with an instrument having sub-micrometric resolution and three-dimensional capabilities takes minutes to complete. State-of-the-art industries tackle this unbalance by measuring a few randomly selected parts from the produced batch. This approach is particularly unsuitable for micro productions, where the micrometric tolerances require a total quality assurance since the outcome is typically much more sensitive to material and process setting variations. Therefore, it is of primary importance to reduce the off-line metrology effort that acts as bottleneck of micro manufacturing technologies. Novel solutions have to be conceived and applied in order to control the dimensional quality of each moulded part in-line, i.e. during the manufacturing procedure.

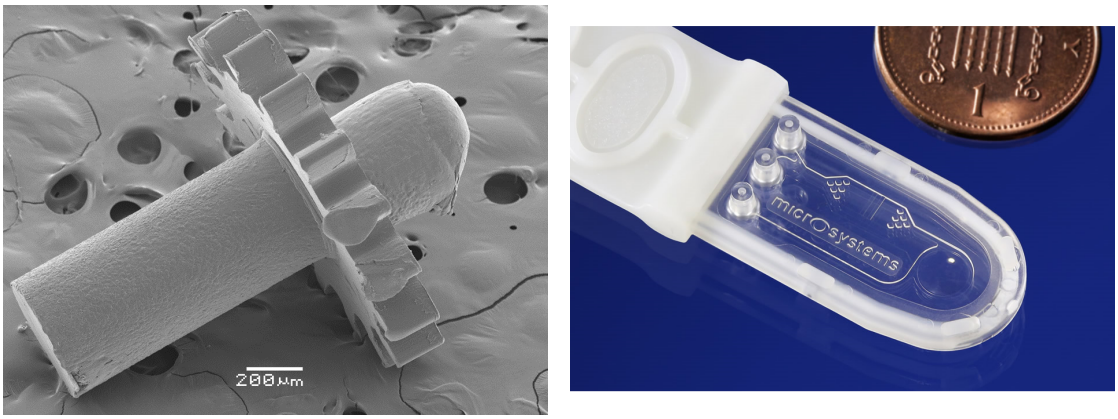

(a) **(b)**

Figure 1.1: Examples of micro plastic parts produced by µIM: (a) micro gear, (b) microfluidic platform [7].

1.2 Project definition and objectives

The present Ph.D. project aimed at tackling the aforementioned challenges in µIM quality assurance, thus advancing the technology beyond the current state-of-the-art. This was done by formulating and consequently implementing a novel approach based on the product and process fingerprint concept. The two are defined as:

- Product fingerprint: a unique dimensional outcome (a value of a particular dimension, a geometrical error, etc.) that is sensitive to process variations and correlated to the overall quality of the micro part. By controlling this specific feature, the conformance to specifications of all tolerances of the object can be achieved.
- Process fingerprint: a variable strongly correlated to the quality of the produced component and controllable in-line during the manufacturing procedure. By applying real-time monitoring techniques, the value of the process fingerprint can be measured at each cycle, thus giving valuable indications on the characteristic of each manufactured component without the need of additional off-line metrology operations.

The objective of the project was to combine the two concepts in order to implement a real-time process control aiming at zero-defect manufacturing in µIM. In particular, once the two fingerprints are identified, a closed-loop process can be established, thus eliminating the need for time-consuming off-line metrology tasks and significantly shortening the process optimization phase. Since this novel approach targeted the manufacturing moulding industry, real industrial moulded components were investigated.

In order to design and implement a process/product fingerprint framework, an extensive experimental campaign must be carried out, followed by a robust statistical analysis. The procedure can be broken into the following steps (see Figure 1.2):

- Experiments: the main µIM process parameters are varied according to a statistical design in order to identify the most significant ones. In fact, both product and process fingerprints must be sensitive to the variations of the process to act as an effective optimization tool.
- Process monitoring: during the experiments, data are collected using various types of sensors that can be either internal or external to the moulding machine architecture.
- Off-line metrology: the produced parts are characterized using a high-accuracy measuring instrument. In this phase, the selection of the product fingerprint candidates is carried out: the most relevant part features are measured and considered as possible product fingerprint.
- Processing of monitored data: starting from the time-curves of the variables that are monitored in-line, indicators capturing their most significant features are identified and considered as process fingerprint candidates.
- Analysis of product data: results of the off-line metrology phase are analysed. The candidate showing the highest sensitivity to process variation and being mostly correlated to overall part quality is selected as product fingerprint.

- Analysis of process data: the process fingerprint candidates are analysed with respect to process sensitivity and correlation to the dimensional quality of the produced part, and the one having both characteristics is selected.
- Definition of the in-line quality assurance strategy: product and process fingerprints are combined and a quality assurance procedure based on in-line monitored data is defined.

This framework was applied to two different industrial case studies: a 3D micro component and a laser nano-structured surface, both intended for medical applications. Therefore, the approach was tested when replicating both micro-scaled geometries and nanometric surface texture.

In parallel to this, µIM process simulations can be implemented in order to extend the fingerprint concept to a digital twin, thus making the process optimization totally virtual and, as such, much less time-consuming and more cost-efficient. The validation of the simulation results with respect to the real fingerprint is the primary challenge here.

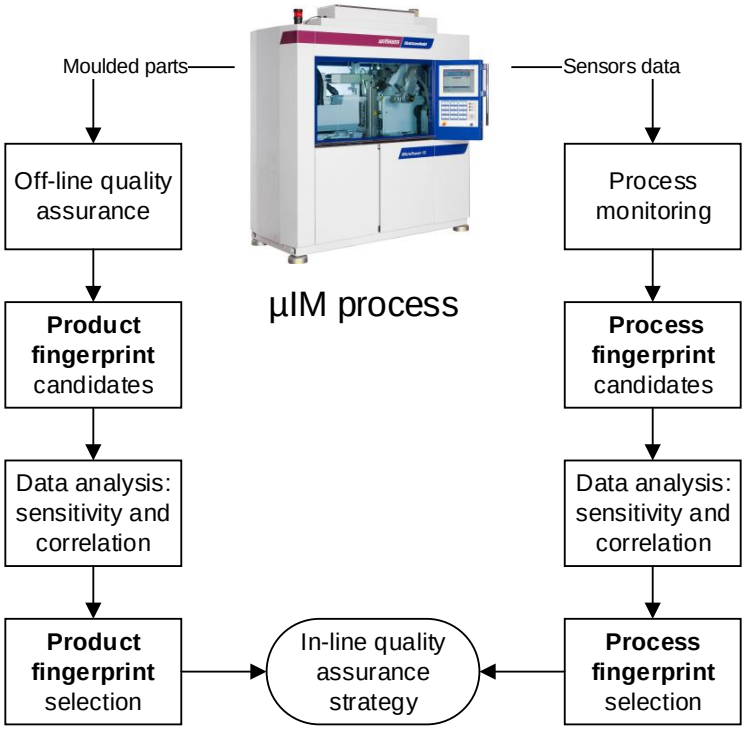

Figure 1.2: Flowchart representing the method used to identify product and process fingerprints leading to the definition of an in-line quality assurance strategy.

1.3 Research questions

The goal of this project was primarily to define an in-line quality assurance framework for industrial micro moulded components by applying the process/product fingerprint approach. In addition to this, the project also aimed at improving the µIM state-of-the-art, first by investigating the moulding capabilities of polymeric materials such as thermoplastic elastomers (TPEs), whose use in µIM applications was never thoroughly characterized in literature, and then by characterizing an indirect method for mould assessment based on the replica moulding technology. These two topics have high importance in the µIM scenario: on one hand, extending the technology capabilities to new materials is necessary to embrace the development of new industrial applications, on the other hand, a calibrated indirect method to assess the mould dimensions that are not accessible with high-accuracy instrument is strongly needed.

The new knowledge created in this Ph.D. project benefits both the scientific and the industrial communities of µIM, as it provided new insights on the technology and, at the same time, can be put into practice by the industry to improve the quality control systems. In particular, the following research questions were formulated:

- What is the precision and accuracy of µIM when micro moulding TPE? What are the effects of the main process parameters on the part geometry?
- How can the product/process fingerprint framework be effectively applied to a 3D micro component?
- Is it possible to define a clear in-line quality assurance strategy for this component based on the combination of product and process fingerprints?
- How can the product/process fingerprint framework be applied to the replication of a nano-structured surface?
- Is it possible to define a clear in-line quality assurance strategy for nano-structured surfaces?
- How can process simulations turn into a useful tool when dealing with the optimization phase of µIM?
- What is the accuracy of the replica moulding technology applied to micro milled mould features?

1.4 MICROMAN project

The research reported in this Ph.D. thesis was undertaken in the context of MICROMAN project ("Process Fingerprint for Zero-defect Net-shape MICROMANufacturing" [8]). MICROMAN is a European Training Network (ETN) supported by

Horizon 2020, the EU Framework Programme for Research and Innovation (Project ID: 674801). MICROMAN started in October 2015 and will end in October 2019.

The project, which included 8 European universities and 14 industrial companies as partners, funded a total of 13 Ph.D. projects undertaken by 13 Early Stage Researchers (ESRs). In particular, each one focuses primarily on a single micro manufacturing technology (see Table 1.1) and an industrial application, allowing MICROMAN to cover almost the totality of the existent miniaturized processes.

Table 1.1: MICROMAN project partners and investigated micro manufacturing processes. The present thesis is part of the work of ESR 1.

ESR no.	µ manufacturing process	Partner	Country
1	µIM	DTU	DK
2	µ polishing	DTU	DK
3	µEDM	KU Leuven	BE
4	µECM milling	KU Leuven	BE
5	µECM milling	TU Chemnitz	DE
6	µ plasma polishing	TU Chemnitz	DE
7	µ grinding	University of Bremen	DE
8	µIM	University of Bremen	DE
9	µ forming	University of Strathclyde	UK
10	µ extrusion	Politecnico di Milano	IT
11	µ metrology	University of Nottingham	UK
12	µ sintering	DTU	DK
13	µIM	University of Bradford	UK

The general aim of MICROMAN was the identification of the manufacturing fingerprint of the processes defined in the ESR projects, leading to an overall significant improvement in the European micro manufacturing scenario in terms of both quality and productivity. Being an ETN project, 8 workshops, each one focusing on a single process, were organized by the academic partners and attended by the ESRs in order to provide an all-round, yet specialized, training on micro manufacturing.

1.5 Structure of the thesis

This Ph.D. thesis is structured according to the different research branches that were developed during the project.

Chapter 2 is an overview of the state-of-the-art of µIM and the related key-enabler technologies. The micro tooling technologies and measurement techniques commonly used in combination with µIM are also presented, with particular emphasis given to the ones employed throughout the project.

In Chapter 3, a literature review on the latest development of µIM process optimization and monitoring is presented. The chapter also contains an overview of the effects of the most significant µIM process parameters on various characteristics of the moulded components.

Chapter 4 deals with the analysis of the precision and accuracy of µIM using TPE. The case study based on an industrial micro ring, which is part of a multi-material micro assembly, is outlined. The specifically designed multi-cavity mould is introduced along with the experimental approach. The results of the study are presented and a novel shrinkage behaviour of the micro ring identified. Functional tests were performed in order to identify a clear relationship between process settings and part functionality. An alternative process design based on micro overmoulding was also investigated with the aim of increasing the productivity of the final assembly.

The application of the product/process fingerprint framework to a 3D micro plastic component for medical application is discussed in Chapter 5. The monitoring approach and the fingerprint candidates selection are outlined in detail. The effects of µIM process settings variation on both product and process variables are analysed. Eventually, the fingerprints are identified and combined to generate the proposal of an in-line quality control strategy.

Chapter 6 presents the study aimed at applying the product/process fingerprint method to a micro moulded part featuring a laser nano-structured surface. A different process monitoring procedure based on flow visualization is described. The identification of proper surface topography parameters that are valuable for the characterization of the replication at the nano scale is also a focus of this chapter. The best fingerprint based on the flow visualization experiments is selected and an in-line control strategy for surface replication accuracy proposed.

In Chapter 7, all the work related to µIM process simulations is presented. The mathematical background and the state-of-the-art of the modelling approach are outlined. The simulation results and validation procedure are then dealt with, with particular attention to the prediction of the effects of µIM process parameters on functional geometries in both real and virtual domain.

Chapter 8 deals with the investigation of the capabilities of the replica moulding technology for the indirect measurements of mould micro features manufactured by micro milling. The replication performance of both surface texture and geometry is addressed by using specifically designed benchmark samples having the typical features of micro moulds.

Chapter 9 concludes the thesis by answering the research questions and giving an overview of the most important findings of the work. A view of the future research based on the thesis results is also outlined.

2 State-of-the-art of micro injection moulding and key-enabling technologies

An overview of the micro injection moulding process is given. The main differences with conventional injection moulding are described to highlight the peculiarities of the micro technology with respect to machine design, tooling, flow phenomena and replication accuracy. In the last part, the measurement solutions applicable to micro moulded parts are presented, with particular focus on the instruments used in the thesis, namely focus variation and confocal microscopes.

2.1 Conventional injection moulding

Conventional injection moulding (IM) stands out as the most common manufacturing process for the production of parts made of polymeric materials. Among its advantages, it enables the fast and extremely repeatable production of components featuring complex shapes and detailed features, making post-processing procedures in most cases unnecessary [9]. The process can be also fully automated, allowing the achievement of the extremely high throughput rates needed in mass-production.

A conventional injection moulding machine is divided into two parts [10]: the injection unit and the clamping unit (see Figure 2.1). The first one undertakes the task of melting the plastic compound, conveying the melt towards the mould and finally injecting it. The main component of the injection unit is the reciprocating screw. This screw has a peculiar geometry and, with its rotation, moves the melt forward and helps in generating the heat required for melting the plastic granules. Typically, 50 % of the required heat is generated by the friction created by the screw rotation. Electrical band heaters implemented on the outside of the barrel provide the other half. After enough polymer melt is prepared, the screw is shifted forward generating the injection pressure. A back-flow valve prevents the melt from flowing back inside the barrel.

The clamping unit presents two main components: the mould and the mechanical clamping. The mould holds a central role in the whole process since it enables the actual formation of the part by replication. It can have one or more cavities and

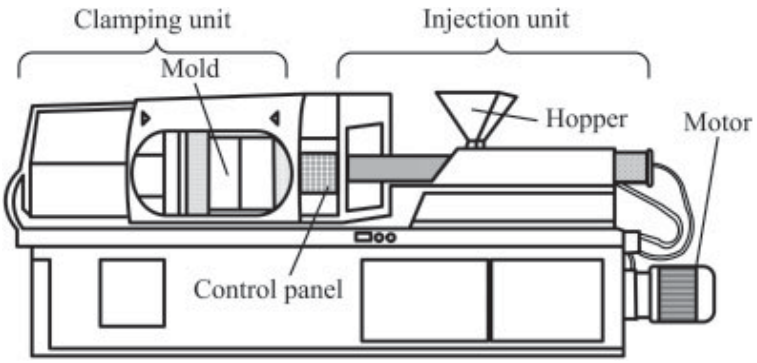

Figure 2.1: Schematic view of a conventional injection moulding machine: the main components are highlighted [11].

two or three plates, of which typically one is fixed and the others movable. The mechanical clamping has the task of keeping the mould plates closed while the melt is injected and opening them to eject the part [11]. Since the injection pressure can reach values close to 2000 bar, depending on the cavity size, forces of thousands of tons might be required to maintain the mould closed during the cycle.

The injection moulding cycle can be divided into five phases based on the machine procedures (see Figure 2.2) [9, 12]:

- Filling and packing: in this phase, the molten material is injected inside the mould cavity by the screw that moves forward providing the required pressure. After the end of the filling, more material is pushed into the mould during the packing phase in order to compensate for the shrinkage of the part that cools down and thus contracts.
- Plasticization and metering: after the packing is finished, the machine starts the plasticization and metering in order to prepare the shot of the following cycle. The screw restarts its rotation and moves backward to melt more material.
- Cooling: this phase runs in parallel to the previous one, and it involves the injected material that cools down because of the mould walls extracting the heat from the cavity, allowing the part solidification and consequent shrinkage.
- Mould opening: the mould opens once the part has reached the desired ejection temperature.
- Ejection: once the mould plates are open, the now solid part is ejected either mechanically or pneumatically.

Conventional injection moulding machines can be adapted to the manufacturing of micro parts. When this solution is adopted, the main issue relates to the minimum shot weight, which is typically one order of magnitude larger than the weight of a micro part for these machines [3]. Therefore, relatively huge sprues need to be

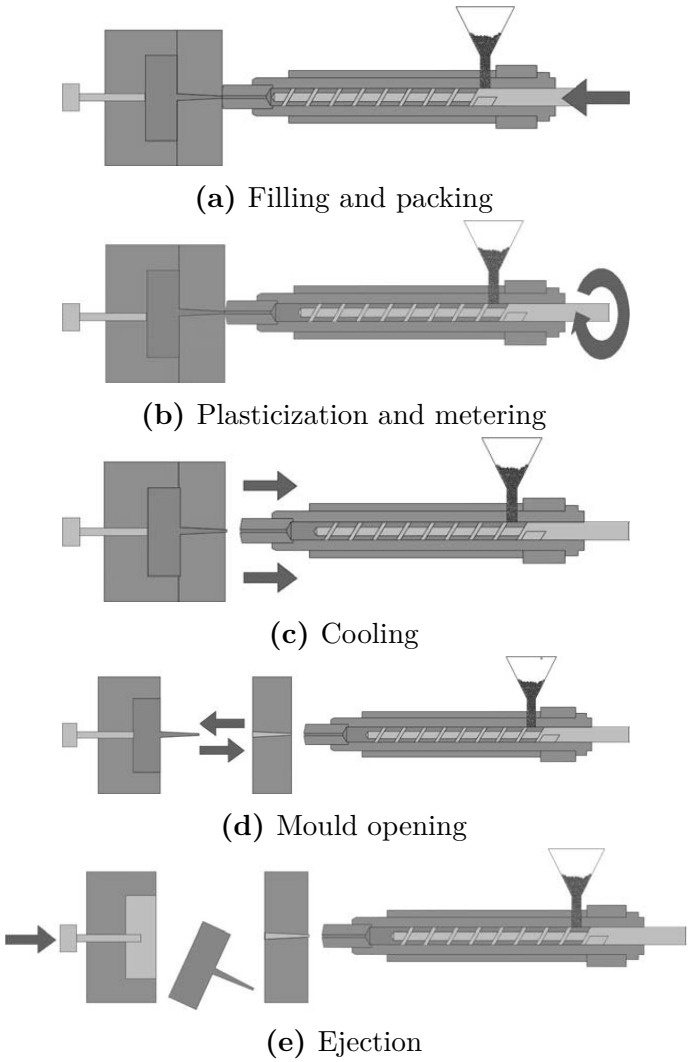

(a) Filling and packing

(b) Plasticization and metering

(c) Cooling

(d) Mould opening

(e) Ejection

Figure 2.2: The phases of the injection moulding cycle with a conventional machine [9].

utilized, leading to a relevant amount of wasted material. Moreover, it becomes extremely difficult to dose the right amount of material and control the filling process. The positioning accuracy of the reciprocating screw is usually not high enough to provide the shot-to-shot consistency required to meet the tight tolerances of micro productions. Finally, taking into account the very small shots needed to mould micro components, conventional injection moulding machines tend to cause prolonged residence times inside the barrel, leading to the risk of material degradation. For these reasons, dedicated micro injection moulding machines were developed and commercialized.

2.2 Micro injection moulding

In order to distinguish between conventional and micro injection moulding, it is of primary importance to fully define to which categories of plastic parts the term "micro" applies. The international moulding community has agreed on breaking down the scenario into three categories [13, 14]:

- Micro-structured parts: parts with outer dimensions in the millimetre range or larger, but featuring local structures in the micrometre range.
- Micro precision parts: parts with larger outer dimensions but tolerances in the micrometre range.
- Single micro parts: parts with outer dimensions in the micrometre scale and mass in the milligram range.

In terms of dimensional capabilities, µIM allows replicating features of various shapes (e.g. channels, pillars, grooves, ripples, holes) with dimensions down to the nano scale [15]. Figure 2.3 shows the attainable replication in lateral and vertical dimensions for the main polymer processing techniques. What can be clearly seen is that µIM extends the lower limits of conventional moulding. Moreover, it is also capable of producing features smaller than those manufacturable with other precision polymer processes such as injection compression moulding (ICM) and hot embossing. Soft lithography techniques are comparable to µIM in terms of attainable dimensions but also have much longer cycle times (2 minutes for nano imprint lithography [15]), making them not as suitable for mass production as µIM is.

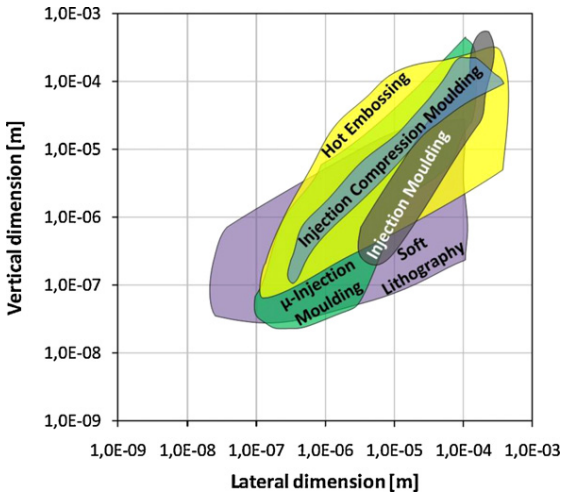

Figure 2.3: Replication capabilities of polymer processing techniques in terms of lateral and vertical dimensions [15].

The first phase of µIM history dates back to the 1985-1995 period [3]. In those days, conventional machines were used for manufacturing macro parts featuring micro

details. The increasing demand for miniaturized products drove both the academia and the industry to create new solutions that allowed producing single micro parts. This started the second phase of µIM development: from 1995 to 2000, dedicated µIM machines were designed and successfully introduced in the market. Minimum shot weights were drastically reduced and replication of small features could be finally achieved.

Nowadays, the µIM market accounts for circa 13 USD billions [16]. In the last five years, an annual growth rate of 600 USD millions was observed, demonstrating that the market for the technology is in rapid expansion. The segment with the highest potential is medical and healthcare, which accounted for 35 % of the total market in 2013 and is on a positive trend [16].

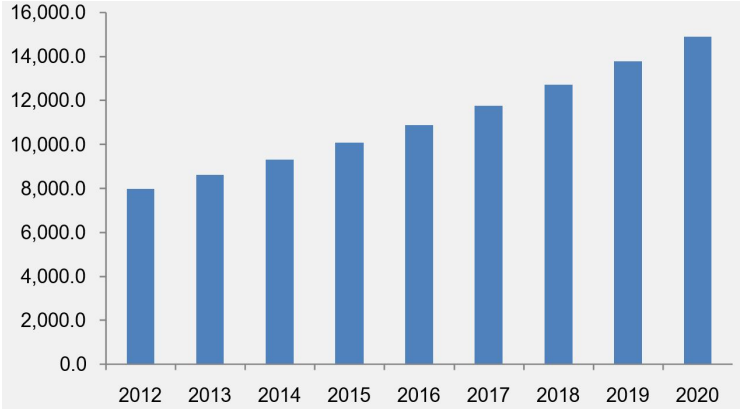

Figure 2.4: Global µIM market revenue in USD million from 2012 to 2020 [16].

Although µIM is mainly employed to produce components made of thermoplastics, the technology potential has also been extended to powder-based ceramics and metals [17]. In the present chapter, only the main application of µIM, i.e. polymeric materials, is considered and discussed.

2.2.1 Micro injection moulding machine

The main idea that allowed the downscaling of conventional injection moulding machines was the separation of the injection unit in two parts: a screw or a plunger for plasticizing and a piston for metering and injection. With this new architecture, the dosing of the polymer melt becomes extremely more accurate, since the separated injection plunger is much lighter and more controllable in comparison to the conventional reciprocating screw. Moreover, µIM machines embed fully electrical and consequently more precise drives, which allow achieving higher injection speeds that are important to fill the tiny mould details. The machine itself is smaller and lighter. Finally, a shorter residence time in the machine is achieved, thus helping in reducing the risk of material degradation. Due to the small cross section of the micro

moulded components, the maximum clamping force of these machines is extremely low, in the order of tens of tons.

Figure 2.5 shows two examples of micro injection moulding machines concepts developed by famous machine manufacturers: the "MicroPower" and the "formicaPlast", manufactured by Wittmann-Battenfeld (Kottingbrunn, Austria) and Klöckner DESMA (Achim, Germany) respectively. The first has a plasticization screw of diameter 14 mm, which has the function of melting and homogenizing the polymer, and an injection piston of diameter 5 mm, which drives the melt inside the cavity with high speed and pressure [18]. The second has two pistons: one for plasticization (diameter 6 mm) and the other for injection (diameter 2-5 mm) [19].

The phases of the moulding cycle (see Figure 2.2) are common to both the conventional and the micro technology.

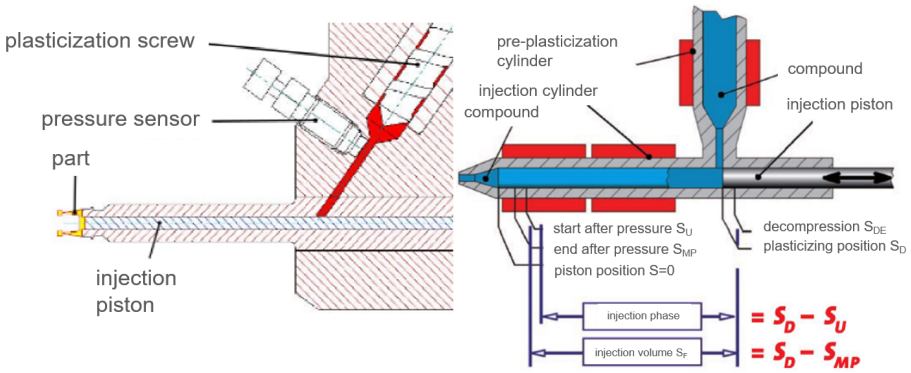

(a) MicroPower **(b)** formicaPlast

Figure 2.5: Schemes of two µIM machine concepts introduced by (a) Wittmann-Battenfeld [18] and (b) Klöckner DESMA [19]. In the second, a plasticization plunger replaces the plasticization screw.

2.2.2 Tooling for micro injection moulding

As all the replication processes, micro injection moulding relies on the availability of machining technologies for the manufacturing of high accuracy inserts and moulds. Traditional tooling methods, such as milling or electro-discharge-machining (EDM), are generally not capable of providing the accuracy required for the production of micro components. Therefore, new tooling techniques have been developed in the last two decades in order to meet the new demanding precision and accuracy requirements. Micro cutting technologies, laser machining, electro-chemical machining, µEDM, diamond machining and LIGA processes are nowadays commonly employed for the fabrication of micro moulds.

Table 2.1 summarizes the most common micro tooling technologies and their capabilities. Each process has peculiar advantages related to the achievable structure size, tolerance and aspect ratio. For example, ion beam LIGA produces the smallest structures but, on the other hand, the aspect ratio is limited, whereas x-ray LIGA manufactures bigger structures but with a much higher aspect ratio. Moreover, not all technologies are capable of machining a wide variety of materials. A characteristic that has to be taken into account is the material removal rate (MRR) of the tooling technique, which is directly connected to the machining time and thus the productivity. In this regard, micro milling stands out as fastest process [20, 21] and is thus widely employed in the micro mould making industry when features in the micrometre range are the target [22, 23]. µEDM is also widely used for manufacturing moulds having micro-scaled features [24], taking advantage of its thermal nature and the consequent insensibility to the hardness of the machined material, which turns particularly useful when a single micrometric accuracy is required.

Table 2.1: Micro tooling process used in µIM and their main capabilities. Adapted from [4].

Tooling technology	Structure size	Tolerance	Aspect ratio	Materials
Ion beam LIGA	0.1-0.5 µm	0.02-0.5 µm	1	Any
X-Ray LIGA	0.5-1.0 mm	0.02-0.5 µm	10-100	Electroformable materials
E-beam LIGA	0.1-0.5 µm	n/a	1-2	Electroformable materials
Femto-second laser	1 µm	<1 µm	1-10	Any
Short pulse ECM	few microns	<1 µm	8	Conductive materials
µEDM	10-25 µm	3 µm	10-100	Conductive materials
Micro milling	25 µm	3 µm	10-50	Metals and polymers
Deep reactive ion etching	n/a	<1µm	10-25	Silicon

When taking into account the mould architecture, one important difference between IM and µIM concerns the cooling phase. In fact, a complete filling of micro and nano structures normally requires a very high mould temperature. However, the setting of a high mould temperature comes with an extended cycle time due to the longer cooling time. Therefore, new techniques have been developed in order to have a hot mould during injection and a cold mould during the cooling phase, thus tackling

this issue. All these methods are addressed as variotherm systems [25], which are based on a great variation of the mould temperature during the injection cycle (see Figure 2.6). Different researchers and industries have investigated many heating methods: convection heating, radiation heating, conduction heating and induction heating have all been experimented. The employment of the variotherm process leads to several advantages, such as reduced flow-induced molecular orientation, weld lines minimization, morphology control and improved replication quality of high aspect ratio features [25].

In order to counteract damage due to thermal stress, adhesion and friction, which are particularly severe in µIM, surface coatings can be used to enhance the mould surface properties and consequently increase its lifetime [26]. Silicone oxide (SiO_x), alumina (Al_2O_3) and diamond-like carbon can be successfully used as protective coatings while simultaneously reducing the flow resistance [27].

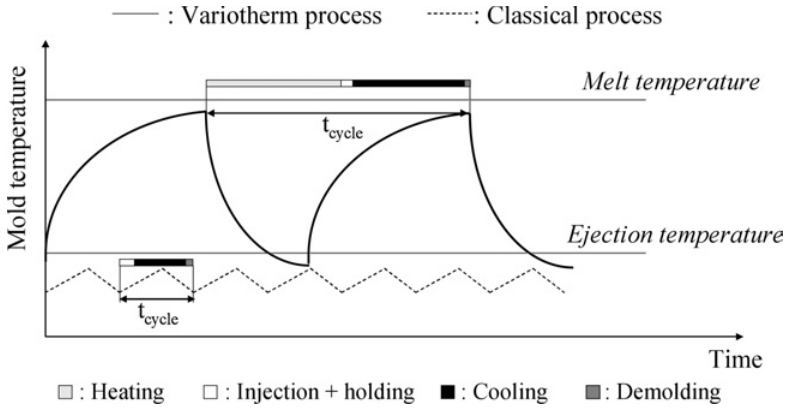

Figure 2.6: Comparison between mould temperature in the variotherm and conventional moulding process [4].

2.2.3 Peculiar flow phenomena in micro injection moulding

As IM is scaled down to µIM, new physical phenomena become important, whereas they were negligible in the macro scale. They arise because of the conditions experienced by the polymer melt when flowing in micro and nano geometries and are particularly important when modelling the process.

A first and major phenomenon that is typical of polymer flowing in micro and nano channels is the so-called wall slip. In injection moulding, the wall shear stress increases with the shear rate. When the wall shear stress exceeds a critical value, the wall slip phenomenon occurs [28–30], therefore invalidating the classical no-slip boundary conditions, i.e. a null velocity of the polymer melt on the mould walls. This is more likely to occur in µIM because of the small dimensions of the channels that in turn generate extremely high shear rates in the melt [31]. It has been shown that

the slip condition allows achieving a significant reduction of the injection pressure, thus increasing the capabilities of the moulding process for the design of thinner parts [32].

Another physical phenomenon that plays a more important role in µIM than in IM is related to the surface tension, which depends on the cohesive forces between the polymer molecules. As the cavity thickness decreases, the contribution of the surface tension at the melt front increases [33], thus influencing the pressure required to flow the polymer. In particular, it has been reported that the effect of surface tension cannot be neglected for channel sizes below 150 µm [34].

Finally, also the viscosity behaviour is affected by the size of the channel in which the polymer flows. In fact, significant increases in viscosities near the walls of micro channels (up to 130 % with respect to the bulk viscosity) have been observed. This is believed to be caused by either the high intermolecular interaction or the immobility of the molecular layers in contact with the mould surface [28, 31]. This generates an unbalance of viscosity that should be considered when modelling the material characteristics for process simulation purposes.

2.2.4 Precision and accuracy of micro injection moulding

As mentioned before, conventional injection moulding machines can be used to manufacture micro components. This typically happens when small production batches are needed and the investment cost related to the purchase of a µIM machine, which is less versatile, is not justified. Therefore, it is worth comparing µIM and IM when the same geometry is moulded in order to characterize the differences in terms of replication accuracy and precision.

In literature, no study reports a comparison between IM and µIM based on quantitative dimensional data. In fact, most researchers focused on morphological differences between micro and macro parts [35, 36], demonstrating that the dimensional scale of the moulded component strongly affects the size of the crystalline entities. A study was then carried out in order to investigate the discrepancies between the two technologies in terms of replication capability [37, 38].

Case study

The investigated micro part was a TPE component used in medical applications. Figure 2.7 shows the geometry of the micro part, which is cylindrical and has a through hole generated by a pin coaxial to the cavity. Four diameters are indicated: outer top diameter (ODt), inner top diameter (IDt), outer bottom diameter (ODb) and inner bottom diameter (IDb). In particular, ODt and IDb were considered for the comparison of replication accuracy and precision, while the others, along with

the two lengths L1 and L2, were used to calculate the volume of the produced parts for the density calculation. Being the dimensional tolerance specified as ±50 µm for the diameters and the nominal part mass equal to 20 mg, the component is indeed a micro plastic part according to the definitions given at the beginning of section 2.2. The polymer used for both IM and µIM experiments was a Thermolast® grade from Kraiburg TPE GmbH (Waldkraiburg, Germany) with a nominal density of 0.89 g/cm^3.

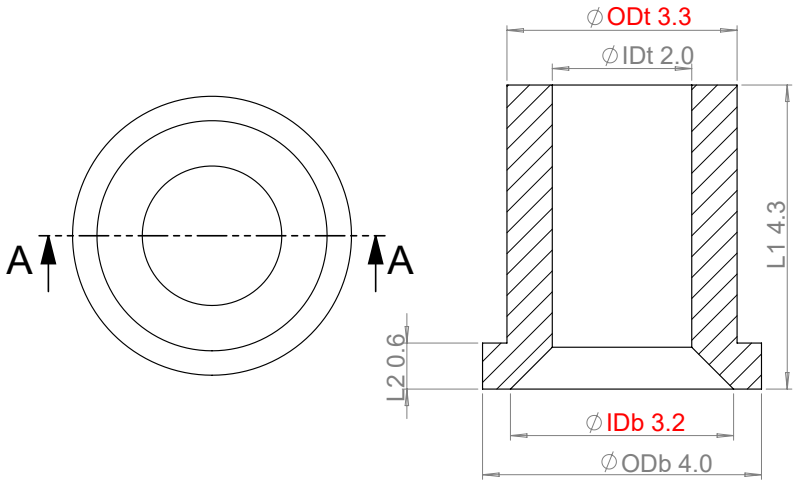

Figure 2.7: Micro part used for the comparison between IM and µIM. The measured dimensions are indicated with their nominal value in mm. The dimensions used in the replication accuracy comparison are indicated in red.

Experimental set-up

Conventional injection moulding experiments were performed using an Arburg Allrounder 270 U machine having an 18 mm diameter reciprocating screw and a maximum clamping force of 400 kN. This machine is equipped with hydraulic drives. A two-plate mould with four cavities was used as the master for replication (see Figure 2.8 (a)). The volume of the feed system was equal to 980 mm^3, accounting for 92 % of the total amount of injected polymer. The use of pin gates allowed to achieve automatic detachment of the parts from the feed system.

Micro injection moulding experiments were carried out with a state-of-the-art Wittmann-Battenfeld MicroPower 15 µIM machine (see Figure 2.5 (a)) that employs electrical drives and whose maximum clamping force is equal to 150 kN. A different two-plate mould with four cavities was used in this case (see Figure 2.8 (b)). The feed system was designed with a pin gate and had a volume of 174 mm^3 that accounted for 66 % of the total injected amount of TPE. It is clear that µIM allowed a significant reduction of the material waste (see Figure 2.9), thus representing a

valuable improvement with respect to production cost reduction. Table 2.2 shows the setting used for moulding with both the machines. The only difference between the two set-ups was related to the injection speed. In fact, a higher value was used with the µIM machine in order to balance for the smaller injection section. It is also worth noticing that adopting µIM allowed setting a shorter cycle time and thus increasing the throughput of the process.

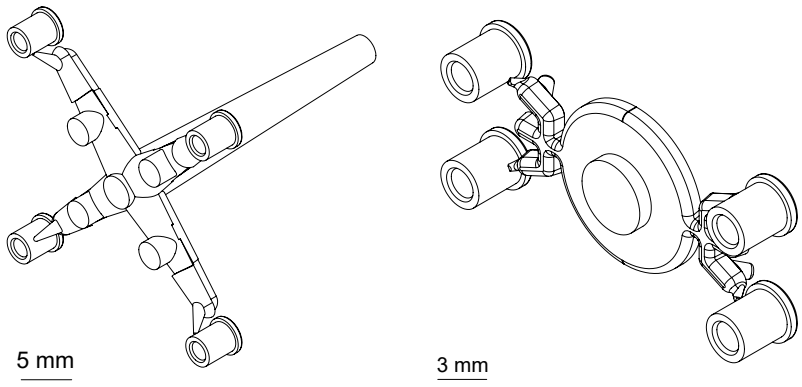

Figure 2.8: 3D views of the feed systems used in combination with: (a) the IM machine and (b) the µIM machine

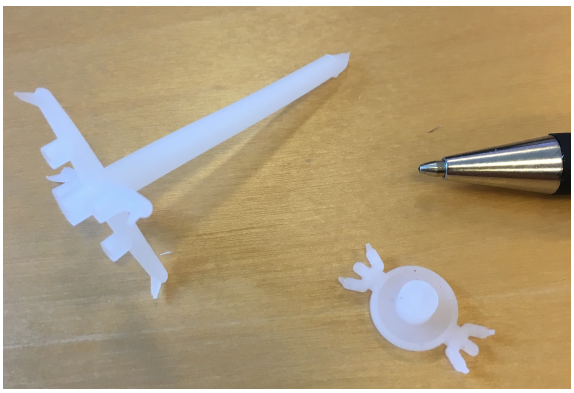

Figure 2.9: Comparison of the feed systems used for IM (left) and µIM (right).

Measurements

A precision scale having 0.1 mg resolution (AW220, Shimadzu Corp., Kyoto, Japan) was used to carry out mass measurements. After discarding the first fifty shots, ten parts were collected per each one of the four mould cavities and then weighed for both IM and µIM machines. The 80 moulded micro components were also dimensionally assessed. In particular, ODt and IDb were measured using a 3D focus variation microscope (Alicona InfiniteFocus) with a 5× magnification objective (see

Table 2.2: Optimized process parameters for IM and µIM.

Process parameter	IM	µIM
Injection speed/(mm/s)	40	160
Holding pressure/bar	350	350
Melt temperature/°C	220	220
Mould temperature/°C	40	40
Cycle time/s	17	8

subsection 2.3.2 for details on the instrument characteristics). In particular, the top and bottom sides of each part were acquired and then levelled by applying a 1st order planar correction. This operation consisted of subtracting the planar deviation, identified as the least square plane fitted to the original point cloud, from the raw acquisitions. After that, the two measurands were extracted by fitting the points corresponding to the circles of interest using the image processing software MountainsMap® (Digital Surf, Besançon, France). Each acquisition was repeated three times in order to provide statistical robustness to the output. The other dimensions IDt, ODb, L1 and L2 (see Figure 2.7) were measured using an optical CMM with 0.5 µm lateral resolution (DeMeet 220, Schut Geometrical Metrology, Groningen, Netherlands).

Cavities of both IM and µIM moulds were measured with an optical microscope featuring 2.6 µm lateral resolution (Infinity X-32, DeltaPix, Smørum, Denmark). ODt was measured on the mould cavities, while IDb on the pins. This procedure was necessary in order to characterize the replication of the two processes. In fact, the mould geometries were calibrated and a reference for the replication was obtained. The effect of any difference among the dimensions of the four cavities was thus eliminated from the comparison of the two technologies.

Results

The replication accuracy was evaluated with the variable Δ_D, which was defined as:

$$\Delta_D = \frac{D_{polymer} - D_{mould}}{D_{mould}} \tag{2.1}$$

where $D_{polymer}$ is a diameter measured on the parts and D_{mould} is the correspondent geometry measured on the mould. The use of this replication indicator allowed to get rid of the influence of any deviation between different cavities when comparing the two processes.

Figure 2.10 (a) shows the replication results for IDb. In general, µIM allowed achieving better replication than IM. In fact, Δ_{IDb} was always closer to zero and therefore the produced parts were more similar to the mould dimensions when using µIM. This was because the filling phase was more efficient as a result of the faster injection and the holding phase was more effective due to faster switch-over and smaller injected volume. Concerning cavity balance, both the technologies resulted in an accurate multi-cavity replication process: the interval bars overlap for the four cavities of IM and µIM. Even when considering the precision of the two processes, µIM was advantageous, being the distribution of all Δ_{IDb} data narrower than for IM (see Figure 2.11 (a)).

Figure 2.10 (b) shows the replication results for ODt. As for IDb, µIM generally provided better replication. However, this conclusion is not as straightforward as before: a certain discrepancy between the different cavities was present for both processes. In particular, cavities 1 and 3 of IM were replicated with a level comparable to µIM, while cavity 2 and 4 resulted in a lower replication performance, demonstrating also the presence of cavity unbalance. µIM also provided results that varied with the cavity number, though less than the other process. As regards the precision of Δ_{ODt} results, the distribution resulting from µIM experiments was once again narrower than that of IM (see Figure 2.11 (b)). Differently from the previous case, the two distributions overlap, meaning that the replication performance of the two technologies was comparable.

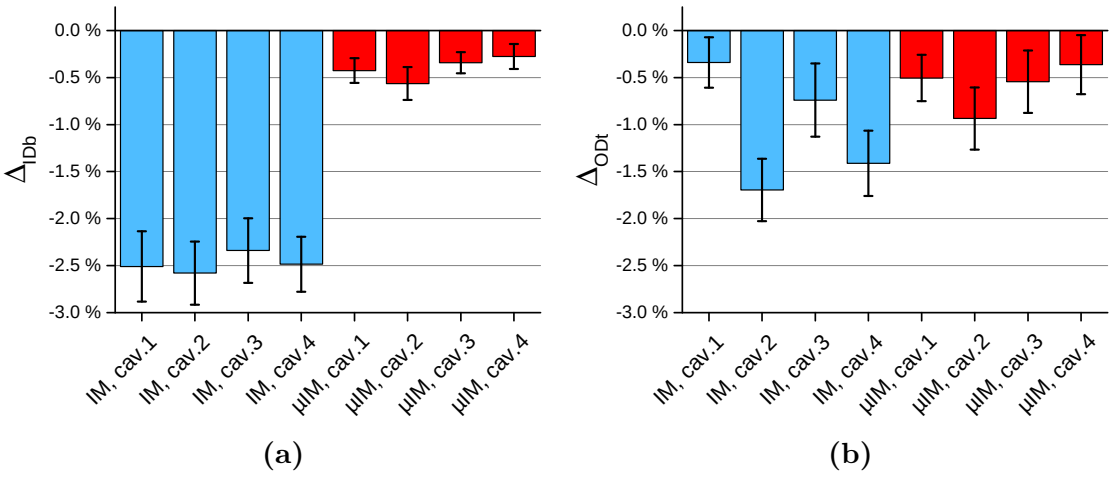

Figure 2.10: (a) Δ_{IDb} and (b) Δ_{ODt} results for IM (light blue) and µIM (red). The interval bars indicate the 95 % confidence intervals for the mean.

When comparing the replication level of IDb and ODt, it is possible to observe that the benefit introduced by the µIM machine was more pronounced for IDb. In fact, for ODt, there was not the same replication improvement observed for IDb. This might have been caused by the fact that IDb was obtained by replicating an internal geometry (i.e. the pin), while ODt by replicating an outer geometry (i.e. the external

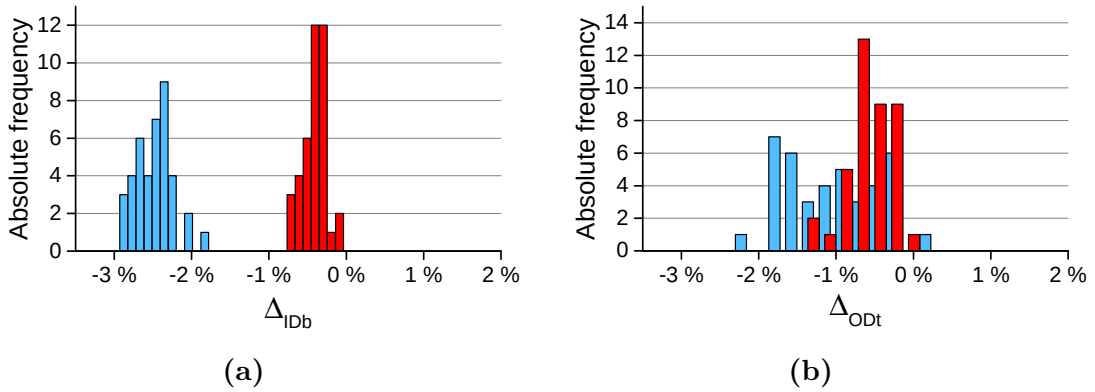

Figure 2.11: (a) Δ_{IDb} and (b) Δ_{ODt} absolute frequency distributions for IM (light blue) and µIM (red).

cavity). Thus, the polymer was free to shrink in correspondence with ODt but not with IDb, since the presence of the pin did not allow a free deformation of the injected part. A condition of constrained shrinkage typically generates a concentration of residual stresses on internal geometries (e.g. holes) that increases the shrinkage of the moulded part once it is ejected. Being the shrinkage amount of IDb substantially decreased when applying µIM, it may be possible that the use of µIM instead of IM allowed reducing the residual stresses.

Along with the replication accuracy of IDb and ODt, the density of the parts moulded with IM and µIM was also determined as the ratio between the measured mass and the volume. In particular, the volume of a single part was calculated in an approximate way as:

$$V_{\mathrm{part}} = \pi \frac{\mathrm{ODt}^2 - \mathrm{IDt}^2}{4}(\mathrm{L1} - \mathrm{L2}) + \pi \frac{\mathrm{ODb}^2 - \mathrm{IDb}^2}{4}\mathrm{L2} \tag{2.2}$$

The results of the density calculations are reported in Figure 2.12. What stands out is that the parts moulded with µIM had a significantly higher density, closer to the nominal value of the material data-sheet equal to 0.89 g/cm^3. The reason for this lies in the more efficient holding phase achieved with the µIM machine. In fact, the scope of this phase is to minimize the shrinkage of the moulded part by decreasing the reduction of specific volume suffered by the polymer melt. Therefore, a more efficient holding yields a higher density of the moulded part. The smaller injected volume played a central role here: being the mould temperature equal in the two cases (see Table 2.2), the smaller feed system adopted in combination with the µIM machine allowed to postpone the freezing of the gate, thus leaving a wider window open for the action of the holding pressure.

As regards the dispersion of the results, it is evident that parts produced with IM had a more heterogeneous density, proving that the adoption of µIM was also beneficial

with respect to repeatability. This was most probably caused by the enhanced precision of the µIM machine due in turn to its electrical drives, lighter injection piston and more homogeneous polymer melt.

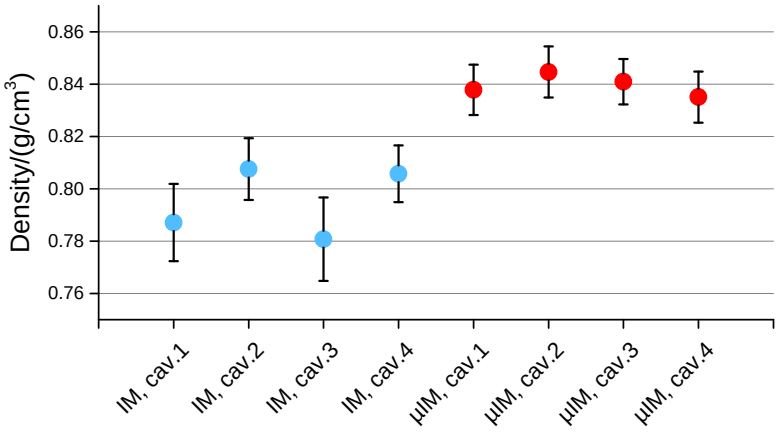

Figure 2.12: Density calculations for IM (light blue) and µIM (red). The interval bars indicate the standard deviations of the ten measured parts.

Conclusions

The comparison between IM and µIM based on dimensional and density outcomes allowed to draw important conclusions on the differences between the macro and micro scale technologies:

- Adopting µIM instead of IM resulted in a consistent reduction of material waste due to a smaller feed system (155 mg against 873 mg).
- For the inner diameter IDb, µIM provided a relevant improvement in terms of replication accuracy and more precise results.
- For the outer diameter ODt, µIM led to an improvement, though less relevant than for IDb.
- As revealed by the density calculations, µIM produced parts having a higher and more repeatable density, proving that a more efficient holding phase was attained with the µIM machine.

These observations clearly demonstrated that, when micro plastic parts are manufactured, adopting µIM instead of IM carries substantial benefits with respect to production quality. This quantitatively proves that µIM is indeed the preferable choice in terms of product and process performance.

2.3 Micro injection moulding key-enabling technologies

A significant challenge introduced by the downscaling of conventional injection moulding is related to quality assurance. In fact, the dimensional scale of moulded micro components and the involved tight tolerances (usually in the order of ±10 µm and below) require extremely accurate and precise instruments in order to verify the production quality. Assessing surface topography has also become of primary importance. This particular field has evolved consistently in the last fifteen years [39] since more and more structured surfaces are needed in the market. Therefore, nanometric resolutions and three-dimensional measuring capabilities are both necessary, and new measuring solutions have been developed accordingly throughout recent decades [6].

Table 2.3 shows examples of measuring systems used for assessing the quality of micro moulded parts. Optical instruments are the most common. It is also worth noticing that all the listed instruments can only perform off-line, i.e. after the part has been moulded. This limitation is related to the measuring time, which is, in all cases, much longer than a single moulding cycle, and to the high sensibility to phenomena, such as vibrations, that are common in a production environment. Examples of in-line measurements of moulded parts in literature are based on 2D camera systems and are only applicable to macroscopic components [40].

Table 2.3: Measuring solutions for micro injection moulded components.

Measurand	Instrument	Reference
Height of micro pillars	3D optical profiler	[41]
Height of micro features	3D optical profiler	[42]
Surface topography	3D optical profiler	[43]
Step height and diameters	CMM	[44]
Area of pores in a micro filter	Confocal microscope	[45]
Replication quality	Confocal microscope	[46]
Height of micro pillars	AFM microscope	[47]
Surface topography	AFM microscope	[14]
Height and width of micro features	AFM microscope	[48]
Weld lines depth	Focus variation microscope	[49]
Weld lines position	Optical CMM	[50]
Diameters, widths and thicknesses	CT	[51]
Dimension of micro pillars	White-light interferometer	[52]

In general, the instruments used in micro and nano metrology can be classified according to their underlying physical principles. Five categories can be identified [6]:

- interferometry

- microtopography measuring systems:

  stylus profilometers

  optical instruments

- Scanning electron and scanning probe microscopy
- light scattering methods
- other techniques

Figure 2.13 shows the measurement capabilities of some of the aforementioned instruments. It is worth noticing that traditional CMMs, which represent the preferable solution to perform accurate form measurements in the macro scale, are limited to dimensions above the micrometre range.

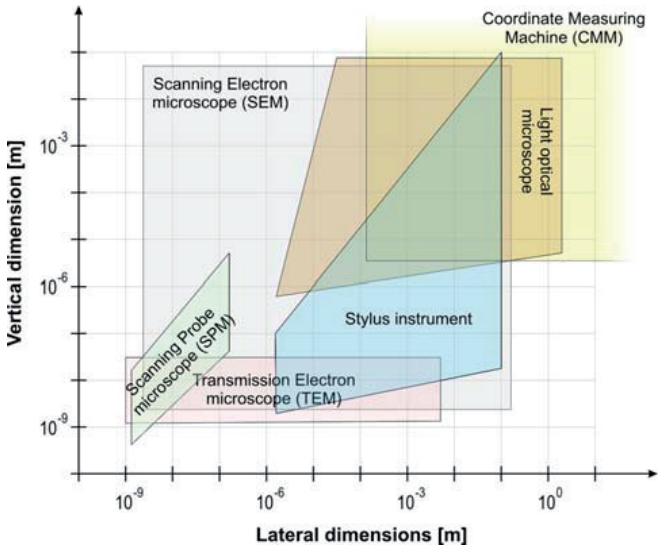

Figure 2.13: Capabilities of measurement instruments in the micro and nano scale [6].

Both focus variation and confocal microscopes are optical instruments and thus belong to the second class. Optical instruments are relatively new devices that are often designed for surface topography measurements [53]. Their main advantages with respect to conventional contact profilometers are contact-less nature, shorter measuring time and versatility. In particular, the absence of any physical contact between the sample and the instrument turns very useful when micro components are the target. Finally, they allow a direct 3D surface texture measurement. In fact, surface topography can be either described by a profile measurement of by an areal texture measurement. The first is a mono-dimensional characterization and its output is a height function $z(x)$ defined across a line on the surface. The second one is bi-dimensional and describes the surface as a height function $z(x,y)$ defined across planar coordinates. Only the second type of measurement is capable of fully

characterizing the topography, having more statistical value and providing a more realistic 3D representation of the surface [54].

The limitations of optical instruments are mainly related to the optics: different types of aberration can affect the lenses, while the limited numerical aperture of the objectives sets an upper limit for the detectable slope of the measured surface [54]. Another limitation is due to the lateral spatial resolution: the minimum distinguishable distance on the plane perpendicular to the microscope axis is limited by diffraction. In other cases, is the pixel size that defines the lateral resolution limit. An ulterior drawback of optical instruments is related to their complicated working principles, which often make them a "black-box" for the users. In fact, few existing models are able to describe the transfer function of these instruments. This is mainly due to the difficulty of accurately modelling the electromagnetic phenomena involved in the measurement procedure.

The next sections focus on the typologies of optical instruments that were mostly used in the project, namely confocal and focus variation microscopes.

2.3.1 Confocal microscopes

Confocal microscopes are optical instruments suitable for 3D measurements of surface topography. To perform the measurement, the surface of the object is scanned point by point by a measuring beam and the collected image is filtered through a pinhole that eliminates out-of-focus light, thus maximizing the quality of the acquisition [55]. This procedure is carried out by a photodetector that provides a high signal when the surface is on the focal plane. In order to measure the height at each scanned point, the objective moves along the vertical axis, therefore sectioning the sample with multiple imaginary planes. For each planar coordinate (x,y), the vertical coordinate z where the highest of the signals is recorded, corresponds to the height location of the 3D surface [54].

Several different commercial confocal microscopes exist and they can be grouped in three main classes: laser scanning microscopes, disc scanning microscopes and programmable array scanning microscopes [54]. Only the first one is here described since one of the instruments used in this project belongs to this category.

In a laser scanning confocal microscope, a laser beam illuminates a pinhole whose image is generated on a point of the sample on the focal plane. The reflected light turns back and it is imaged on a second pinhole called confocal aperture. Here the detector records the signal and calculates the height of the measured point [54]. Figure 2.14 illustrates the scheme of this type of system. The size of the pinhole is an important parameter since it determines the illuminated area on the sample surface. As light source, a laser with a wavelength as short as possible has to be used and thus diode lasers are frequently adopted.

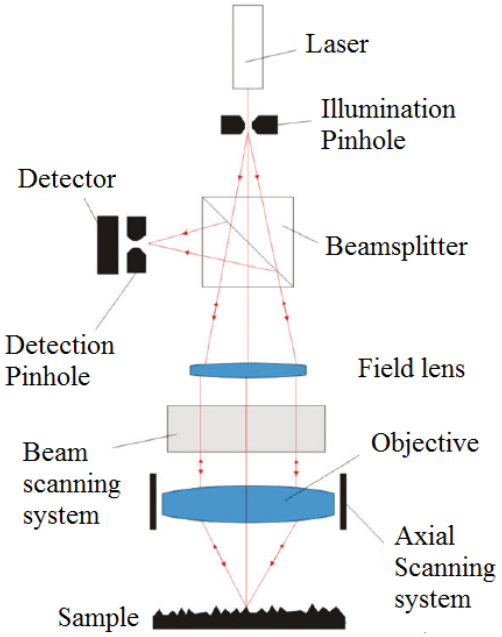

Figure 2.14: Scheme of a laser confocal microscope [54].

The main advantage of this type of instruments is the high numerical aperture of the objective, which determines a high measurable maximum slope of approximately 75° [6]. This characteristic turns particularly useful when complex structured surfaces are measured. On the other hand, the system is sensitive to vibrations and must be properly isolated. When measuring smooth tilted surfaces, a tilting stage to restore the perpendicularity between the surface and the optical axis is recommended [54]. A crucial point of the measurement procedure is setting the best optical parameters. In particular, they must be set depending on the nature of the surface: if the material is very reflective, a low level of light intensity should be selected to avoid saturated pixels and spikes. Other problems regard optical aberration and diffraction, which might give an artificial concavity to the acquired surface.

In this project, an Olympus Lext OLS4100 laser scanning confocal microscope was used to measure surface topography at the nano scale (see Figure 2.15). This instrument exploits two light sources: a laser having a wavelength of 405 nm and a coherence scanning interferometer. The data provided by the two sources are combined into the final acquisition.

Table 2.4 shows the main properties of the microscope for each of its objective lenses. The declared vertical resolution is 10 nm and equal for all the magnifications.

Figure 2.15: Olympus Lext OLS4100 microscope [56].

Table 2.4: Main properties of Olympus Lext OLS4100 objective lenses.

Magnification	Field of view/µm	Numerical aperture	Working distance/mm	Lateral resolution/µm
5×	2560×2560	0.15	20	0.62
10×	1280×1280	0.30	11	0.31
20×	644×644	0.60	1	0.16
50×	258×258	0.95	0.35	0.06
100×	129×129	0.95	0.35	0.03

2.3.2 Focus variation instruments

Focus variation instruments use vertical scanning with limited depth of focus. This technology is relatively new in the measurement field, and its fast and spread commercial success is mainly due to the ability to measure both roughness and 3D form [57]. The main components of a focus variation instrument are shown in Figure 2.16.

The height measurement is carried out by searching the best focus position of the objective pointing at the sample [54]. The relative movement between sample and scanning objective generates a change of focus correlated to a change of contrast captured by a CCD sensor. Once the curve of the contrast along the vertical axis has been determined, it is possible to calculate its maximum and thus obtaining the height of the sample in that specific pixel. By repeating this process for each optical element, it is possible to reconstruct a surface entirely. For each pixel, the amount of focus can be evaluated by means of the following general equation:

$$\mathrm{F}_z\left[x, y\right] = \mathrm{FM}\left[\mathrm{reg}_{\mathrm{w}}\left[\mathrm{I}_z, x, y\right]\right] \tag{2.3}$$

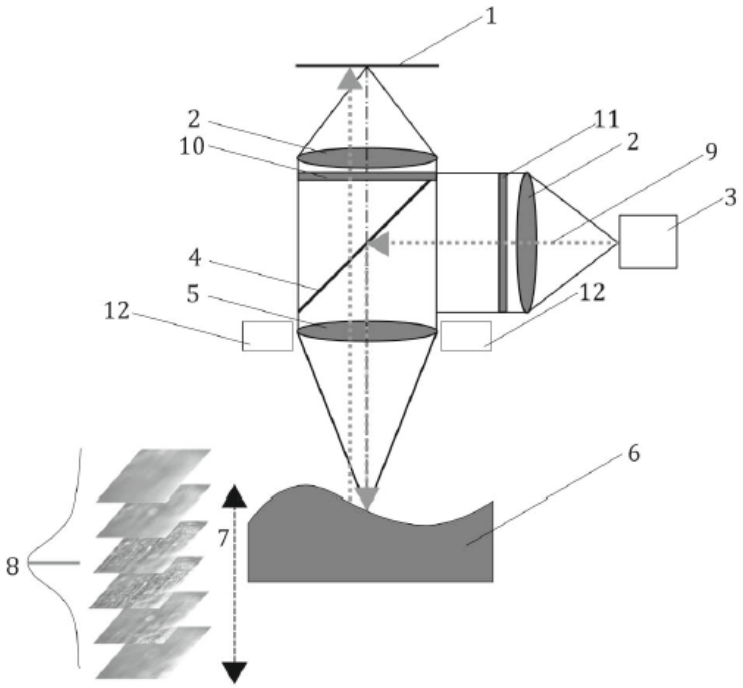

Figure 2.16: Scheme of a basic focus variation instrument: (1) CCD sensor, (2) lens, (3) white light source, (4) semi-transparent mirror, (5) objective lens, (6) sample, (7) vertical displacement provided by the driving unit, (8) contrast curve, (9) light emitted by the illumination unit, (10) optional analyzer, (11) polarizer and (12) optional ring light [54].

where I_z is the content of the image, which represents the input, along with the plane coordinates, of reg_w, a region operator. The information extracted by this operator is then used to calculate the amount of focus through the focus measure FM [54]. After this computation, a focus curve is defined: the z coordinate at its maximum is extracted with a numerical maximization method and the height measurement of the point is obtained. This procedure is carried out at each pixel in order to completely reconstruct the surface topography of the sample.

The main advantage of focus variation instruments is their versatility. Due to their relatively high working distance, complex components can be placed under the objective lenses. Moreover, these instruments can successfully acquire tilted surfaces [58], whereas confocal microscope cannot [59], making them suitable also for the measurement of 3D geometries such as edge radii. Moreover, being the illumination source a white light, the instrument also provides information on the colours of the sample. There are two main limitations to focus variation microscopes. The first is related to the impossibility of measuring translucent and transparent materials. The second concerns the inferior limit on the detectable roughness: since the CCD sensor must observe enough contrast to perform a measurement, a very

small topography variation is not captured. Therefore, these instruments are not advisable if very smooth surfaces (Ra<100 nm [59]) are targeted.

In this project, an Alicona InfiniteFocus focus variation microscope was used to measure micrometric geometries (see Figure 2.17). Table 2.5 shows the main properties of the microscope for each of its objective lenses. The vertical resolution must be set at the machine interface before each acquisition.

Figure 2.17: Alicona InfiniteFocus microscope [60].

Table 2.5: Main properties of Alicona InfiniteFocus objective lenses.

Magnification	Field of view/µm	Numerical aperture	Working distance/mm	Lateral resolution/µm
5×	2858×2175	0.15	22	1.75
10×	1429×1088	0.30	16	0.88
20×	714×542	0.40	13	0.44
50×	288×218	0.55	10	0.18
100×	146×111	0.80	3.5	0.09

When comparing the characteristics of the confocal and the focus variation microscopes, the major notable difference concerns the lateral resolution. Olympus Lext allows achieving a resolution three times smaller than Alicona, thus being the preferable choice when finely-spaced surface textures have to be assessed. On the other hand, the larger working distance of Alicona allows measuring complex components, whereas only flat specimens can fit under the 50× and 100× lenses of Olympus Lext (see Table 2.4).

3 Process optimization and monitoring in micro injection moulding

The most recent advances in µIM process optimization and monitoring are presented in this chapter. As for process optimization, the effects of the main µIM process parameters on the quality of micro moulded parts are described and discussed. The statistical optimization approach used throughout this project (Design of Experiments) is also described. As for process monitoring, the main techniques for in-line µIM monitoring are highlighted, with particular attention to their link to part quality and thus to their potential use in a product/process fingerprint framework.

3.1 Process optimization in micro injection moulding

Process optimization is defined as the discipline of adjusting a process in order to optimize a specific set of outputs. In manufacturing, various process parameters can be tuned to attain a product having the desired characteristics (e.g. physical properties, geometry, chemical composition, etc.), which represent the outputs. Process optimization relies on the determination of a connection between process parameters and the outputs. In order to establish this connection, the effect of the single input parameters and their interactions must be understood and characterized.

3.1.1 Micro injection moulding process parameters

µIM, as its macro counterpart, has a large number of parameters that can be tuned. The most important ones are [61, 62]:

- melt temperature, T_{melt}
- mould temperature, T_{mould}
- injection speed, v_{inj}
- holding pressure, p_{hold}

- holding time, t_{hold}

The melt temperature is defined as the temperature of the polymer melt entering the mould. In a µIM machine, this parameter can be typically set at different locations by means of electric heaters and thermocouples: at the screw, at the metering system and at the nozzle [46] (see Figure 3.1).

The mould temperature is the temperature of the mould, which can be set on both fixed and movable halves (see Figure 3.1) and also on the middle plate if a three-plate system is used. The heating of the mould is typically performed using heating cartridges since high T_{mould} values are typically needed in µIM. Other solutions such as convection, radiation and induction heating are also used. The variation of T_{mould} over a moulding cycle has a big impact on properties such as surface quality, shrinkage and weld lines [25]. With this respect, conformal cooling channels can be exploited to reduce the cycle time while, at the same time, keeping a high T_{mould} during the filling and holding phases [63].

The injection speed is the speed of the injection plunger, which drives the polymer melt inside the cavity (see Figure 3.1). Its value, along with the plunger diameter, determines the flow rate and consequently the filling time. As the plungers of µIM machines are much lighter than the reciprocating screws of conventional machines, higher levels of v_{inj} are achievable. Typically, a profiled injection speed can be given at the machine interface in order to balance for abrupt changes of sections in the cavity.

The holding pressure is the value of the pressure during the holding phase of the moulding cycle. There are various criteria for defining the switch-over point, i.e. the switch from the velocity-controlled filling to the pressure-controlled holding. In fact, it can be based, for instance, on the values of screw position, injection time and injection pressure [64]. µIM machines are capable of performing faster switch-overs than conventional ones since the smaller inertia of the injection plunger with respect to conventional reciprocating screws leads to a shorter response time.

The holding time is the time of application of the holding pressure after the filling of the cavity has been completed. A longer t_{hold} might benefit the part quality in terms of shrinkage reduction, provided the gate is not yet frozen, happening that makes the application of p_{hold} useless. Being the surface-to-volume ratio of micro components much higher than that of macro ones, the solidification of the polymer melt happens much more quickly, thus making the tuning of the holding time particularly difficult. Therefore, the effect of this parameter is not often investigated in µIM experiments.

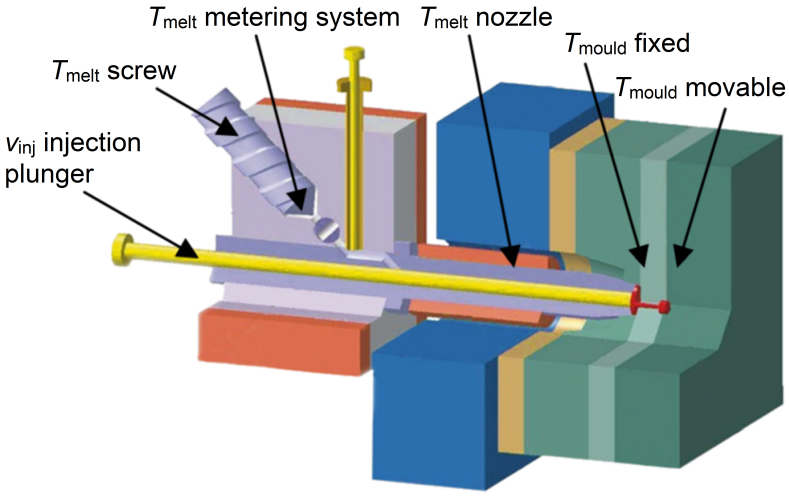

Figure 3.1: Locations of moulding parameters settings in a µIM machine. Adapted from [46].

3.1.2 Effects of the variation of micro injection moulding process parameters

As for IM, changing the settings of the µIM process parameters has a big impact on the quality of the moulded product. Each of the aforementioned parameters has a distinct effect on the characteristics of the final part.

Melt temperature

The effect of T_{melt} is directly related to the dependence of viscosity on temperature. Viscosity is the most important property of a polymer melt with respect to injection moulding applications and describes the resistance to flow [65]. Therefore, a higher viscosity value leads to the need for a higher pressure to flow the material inside the mould channels. Being the cavities particularly small in µIM, the reduction of viscosity is of primary importance to fill the cavity completely. With this respect, tuning T_{melt} turns useful. In fact, an increase in temperature causes a decrease of viscosity since the free volume between the polymer molecules increases, thus lowering the intra-molecular friction [66] (see Figure 3.2). For this reason, setting a high melt temperature generally facilitates the filling of the cavity. The setting of this parameter also influences some of the most common defects of moulded parts such as sink marks, glass fibre streaks, gloss appearance, weld lines, jetting, dark spots and flash formation [9]. In most cases, selecting a higher T_{melt} helps in reducing the size of these defects. However, the melt temperature is superiorly limited by the occurrence of material degradation and thus its value must be optimized within a limited process window.

In µIM literature, the increase of T_{melt} has been reported as beneficial for micro feature replication [67], mass maximization [68], shrinkage reduction [69] and flow length enhancement [70].

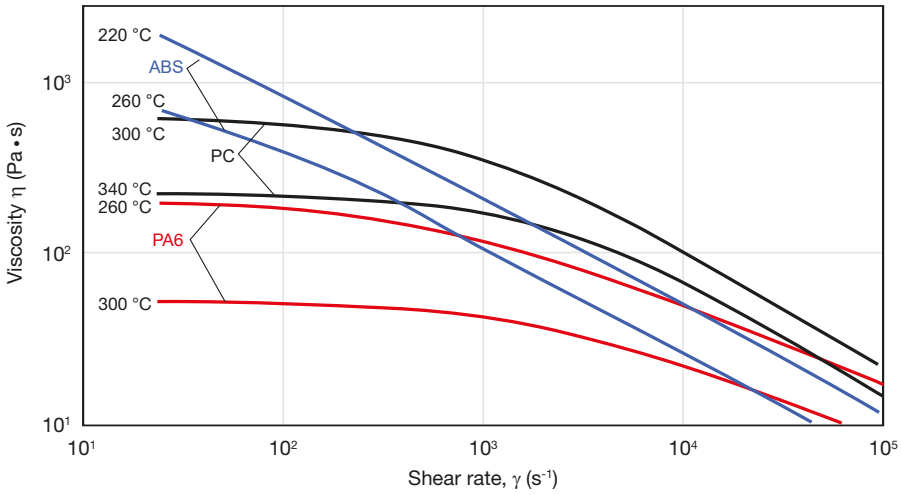

Figure 3.2: Viscosity curves for various polymers at different temperatures [66].

Mould temperature

In µIM, the cooling of the polymer is more rapid than in IM, since the surface-to-volume ratio of the produced parts is much higher [4]. This results in a great increase of viscosity that in turn hinders the complete filling of the cavity. Therefore, having a hot mould surface is of primary importance, particularly when micro or nano structures are replicated [41, 47, 48, 52, 71, 72]. A hotter mould surface decreases the viscosity of the polymer melt at the mould interface, allowing to fill even its finest details, and, at the same time, delays the solidification of the melt inside the cavity. The need for a very high T_{mould} leads to settings that are much higher than those recommended by material manufacturers [73–76], thus pushing the standard process window to its limits. In certain cases, T_{mould} has been set to values near melting or glass transition temperature of the polymer in order to accurately replicate micro structures [77]. The value of the mould temperature also influences the quality of moulded parts with respect to defects such as sink marks, stress cracks and weld lines [9].

The effect of T_{mould} on the surface replication is usually greater than that of T_{melt} in µIM. This has been observed for micro ribs of section 150 µm × 200 µm [78], micro channels of section 150 µm × 250 µm [79], micro channels of section 70 µm × 200 µm [45], micro pillars with 4 µm diameter [41] and ripples having 600-900 nm pitch and few hundreds of nanometres height [80].

Injection speed

The influence of the injection speed on the moulding process is mostly related to the shear-thinning behaviour of polymers. At low deformation rates, the entangled molecules of the material have a hard time sliding past each other [66]. As the rate of deformation increases, the increased shear stress disentangles the molecules, which slide more easily, thus decreasing the overall viscosity and consequently the pressure needed to flow the polymer inside the cavity (see Figure 3.3). Being the shear rate positively dependent on the injection speed, increasing this parameter reduces the resistance to flow and enhances the filling performance of the moulding process.

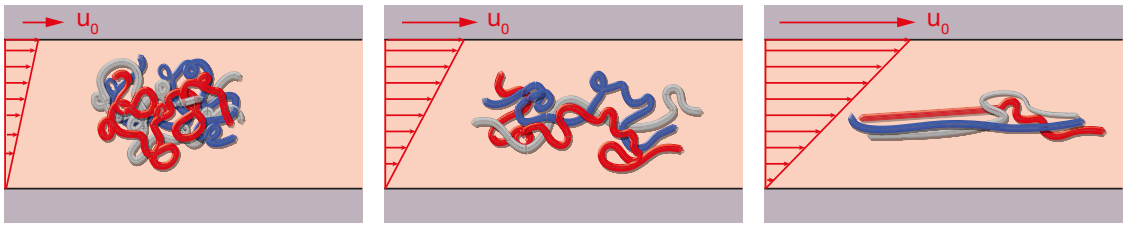

Figure 3.3: Molecular structure of a polymer at increasing shear rates [66].

Increasing the injection speed also helps in counteracting the so-called hesitation effect, i.e. the solidification of the polymer melt at the entrance of high-aspect ratio features [81]. In fact, a high v_{inj} reduces the substrate filling time, thus allowing the melt to flow inside the smallest features. An increase of the mould temperature also reduces the hesitation by delaying the solidification of the polymer.

Setting a high value of v_{inj} in µIM has been reported as critical for the replication of micro features such as 3 µm wide grooves having an aspect ratio of 5 [42] and micro pillars with 100 µm diameter and 400 µm high [67]. Moreover, it also impacts the mass of the produced component [82]. The value of the injection speed should be set as high as possible in µIM, keeping in mind that very high flow rates can generate polymer degradation and cosmetic defects on the surface of the part [83]. Common defects such as sink marks, colour streaks, glass fibre streaks, Diesel effect, jetting and surface defects can also be successfully reduced by increasing v_{inj} [9].

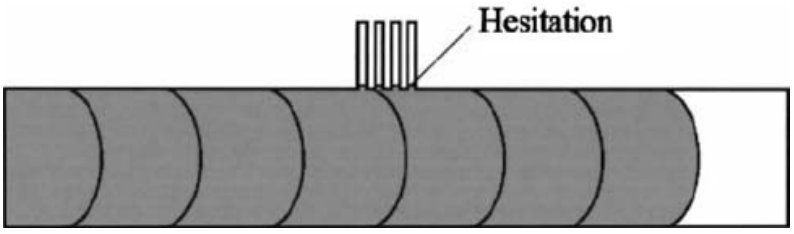

Figure 3.4: Hesitation effect in high aspect ratio micro features [81].

Holding pressure

The holding pressure acts in the second phase of the moulding process when the cavity is almost filled. A p_{hold} increase typically leads to shrinkage and warpage reductions. This effect is strictly linked to the freezing of the gate: once the gate has solidified, the effect of p_{hold} is totally null. A faster injection, which delays the gate freezing, is therefore very important to make the holding pressure effective. In µIM, where the part represents only a minimum fraction of the injected volume, p_{hold} variations can impact the filling performance significantly.

In µIM, increasing the value of p_{hold} influences micro features replication [42], mass of the moulded parts [68, 82], dimensions of the final products [61], shrinkage [84] and magnitude of the ejection force [43].

3.1.3 Optimization of micro injection moulding process parameters using Design of Experiments

The first step of an optimization phase is the definition of inputs and outputs. In µIM, the input variables are typically the aforementioned process parameters. As regards the outputs, many can be considered, e.g. shrinkage [69, 85], height of replicated nano pillars [47], weld line position and orientation [50], height of replicated micro grooves [86], demoulding force [87] and flash size [70]. It can be noted that, in most cases, the output is a dimensional characteristic, since the most common optimization in µIM is carried out with respect to the dimensional quality of the moulded part with the final aim of meeting the design specifications.

Considering that many process parameters impact the quality of moulded parts and complex correlated physical phenomena are involved, numerical models based on process simulations can hardly provide the link between input and output variables. Moreover, multiple quality criteria may have to be assessed simultaneously. Therefore, empirical approaches based on statistical models are the most common way to tackle the optimization problem. Among them, artificial neural networks (ANN), regression analysis and Design of Experiments (DoE) are used [88].

DoE is the most common tool applied in µIM experiments [43, 46, 67, 68, 78, 84, 89–92] since it is capable of providing results that can be easily interpreted and allows to draw clear conclusions on which process parameters are important for the considered outputs. DoE was born as a method for analysing multivariate experiments, where the effects of multiple factors had to be investigated at the same time and thus comparisons based on simple statistical tests were hardly applicable [93]. The statistical framework of DoE is the Analysis of Variance (ANOVA). This method was developed by Sir Ronald Fisher in the 1920s and was first applied to agricultural experiments.

The first step of ANOVA is the definition of a linear regression model, which consists of the appropriate selection of the predictors among the input variables and their possible interactions. In the ANOVA, the total variance of the model is partitioned into different sources of variation, namely the one introduced by pure variability (referred to as "error") and the one caused by the variations of the level of the various factors (i.e. input variables or process parameters). These two contributions are mathematically described by two different sums of squares (SS). These two SS values are evaluated by considering their ratio, which has a Fisher distribution and can thus be used in a robust F-test with the null hypothesis stating that all means are equal, i.e. the experimented factors have no influence on the output. The result of the test allows determining whether the variation induced by the factors is more important than the random variability represented by the error (i.e. the factor is significant with respect to the selected output) or vice versa [93]. The results are usually summarized in the ANOVA table, which displays the SS of the error and of each factor as well as the result of the F-test in terms of p-values. Once the influencing factors are identified, their value can be tuned in further experimentations in order to optimize the level of the significant process parameters. As the mathematical formulation of ANOVA becomes more and more complex with increasing number of factors, dedicated software tools such as Minitab [94] were developed to simplify the analysis procedure.

Among the numerous experimental configurations under the DoE umbrella, the two-level factorial designs (2^k plans) deserve a special mention. In this experimental design, k factors are varied on two levels, usually referred to as "low" and "high". This scheme is particularly useful at the early stage of experimental work when many factors are likely to be investigated [93]. Consequently, 2^k plans are widely used in µIM, where typically up to 4 input variables must be investigated along with their interactions. In some cases, the adoption of a fractional design can turn useful to reduce the number of experimental runs. However, the resolution of the plan decreases leading to the aliasing between main effects and interactions [93].

The most useful graphical tools to illustrate the results of a DoE campaign having more than two factors are main effects plot, interaction plot and Pareto chart of effects. The first depicts the mean levels for all the experimented factors, thus providing a clear visual comparison between the effects of different process parameters as well as the sign of the variation induced on the response variable. When this tool is applied to µIM and a dimensional geometry is the output, it is very important to include the measurement uncertainty in the main effects plot [50]. The uncertainty U is a parameter used to characterize the dispersion of the values that could be reasonably attributed to the measurand [95] and assumes more relevance in combination with micro products. The uncertainty, which is depicted as interval bar (see Figure 3.5), could in fact partially or totally hide the effects of the experimental variables on the measured output, thus changing the conclusions of the data analysis.

The interaction plot shows the relationship between two factors, by displaying the levels of one factor on the x-axis and separate lines for the means of each level of the other factor. The interpretation of this graph is rather simple: parallel lines reveal that there is no interaction. On the other hand, if the lines are not parallel, a certain interaction exists between the two considered factors.

Finally, the Pareto charts of effects is a graphical tool capable of summarizing the findings of the ANOVA table. In particular, it shows the absolute value of the standardized effects of the factors that are included in the model. These effects are plotted in the form of a histogram with a reference line representing the significance level above which the effects can be considered as significant based on the F-test of ANOVA. Therefore, just by looking at this graph, it can be determined which parameters have an impact on the output of the experimentation. The measurement uncertainty can be included in this type of plot in form of interval bars for each effect (see Figure 3.6) by assuming that the response values follow a normal distribution with mean and variance equal to the measurand value and its uncertainty respectively [50].

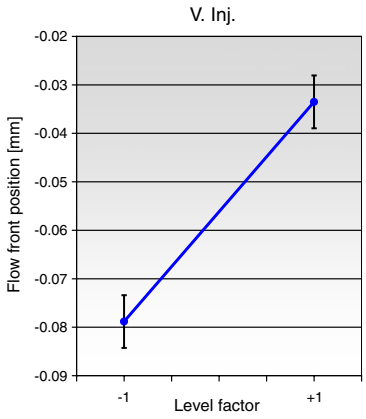

Figure 3.5: Example of uncertainty applied to the main effect of injection speed in a flow front position analysis [50].

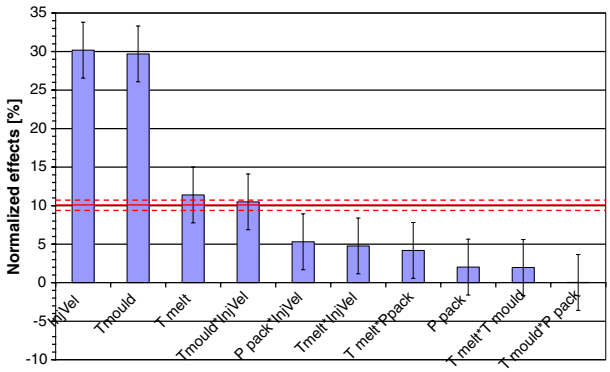

Figure 3.6: Example of uncertainty applied to the Pareto chart of effects in a μIM experiment [50].

3.2 Process monitoring in micro injection moulding

Process monitoring plays an important role in any manufacturing process since measuring the operating conditions helps in detecting any drift in the process performance, which may have an influence the quality of the final part [96]. This real-time characterization becomes even more important in µIM, where small variations of process conditions can have a significant influence on the outcome [14]. Therefore, the information provided by in-process measurements is an extremely powerful tool to optimize the process.

Process monitoring of µIM covers a variety of monitoring techniques since multiple variables act simultaneously during moulding. All of these are based on the use of recording elements that must have a very fast response in order to cope with the fast evolution of µIM [96]. In particular, µIM monitoring can be divided into two branches: one based on the use of sensors and the other on the use of flow-visualization systems.

The most important variables of µIM that are monitorable by means of sensors are [96]:

- volumetric flow rate
- temperature
- pressure

The flow rate is related to the shear stress and consequently to the viscosity of the polymer melt (see subsection 3.1.2). Most of the commercial machines directly perform the measurement of the injection speed without the use of external sensors. In order to verify the performance of a µIM machine, Whiteside at al. [97] placed an external laser displacement sensor to monitor the position of the plunger of a Wittmann-Battenfeld MicroPower 15 µIM machine. With this sensor, they were able to calculate the real injection velocity and compare it to the one set at the machine interface, thus verifying the machine performance.

Temperature monitoring in µIM is a powerful way to capture the thermal history of the polymer melt, which greatly impacts the flow length [98] as well as the molecular structure of the moulded part. Temperature measurements can also be used to characterize the thermal resistance at the polymer-mould interface [99]. Typically, contact thermocouples and infrared (IR) sensors are the preferred choice to measure the temperature in various positions of the mould [96]. Contact thermocouples can be easily mounted within the mould and put in contact directly with the polymer melt. The major disadvantage of these sensors is the high thermal inertia of the metallic elements that causes a relatively slow response to temperature variations. IR sensors are, on the other hand, more responsive to temperature changes but need a specific calibration for each moulded material and require a more complex mould

architecture [100]. Moreover, most polymers are quite transparent in the IR region (wavelengths in the 1.5-5 µm range), posing challenges in the determination of the exact melt temperature.

3.2.1 Pressure monitoring using sensors

Pressure monitoring is the most commonly employed µIM monitoring method based on the use of sensors. The pressure is, in fact, the driving force that pushes the polymer melt inside the cavity, and thus carries valuable information on filling time and viscosity. The phases of the moulding cycle can also be evaluated by examining the recorded pressure curves [101] (see Figure 3.7), providing useful insights on how the process is performing and on its repeatability. Typically, piezoelectric transducers are used in µIM given their short response time and high resolution [96]. They are typically mounted flush with the cavity surface in order to record the pressure of the melt when it encounters the sensor front face [41, 102]. This practice is referred to as direct measurement of the pressure. In other cases, a piezoelectric sensor is used in an indirect measurement of the pressure by placing it behind one of the ejector pins, thus allowing also the measurement of the ejection force [21, 103]. When very small components are moulded, given the size of conventional piezoelectric transducers (see Figure 3.8), it may not be possible to use them without drastically changing the cavity shape and consequently the part design [46]. A possible solution to this problem is monitoring the pressure at the injection plunger (the so-called hydraulic pressure in IM). This quantity is always stored in the machine data and can be extracted without using any external sensor. The drawback of this approach is the discrepancy between the cavity and the hydraulic pressures due to pressure losses generated within the nozzle and the feed system and to the high compressibility of polymer melts. Therefore, this type of pressure measurement might not be representative of how the polymer is behaving inside the cavity.

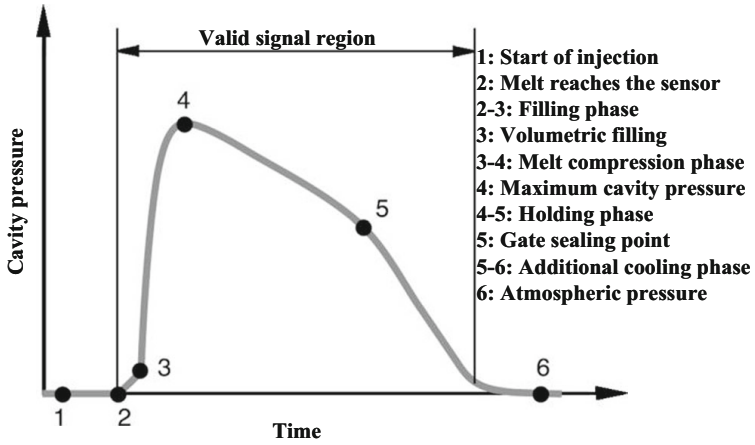

Figure 3.7: Typical trend of injection pressure at the gate measured by a pressure sensor [101].

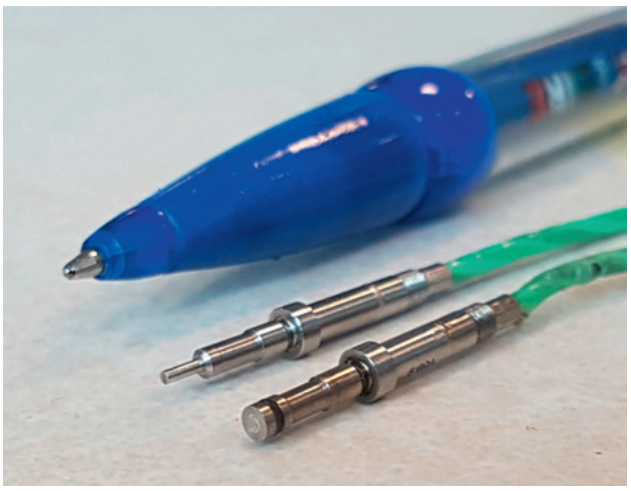

Figure 3.8: Piezoelectric pressure sensors (Kistler 6182 and 6183) used in µIM monitoring [96].

In µIM literature, many phenomena have been thoroughly investigated using data derived by real-time pressure measurements.

Griffiths et al. examined the effects of the main µIM parameters on the cavity pressure measured indirectly with a transducer placed behind the ejector pin when moulding a microfluidic platform in PP, ABS and PC [92]. From the monitored curves, they extracted various indicators such as maximum pressure, slope of the pressure and integral of pressure over time. These variables were dependent on both materials and processing conditions. In particular, T_{mould}, v_{inj} and p_{hold} had the biggest influence, demonstrating that tuning µIM has a significant impact on the polymer melt conditions.

In another study by the authors, the dependence of the ejection force and cavity pressure on µIM parameters was investigated with a pressure sensor placed behind the ejector pin when moulding a microfluidic part in COC [87]. The injection pressure was also monitored with a transducer located behind the injection plunger. The results showed that there was a great positive correlation between integral of the pressure over time (i.e. the pressure work) and the maximum ejection force needed to eject the part from the cavity. It was also shown that, in order to minimize the ejection force and consequently the risk of damaging the part, the low levels of T_{melt}, T_{mould}, v_{inj} and p_{hold} had to be selected.

Mendibil et al. examined the effects of µIM parameters on pressure signals in different mould locations while moulding a part with micro pillars in POM [46]. In particular, signals acquired in the cavity and runner locations were compared with the quality of the replicated pillars, which was evaluated in a qualitative way with confocal and SEM images. It was shown that higher pressure signals led to a higher probability to produce well-replicated parts. Moreover, the authors demonstrated that the

signals provided by the sensor arranged in the cavity were more sensitive to process variations than those acquired at the runner location.

In µIM research, pressure signals derived from piezoelectric transducers have also been used to numerically determine the heat transfer coefficient for different mould coatings [27]. In particular, the HTC value was calculated by fitting simulated and experimental pressure curves for an open flow micro channel with thickness varying from 400 to 800 µm moulded in PS and PET.

Chen et al. used pressure data gathered with pressure transducers in an in-house melt viscosity measurement system for POM flowing in 150 to 300 µm thick micro channels [34]. In particular, the pressure drop measured over the micro cavity allowed to calculate the viscosity using capillary and slit flow models, which was then compared to measurements performed with a conventional capillary rheometer. The results showed how the melt viscosity obtained using the traditional instrument was 5 to 35 % higher than that characterized by means of the in-house system developed by the authors.

A piezoelectric sensor applied at the injection location was used by Tosello et al. [104] to validate µIM simulations applied to a micro tensile test bar in PS. Simulated and real injection pressure profiles were compared in order to identify the most suitable material model in the simulation domain. Moreover, consecutive short-shots were directly correlated to the injection pressure profile, showing that monitoring the pressure is crucial to characterize the filling performance of the moulding process.

The state-of-the-art of µIM monitoring based on the use of sensors still lacks a study dedicated to the correlation between recorded signals and replication quality of the moulded parts. This thesis had the aim of extending the state-of-the-art by investigating such correlation and exploit it in an in-line quality assurance strategy based on the product/process fingerprint framework.

3.2.2 Flow visualization systems

One disadvantage shared by all monitoring strategies based on the use of sensors is that they offer a single point of measurement [96]. This represents a limitation in terms of process characterization since a wider picture of what is happening in the cavity during moulding can turn very useful. A possible solution to this issue could be collecting data using multiple sensors placed in various locations. However, this strategy requires heavy modifications of both mould and part design and still provides a quite discrete characterization of the polymer melt behaviour. To tackle this challenge, the most promising solution is the use of imaging devices to directly visualize what is happening in the mould cavity in terms of polymer melt displacement [96]. By doing this, a visual evaluation can be performed and a larger amount of data can be gathered than when using single sensors.

There exist some expedients to be adopted when setting up a flow visualization apparatus. The mould must, in fact, have a lateral opening to allow the access for the imaging device [105]. Behind the opening, a reflective mirror is then used to image the cavity through a glass window that can cover the entire side of the mould (see Figure 3.9) or just the cavity. The window material should be selected by considering its transparency to IR ranges and thermal properties. With this regard, sapphire represents the preferred choice for its high mechanical properties and similarity to the thermal behaviour of tool steels in terms of heat capacity and HTC [96].

Since cavities in µIM fill in few tenths of milliseconds, an optical system capable of performing very high-speed acquisitions is needed to capture the evolution of the process. Typically, frame rates in the order of 10^2-10^4 frames per second are used [3]. Along with the acquisition speed, also the field of view, the resolution and the sensitivity should be considered when selecting the appropriate visualization system. In particular, the size of the field of view defines what portion of the cavity can be imaged. The spatial resolution, which is determined by the pixel size, should be high enough to distinguish the details of micro cavities. As regards the illumination, the coaxial "through the lens" technique is often used [96]. This method relies on the use of an optical element that is capable of both transmitting and reflecting light: a half-silvered mirror normally serves this purpose.

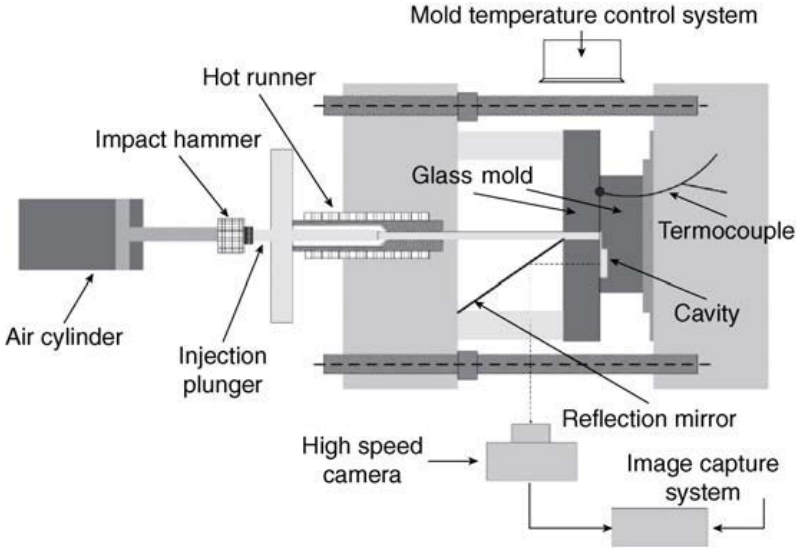

Figure 3.9: Scheme of a mould system equipped for flow visualization [3].

High-speed infrared cameras can also be employed for flow visualization. These systems provide information not only on the filling pattern but also on the temperature field in the cavity over time [106] (see Figure 3.10). Infrared cameras must be calibrated by imaging a surface at a known temperature through the entire optical system, including the reflective mirror and the glass window. The polymer melt material also has an influence on the temperature output, since, as previously mentioned, most polymers are quite transparent in the IR region. The addition of a

fraction of carbon black material to the polymer has been reported as beneficial in this regard [106], even though this procedure changes the properties of the melt and consequently of the final part.

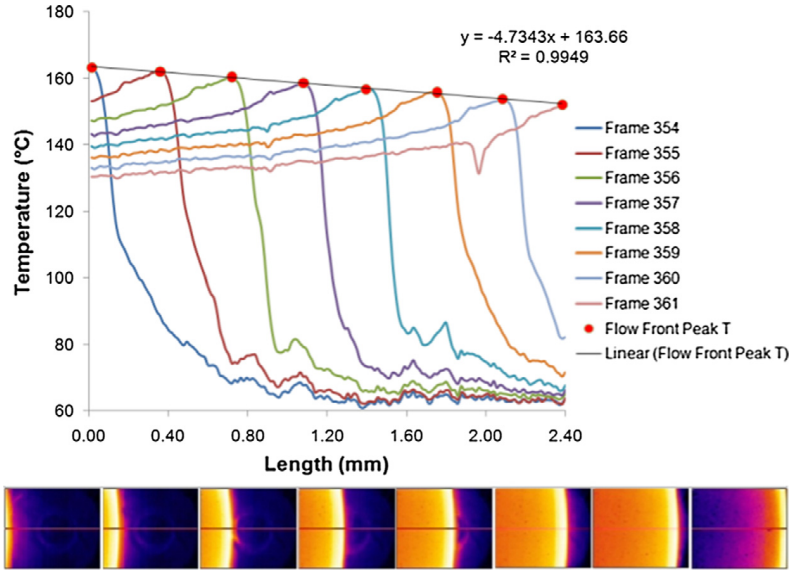

Figure 3.10: Temperature distribution in the cavity at sequential time frames gathered with a high-speed infrared camera [106].

Flow visualization set-ups are rarely adopted in the industry because complex and expensive acquisition systems along with extensive mould modifications are needed. Moreover, the moulded component must have a relatively extended flat surface that is generated by the glass window through which the cavity is imaged.

In µIM research, flow-visualization systems have been used for various purposes.

Han et al. [107] used a light-reflection method and a mould with a glass insert to visualize the flow of PMMA while filling micro grooves having a pitch of 100 µm and a height of 50 µm. They tested the effect of the variation of mould temperature, cavity thickness and injection rate on the flow development and the final replication of the micro features. It was demonstrated that the groove layout had a big impact on the filling. In particular, the parallelism between the grooves and the flow direction maximized the filling performance of the process.

Sorgato et al. [108] investigated the effect of air evacuation on the cavity temperature of COC using a high-speed infrared camera and a mould equipped with a sapphire window. It was shown that temperature curves extracted by thermal acquisitions had two peaks, the first related to the burn effect caused by rapid air compression and the second to the actual flow front temperature. ANOVA was applied to show that variations of mould temperature, injection speed and evacuation conditions all had a significant influence on the melt temperature inside the cavity. In particular,

using vacuum venting led to a consistent decrease of this temperature, thus acting as detrimental with respect to the achievable flow length and replication.

High-speed infrared acquisitions through a sapphire window were also used to determine the HTC at the cavity-polymer interface when moulding PP and PS in 500 µm thick discs [106]. In particular, the HTC in a numerical model was tuned in order to match the one calculated based on temperature data extracted from the infrared camera. ANOVA was also applied to study how the variations of melt temperature, mould temperature, injection speed, holding pressure and texture of the sapphire window affected the cooling of the polymer melt. It was observed that the T_{mould} value dominated the cooling conditions.

Guerrier et al. [109] used high-speed acquisitions to validate injection moulding simulations of a 500 µm thick flat part in ABS and PC. It was concluded that the model was capable of accurately predicting the flow pattern thanks to the accurate modelling of the implemented induction heating that was built to resemble the one used in real experiments.

In another study, Masato et al. [110] used flow-visualization to characterize the velocity of molten PS flowing in a 400 µm thick open flow cavity coated in three different protective materials. The velocity profiles at seven different injection speed levels were measured using Particle Image Velocimetry (PIV), a technique that exploits the presence of particles in the polymer to track the filling development. The results showed that a strong and stable slip regime was achieved at a high level of injection speed for both coated and uncoated cavities.

Similarly to monitoring based on sensors, data provided by a flow-visualization apparatus have not been quantitatively correlated to the replication quality yet. This thesis went beyond the state-of-the-art by investigating the use of flow-visualization measurements as a tool for in-line quality optimization of micro moulded parts in a product/process fingerprint framework.

4 Precision and accuracy in micro injection moulding of TPE micro rings

The present chapter deals with µIM of thermoplastic elastomer (TPE) micro rings. Firstly, the precision and accuracy of the process were investigated in an experimental campaign. Microscopy inspections and weld line measurements allowed to define a suitable process window. The effects of main µIM process parameters on the functional features of the part were then analysed, with particular attention to the shrinkage behaviour. The produced parts were also tested, thus linking part functionality and µIM process conditions.

The same components were also produced in a different mould using an overmoulding set-up. This process was also characterized with respect to the quality of the final multi-material component.

The research presented in this chapter was published in [111] and [112] and partially taken from these papers.

4.1 Micro injection moulding of TPE micro rings

At the current state-of-the-art, µIM has been mostly developed in the field of rigid thermoplastics. This happened because these materials, having low cost as well as good mechanical properties and being relatively easy to process, cover the most part of the polymers processed by µIM. Indeed, the current main application of µIM is represented by the microfluidic industry, which relies on the manufacturing of rigid micro- and nano-structured 2.5D components [81]. The µIM research on other classes of polymeric materials is very limited.

TPEs are materials that combine the processability of thermoplastics with the elastomeric behaviour of vulcanized rubbers [113]. The main difference between rigid thermoplastics and TPEs is related to mechanical properties: the first are stiff and rigid, while the second are flexible and soft. TPEs exhibit the distinctive mechanical characteristics of thermoset rubbers and are simultaneously easy to process as thermoplastic polymers. This ambivalent behaviour is due to their structure. TPEs

are phase-separated systems, in which one phase is hard at room temperature and the other is an elastomer [113]. The hard phase provides strength and acts as physical cross-link, whereas the elastomeric one interconnects the rigid phases conferring flexibility and elasticity to the material. The transition temperatures of TPEs, and consequently the moulding process window, are determined by the characteristics of both phases. Below the glass transition temperature of the elastomeric phase, the TPE is brittle and stiff. Above this level, the material is soft and elastic and exhibits a rubber-like behaviour. Finally, when the temperature is higher than the melting temperature or glass transition temperature of the hard phase, the TPE turns into a viscoelastic fluid and becomes processable by means of technologies such as injection moulding. Figure 4.1 graphically shows the dependence of the mechanical behaviour of TPEs on temperature.

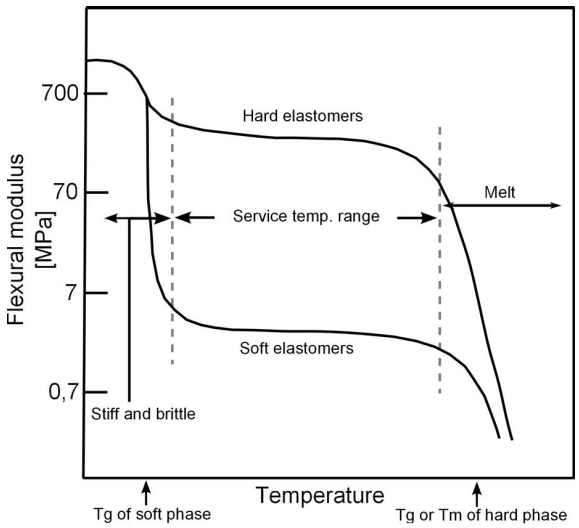

Figure 4.1: Flexural modulus of TPEs in dependence on temperature [114].

Given their peculiar characteristics, TPEs are often preferred to thermoset rubbers because of their simpler manufacturing process and shorter fabrication time [113]. The possible re-moulding is also an important advantage. Moreover, the exceptional repeatability of injection moulding allows manufacturing TPE components with tighter tolerances compared to conventional thermoset rubbers. Therefore, thermoplastic elastomers are the best choice for manufacturing precision and micro plastic components featuring softness and flexibility.

Although IM of TPEs is well established and commonly used to manufacture macro components [115], very few studies report their use in µIM. Alabran et al. [116] studied the effects of moulding conditions and tooling on the replication of nano features (patterns size ranging from 100 to 1500 nm) using two different thermoplastic polyurethanes and varying only the mould temperature. Attia et al. [117] proposed and validated a micro overmoulding process of TPE (a styrene-ethylene-butylene-styrene (SEBS) copolymer) for the fabrication of a 3D microfluidic system having a

PMMA substrate. The device was tested against leakage, but no study regarding the process parameters effect on the dimensional quality was performed.

This study aims at going beyond the current µIM state-of-the-art by characterizing the replication capabilities in terms of dimensional precision and accuracy of a TPE material when moulded in micro-cavities.

4.1.1 Case study

The object of the study was a TPE micro suspension ring used as a dampening element in a phono-cartridge used to play high-definition music. The functionality of this object is described thoroughly in section 4.2. Since the application demanded both high dimensional accuracy and dampening properties, µIM of TPE represented the preferable solution to meet the functional requirements. Figure 4.2 shows the shape and main dimensional features of the micro ring.

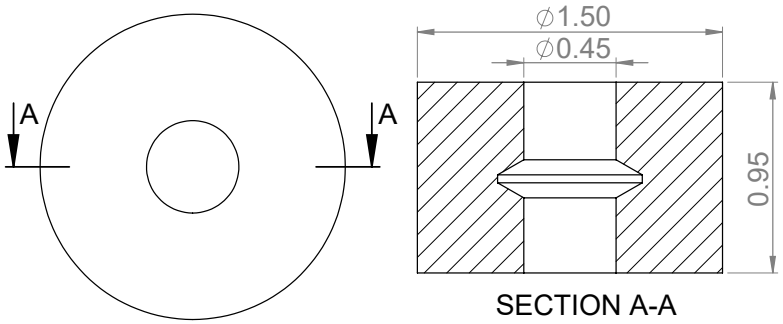

Figure 4.2: Geometry and nominal dimensions in mm of the micro ring.

The internal geometry of the ring has a conical structure, making the component three-dimensional. Being the part mass equal to 2.2 mg and the dimensional tolerances ±10 µm on both internal and external diameters, the component falls in the category of micro products according to the aforementioned definitions (see section 2.2). The present work focuses on the outer diameter (OD) and inner diameter (ID) of the rings since they were the most significant geometries with respect to the part functionality. In fact, their accuracy and precision were substantial for a correct assembly of the component.

4.1.2 Mould design

A three-plate mould with replaceable insert was developed and used in the experiments. The main advantage of this mould configuration is that the part is separated automatically from the feed system by means of the displacement of the middle plate. Both the mould plates and the insert were made from tool steel. Four cavities were

machined on the insert and the internal geometry of the micro rings was created by means of micro pins protruding from the fixed ejection plate. Both the cavities and the micro pins were machined using micro-electro-discharge-machining (µEDM). The four cavities were designed with a diameter 1.550 mm while the pins with a diameter 0.480 mm based on the nominal shrinkage of the TPE material and the target part dimensions. The feed system consisted of a cylindrical sprue with diameter 5 mm connected to the cavities with four runners and pin gates. Figure 4.3 (a) and (b) illustrate the design of the three-plate mould, while Figure 4.3 (c) shows how the feed system was located in the mould system.

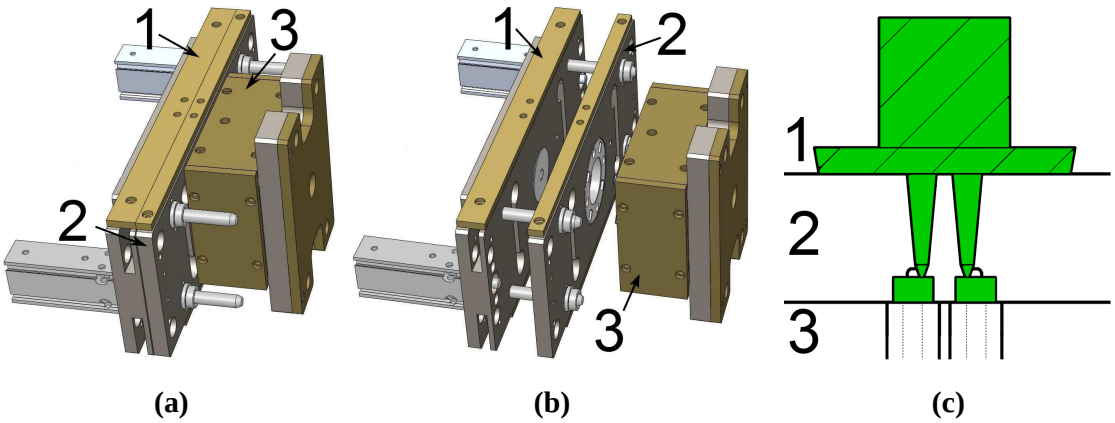

Figure 4.3: (a) Closed mould, (b) Open mould and (c) Mould cross-section. The three plates (1, 2 and 3) and the TPE material (in green) are indicated [114].

The four micro rings were ejected by means of ejector tubes, thus ensuring a fully automatic procedure. The ejection system relied on the softness and elasticity of TPE. In fact, the undercut caused by the internal geometry of the rings (see Figure 4.2) would have made the ejection impossible if a rigid thermoplastic material were used. Figure 4.4 (a) and (b) show the details of the micro cavities on the ejection and injection plates respectively.

4.1.3 Experimental details

µIM experiments were performed using a Wittmann-Battenfeld MicroPower 15 µIM machine (maximum clamping force: 150 kN, maximum injection velocity: 750 mm/s). The machine has a 14 mm plasticization screw and a separated 5 mm injection plunger (see Figure 2.5 (a) for details on the architecture). The TPE used was a styrene-ethylene-butylene-styrene (SEBS). This material was suitable for the application due to its high flowability and dampening characteristics. Table 4.1 shows the main properties of the polymer. The extremely low viscosity, indicated by the high Melt Volume Rate (MVR) value, makes the TPE suitable for µIM, since a very

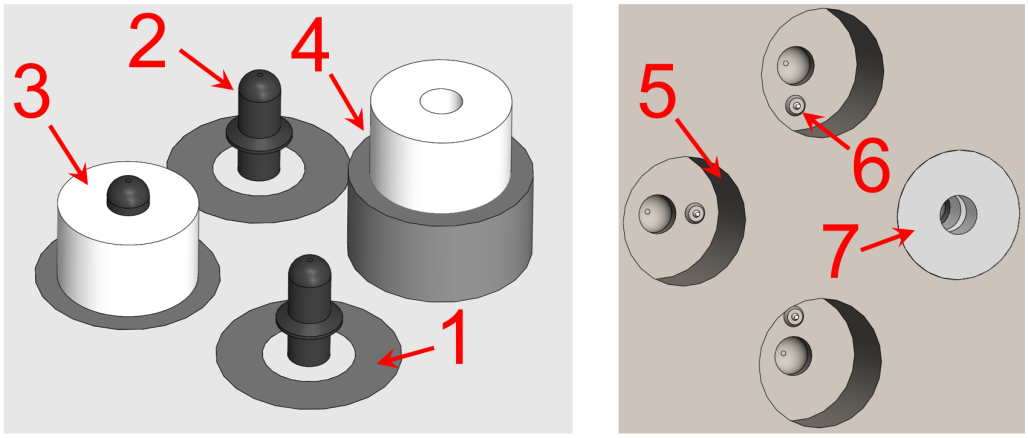

(a) (b)

Figure 4.4: (a) Close-up of the ejection side of the mould [114]. 1: ejector tube in neutral position. 2: Pin generating the internal ring geometry. 3: Moulded suspension ring before ejection. 4: Ejected suspension ring with ejector tube in the forward position. (b) Close-up of the injection side of the mould. 5: Cavity wall. 6: Asymmetrical gate. 7: Moulded ring inside the cavity.

low flow resistance facilitates the complete filling of micro cavities. On one hand, this characteristic had a positive impact on the feasibility of the process. On the other, the low viscosity made the appearance of product defects such as flashes more probable. Another consequence of the low viscosity is that the mould temperature used when moulding the TPE was set to a lower level if compared to the ones typically selected when moulding rigid thermoplastics.

Table 4.1: Main properties of the TPE material.

Property	Units	Value	Test method
Density	g/cm^3	0.90	ISO 2781
Melt Volume Rate (MVR)	$cm^3/10min$	75.6	ISO 1133
Melting point	°C	153	DSC

To identify a suitable process window for the µIM process, a preliminary study was performed. Three different combinations of process settings were tested and the resulting production batches evaluated. The first combination was called “Data sheet” since it corresponded to the settings recommended by the material manufacturer. The second, called “High”, employed levels of process parameters higher than the recommended ones. This was done to observe possible improvements in filling and replication quality. Finally, the process settings of the third combination, called “Improved”, were found as part of an operational optimization aiming at achieving better cavity filling and smaller defects. This optimization was based on

inspections under an optical microscope right after moulding. Table 4.2 lists the process parameters used in the preliminary study.

Table 4.2: Process parameters for the three combinations investigated in the preliminary study.

Process parameter	Data sheet	High	Improved
Melt temperature/°C	185	200	200
Mould temperature/°C	40	60	40
Clamping force/kN	100	100	30
Injection speed/(mm/s)	120	200	85
Holding pressure/bar	300	750	275

To evaluate the quality of the micro rings produced using the three different process settings combinations, a scanning electron microscope (SEM) was used to perform a qualitative evaluation. Moreover, the depth of the weld line on the injection side, caused by the asymmetric gating of the ring (see Figure 4.4), was also taken into account to identify the best process settings. In fact, weld lines are a critical defect because they are both a visual defect and a zone of reduced strength for the moulded part [118]. For this evaluation, ten produced rings per process combination were randomly selected and successively inspected.

The outcome of the preliminary study was used as a starting point for the following experimental phase, in which a DoE approach was employed to analyse the effects of the µIM parameters on the rings OD and ID. Four parameters were varied: melt temperature, mould temperature, injection speed and holding pressure. A general full factorial design was carried out. Melt and mould temperature were varied on two levels, while three levels of injection speed and holding pressure were tested (see Table 4.3). This specific experimental design was chosen because initial tests showed that melt and mould temperature did not have any relevant non-linear effects on the outputs. Considering also that a long time was needed to reach thermal equilibrium and therefore to change the level of the two temperatures, it was decided to vary them only on two levels to reduce the experimental effort.

Table 4.3: DoE process settings.

Process parameter	Levels
Melt temperature, T_{melt}/°C	210, 225
Injection speed, v_{inj}/(mm/s)	50, 70, 90
Holding pressure, p_{hold}/bar	300, 500, 700
Mould temperature, T_{mould}/°C	30, 40

After discarding the first ten moulded parts, five replications were produced and kept for evaluation for each one of the 36 process parameter combinations of the

DoE plan. Considering the presence of four cavities in the mould insert, 720 micro rings were produced and measured. By doing this, also the variation of the measured outputs introduced by the different cavities was evaluated.

4.1.4 Measurement strategy and uncertainty evaluation

The depth of the weld line was measured using the focus variation microscope Alicona InfiniteFocus with a 5× magnification objective (see Table 2.5 for the detailed characteristics). The entire weld line on the injection side was acquired. The depth was then evaluated in five different positions (see Figure 4.5) using cross-sectional profiles. In particular, the depth was defined as the distance between the point having minimum height and the plane fitting the flat surface of the micro ring.

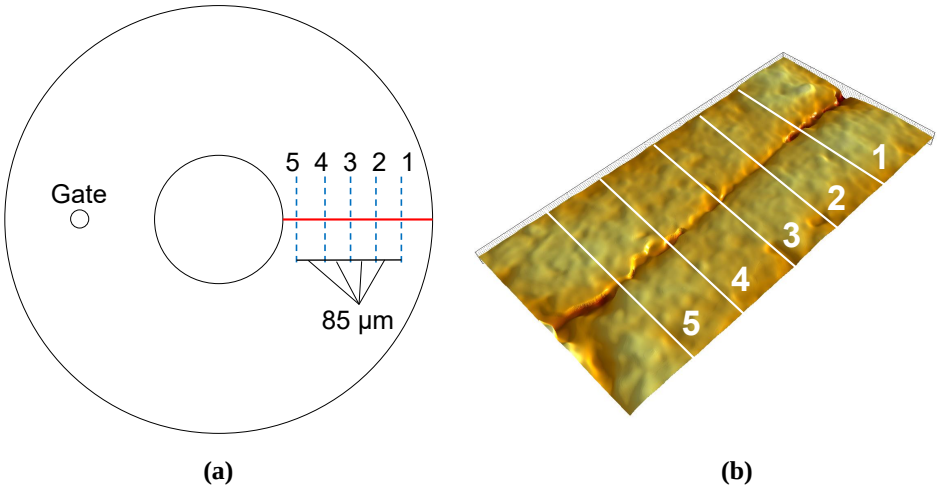

Figure 4.5: (a) Scheme of the five measuring positions along the weld line, which is represented in red. (b) Three-dimensional scan of the weld line and cross-sectional measurement profiles.

Alicona InfiniteFocus was also used to measure the outer and inner diameters of the micro rings. OD and ID measurements were extrapolated from each 3D optical reconstruction by fitting the points of the two circles (see Figure 4.6) using an image processing software (SPIP 6.7.3, Image Metrology A/S, Hørsholm, Denmark). In particular, the face of the ring corresponding to the injection side was captured. For each moulded part, three consecutive acquisitions were carried out and their average value was then taken as output. The four mould cavities were also measured to assess the replication level. In fact, a complete knowledge of the tool geometry is fundamental in order to characterize the actual capability of the µIM process. For this purpose, an optical CMM with 0.5 µm lateral resolution (DeMeet 220, Schut

Geometrical Metrology, Groningen, Netherlands) was used to measure the diameters of the cavities (corresponding to OD) and the pins (corresponding to ID).

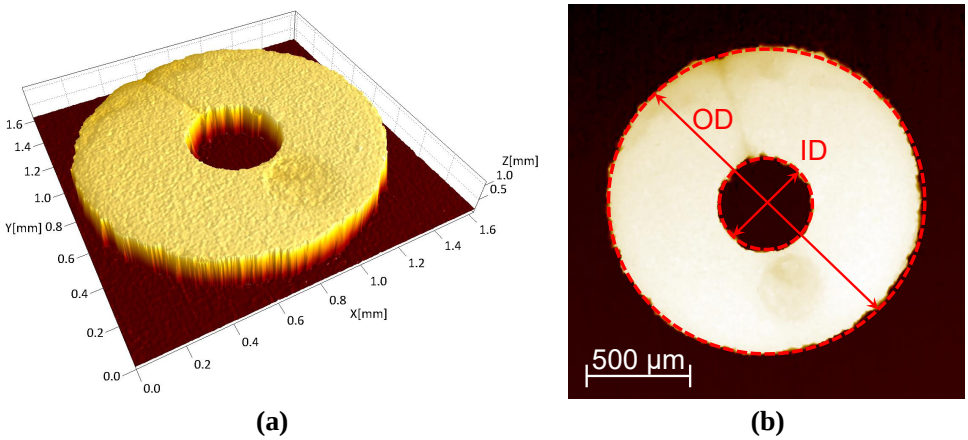

Figure 4.6: (a) Three-dimensional scan of a suspension ring. (b) Interpolated inner and outer circle providing OD and ID measurements.

The measurement uncertainty U was evaluated in order to take into account the precision of the measurement results in the investigation of the effects of µIM parameters. U was calculated following ISO 15530-3 [119], which is based on the substitution method: by measuring a calibrated artefact sharing similar characteristics with the actual measurand, the systematic error of the measuring instrument is quantified. In this case, a calibrated circle of diameter 1 mm was employed. Five uncertainty sources were considered: u_{cal}, related to the calibration certificate of the artefact; u_{p}, the uncertainty associated with the measurement procedure calculated as standard deviation of ten repeated measurements on the calibrated circle; u_{res}, introduced by the lateral resolution of the instrument and calculated considering a rectangular distribution interval; and u_{w}, related to material and manufacturing variations of the actual measurand. For the mould measurements, u_{w} was calculated as the standard deviation of ten repeated measurements of the mould OD and ID, while, for the moulded parts, as the standard error of the measurements of the parts produced with each combination of µIM parameters. Therefore, u_{w} also included the variability of the process. The expanded uncertainty U was finally obtained using the law of propagation of uncertainty [95]:

$$U = k \times \sqrt{u_{\mathrm{cal}}^2 + u_{\mathrm{p}}^2 + u_{\mathrm{res}}^2 + u_{\mathrm{w}}^2} \tag{4.1}$$

considering a coverage factor k of 2 in order to achieve a 95 % confidence interval. Table 4.4 shows the uncertainty budget for the measurements of both mould cavities and moulded parts.

Table 4.4: Average values of uncertainty contributions and expanded uncertainty of OD and ID measurements for both mould and moulded parts.

Uncertainty contribution	Mould cavities		Moulded parts	
	OD/µm	ID/µm	OD/µm	ID/µm
u_{cal}	0.50	0.50	0.50	0.50
u_{p}	0.09	0.09	0.09	0.09
u_{res}	0.14	0.14	0.51	0.51
u_{w}	0.83	0.71	0.71	1.96
$U(k = 2)$	2.0	1.8	2.0	4.2

4.1.5 Results of the preliminary study

To evaluate the quality of the main features of the micro rings, three details were analysed: the injection side view, the internal geometry and the hole at the ejection side. To examine the internal geometry, the parts were cut in half. Figure 4.7 shows the SEM scans of rings produced with the three different process combinations used in the preliminary study (see Table 4.2).

With the "Data sheet" settings, it may be observed from the injection side view that the residual gate mark, generated by the automatic detachment of the feed system from the part, was relatively small and did not protrude from the surface, which is convenient for micro assembly operations when flat surfaces are required. A small weld line was present, caused by the not symmetric gating of the part. When examining the cross-section, it can be observed that the internal geometry was not well defined: the corners looked more rounded than in the design (see Figure 4.2). This difference was most probably caused by the capabilities of the µEDM process, which could not machine perfectly sharp angles on the pin. The hole on the ejection side had a relevant defect caused by the presence of a weld line. The entrapped air, which prevented the polymer melt from achieving a complete filling of the micro cavity near the central pin, was the cause of this imperfection.

The "High" process setting combination led to a smoother surface on the injection side. This implies that a better filling of the cavity was attained because of the increased speed and mould temperature. On the other hand, the gate mark was bigger and significantly protruded from the upper ring surface, posing a serious challenge for the mounting of the ring. The weld line was also deeper and a large defect, generated by entrapped air, appeared at its end. The increased injection speed helped the formation of this imperfection. From the cross-sectional view, it is evident that the internal geometry was more detailed than when using the "Data sheet" settings. This higher replication was achieved through the increase of holding pressure. The rounding on the internal angles was still present, confirming that this imperfection was due to the tooling process capabilities. An evident defect can be

seen on the circumference of the hole in the ejection side view. This defect was significantly larger than that appeared with the "Data sheet" settings. This was once again due to the increased injection speed that contributed to the formation of entrapped air near the pin.

The rings produced with the "Improved" settings had a very small weld line on the injection side. The gate mark was also smaller than in the "High" case. A comparable level of filling was also achieved as shown by the smooth surface in the injection side view, which also shows that no air entrapment prevented a complete filling of the part. The internal geometry appeared as finely detailed. The hole on the ejection side still presented the same type of defect as in the two previous cases, although its size was significantly reduced if compared to the micro rings produced with "Data sheet" and "High" combinations of process parameters.

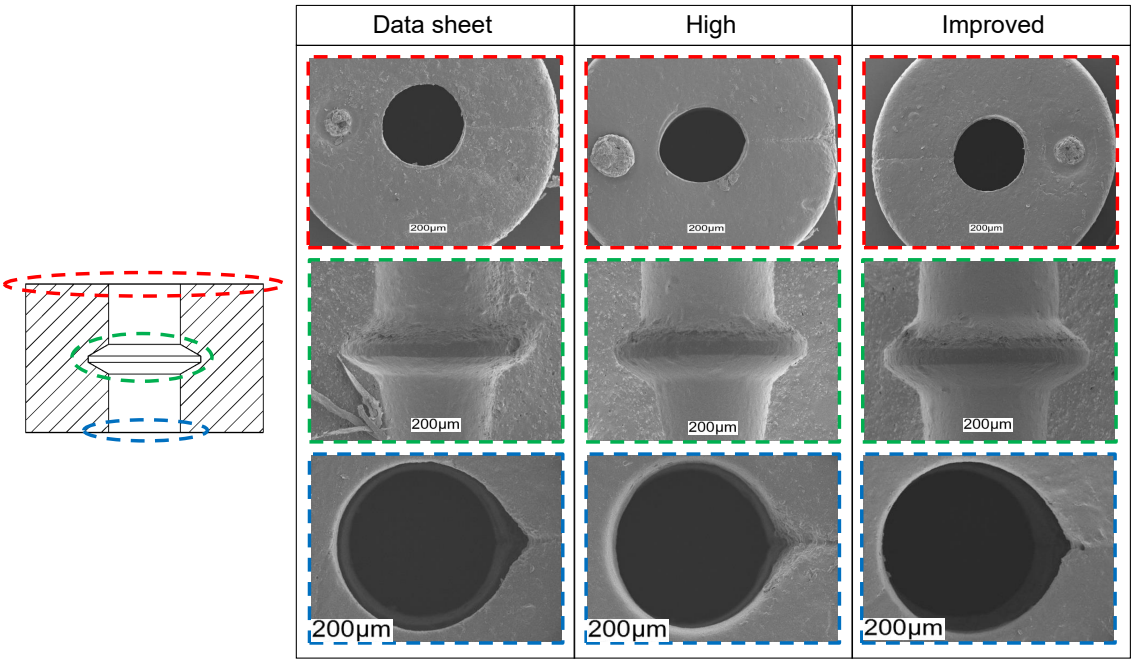

Figure 4.7: SEM images of micro rings moulded with the three different process combinations of the initial study [114]. The injection side view (red), the cross-sectional view (green) and the hole on the ejection side (blue) are shown.

In conclusion, the SEM inspections showed that high pressure and injection speed enhanced the filling, but simultaneously caused relevant defects due to air entrapments [114]. Air trap imperfections were mostly observed when moulding with the "Data sheet" and the "High" settings, indicating that the low values of injection speed and clamping force selected for the "Improved" batch (see Table 4.2) were needed to facilitate the evacuation of the air from the cavity. This result is in accordance with the observations of Griffiths et al. [120], which proved that the volume of evacuated air is lower at higher values of injection speed.

The weld line depth measurements confirmed these findings. Indeed, the "Improved" settings resulted in the smallest depth in all the five measuring positions (see Figure 4.8). On the other hand, the weld line was deepest for the rings produced with "High" process parameters because of the higher injection speed that hindered the air evacuation from the cavity. Taking the different measuring positions into account, the weld line was always deeper moving from the inner to the outer diameter. This demonstrates that the air entrapment was formed on the external part of the cavity, where the polymer flow ended its path. Considering both SEM inspections and weld line depth measurements, the "Improved" process settings combination was the best solution since it allowed minimizing the defects of the micro part. Thus, it was selected as a starting point for defining the levels of the process parameters in the following DoE investigation. In particular, the clamping force was always kept at 30 kN throughout the DoE campaign to allow a proper evacuation of the air from the cavity.

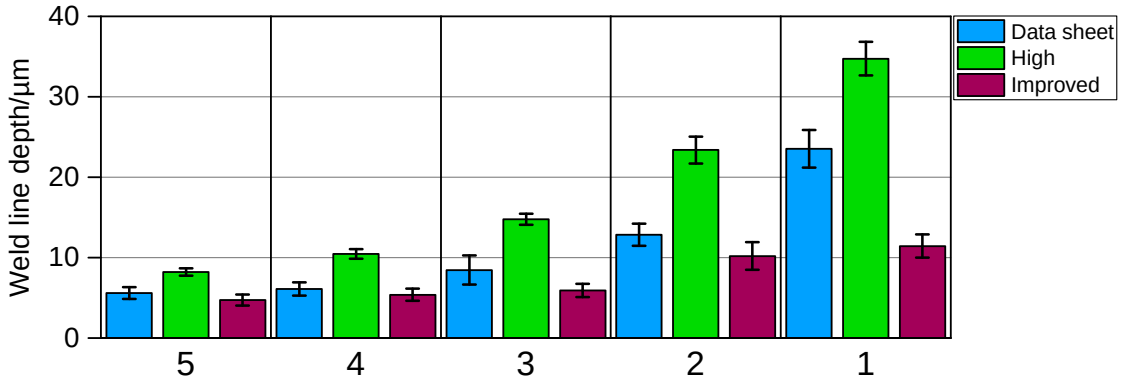

Figure 4.8: Weld line depth for the three different settings of the preliminary study in the five different measuring positions [114]. The interval bars represent the standard deviations related to the ten measured parts.

4.1.6 Results of mould measurements

The µEDM tooling process was very accurate: the deviations between target and measured dimensions ranged between -0.4 µm and 1.6 µm for OD and between 0.8 µm and 2.7 µm for ID (see Figure 4.9). Considering the expanded uncertainties, the measured values met the mould design specifications except for the inner diameter of cavity 1 and 2.

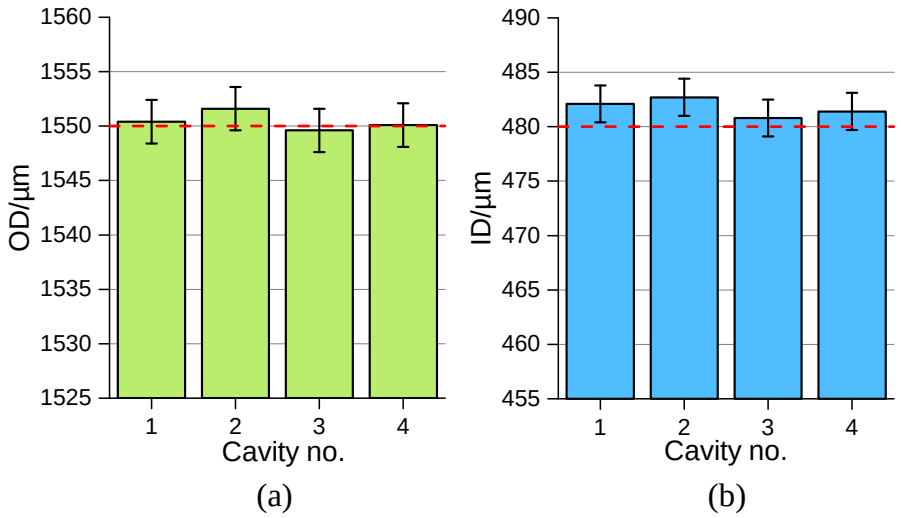

Figure 4.9: Results of cavity measurements for OD (a) and ID (b). The error bars represent expanded uncertainties, while the red dashed lines indicate the mould target dimension.

4.1.7 DoE results

OD results

Figure 4.10 shows the main effects plot of OD for the moulded rings. The uncertainty related to the particular combination of process parameters was also shown to verify that the variability did not hide the influence of the process. From the graph, it is possible to observe that the TPE micro rings production was consistent across the four cavities. This is important since it proved that, on one hand, the polymer melt conditions (temperature, shear rate, pressure, and in turn specific volume and final shrinkage) were equivalent in the four cavities. On the other hand, it also demonstrated that, under controlled conditions in terms of both tooling and moulding, it is possible to achieve single micrometre digit accuracy and precision in multi-cavity µIM, which had not been shown in literature yet.

The effects of mould temperature and holding pressure were preponderant since they presented the highest slope, which indicates a great significance on the response. The increase in these parameters had a positive effect on OD. This type of behaviour, which means that high mould temperatures and pressures enhanced the filling of the cavity, was also observed in other µIM experiments on rigid thermoplastics (see subsection 3.1.2). Indeed, a high level of T_{mould} opposes the premature cooling and subsequent rise in viscosity of the polymer melt while a high value of p_{hold} allows more material to enter the cavity before the gate freezes. The increase of mould temperature and holding pressure led to an average OD increment of 7 µm. The influence of melt temperature was less relevant: an increase of T_{melt} led to an average OD decrease of 3 µm. This negative effect of the melt temperature is unusual, since a

high T_{melt} generally facilitates the filling of the cavity by means of a reduced polymer melt viscosity. This may have been caused by the fact that, cooling down from a higher temperature, the ring OD suffered a larger amount of shrinkage at the end of the moulding process. A non-linear trend between OD and the injection speed was observed. In particular, incrementing v_{inj} led to an increase of the replication level due to the faster injection, which in turn decreased the polymer viscosity. This behaviour was true until a certain injection speed since OD plot has a negative slope when moving from 70 to 90 mm/s. This observation, which has already been reported in µIM literature by Bellantone et al. [68] for part mass measurements, indicates that a local optimum for v_{inj} existed within the explored range. The physical explanation behind this phenomenon may be that an increase of residual stresses caused a larger shrinkage of the part OD. In fact, residual stresses are typically larger at high values of the injection speed because the polymer melt cools down more drastically.

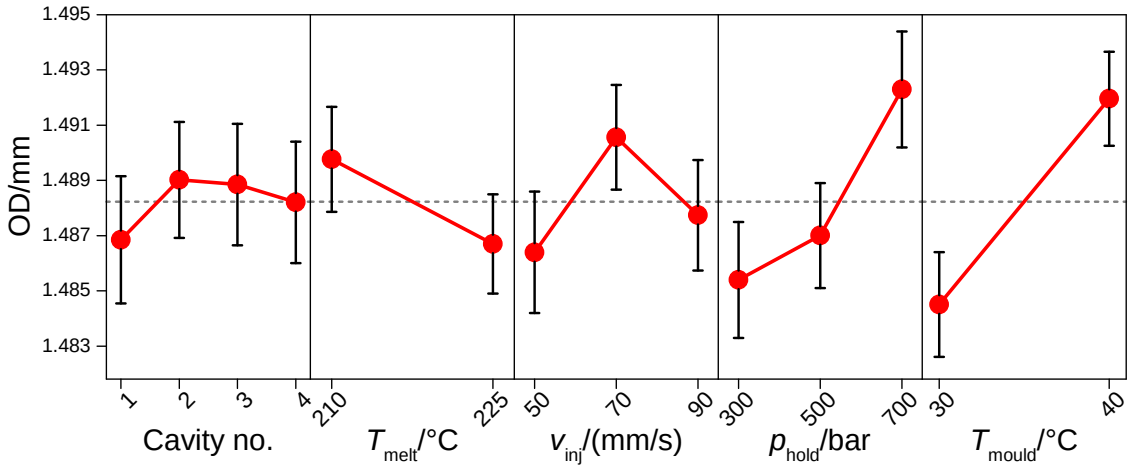

Figure 4.10: Main effect plots for OD. The error bars represent the expanded uncertainties related to the particular process parameter level. The grey dashed lines indicate the total averages.

ID results

Figure 4.11 shows the main effects plot for ID. As for OD, the cavity number did not have any influence, confirming the high precision of the tooling and moulding processes. The mould temperature showed again a high influence on the output. Incrementing T_{mould} from 30 °C to 40 °C led to an ID decrease of 9 µm. Therefore, the mould temperature had an opposite effect on the two measured diameters. Oppositely to the previous case, the holding pressure effect was negligible: the uncertainties of the main effects plot for the three different levels of p_{hold} overlap. This different significance of p_{hold} was due to the mould design: given the position of the gate (see Figure 4.4 (b)), the last portion of the cavity filled by the polymer melt stood on

the outer ring circumference, as also proven by the weld line depth analysis (see Figure 4.8). Thus, the holding pressure, which came to act only in the last phase of the moulding process when the cavity was almost filled, mainly influenced the outer diameter, which was filled at last. The influence of the melt temperature was greater than for OD. In particular, the increase of T_{melt} caused an average ID increment of 9 µm. As for T_{mould}, this trend was opposite to that observed for OD. Finally, the injection speed had a non-linear effect on ID. However, as for the other process parameters, this effect was contrary to the one observed when dealing with OD: selecting the central level of v_{inj} led to the smallest ID and, simultaneously, to the largest OD.

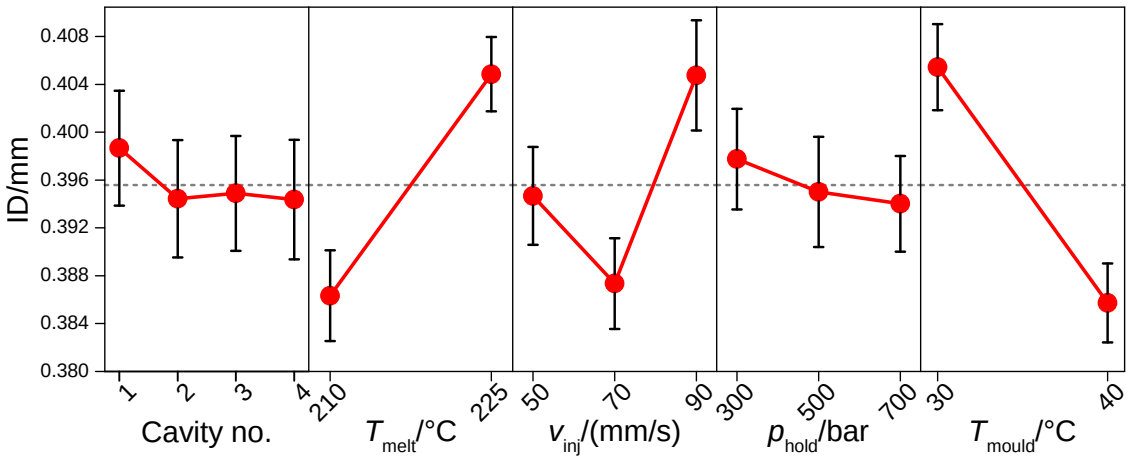

Figure 4.11: Main effect plots for ID. The error bars represent the expanded uncertainties related to the particular process parameter level. The grey dashed lines indicate the total averages.

Shrinkage characterization

The variation of the four process parameters had opposite effects on the two ring diameters. When OD increased, ID always decreased and vice versa. This behaviour has never been observed before for micro moulded components, and it may be directly related to the particular annular geometry of the suspension rings. Being both OD and ID on average smaller than their target dimensions, this phenomenon posed great challenges in meeting the design requirements, since a simultaneous increase of both the diameters was impossible to achieve by just tuning the moulding parameters in the investigated process window.

To investigate this experimental evidence further, the shrinkage of the two measured outputs was compared by defining a reference diameter $\mathrm{D_{ref}}$ (see Figure 4.12). This quantity was equal to the average between OD and ID for each of the four mould cavities and was therefore constant with the cavity number. This geometrical

reference was chosen since it allowed to evaluate potential asymmetries of the outer and inner ring diameters. The deviation Δ was selected as shrinkage indicator and was calculated as:

$$\Delta_{OD} = OD - D_{ref} \tag{4.2}$$

$$\Delta_{ID} = |ID - D_{ref}| \tag{4.3}$$

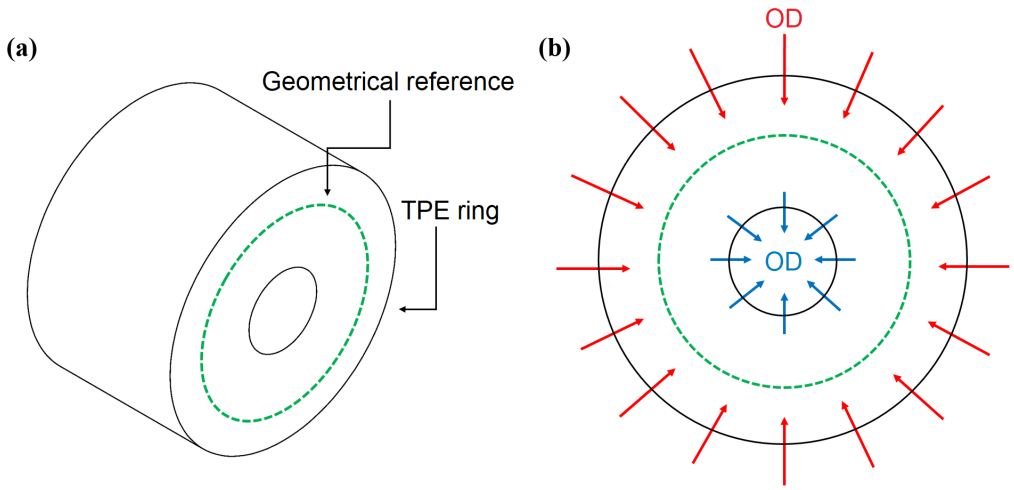

Figure 4.12: (a) Side view of the part indicating the position of the geometrical reference. (b) Schematic view of the shrinkage behaviour of the micro rings.

Figure 4.13 reports the main effect plots of Δ_{OD} and Δ_{ID}. The effect of the cavity is not shown since it has already been verified to be negligible. It can be seen that the shrinkage of ID was always larger than that of OD. In particular, the average deviations were equal to 624 µm and 469 µm for inner and outer diameter respectively, generating a distortion of the initial part design. This phenomenon was most probably caused by the fact that ID was object of constrained shrinkage during moulding, while OD was not. Indeed, the presence of the pin did not allow the inner surface to shrink freely during cooling, while the outer one was free to shrink. This constrained shrinkage generated a concentration of tensile stresses in the micro ring at the inner diameter, causing a higher shrinkage of ID after demoulding.

The comments on the effects of the process parameters on the two diameters are also valid for the deviation since Δ is just scaled by a factor (D_{ref}) that is almost constant for all the four cavities. As anticipated, the process parameters had the same influence on the deviations of outer and inner diameters, being the trends of the main effect plot similar in the two cases. However, the magnitude of the effects, which is evaluable with the slopes of the main effect lines, was significantly different:

the effects were much larger for ID. The only exception was represented by the holding pressure that was significant only for OD, as explained before. For the other experimental factors, the ratio between ID and OD slopes ranged from 1.8 (observed between 50 and 70 mm/s of v_{inj}) to 6.0 (observed for T_{melt}), demonstrating that the shrinkage behaviour of the inner diameter was significantly more sensitive to the variation of process settings.

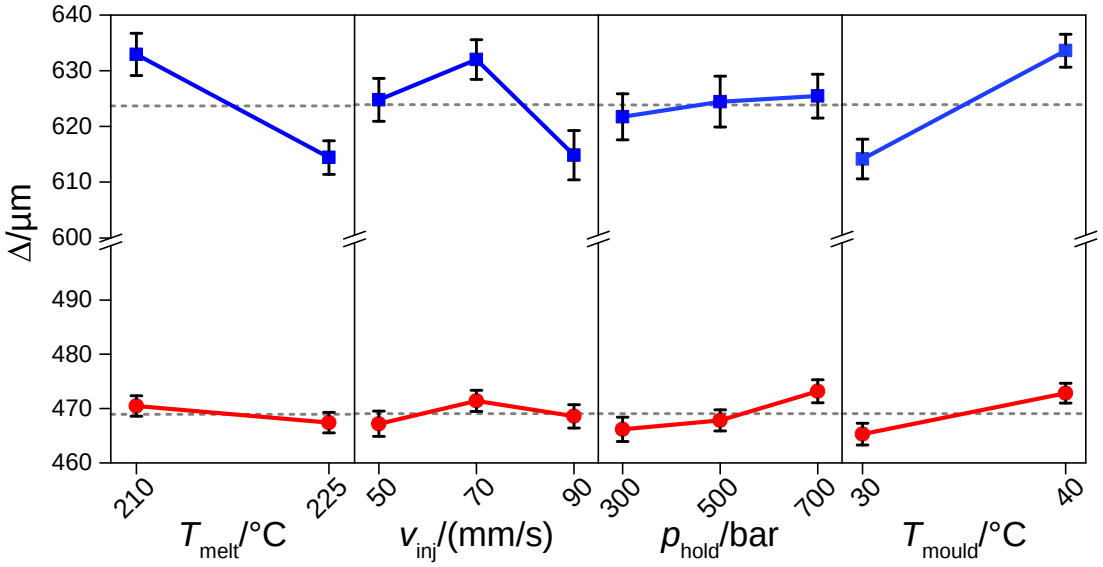

Figure 4.13: Combined main effect plots for the deviations Δ of OD (in red) and ID (in blue). The error bars represent the expanded uncertainties related to the particular process parameter level. The grey dashed lines show the total averages. The vertical axes were broken to facilitate comparisons among measured trends.

4.1.8 Conclusions

This study aimed at characterizing and assessing the µIM technology of micro dampening rings. For the first time in literature, a comprehensive investigation has been carried out on a micro component moulded using TPE. The peculiar characteristics of this class of polymers make them the only suitable candidate to manufacture micro polymer parts featuring softness and flexibility. The following conclusions can be drawn:

- The preliminary investigation showed that low values of clamping force and injection speed were needed to reduce defects such as weld lines by minimizing air entrapment in the cavity.
- For both outer and inner diameter of the rings, the four different cavities ensured a robust, effective and repeatable multi-cavity µIM production, as the

measured dimensions in all parts from the four different cavities were equivalent within the single-digit micrometre measurement uncertainty.

- For the outer diameter, mould temperature and holding pressure were the most relevant process parameters, as they both helped in increasing OD. Melt temperature and injection speed were less significant.
- For the inner diameter, mould temperature and melt temperature showed the most significant effects. On the other hand, the holding pressure was not significant, since the cavity was filled at last on the outer diameter.
- Both inner and outer diameters showed a non-linear dependence with respect to the injection speed, demonstrating that there were contrasting effects at play: a positive one due to the reduction in viscosity and a negative one caused by the build-up of residual stresses.
- The four process parameters had, in all the experimental ranges, an opposite effect on the two measured diameters: an increase of OD always appeared with a decrease of ID and vice versa. Being the measured diameters smaller than the design targets, this behaviour posed great challenges in terms of process optimization.
- By setting the average mould diameter as the reference, it was found that ID shrank more than OD. This was caused by the constrained shrinkage that affected only the ring inner surface, which was not allowed to shrink freely because of the presence of the central pin. Moreover, ID was also more sensitive to process variations.

4.2 Functional testing

Based on the results of the previous study, selected moulded micro rings were tested. The tests were performed at the facilities of Ortofon A/S [121], manufacturer of the final product in which the micro rings are employed.

The functional task of the ring is to hold in place an aluminium tube connected to a magnet rod. The aluminium tube holds, at one of its extremities, a diamond tip. This sub-assembly is then mounted into a phono-cartridge that is directly used to play vinyl. In particular, the vinyl tracks, being put in contact with the diamond tip, cause a vertical displacement of magnet that in turn generates the electric signal that is then converted into stereo music. The micro ring, being stretched around the magnet and standing at the interface between the two sub-components, serves the critical purpose of holding the parts in place and dampening the vibrations induced by the displacement, which happens at high frequency due to the high rotational speed of the vinyl. Figure 4.14 shows the assembled micro ring along with the aluminium tube and the magnet rod.

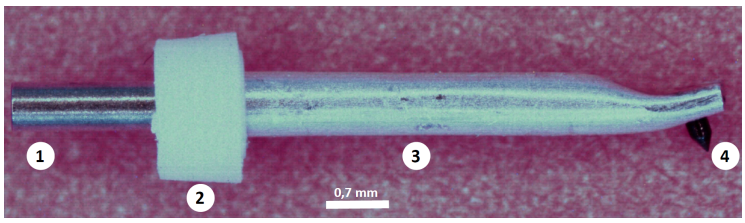

Figure 4.14: Sub-assembly with a micro ring. 1: magnet rod. 2: moulded ring. 3: aluminium tube. 4: diamond tip.

Being the mounting operations and the subsequent testing quite time-consuming, only a portion of the 720 rings produced in the DoE campaign was selected. To carry out a significant test capable of correlating the functionality to the measured diameters, the rings having the smallest and the largest OD and ID were selected. Since, as shown before, the effects of µIM parameters had an opposite impact on the two diameters, only two DoE combinations were needed: DoE no. 1 provided the smallest OD and largest ID, while DoE no. 27 provided the largest OD and smallest ID. Considering the five repetitions and the four cavities, 40 rings were functionally tested. Table 4.5 reports the process settings of the two DoE combinations selected for the functional tests.

Table 4.5: Tested DoE combinations and related geometrical outputs. OD and ID values are the averages of the 4 cavities and 5 repetitions.

DoE no.	T_{melt}/°C	T_{mould}/°C	v_{inj}/(mm/s)	p_{hold}/bar	OD/mm	ID/mm
1	210	30	50	300	1.465	0.439
27	210	40	90	700	1.499	0.380

The assembly operation consisted of two steps:

- In the first, the rings were mounted on the metallic cantilever. This cantilever is made by the assembly of the aluminium tube and the magnet rod. The aluminium part works as a structural component, while the magnet functions as a generator for the electrical signal that is used to play stereo music. This first operation is carried out on an automatic assembly machine made of 8 stations positioned on a circular line. Each station carries out a specific task: press-fitting of the magnet in the aluminium tube, fitting of the diamond tip on the aluminium tube, stretching of the ring onto the cantilever, etc. The moulded rings are fed into the assembly machine by means of a bowl feeder.
- In the second, the output of the previous operation is press-fitted inside a plastic case using another specific assembly machine. Before the actual press fitting, the position of the ring on the metallic cantilever is checked visually in order to make sure that the diamond tip is well positioned with respect to the

assembly axis. An incorrect position of the ring on the metallic cantilever can be observed at this stage. Figure 4.15 shows the final assembled phono-cartridge.

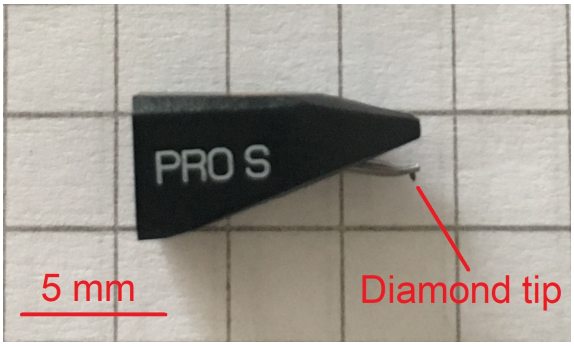

Figure 4.15: Assembled phono-cartridge for functional testing. The diamond tip protruding from the metallic cantilever is indicated.

Since no ISO standard currently exists on the functional assessment of phono-cartridges, the standard procedures created by Ortofon A/S were followed. These tests are performed to approve any cartridge released on the market.

The assembled cartridges were mounted on a specific head-shell connected to an LP test-plate having 50 to 100 µm wide tracks. The test was performed with a 1 KHz sinusoidal signal input. The output signal, produced by the vibration of the magnet between the cartridge coils, was recorded, converted via an AD-converter and filtered to optimize the data analysis, which was carried out on a coupled computer. Figure 4.16 shows the test equipment and a cartridge during actual testing.

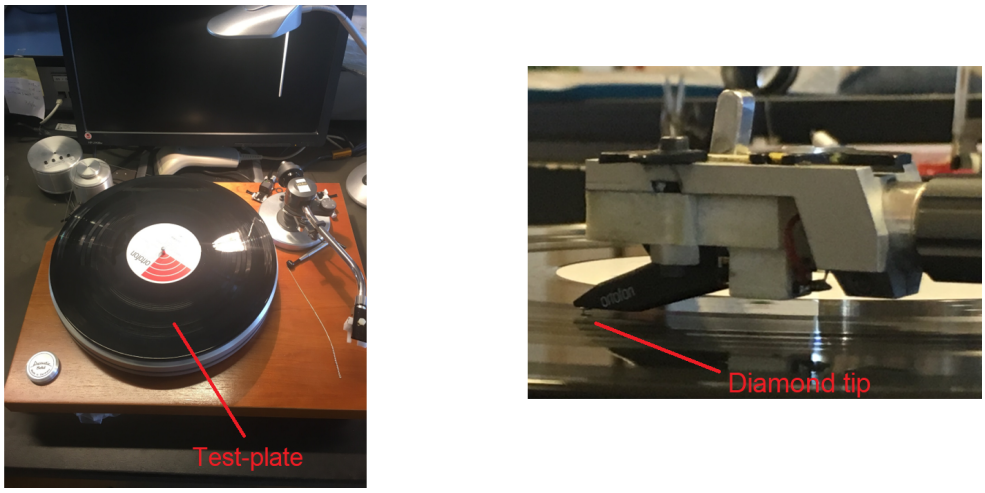

(a) **(b)**

Figure 4.16: (a) Testing apparatus and (b) cartridge during functional testing.

The output quantities of the functional test were:

- Sensitivity. It is the measure of the voltage output generated by the cartridge. Being this output influenced by the magnitude of the magnet deflection, it is strongly dependent on the correct dampening provided by the suspension ring. In particular, OD and ID play an important role here, since they influence how the magnet is held in place. In order for a tested cartridge to be considered in tolerance, the sensitivity must be between 3.5 mV and 8 mV for both left and right stereo channels.
- Separation. This quantity measures the separation between the two stereo channels and is directly correlated to the level of stereo sound that can be achieved [122]. For phono-cartridges, the separation level must be larger than 20 dB in order to be functionally accepted.
- Balance. This is a measure of the difference in dB between right and left channel signals, and is therefore correlated to the sensitivities of the two channels. The ideal value for this output is 0 dB. A positive balance means that the right channel is higher than the left one, whereas a negative balance value means otherwise. In this case, the tolerance band is 4 dB wide and centred around 0 dB.

Figure 4.17 shows the results of the functional tests. As regards sensitivity, all the tested samples provided values within the tolerance range. For both the channels, the sensitivity assumed very similar values, as also confirmed by the correspondent low balance. As for the separation, 3 parts out of 40 (i.e. 7.5 %) failed the test, being the separation lower than the imposed limit of 20 dB. All these parts belonged to DoE no. 1, proving that rings with small OD and large ID are more likely to fail the test. A lower separation was in all cases observed for the right channel. Finally, the balance curve was always within the tolerance limits: except for one sample, it was always in the interval ± 1 dB, demonstrating that a high level of balance was achieved with the cartridge mounting the micro moulded TPE rings.

From the results of the functional tests, it can be concluded that, in general, the produced micro rings performed well, demonstrating that the moulded rings can be actually used in a real commercial application. The only cartridges that failed the tests mounted rings manufactured with the process settings of DoE no. 1, which was the one resulting in parts having the maximum ID and the minimum OD. This was most probably caused by the fact that a large inner diameter made the connection between the ring and the metallic cantilever loose, making the system not sensible enough to the displacement induced by the tracks of the test plate. Therefore, the process combinations of DoE no. 27 were advised for the final production of micro rings.

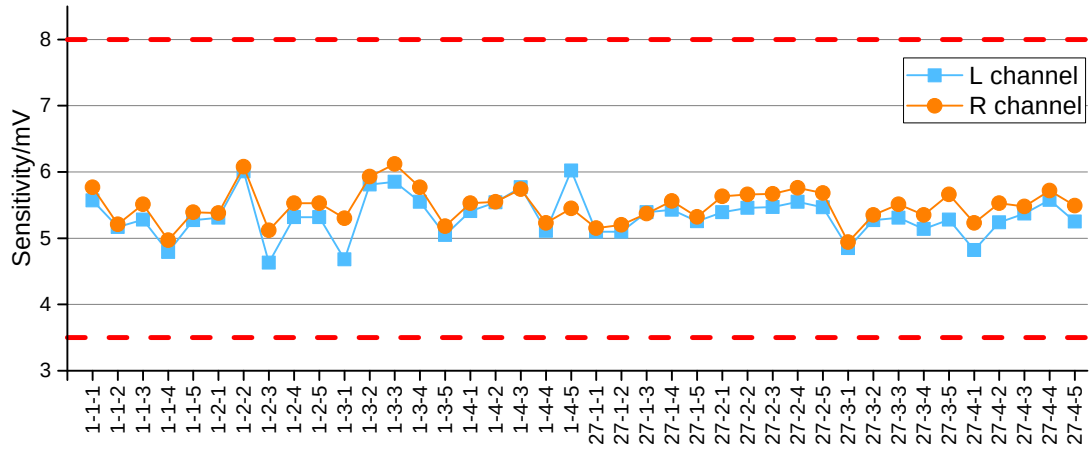

(a) Sensitivity

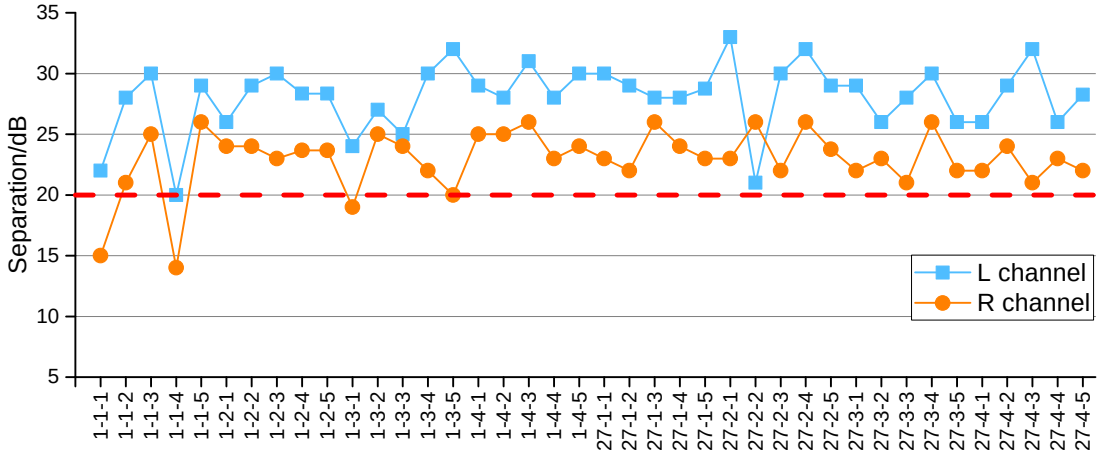

(b) Separation

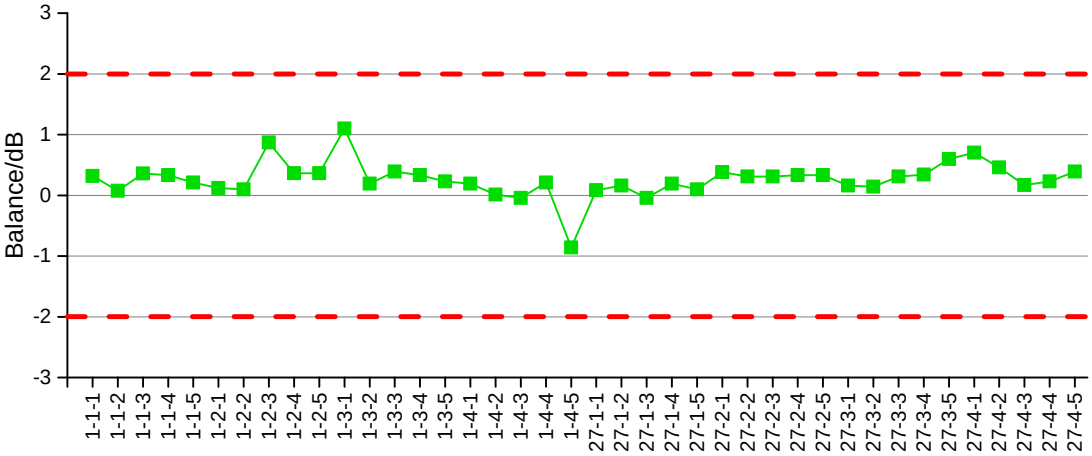

(c) Balance

Figure 4.17: Results of the functional tests. The red dashed lines represent the tolerance limits. The horizontal axis shows number of DoE, cavity and replication.

4.3 Micro insert moulding

A different solution to manufacture the sub-assembly made by the micro ring, the aluminium tube and the magnet rod was evaluated. In particular, a micro insert moulding process was designed and experimentally investigated.

4.3.1 Case study and mould design

In the new configuration, the aluminium tube and the magnet rod were firstly press-fitted together, resulting in the metal insert for the subsequent over-moulding. The TPE material was in fact moulded around this substrate. The main advantage of this alternative process is a great reduction of production costs due to the elimination of the aforementioned mounting procedures from the process chain. The objective of this study was to assess the quality of the over-moulded parts with respect to process setting variations.

The multi-material component along with its dimensions are shown in Figure 4.18.

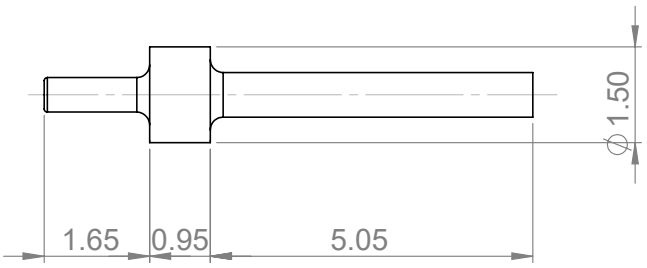

(a)

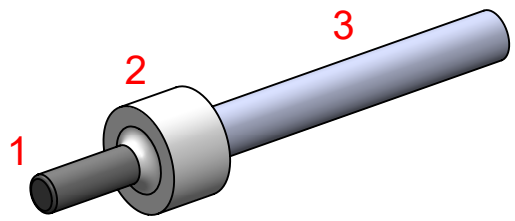

(b)

Figure 4.18: (a) 2D model and main dimensions in mm of the micro insert moulded part. (b) 3D model of the component. 1: Magnet rod. 2: TPE micro-ring. 3: Aluminium tube.

The same three-plate mould frame presented in subsection 4.1.2 was used. In this case, an insert having two cavities was designed to allow the positioning of the metallic substrate, which was picked up from a specifically designed magazine tool

and successively inserted inside the mould by using the robot arm coupled with the machine. The part was then demoulded and replaced by the next substrate in the free spot left inside the magazine tool using the same robot arm. A fully automated manufacturing process was therefore ensured. Similarly to the µIM case, the feed system was designed with a sprue having 5 mm diameter and with asymmetric pin gates (see Figure 4.19), which were detached automatically during ejection at the movement of the middle plate.

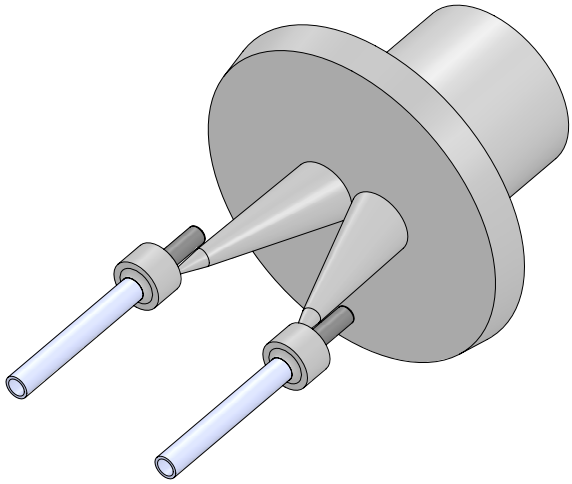

Figure 4.19: Feed system used in the micro insert moulding process.

4.3.2 Experimental details

The micro insert moulding experiments were carried out using the same Wittmann-Battenfeld MicroPower 15 µIM machine used for manufacturing the micro rings. The same TPE material was also used, given its dampening properties and low viscosity.

Preliminary experiments allowed to identify an initial process window by taking into account the most visible defects affecting the part quality. In particular, extensive flashes and gate mark were present at high values of holding pressure. These two defects were always observed in parts moulded with p_{hold} higher than 150 bar, regardless of the other settings. To find a level of this parameter that could guarantee a complete filling without degenerating in flashes and gate marks, a short-shot analysis was applied. By doing so, the optimal level of the holding pressure was found at 80 bar. The fact that these defects did not appear when moulding the micro rings in the previous study, even employing holding pressure values higher than 150 bar, was probably due to the different mould design and to the presence of wider venting channels. Figure 4.20 shows two examples of a defected and a defect-free part.

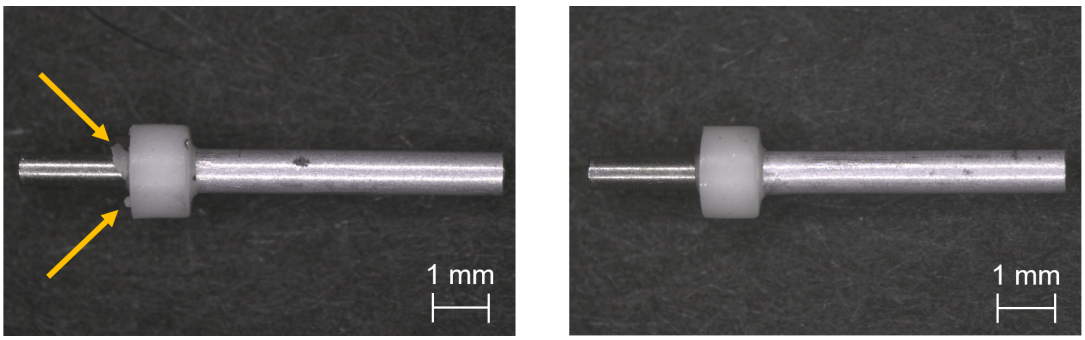

(a) **(b)**

Figure 4.20: Micro part moulded with holding pressure equal to (a) 200 bar and (b) 80 bar. The flash and gate mark are indicated by the upper and lower yellow arrows respectively.

In order to analyse the effects of the other process parameters on the part quality, mould temperature, melt temperature and injection speed were varied on three levels each (see Table 4.6). Values similar to those employed in the previous experimental investigation (see subsection 4.1.3) were defined. In this case, the three experimental factors were changed one at time while keeping the central point ($T_{\mathrm{melt}} = 210$ °C, $T_{\mathrm{mould}} = 40$ °C and $v_{\mathrm{inj}} = 90$ mm/s), thus generating a one-factor-at-time (OFAT) experimental plan. This type of design allows evaluating numerous levels of various process parameters with relatively low experimental effort. On the other hand, it is inherently unbalanced and the single effects must be evaluated separately. Five parts for each cavity were stored after discarding the first ten, resulting in a total number of 70 analysed multi-material components.

Table 4.6: Process settings for the investigation of the micro insert moulding process.

Process parameter	Levels
Melt temperature, T_{melt}/°C	200, 210, 220
Mould temperature, T_{mould}/°C	30, 40, 50
Injection speed, v_{inj}/(mm/s)	80, 90, 100

4.3.3 Measurement strategy

To assess the quality of the moulded parts, two geometrical characteristics were considered. The first one is the diameter D of the micro rings, being, as previously discussed, fundamental for the functionality. The second one is the alignment between the ring axis and the metal substrate axis, described by the angle α. The value of the latter is important since it is an indicator of the accuracy of the multi-material assembly required for correct operation of the phono-cartridge. If a misalignment was

present, the over moulded component might not provide the desired dampening. The main reason that could cause this misalignment is the so-called core-shift phenomenon, which occurs in insert moulding processes as a spatial deviation of the insert from the original position due to unbalanced polymer melt pressure in the cavity. In the particular case under study, it might have happened since the gate was not symmetrical with respect to the metal insert axis (see Figure 4.19).

The same optical CMM machine used for the mould measurement in the µIM investigation (DeMeet 220, Schut Geometrical Metrology, Groningen, Netherlands) was employed to characterize the micro insert moulded parts. Being these measurements two-dimensional, the diameter and the alignment angle were measured in three different circumferential positions around the component axis in order to consider their variation in the 3D space. Thus, three measurement outputs were available for each part. Each measurement was repeated five times, showing high repeatability, being the maximum observed standard deviation equal to 0.5 µm for D and 0.05° for α. Figure 4.21 shows the measurement scheme and a view of the optical CMM interface.

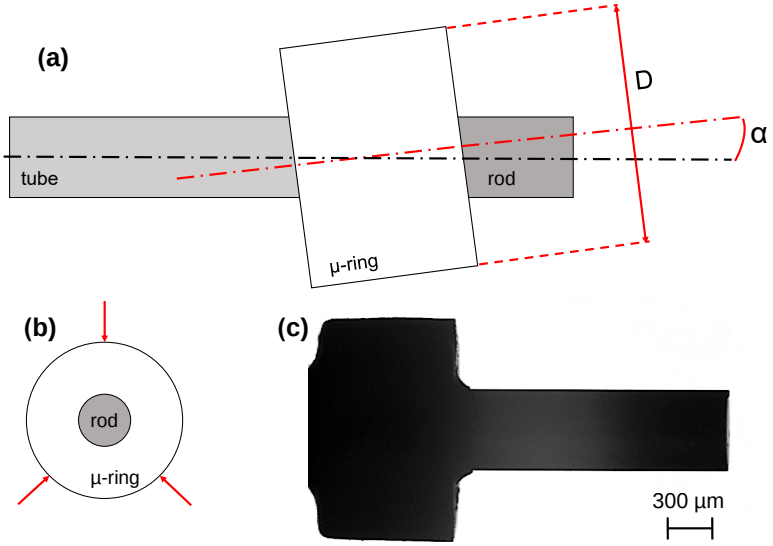

Figure 4.21: (a): Measurement scheme. The diameter D and the angle α are indicated. (b) The three circumferential measuring positions. (c) Micro assembly as viewed by the optical CMM.

Along with the diameter D and the angle α (both considered in the analysis as the average of the measurements in the three circumferential positions), the difference between the maximum and minimum values of D among the three positions was considered. This quantity was calculated as:

$$R = Max(D_i) - Min(D_i) \qquad i = 1, .., 3 \qquad (4.4)$$

and was defined in parallel to the roundness [123]: a large value of R corresponds to low roundness while a low value of R characterizes a micro ring with a high roundness. The mould cavities were not measured because of production reasons.

4.3.4 Results and discussion

Since an OFAT experimental design was carried out, the effects of the process parameters on the measurement outputs were analysed separately. In particular, interval plots were used for the analysis, since they allow to compare the results for the different levels of the experimental factors by also considering the dispersion in the form of an interval bar.

Figure 4.22 shows the results for the two cavities. It can be observed that changing the cavity had no effect on D, R and α, since the interval bars overlap in all cases. This proves that, similarly to the µIM case, an effective multi-cavity micro insert moulding process was achieved, thus allowing to manufacture, with each shot, two parts having the same dimensional characteristics.

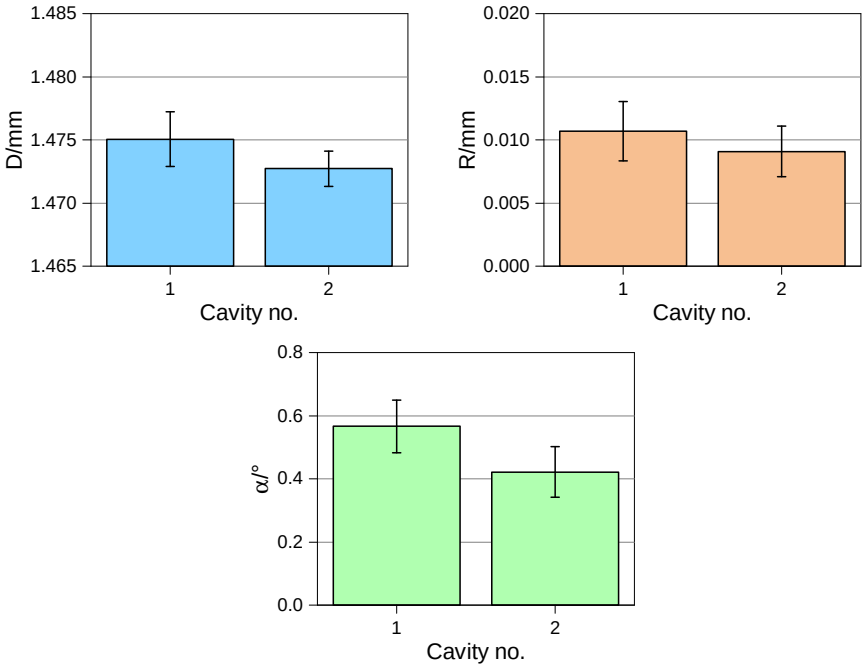

Figure 4.22: Interval plots of the three measurands against the cavity number. The interval bars represent standard errors.

Figure 4.23 shows the interval plots for the diameter D. All the process parameters were significant since their variation resulted in a change of the response considering the interval bars. In particular, the central values of T_{melt}, T_{mould} and v_{inj} provided the largest D, which was equal to 1.480 mm. The highest levels of the parameters

resulted in the smallest D: this was unexpected since typically high melt temperatures, mould temperatures and injection speeds are used to favour the complete filling of the cavity by lowering the viscosity and preventing premature freezing of the gate. In this particular case, however, the results showed that the replication quality increased up to a certain limit of T_{melt}, T_{mould} and v_{inj}, after which it dropped. This behaviour suggests that the viscosity of the TPE material underwent a too drastic reduction when moulding with the high levels of the parameters, resulting in a not optimal filling of the mould cavity. These results are congruent to what observed in the µIM experiments for OD (see subsection 4.1.7): the diameter increased when increasing T_{mould} from 30 °C to 40 °C and decreased when increasing T_{melt} beyond 210 °C. As for the injection speed, a similar non-linearity of the replication was observed, even though higher levels of the process parameters were explored in this case.

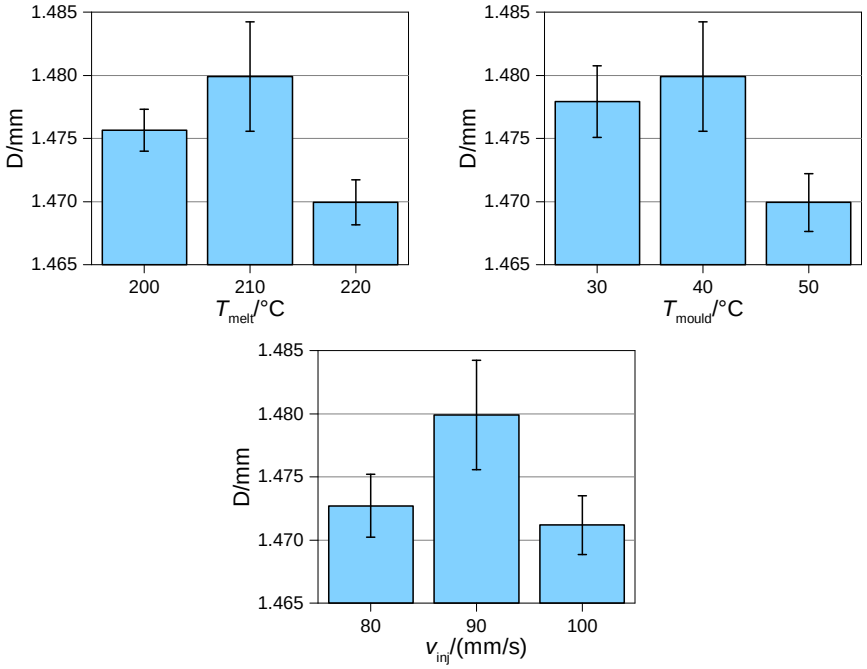

Figure 4.23: Interval plots of D against the three process parameters. The interval bars represent standard errors.

The roundness parameter R was not influenced by T_{mould} but only by T_{melt} and v_{inj} (Figure 4.24). The lowest R (equal to circa 0.005 mm), which reflects a higher dimensional stability of D among the three circumferential positions and thus a better roundness, was measured when moulding at high levels of these two parameters.

Figure 4.25 compares the trends of D and R with respect to the levels of the experimented variables. What stands out is that both D and R were minimized at high levels of T_{melt} and v_{inj}, proving that it was only possible to over-mould very circular rings when their diameter was minimum. Therefore, within the investigated range, rings having simultaneously high D and low R were not obtainable, posing a

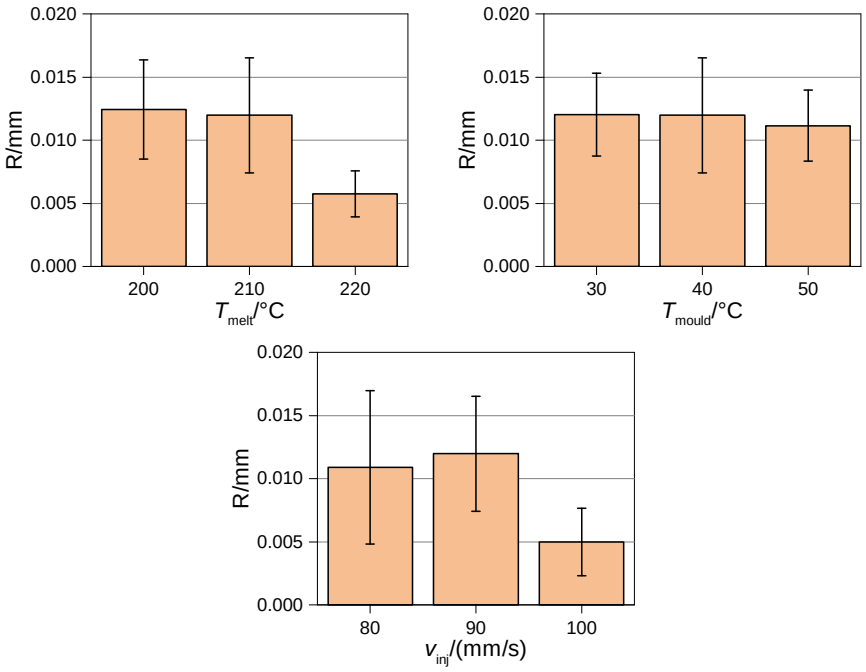

Figure 4.24: Interval plots of R against the three process parameters. The interval bars represent standard errors.

great challenge with respect to the conformance to design specifications. A possible solution could be identifying a trade-off between maximizing D and minimizing R by evaluating which of the two characteristics, i.e. diameter dimension and roundness, has the biggest impact on the product functionality and consequently setting the process parameters accordingly.

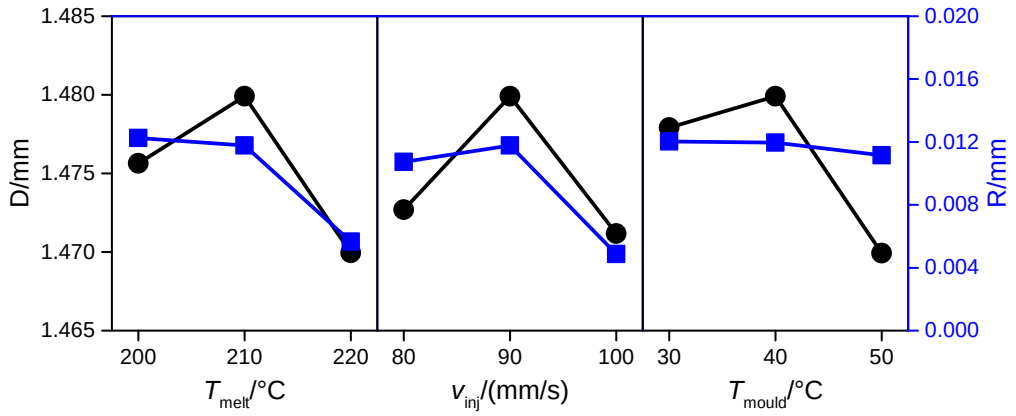

Figure 4.25: Combined main effects plot for D (in black) and R (in blue).

The results of the alignment angle α are reported in Figure 4.26. In this case, there was no significant effect of the three process parameters on the measured output, since the results for the different levels show overlapping error bars. This demonstrated

that the alignment of the micro assembly did not depend on any of the investigated moulding parameters. It is also important to notice that the average angle ranged between 0.4° and 0.6°. Such a low value proved that the metallic substrate and the over-moulded rings were aligned and that no relevant core-shift affected the quality of the produced parts. These values of α are in fact satisfactory for the application of the multi-material component.

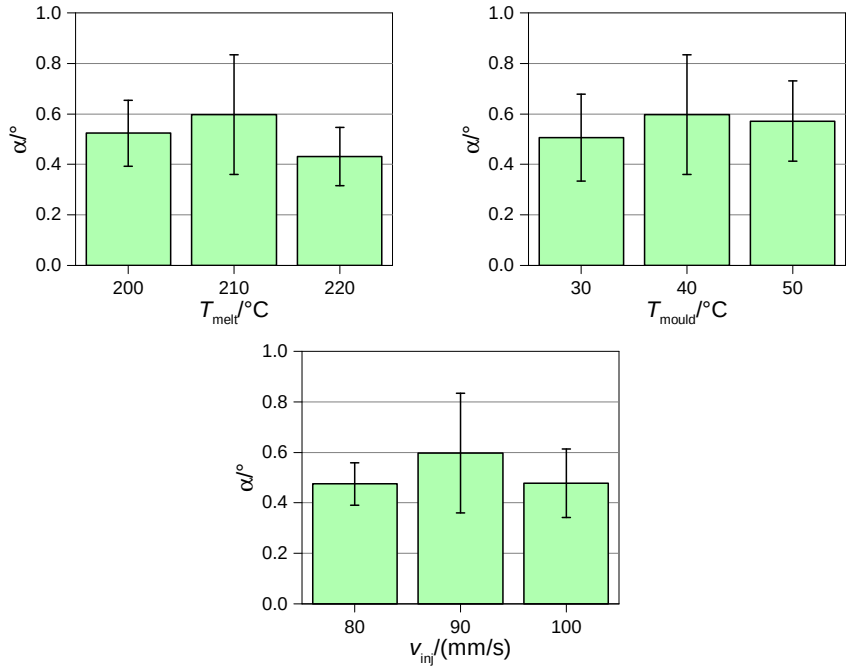

Figure 4.26: Interval plots of α against the three process parameters. The interval bars represent standard errors.

4.4 Summary and conclusions

This chapter focused on the study of the micro moulding process of thermoplastic elastomer (TPE) micro rings used as a component for high-performance phono-cartridges. For the first time in literature, a comprehensive investigation on the precision and accuracy of µIM of TPE was carried out.

The first section focused on the design, development and study of the µIM process for producing the micro components. A three-plate mould embedding a replaceable insert with four cavities was designed. The three-plate architecture allowed to perform the automatic detachment of the parts from the feed system, thus ensuring a fully automated process. A preliminary study based on SEM inspections and weld line depth measurements with a focus variation instrument was performed to determine a suitable process window. In particular, three different combinations of process

settings were taken into account. This preliminary analysis showed that selecting low values of clamping force (30 kN) and injection speed (below 100 mm/s) was of primary importance to reduce the size of the weld line by minimizing the quantity of air entrapped in the cavity. Based on these considerations, a general full factorial DoE plan was carried out to investigate the effects of melt temperature, mould temperature, injection speed and holding pressure on the outer (OD) and inner diameter (ID) of the micro rings, which were assessed using the same focus variation instrument. It was verified that the µIM process ensured a robust multi-cavity production, having the parts moulded in different cavities congruent dimensions. OD was influenced mostly by mould temperature and holding pressure, whereas ID by mould temperature and melt temperature. The four process parameters had, in all the ranges, an opposite effect on OD and ID. This was confirmed by the calculation of the shrinkage with respect to a reference diameter, which also allowed to show that the ID suffered a larger amount of shrinkage than OD. This was due to the constrained deformation affecting the inner surface of the ring, which in turn enhanced residual stresses, whereas the outer one was free to contract due to the absence of obstacles.

The second section showed the results of the functional tests carried out on specifically selected moulded micro rings. In particular, the rings produced with two DoE combinations, those yielding maxima and minima of OD and ID, were tested. After assembling the rings in the phono-cartridge, their performance was verified against the three main quantities (sensitivity, separation and balance) that have an influence on the quality of the produced sound. The results showed an overall good performance. The only failures were observed in combination with rings having the maximum ID, strongly suggesting that low ID values are more advisable with respect to the functionality of the assembly.

In the third section, an alternative manufacturing process based on the micro insert moulding of the micro rings around a metal substrate was investigated. This configuration was preferable in terms of production costs since it led to a significant reduction of the production time. The same three-plate mould used to manufacture the single rings was employed. However, in this case, an insert having two cavities was used. A fully automated process, which comprised the insertion of the metal substrate in the cavity by a robot arm before over-moulding, was attained. An experimental plan following a one-factor-at-time (OFAT) scheme was carried out to test the effect of melt temperature, mould temperature and injection speed on diameter, roundness (calculated as the deviation between the maximum and the minimum diameter in three circumferential positions) and alignment of the over-moulded assembly. Measurements were performed with a 2D optical CMM. The diameter and the roundness had a similar dependence on the experimental variables. Therefore, it was not possible to maximize the diameter and minimize its deviation at the same time, suggesting that a trade-off based on the final functionality has to be defined. As for the alignment, angles of circa 0.5° were measured between the

axis of the micro ring and that of the metal substrate. It was then concluded that no phenomenon such as core-shift had an impact on the component quality.

In summary, clear conclusions on the dependence of dimensional precision and accuracy of micro rings on the main µIM process parameters were provided. Their impact on the final functionality of the parts was also partially characterized, giving strong suggestions on the final set-up of the process to be adopted in a successful industrial production.

5 Development of product/process fingerprints of a 3D micro moulded component

The present chapter describes the application of the product/process fingerprint framework to a 3D micro component manufactured by µIM. The aim was to develop and define an applicable strategy for in-line quality assurance based on process monitoring.

An experimental campaign varying the main moulding parameters was carried out to characterize the process, with particular attention to the minimization of the defects affecting the part quality. By combining optical micro metrology and injection moulding process monitoring, the most suitable product and process fingerprints among various candidates were identified. Finally, an in-line quality assurance strategy was proposed.

The research presented in this chapter was published in [124] and partially taken from this paper.

5.1 Introduction

Quality assurance is one of the biggest challenges in modern micro manufacturing. As the produced components get smaller, more accurate and sophisticated measuring solutions are needed to assess the dimensions of these items. In fast replication processes, the challenge becomes even harder to tackle since 3D measuring instruments cannot cope with extremely high throughput rates, thus impeding the complete measurement of the entire production batches. During the process optimization phase, where deep knowledge of the effects of process settings variation is needed, these limitations become very significant, often leading to unsustainable experimental efforts.

In this chapter, a solution for assessing the quality of a 3D micro moulded part in-line is investigated. This method is based on the combination of product and process fingerprints (see section 1.2).

The product fingerprint is a single measurable characteristic of the part that is strongly correlated to the other significant measurands and therefore to the overall product quality. By assessing only this dimensional outcome, the conformance to specifications of all functional tolerances could be ensured. The product fingerprint must also be sensitive to the variations of process settings to work as an optimization tool in µIM. In fact, a change of process parameters has to be reflected in a variation of the fingerprint value if an effective control over the process has to be performed. The process fingerprint, on the other hand, is the process indicator, extracted from in-line monitored variables, that is mostly correlated to the dimensional quality of the moulded component. This variable must be also sensitive to the variation of the main process settings in order to assist the optimization phase. By combining product and process fingerprints, an in-line quality control framework can be designed for a specific micro component.

The procedure applied in this case to determine the two fingerprints is shown in Figure 5.1. Firstly, suitable product and process fingerprint candidates were selected based on preliminary experimental evidence. Then, DoE was used to investigate the sensitivity of the fingerprint candidates to process variations, while coefficients of correlation were used to rank the candidates based on their correlation to the quality of the moulded parts. The findings were finally combined to propose a strategy aiming at in-line dimensional quality assurance.

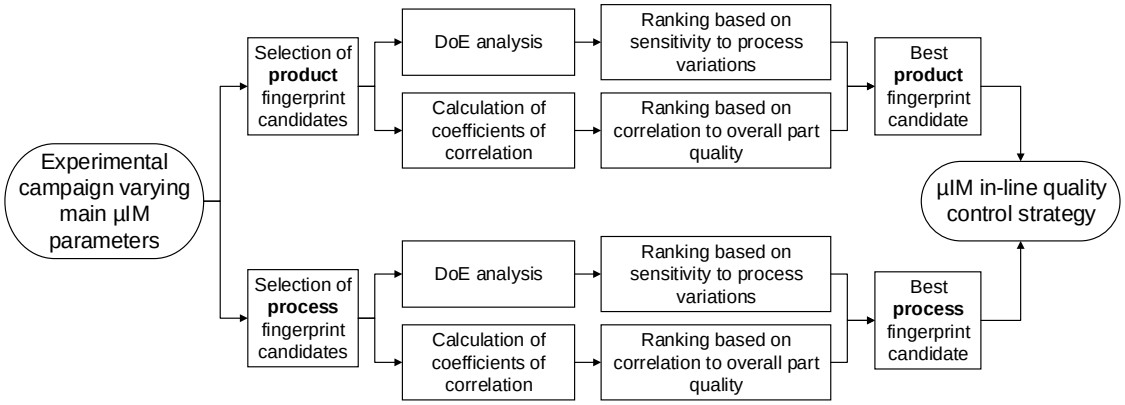

Figure 5.1: Flowchart representing the identification method for product and process fingerprints. The procedure starts with the selection of product and process fingerprint candidates. DoE and correlation analyses allow to determine the best candidates and finally define a µIM in-line control strategy.

5.2 Case study

The component object of the investigation was a POM micro part used in a medical application. Figure 5.2 shows its main dimensions and Figure 5.3 its appearance. Being its nominal volume equal to 0.07 mm^3 (equivalent to a mass of 0.1 mg) and dimensional tolerances of the diameters equal to ± 10 µm, the part falls in the category of micro moulded products according to the standard definitions (see section 2.2). The two structures on the internal surface and the 2° tape of the outer conical one were specifically designed to facilitate the ejection. The extremely small size of the part made it the smallest component manufactured by µIM in the analysed literature (see Table 5.1), being its volume one order of magnitude below typical micro moulded components and thus setting new lower limits for the process. Such a small size also made the use of any in-cavity sensor inapplicable without drastically changing the part design.

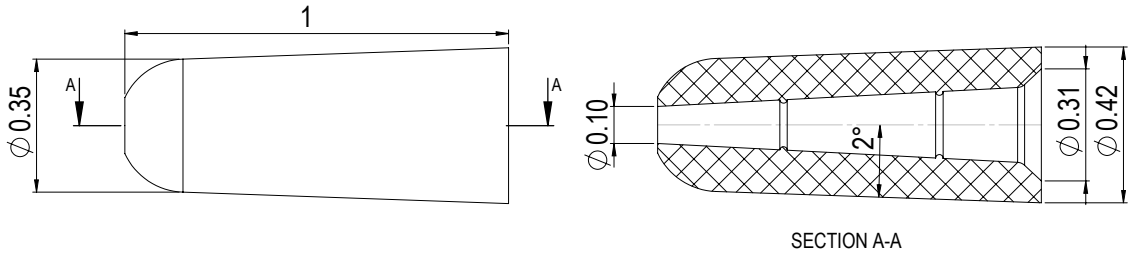

Figure 5.2: Geometry of the analysed micro component. The nominal dimensions in mm are shown.

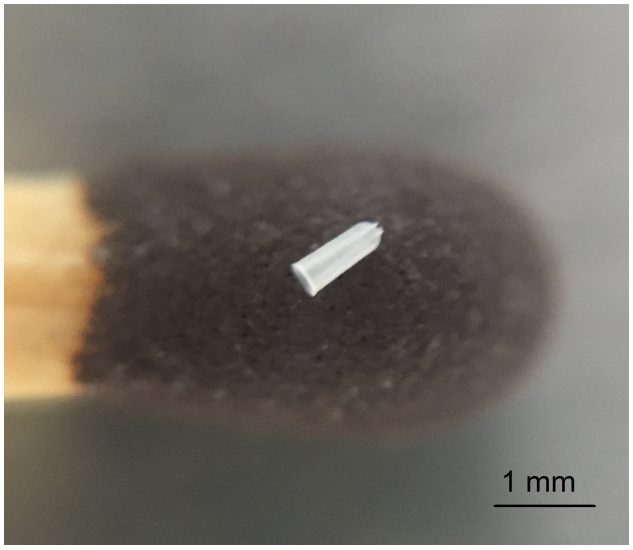

Figure 5.3: Picture of the micro moulded component [125].

Table 5.1: Volumes of micro moulded parts sorted from small to large.

Micro component	Approximate volume/mm^3	Reference
Micro filter	1.0	[45]
Micro ring	2.5	[111]
Part for weld line analysis	6.5	[50]
Part with micro pillars	12.0	[46]
Micro gear	14.0	[126]
Toggle for hearing aids	22.0	[51]
Dog-boned tensile bar	28.0	[68]
Thin-walled part	31.5	[127]
Square part fro shrinkage evaluation	35.0	[85]
Cylindrical part with micro pillars	110.0	[41]
Disc with micro and nano features	113.5	[128]

5.3 Experimental

5.3.1 Mould design

The micro part was moulded using a replaceable insert made of tool steel mounted in a three-plate mould (see Figure 5.4 (a)). This mould configuration enabled the automatic separation of the component from the feed system, thus avoiding a manual operation that would have inevitably introduced variability in the process. The structured hole was created by replicating a micro pin protruding from the movable plate of the mould. The insert cavity and the pin were machined using µEDM. The feed system was made of a cylindrical sprue with a 5 mm diameter, a conical runner and a ring gate having a nominal thickness of 25 µm and axially symmetric with respect to the part. The ejection was carried out by means of a vacuum gripper mounted on a robot arm, thus ensuring a fully automated µIM process. Figure 5.5 illustrates the mould design.

Preliminary experiments highlighted the need for a venting channel to attain a consistent and complete filling of the cavity. This adjustment was required because of the presence of entrapped air in the cavity, which prevented the polymer melt from reaching the end of the cavity in such small channels. Therefore, a circular 5 µm deep venting channel was machined by µEDM on the back of the insert (see Figure 5.4 (b) and Figure 5.5 (c)). If, on one hand, this modification allowed to tackle the unfilling issue, on the other, it generated a flash defect around the largest outer diameter of the component since the polymer melt was allowed to partially fill the gap created by the venting channel.

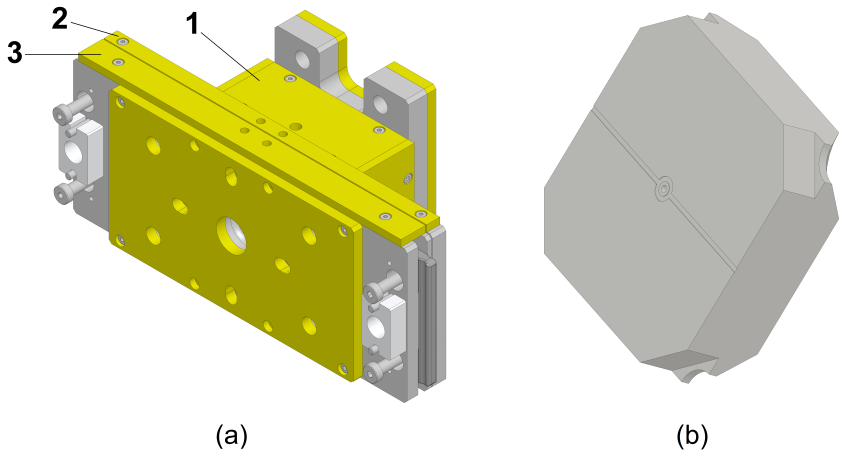

Figure 5.4: (a) 3D model of the mould. 1, 2 and 3 indicate ejection, middle and injection plate respectively. (b) Replaceable insert with venting channel located on the opposite side of the injection point.

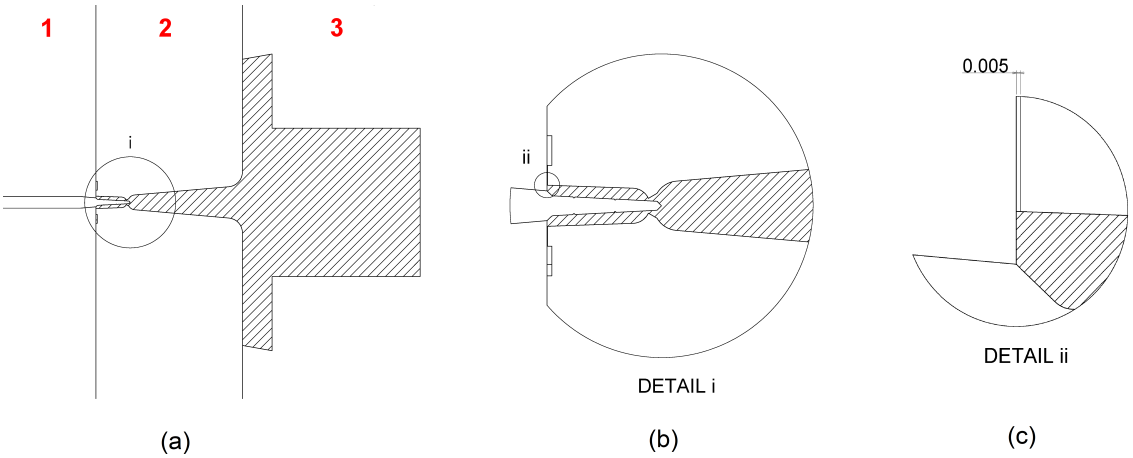

Figure 5.5: (a) Mould cross section showing the part and feed system (hatched) within the three mould plates (numbered in red). (b) Detail of the moulded component and ring gate. (c) Detail of the venting channel machined on the insert at the end of the flow path (nominal thickness in mm).

5.3.2 Experimental design

Micro moulding experiments were carried out using a Wittmann-Battenfeld MicroPower 15 µIM machine (maximum injection velocity: 750 mm/s, maximum clamping force: 150 kN, see Figure 2.5 (a) for details on the architecture). The material used was an unfilled POM (Hostaform® C 27021, Celanese, Irving, TX, USA). This polymer was selected for its low friction coefficient, good mechanical properties and

extremely low melt viscosity. Table 5.2 reports the main characteristic of the material and Figure 5.6 shows its viscosity and pvT plots.

Table 5.2: Main properties of the POM grade. MVR data were gathered at a test temperature of 190 °C and a test load of 2.16 kg.

Property	Units	Value	Test method
Density	g/cm^3	1.41	ISO 1183
Melt Volume Rate (MVR)	cm^3/10min	24.0	ISO 1133
Melting temperature	°C	166	ISO 11357-1, -2, -3

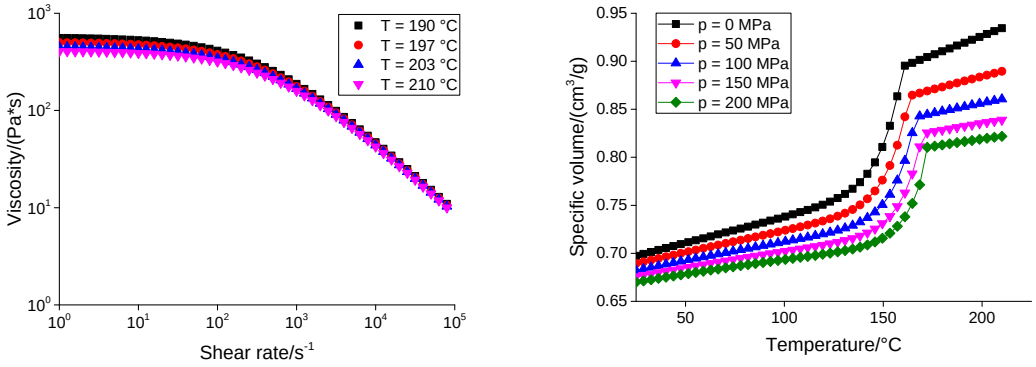

(a) **(b)**

Figure 5.6: (a) Viscosity plot at different temperatures and (b) pvT data at different pressures for the POM material [129].

A DoE approach was adopted to identify product and process fingerprints for the µIM process. Four process parameters, namely holding pressure, injection speed, mould temperature and melt temperature, were varied according to a two-level full factorial 2^4 design. Table 5.3 shows the levels of the experimented variables. The holding pressure was set at relatively low values if compared to typical µIM experiments to avoid an excessive flash formation that would have made the ejection difficult to carry out. For each process setting combination, the first ten produced parts were discarded and the following five were kept for evaluation. Therefore, the factorial design was replicated five times.

5.3.3 Measurement strategy and uncertainty evaluation

Five dimensional features were selected as product fingerprint candidates and assessed for each of the 80 produced micro components. Three of these candidates were geometries with a significant impact on the part functionality. These were the outer top diameter (ODt), outer bottom diameter (ODb) and inner bottom diameter (IDb)

Table 5.3: DoE process settings.

Process parameter	Symbol	Unit	Low level	High level
Holding pressure	p_{hold}	bar	250	500
Injection speed	v_{inj}	mm/s	150	350
Mould temperature	T_{mould}	°C	100	110
Melt temperature	T_{melt}	°C	200	220

(see Figure 5.7 (a)). The other two were related to the main defects affecting the part quality: flash and gate mark. The flash, as mentioned before, was due to the presence of the venting channel. The gate mark was, on the other hand, caused by the detachment of the feed system from the part by means of the displacement of the middle plate. It appeared as a prolongation of the part in the gate area (see Figure 5.7 (b)). Both defects had to be minimized to ensure the part functionality, and therefore their size represented a suitable optimization response and, as such, an ideal product fingerprint candidate. Flash and gate mark of each part were quantified by means of dimensional indicators: the area of the flash A_{flash} was used to measure the flash size, while the length of the gate mark L_{mark} was chosen as the indicator of the gate mark size. The values of both A_{flash} and L_{mark} increase when the two defects become larger.

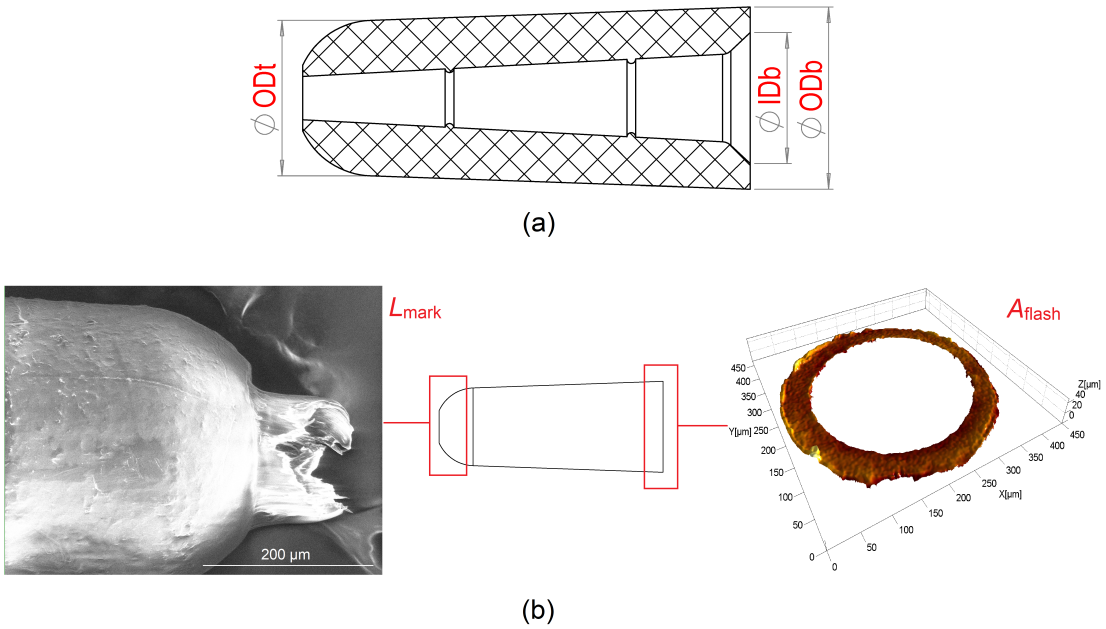

Figure 5.7: Product fingerprint candidates. (a) The three diameters ODt, IDb and ODb. (b) The two part defects and respective size indicators L_{mark} and A_{flash}.

The five product fingerprint candidates were measured using the focus variation microscope Alicona InfiniteFocus with a 20× magnification objective (see Table 2.5 for the characteristics), which ensured 3D capabilities and sub-micrometre resolution, which were both needed to acquire the features of the micro part. To capture the five measurands, two acquisitions were performed for each moulded sample. The measurands ODt and L_{mark} were extrapolated from an acquisition of the top side of the part, i.e. the left side in Figure 5.2. ODb, IDb and A_{flash} were instead measured by acquiring the bottom of the part, i.e. the right side in Figure 5.2. The value of the five measurands was finally extracted from the 3D optical reconstructions using an image processing software (MountainsMap®, Digital Surf, Besançon, France). In detail, the processing procedure was carried out as follows:

- ODt: this diameter was extrapolated from a top acquisition by fitting a circle to the points of the diameter of interest (see Figure 5.8 (b)).
- L_{mark}: this quantity was measured as the vertical distance between the highest acquired point belonging to the gate mark and the flat surface from which it protruded (see Figure 5.8 (c)). This surface was identified in the same way for all the moulded parts by considering a constant height with respect to the plane on which the circle having ODt diameter lay.
- IDb: this measurand was extrapolated from a bottom acquisition by fitting a circle to the points of the diameter of interest (see Figure 5.9 (b)). The 3D acquisition was initially processed by applying a levelling and a threshold along the z-axis. In particular, the threshold was applied to accurately identify only the points belonging to the flash surface, thus eliminating the influence of points acquired inside the hole.
- ODb: this diameter was extrapolated in the same way as IDb. As illustrated in Figure 5.9 (b), the outer perimeter of the flash was not as circular as the ones identifying ODt and IDb, making ODb measurement less accurate than the other ones. This was most probably caused by the imperfect co-axiality of the central pin with respect to the cavity, which created an unbalance in the polymer melt flow inside the micro channel that in turn led to a non-circular outer perimeter of the flash.
- A_{flash}: the flash area was measured by counting the pixels of the surface acquired in a bottom acquisition, such as the one shown in Figure 5.9 (b). After the number of pixels N_{p} was determined, a simple equation was used:

$$A_{\mathrm{flash}} = N_{\mathrm{p}} \times A_{\mathrm{p}} \tag{5.1}$$

  where A_{p} is the area of one pixel, equal to 0.19 µm^2. Although both ODb and A_{flash} are indicators of the size of the flash, the second one was more sensitive to variations of the defect since it was not affected by any non-circularity error as ODb was.

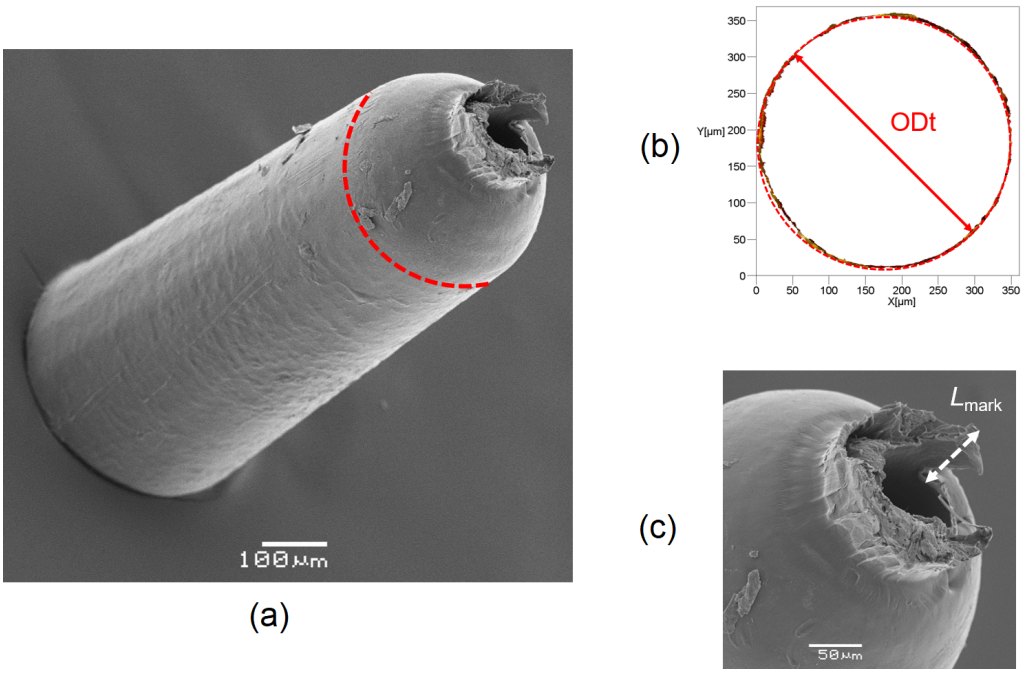

Figure 5.8: (a) SEM image of a moulded micro part: ODt is indicated in red. (b) ODt measurement. (c) L_{mark} definition.

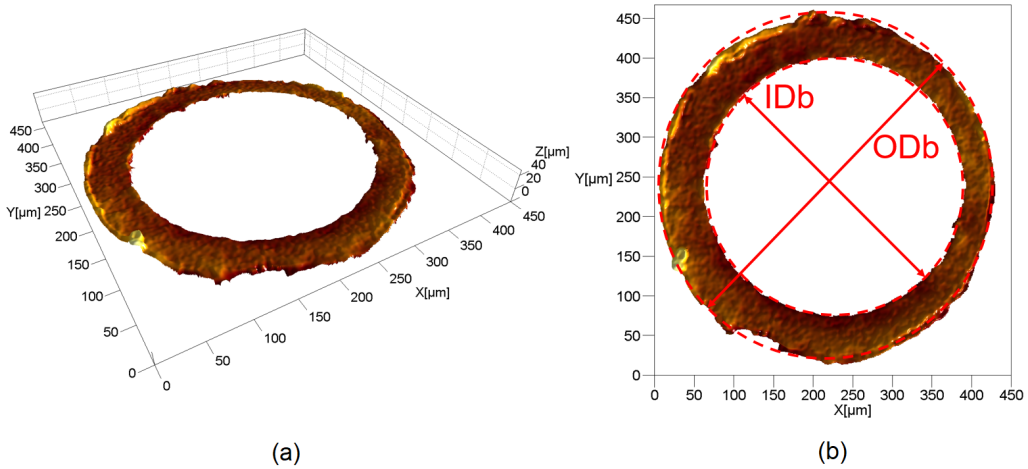

Figure 5.9: (a) 3D acquisition of the bottom of a moulded part. (b) Measurement of IDb and ODb.

Each acquisition was repeated three times and the averages were taken as output.

The mould geometries corresponding to the three diameters were also measured in order to provide a reference to determine the replication performance of the µIM process. The mould diameters corresponding to ODb and IDb were measured with the aforementioned focus variation microscope by acquiring the hole on the insert and

the pin. As for the diameter correspondent to ODt, no direct measurement procedure was applicable due to the inaccessibility for any optical or contact instrument. A fast replication media was thus used to replicate the internal geometry of the insert in order to perform an indirect measurement. In particular, a brown Polyvinylsiloxane (PVS) replication media (AccuTrans® AB, Coltene, Cuyahoga Falls, OH, USA) was poured inside the cavity and acquired after solidification. Having obtained the mould dimensions, the replication capability Δ_{D} was defined as:

$$\Delta_{\mathrm{D}} = \mathrm{D}_{\mathrm{part}} - \mathrm{D}_{\mathrm{mould}} \tag{5.2}$$

where $\mathrm{D}_{\mathrm{part}}$ and $\mathrm{D}_{\mathrm{mould}}$ represent a generic diameter D measured on moulded part and mould respectively. Δ_{D} is an indicator of the replication accuracy of the µIM process and thus the three variables Δ_{ODb}, Δ_{IDb} and Δ_{ODt} were considered as responses for the experimental analysis instead of ODb, IDb and ODt.

The quality of the measurements was verified by calculating the measurement uncertainty U, as the precision of the measurement chain must be characterized when dealing with the small variations at the micro scale. In this study, the uncertainties of five measurands were calculated according to ISO 15530-3 [119], similarly to the previous chapter (see subsection 4.1.4). Two different artefacts were used: a calibrated circle of nominal diameter equal to 250 µm for the uncertainty of ODb, IDb and ODt and a calibrated step height of 1 mm for the uncertainty of L_{mark}. Four uncertainty contributions were included in the calculation of U: u_{cal}, as stated in the calibration certificate of the artefacts; u_{res}, due to the resolution of the measurement instrument and calculated by considering a rectangular distribution; u_{w}, related to material and manufacturing variations of the actual measurand; and u_{p}, introduced by the measurement procedure and calculated as standard deviation of 20 repeated measurements on the calibrated artefacts. In particular, u_{w} was calculated as:

$$u_{\mathrm{w}} = \frac{\max(\mathbf{M}) - \min(\mathbf{M})}{2\sqrt{3}} \tag{5.3}$$

where $\mathbf{M}$ is the vector containing the three measurement repetitions. The expanded uncertainty U was eventually obtained by combining the contributions according to the law of propagation of uncertainty [95]:

$$U = k \times \sqrt{u_{\mathrm{cal}}^2 + u_{\mathrm{res}}^2 + u_{\mathrm{w}}^2 + u_{\mathrm{p}}^2} \tag{5.4}$$

where k was equal to 2 to achieve an approximate confidence level of 95 %. As for A_{flash}, the contributions u_{cal} and u_{p} were not taken into account because no calibrated artefact for area measurement was available. The uncertainty budget for the five measurands is reported in Table 5.4. What stands out is that, for the three diameters, the uncertainty-to-tolerance ratio U/T ranged between 11 % and 12 %.

These values are satisfying since the upper recommended limit in manufacturing is equal to 20 % [51], thus demonstrating that the selected measurement procedure was suitable for measuring the product fingerprint candidates.

Table 5.4: Mean values of uncertainty contributions and expanded uncertainty for the five measurands.

Unc. contribution	ODt/µm	IDb/µm	ODb/µm	L_{mark}/µm	A_{flash}/µm^2
u_{cal}	0.50	0.50	0.50	0.45	/
u_{res}	0.13	0.13	0.13	0.04	0.05
u_{w}	0.19	0.20	0.16	0.73	1.5×10^2
u_{p}	0.12	0.12	0.12	0.37	/
$U(k = 2)$	1.1	1.1	1.1	1.9	3.0×10^2

5.3.4 Process monitoring

For each moulding cycle, two process variables were recorded in-line: the pressure and the velocity of the injection plunger, named p and v respectively. No external sensor was employed since the two were derived from machine data already available for any user. The injection pressure was acquired by means of a strain gauge transducer (Sensorplatte microline, X Sensors AG, Diessenhofen, Switzerland) embedded in the machine and located at the back of the injection plunger (see Figure 5.10). The speed was recorded via the speed of the motor driving the plunger through the control unit of the machine. For both the monitored curves, the frequency of acquisition was set at 167 Hz (corresponding to a sampling interval of 6 ms), being it the lower limit allowed by the machine computer. Pressure and velocity were acquired synchronously and thus did not need any alignment with respect to the time-scale.

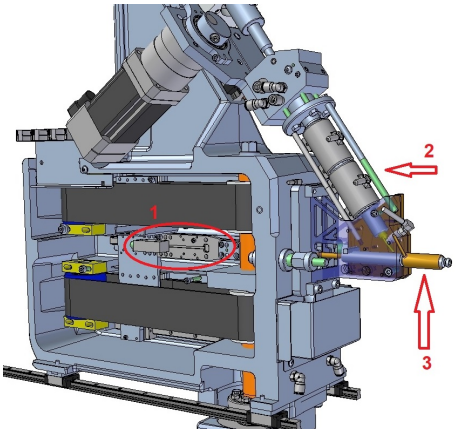

Figure 5.10: Position of the strain gauge pressure sensor (1) with respect to the plasticizing screw (2) and the injection plunger (3). Courtesy of Wittmann-Battenfeld GmbH.

After a visual analysis of the acquired profiles, it was clear that the holding pressure was the parameter that had the biggest impact on their shape. In fact, when the high level of p_{hold} was selected, a monotone trend of the injection pressure was always observed (see Figure 5.11 (a)). The trend culminated in a peak caused by the high pressure drop due to the extremely small dimensions of the gate and mould cavity. After the switch-over point, which was defined by assigning a threshold value on injection pressure, p readjusted to the decreasing linear profile of the holding pressure that was set at the machine interface. This a switch-over strategy was selected to achieve a smooth displacement of the injection plunger. Oppositely, when the low value of p_{hold} was selected, the injection pressure always showed a point of discontinuity (see Figure 5.11 (b)). This behaviour was caused by the plunger suddenly decelerating and then accelerating again: when moulding with p_{hold} equal to 250 bar, the cavity was not filled at the defined switch-over point, thus causing a pressure decrease. Then, the plunger accelerated again during the holding phase, completed the filling, as revealed by the presence of the peak, and re-adapted to the imposed decreasing holding pressure profile. The different level of p_{hold} had an influence also on the shape of the velocity profiles. When moulding with holding pressure of 500 bar, the plunger accelerated until v reached the value of the selected v_{inj} and then stopped in correspondence with the switch-over point (see Figure 5.12 (a)). On the other hand, when moulding with p_{hold} equal to 250 bar, v profiles showed a sudden drop, followed by a new increase until the final stopping (see Figure 5.12 (b)). This difference between the shapes of the curves was due, as for the case of p, to the decrease of pressure and consequent plunger deceleration happening when the cavity was not filled at the defined switch-over condition.

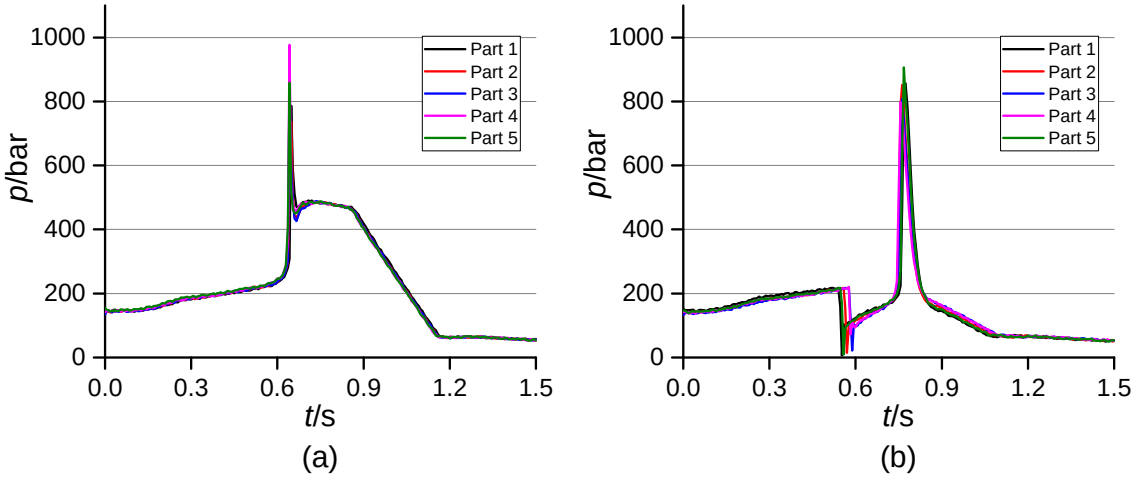

Figure 5.11: Injection pressure profiles for five DoE replicates recorded when moulding at: (a) high holding pressure and (b) low holding pressure. v_{inj} was equal to 150 mm/s in the two cases.

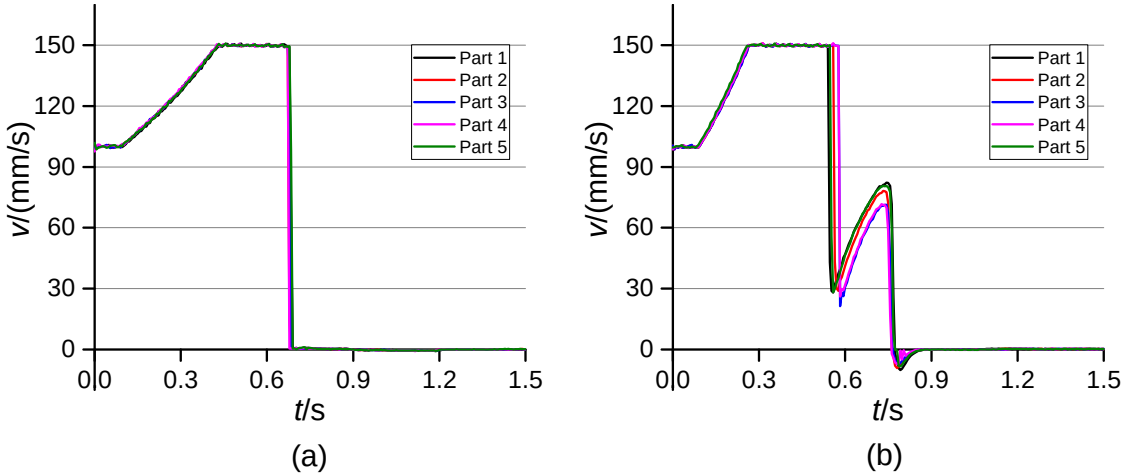

Figure 5.12: Injection velocity profiles for five DoE replicates recorded when moulding at: (a) high holding pressure and (b) low holding pressure. v_{inj} was equal to 150 mm/s in the two cases.

Once p and v were acquired through in-line monitoring, their dependence on µIM parameters was investigated by identifying indicators that acted as process fingerprint candidates. Variables that well characterized the shape and main features of both pressure and velocity profiles were defined.

The process fingerprint candidates derived from the injection pressure curves were:

- p_{max}: the maximum value for each recorded p curve, equivalent to the peak value. Being the pressure peak generated by the pressure drop caused by the small size of the channels, this is an indicator of the filling behaviour.
- p_{mean}: the average pressure in the time interval between the start and the end of the moulding cycle (points A and C in Figure 5.13 (a)). This quantity provides average information on the pressure acting in one moulding cycle.
- I_p: the integral of the pressure in the peak region. This region was identified as the time interval spanning from the abrupt increase of p correspondent to the start of the filling and the point where the injection pressure adapted to the imposed holding profile. This quantity is related to the amount of energy provided by the injection plunger during the filling phase and, as such, is expected to be process dependent, being the filling of the cavity highly influenced by variations of µIM process parameters. In particular, I_p was calculated by applying the trapezoidal rule:

$$\mathrm{I}_p = \mathrm{d}t \times \sum_{t=t_{\mathrm{A}}}^{t_{\mathrm{B}}-\mathrm{d}t} \frac{p(t) + p(t+\mathrm{d}t)}{2} \tag{5.5}$$

where t is the time, t_A and t_B are the times correspondent to points A and B respectively (see Figure 5.13 (a)) and dt is the sampling interval of 6 ms.

- $I_p/\Delta t$: this quantity is equal to the integral mean of p in the peak region, i.e. I_p divided by the integration range $\Delta t = t_B - t_A$ (see Figure 5.13 (a)). This variable differs from I_p because it is not influenced by the range of integration, which is in this case equal to the filling time. Therefore, $I_p/\Delta t$ indicates the average p acting within the pressure peak region.

From the injection velocity curves, two further process fingerprint candidates were extracted:

- v_{mean}: the mean velocity calculated as the average of the v values in the time interval between the start of acceleration of the plunger and its stop at the switch-over (point D to point F in Figure 5.13 (b)). This quantity is related to the average velocity during filling.
- v_{slope}: the slope of the velocity profile between the start and the end of the acceleration (point D to point E in Figure 5.13 (b)). This value is equal to the initial constant acceleration of the plunger.

The maximum value of v was not selected as fingerprint candidate since it was equal to v_{inj} and, as such, only dependent on that µIM parameter.

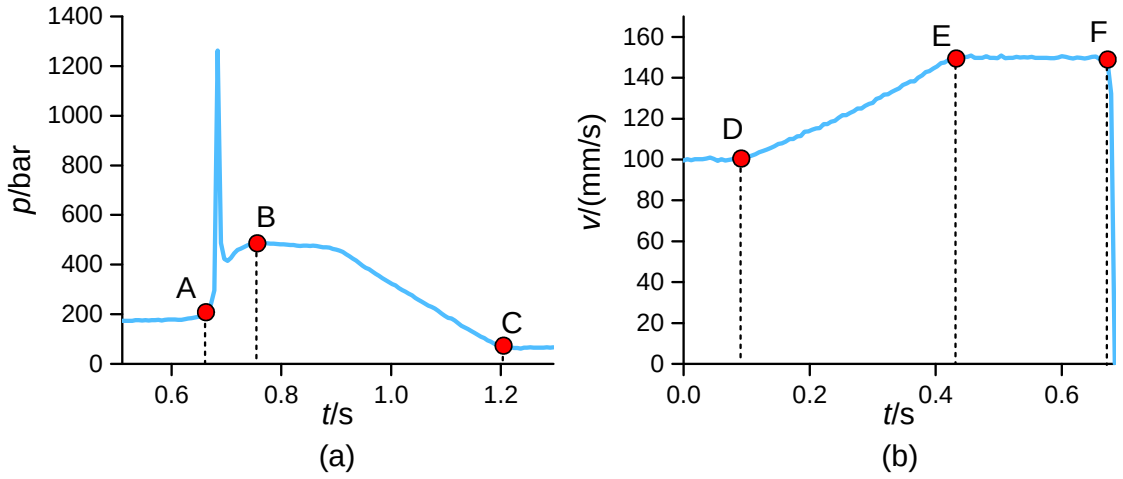

Figure 5.13: Pressure (a) and velocity (b) profiles with points indicating the time intervals used in the calculation of the process fingerprints candidates. The position of the points was univocally determined by tracking slope changes using the first order derivative value.

5.4 Results and discussion

5.4.1 Product fingerprint analysis

Figure 5.14 reports the results of the analysis for the five product fingerprint candidates. The main effects plot and the Pareto chart of the effects are shown in order to systematically determine which parameter had a significant impact on the responses. In both the plots, interval bars are shown. In the main effects plots, they represent the expanded measurement uncertainty (see Table 5.4) that must be taken into account to verify whether the measurement variability is big enough to hide the variation induced by setting a different level of any input parameter. In the Pareto charts, the interval bars represent the standard deviation of the effects obtained by running five separate analyses correspondent to the the five replicates of the DoE design. These deviations were plotted since they allow to quantify the repeatability of the conclusions drawn from the Pareto chart: a low standard deviation of an effect reveals that the significance of that effect is robust with respect to process repeatability. Therefore, an effect whose interval bar overlaps with the significance limit cannot be considered as significant.

Figure 5.14 (a) shows the results for Δ_{ODt}. The most significant process parameter was T_{melt}: its increase led to a 2.5 µm decrease of replication. The other three µIM process parameters did not have a relevant influence on the measured output when considering the measurement uncertainty. As for the interactions, only the one between T_{melt} and v_{inj} had a relevant impact, being its standardized effect larger than the significance limit and its standard deviation bar not overlapping with it.

Figure 5.14 (b) reports the results for the replication of IDb. On average, the replicated IDb was 14.0 µm smaller than the correspondent mould geometry, in a similar way to ODt. The mould temperature was the only significant process parameter. In particular, increasing T_{mould} from 100 °C to 110 °C resulted in a decrease in replication. This behaviour, which may seem opposite to the usual enhancement of replication obtained with higher mould temperatures, was already observed in the previous chapter (see subsection 4.1.7) for the replication of the inner diameter of the micro rings. The Pareto chart of effects showed that only the interaction between T_{mould} and T_{melt} was significant.

Δ_{ODb} was more sensitive to process variations than the previous measurands (see Figure 5.14 (c)). In particular, setting high levels of p_{hold}, v_{inj} and T_{mould} led to an increase of replication that was larger than the measurement uncertainty. In this case, Δ_{ODb} had positive values since ODb is the diameter of the circle that identifies the perimeter of the flash formed at the end of the flow (see Figure 5.9): the replicated diameter was larger than the correspondent one measured on the cavity. Increasing any of the investigated process parameters had a positive effect on Δ_{ODb} and, consequently, on the flash size. This happened because, while using the high

level of the mould temperature, the viscosity of the polymer melt inside the cavity was reduced, thus provoking a better replication and, in this case, a bigger flash. A similar effect was obtained when increasing the injection speed since the viscosity of the melt was reduced because of the shear thinning behaviour of thermoplastic polymers such as POM. Thus, a longer flow path inside the venting channel was achieved, leading to the formation of a larger flash and consequently a larger ODb. Increasing the holding pressure also increased the flash size, since more material was allowed to enter the cavity. These findings were also confirmed by the Pareto chart, which also revealed that the interaction between T_{mould} and p_{hold} had a significant impact on the measured response.

A_{flash} showed very similar trends to Δ_{ODb} (see Figure 5.14 (d)). This was expected since the two-dimensional outputs are both correlated to the flash size. However, the measurement uncertainty was less significant in this case. Moreover, as shown by the Pareto charts, p_{hold} was more significant for A_{flash} than Δ_{ODb}, since the interval bar of its standardized effect does not overlap with the significance limit. Differently from the previous case, also the interaction between mould and melt temperature was significant. Thus, it can be concluded that A_{flash} was more sensitive to process variations than Δ_{ODb} and so was a better product fingerprint candidate related to the flash size.

Figure 5.14 (e) shows the results for the gate mark length L_{mark}. The size of this defect was on average equal to 82 µm, which is relevant if compared to the overall part dimensions. All four investigated process parameters had a significant influence on L_{mark}. Increasing the input variables led to a decrease of the defect size, showing that this product fingerprint candidate was very sensitive to µIM settings variations. The holding pressure had the largest impact since the use of 500 bar provided parts having on average a 30 µm shorter gate mark than those moulded with p_{hold} equal to 250 bar. To investigate more on these effects, SEM images of parts manufactured with different DoE combinations were taken and compared (see Figure 5.15). What stands out is that, when moulding at the low levels of the four parameters, the gate mark was very evident, almost occluding the upper hole of the component and thus disabling its functionality. A zone of deformation was clearly visible around the defect, meaning that the breakage caused by detachment of the gate from the part was of ductile nature. Setting the µIM parameters at the high level allowed a great reduction of the gate mark size and of the area of deformation (see Figure 5.15 (b) and (c)). Selecting the high levels of all the four process parameters generated parts almost free of the defect. The great influence of the process conditions on the gate mark may have been caused by a change of crystallinity of the polymer. In fact, moulding with high levels of the process parameters may have impeded the formation of crystalline structures because of the more drastic cooling rate, thus decreasing the mechanical properties and in turn facilitating the brittle detachment of the gate from the part. It is worth noting that p_{hold}, v_{inj}, T_{mould} and T_{melt} all had an opposite effect on A_{flash} and L_{mark}. This means that a simultaneous minimization of the two defects was impossible inside the experimented process window.

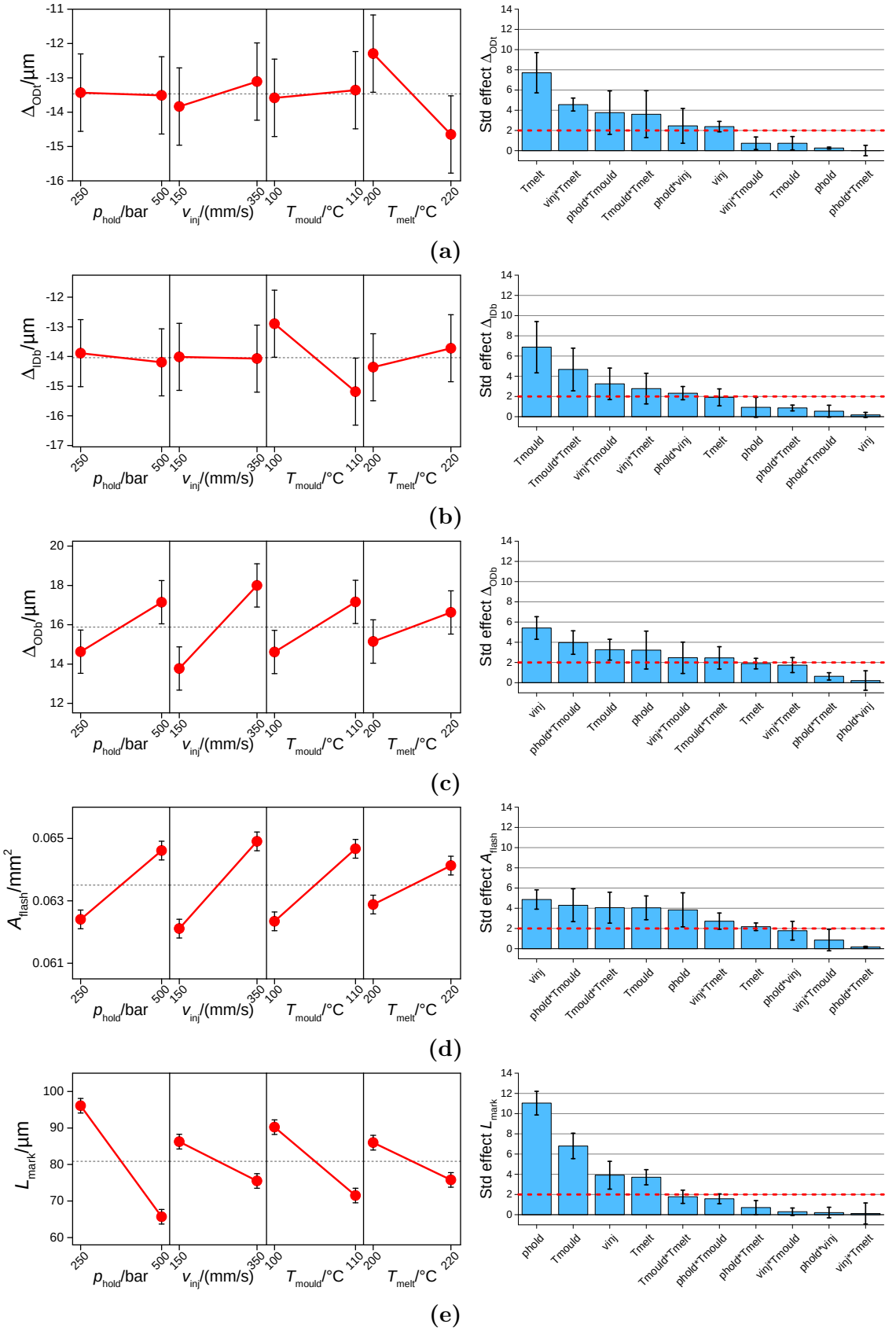

Figure 5.14: Influence of µIM process on the five product fingerprint candidates: (a) Δ_{ODt}, (b) Δ_{IDb}, (c) Δ_{ODb}, (d) A_{flash} and (e) L_{mark}.

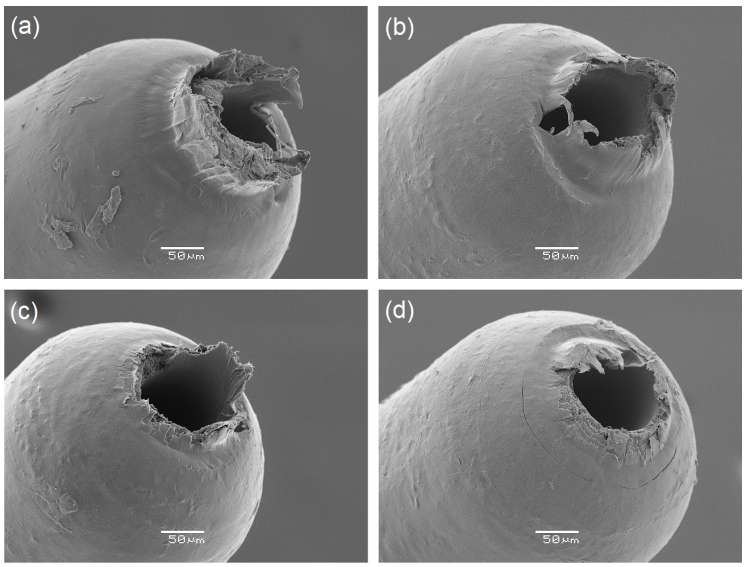

Figure 5.15: Gate mark appearance for different combinations of process parameters [125]: (a) was moulded with low levels of T_{melt}, p_{hold}, T_{mould} and v_{inj}; (b) was moulded with low levels of p_{hold}, T_{mould} and v_{inj}; (c) was moulded with low levels of p_{hold} and (d) was moulded with high levels of the four process parameters.

The analysis of the effects of the µIM parameters on the five product fingerprint candidates allowed to identify A_{flash} and L_{mark} as best candidates with respect to the characteristic of process sensitivity. Both were in fact greatly influenced by all the four investigated parameters and could thus serve to tune the process with the aim of optimizing the quality of the produced parts.

The other characteristic that an effective product fingerprint must have is the correlation to the overall part quality. This is necessary to guarantee an efficient quality control based only on the measurement of a single dimensional feature. To identify the best candidate with respect to this requirement, a correlation analysis was carried out. In particular, the Pearson coefficient of correlation ρ was calculated for each couple of measurands. It was calculated as:

$$\rho(\mathbf{x},\mathbf{y}) = \frac{\sum(\mathrm{x}-\bar{\mathrm{x}})(\mathrm{y}-\bar{\mathrm{y}})}{\sqrt{\sum(\mathrm{x}-\bar{\mathrm{x}})^2 \sum(\mathrm{y}-\bar{\mathrm{y}})^2}} \tag{5.6}$$

where $\mathbf{x}$ and $\mathbf{y}$ are generic vectors containing two datasets and $\bar{\mathrm{x}}$ and $\bar{\mathrm{y}}$ are their respective mean values. This coefficient can vary between -1 and +1, where the first describes a perfect linear negative correlation and the second a perfect linear positive correlation. A ρ equal to 0 indicates that no correlation exists between the two examined sets of values. In this study, ρ was calculated by considering all the 80 values deriving from the DoE campaign for each product fingerprint candidate.

Figure 5.16 shows the correlation coefficients calculated for the ten couples of product fingerprint candidates. It can be seen that the greatest correlation ($\rho = 0.9$) was the one between Δ_{ODb} and A_{flash}. Both the measurands are in fact related to the flash size, as addressed before: the increase of one determined an increase of the other and vice versa, meaning that controlling only one of them allows monitoring the two geometrical outputs simultaneously. A second group of coefficients of correlation ranging from -0.5 to -0.4 can be identified. A_{flash} and L_{mark} shared, in fact, a ρ equal to -0.5, demonstrating that a significant amount of correlation existed between these two fingerprint candidates. This was also mirrored in the main effects plots (see Figure 5.14) where it was shown that the investigated process parameters had an opposite effect on the two defect sizes. Significant negative correlations were also observed between Δ_{ODb} and L_{mark} and between Δ_{IDb} and A_{flash}. The second one was caused by the geometry of the flash: a decrease of IDb resulted in an increase of the flash area according to its definition (see Figure 5.9). The other coefficients of correlation were all lower than 0.3 in absolute value and, as such, negligible if compared to the others.

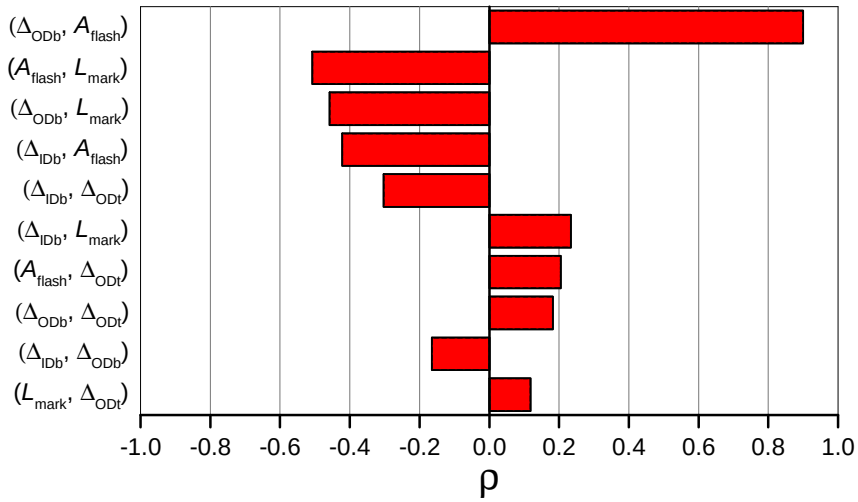

Figure 5.16: Values of the coefficients of correlation calculated between each couple of product fingerprint candidates. Values were sorted largest to smallest in absolute value.

Based on the results of the correlation analysis, it can be concluded that the product fingerprint candidate that was most correlated to the overall part quality was A_{flash}, being the one that showed high levels of ρ in combination with three other measurands, namely Δ_{ODb}, L_{mark} and Δ_{IDb}. Thus, by controlling only this dimensional characteristic, the best control over the overall part quality can be carried out. Taking also into account the requirement of sensitivity to process settings variations, the best product fingerprint for the specific part under analysis was indeed the flash area, followed by the length of the gate mark.

5.4.2 Process fingerprint analysis

A similar type of analysis was carried out to identify the best process fingerprint candidate among the six indicators derived from the monitored pressure and velocity profiles. In this case, the main effects plots were represented with interval bars equal to the standard errors, while Pareto charts were plotted as before.

Figure 5.17 (a) shows the results for p_{max}, which depended mainly on p_{hold} and v_{inj} values. Particularly, an increase of both holding pressure and injection speed led to an increase of the maximum injection pressure. The effect of v_{inj} was due to the fact that flowing a fluid with higher speed requires a higher injection pressure. The effect of p_{hold} is, on the other hand, due to the used switch-over condition: as already anticipated, the machine was set to switch from the filling phase to the holding one when a certain pressure was reached. Thus, when selecting a higher p_{hold}, the injection pressure was allowed to rise more before switching to the holding profile. The interaction between p_{hold} and v_{inj} was also significant.

p_{mean} was predominantly influenced by the holding pressure (see Figure 5.17 (b)). This happened because p_{mean} was calculated as average p along the entire moulding cycle (see Figure 5.13 (a)). This averaging operation minimized the relevance of the peak phase, making the holding phase and the value of p_{hold} preponderant. All the other effects, interactions included, were negligible.

Figure 5.17 (c) illustrates the effect of µIM process parameters on I_p. This fingerprint candidate was mainly influenced by the holding pressure. The second most significant effect was that of v_{inj}. The causes of this are similar to the one discussed for p_{max} dependence on the process variations. In fact, the integral of p in the peak region was strongly influenced by the value of the p peak. However, in this case, there was a larger sensitivity with respect to other process parameters such as T_{mould}, which had a more significant impact on the results but, considering the interval bars of both main effects plot and Pareto chart, could not be considered as significant for I_p.

$\mathrm{I}_p/\Delta t$ showed a process dependence similar to I_p (see Figure 5.17 (d)). However, the operation of normalizing the pressure integral over the integration range considerably diminished the relevance of v_{inj}, which remained still above the significance limit, while enhancing that of T_{mould}, whose effect is above the threshold in the Pareto chart. This may have been caused by the fact that changing the injection velocity setting had an impact on the duration of the peak region and consequently on the filling time. Setting the high level of the mould temperature resulted in an increase of $\mathrm{I}_p/\Delta t$. This is somehow unexpected since increasing T_{mould} usually decreases the polymer viscosity and therefore the pressure needed to drive the melt through the cavity channels. As for the previous case, interactions of v_{inj} were also significant.

Figure 5.18 (a) shows the results for v_{mean}, whose value was influenced mostly by v_{inj}, p_{hold} and their interaction. Increasing the injection speed had a positive effect on v_{mean}, since a higher velocity plateau was monitored. Increasing the holding pressure

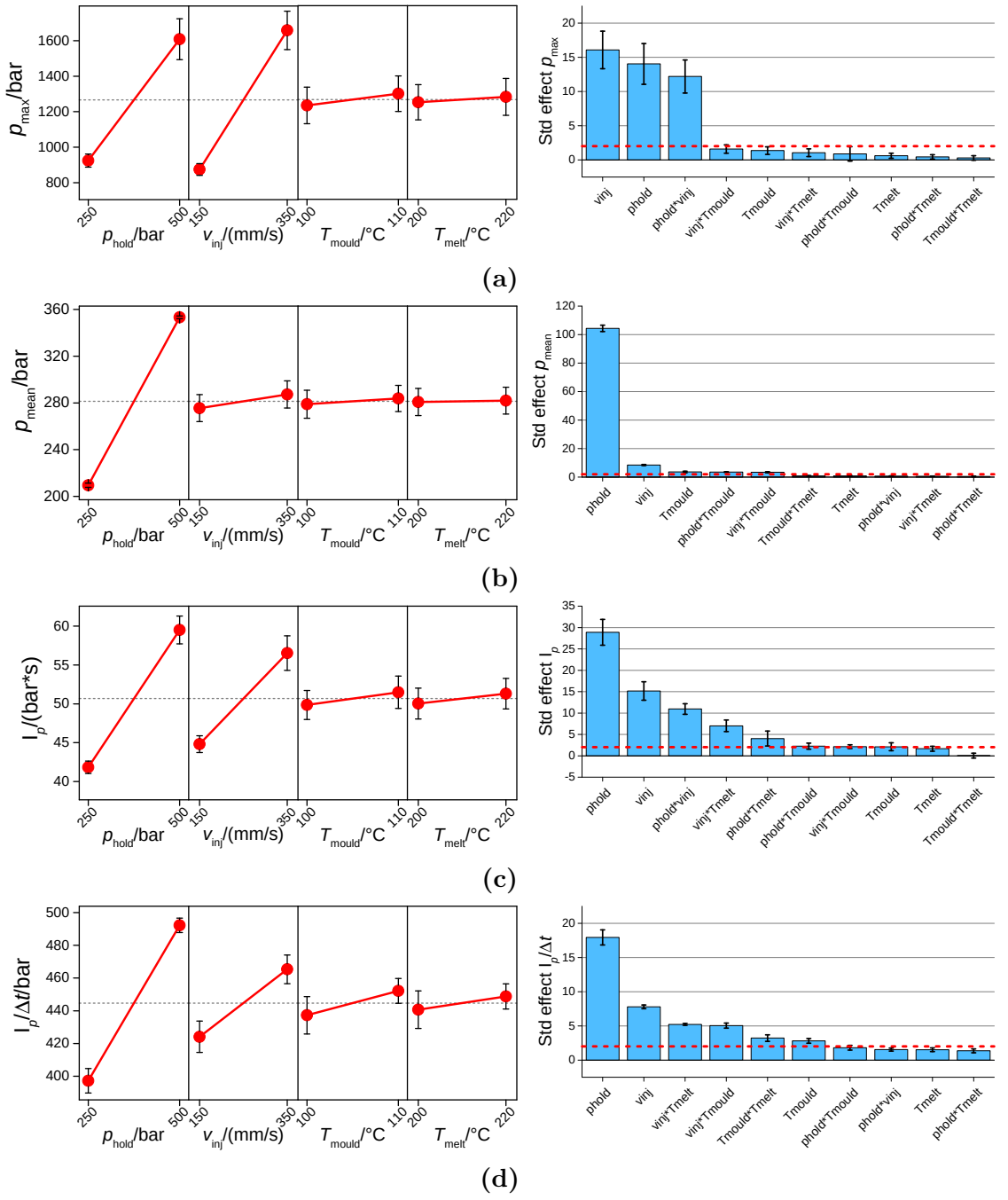

Figure 5.17: Influence of µIM process on the four process fingerprint candidates derived from monitored injection pressure curves: (a) $p_{\max}$, (b) p_{mean}, (c) I_p and (d) $\mathrm{I}_p/\Delta t$.

had a similar impact: this was due to the fact that, when moulding at the high level of p_{hold}, no deceleration of the plunger, and therefore no decrease of speed during the filling phase, was observed (see Figure 5.12 (b)). The significance of the interaction was caused by the fact that, when using high p_{hold}, an increase of injection speed led to a larger increase of v_{mean} than when using a low p_{hold}. Indeed, the deceleration behaviour was similar when using both high and low v_{inj}.

v_{slope} depended only on the injection speed (see Figure 5.18 (b)). In particular, moulding at high v_{inj} led to a substantial increase of the plunger acceleration from 260 mm/s^2 to 1100 mm/s^2. This demonstrated that, when a higher v_{inj} was selected, the machine motor provided the plunger with a higher acceleration in order to reach it in a comparable amount of time.

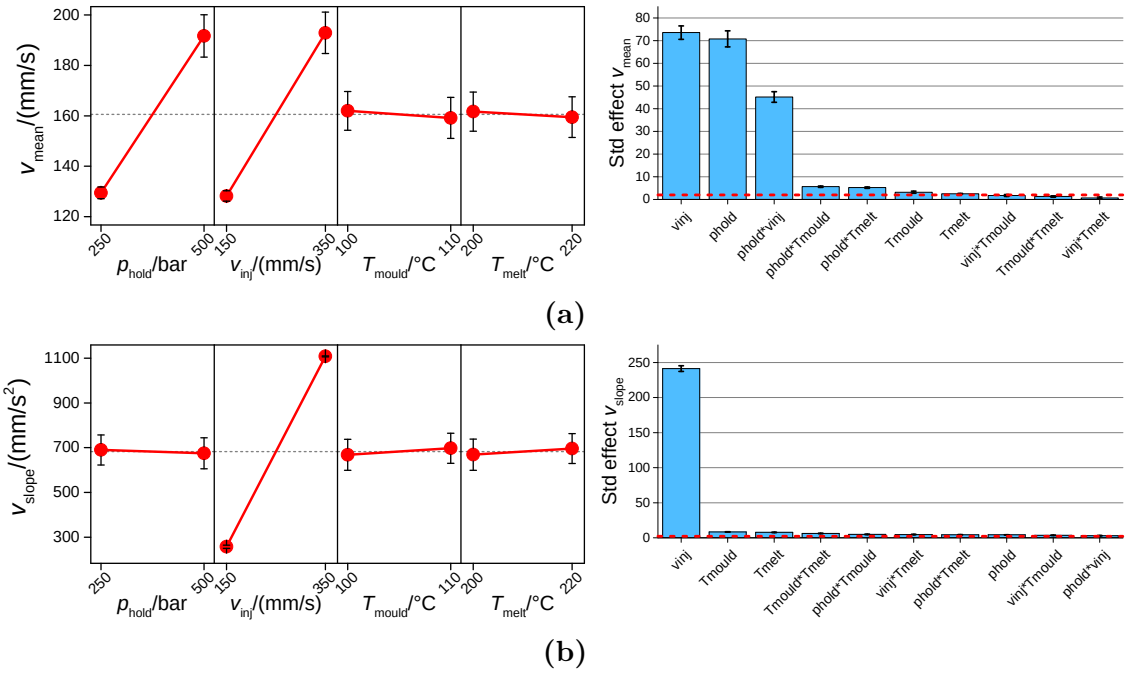

Figure 5.18: Influence of µIM process on the four process fingerprint candidates derived from monitored injection velocity curves: (a) v_{mean} and (b) v_{slope}.

In conclusion, this investigation revealed that holding pressure and injection speed were the most influencing parameters for the six process fingerprint candidates extracted by monitored injection pressure and velocity profiles. On the other hand, mould and melt temperature variations were in most cases not significant. This was because pressure and velocity were both measured at the injection plunger location: quantities measured inside the mould with external sensors are normally more sensitive to T_{melt} and T_{mould} variations. Only the candidate $\mathrm{I}_p/\Delta t$ showed a relevant dependence on T_{mould}, making this indicator the best process fingerprint candidate among those extracted from p and v with respect to sensitivity to µIM

process variation: by in-line monitoring $I_p/\Delta t$ value, variations of holding pressure, injection speed and mould temperature can be observed and quantified.

To evaluate the relation between $I_p/\Delta t$ and the part quality, and therefore the applicability of this variable as in-line quality assurance tool, the same approach used for the product fingerprint correlation analysis was adopted. In this case, the coefficient of correlation ρ was calculated by applying Equation 5.6 to $I_p/\Delta t$ and the five product fingerprint candidates.

Figure 5.19 shows the results. The correlation coefficients appear as divided into two distinct groups: one made of ρ values calculated for L_{mark}, Δ_{ODb} and A_{flash}, which were all larger than 0.7 in absolute value, and the other of ρ values calculated for Δ_{IDb} and Δ_{ODt}. Thus, $I_p/\Delta t$ was highly correlated with the size of the gate mark and the flash, i.e. the defects affecting part quality, and with the dimension of ODb, which was in turn highly related to L_{mark} and A_{flash} (see Figure 5.16). On the other hand, the other two measurands showed no relevant link with the integral mean of p, since the correlation coefficients were equal to -0.25 and 0.21 for Δ_{IDb} and Δ_{ODt} respectively. These findings proved that $I_p/\Delta t$, besides being sensitive to variations of µIM process parameters, was also correlated to the two best product fingerprint candidates. Therefore, it can act as the bridge between process monitoring and part quality, representing the link needed to perform a fast in-line assurance of the investigated moulded component.

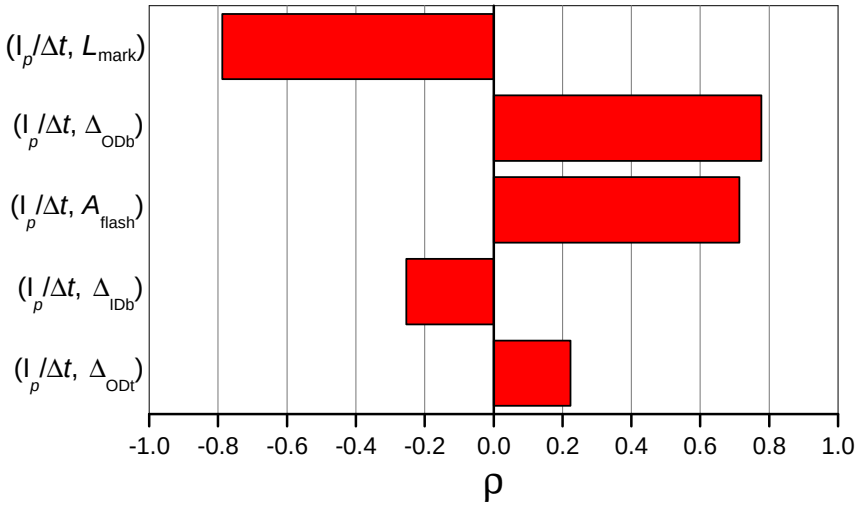

Figure 5.19: Values of the coefficients of correlation calculated between $I_p/\Delta t$ and the five product fingerprint candidates. Values were sorted largest to smallest in absolute value.

5.4.3 In-line quality assurance strategy

Figure 5.20 shows the two best product fingerprint candidates plotted against $I_p/\Delta t$. It can be observed that there existed a relation among the data. In fact, there is an almost linear correlation between L_{mark} and the integral mean. The data also show a limited dispersion around the fitted linear trend, demonstrating that the relation between the two variables was robust inside the range of the experimented variables. Being the slope of trend negative, a higher $I_p/\Delta t$ determined a smaller gate mark on the moulded parts. This finding agrees with the opposite slopes of the main effects plots for the two variables (see Figure 5.14 (e) and Figure 5.17 (d)). By controlling the identified process fingerprint, an accurate control on the size of this defect can be performed: $I_p/\Delta t$ must be kept at values around 500 bar if the size of the gate mark has to be minimized. Oppositely, $I_p/\Delta t$ equal to 300 bar generated a defect having double the size. As regards the size of the flash, indicated by the A_{flash} value, a positive trend can be observed. Therefore, lower $I_p/\Delta t$ values were needed to minimize the size of this defect: the lower the pressure applied during filling, the smaller the flash. In this case, the data were more dispersed than for L_{mark}, resulting in a less precise and accurate prediction. However, the general data trend is still evident. Being A_{flash} correlated to most of the other dimensional measurands (see Figure 5.16), the quality optimization can be effectively carried out by monitoring $I_p/\Delta t$ for every moulding cycle, thus assessing the quality of all moulded parts.

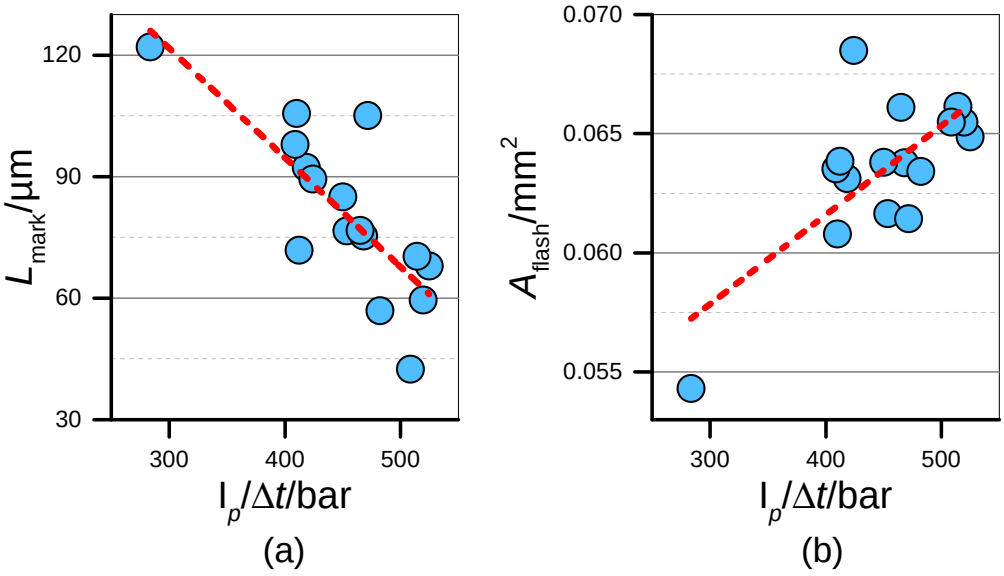

Figure 5.20: (a) L_{mark} and (b) A_{flash} versus $I_p/\Delta t$. Red dashed lines represent the linear trends. Each point is the average of the five DoE replicates.

5.5 Summary and conclusions

The product/process fingerprint framework was applied to a 3D micro moulded component with the aim of defining an in-line procedure for quality assurance based on process monitoring.

As product fingerprint candidates, the main dimensional features of the part were identified and measured off-line. Particular attention was paid to the quantification of the two defects that affected the part quality, i.e. flash and gate mark. The process fingerprint candidates were, on the other hand, defined based on in-line monitored pressure and velocity curves. No external sensor was used since the monitored profiles were extracted from the machine control unit. The best candidates were then selected by considering two characteristics: sensitivity to process variations and correlation to part quality.

The following conclusions can be drawn from this chapter:

- The variation of µIM process settings had a relevant impact on the geometry of the micro component. Particularly, the flash area and the length of the gate mark showed the largest sensitivity to the change of process parameters. Therefore, optimising the process is of primary importance for obtaining parts having the desired features.
- The variation of the four investigated process parameters had an opposite effect on the size of the two defects: an increase of the flash size always happened with a decrease of the gate mark size and vice versa. Their simultaneous minimization was thus not possible to obtain within the investigated process window, posing a great challenge with respect to quality optimization.
- The morphology and appearance of the gate mark were strongly influenced by the moulding settings. In fact, a zone of deformation, which significantly increased the size of the defect, was clearly visible only when moulding with low levels of the parameters.
- The flash area was the measurand with the highest level of correlation to part quality, as demonstrated by calculating coefficients of correlation. By measuring the effects of µIM parameters on this indicator, robust conclusions can be made also on three other measurands: ODb, L_{mark} and IDb. Therefore, A_{flash} was the best product fingerprint candidate for the micro component.
- The process fingerprint candidates extracted from in-line monitored injection and velocity curves were mostly influenced by p_{hold} and v_{inj}. The only one that showed a significant dependence on T_{mould} was the mean integral of the pressure during filling $\mathrm{I}_p/\Delta t$. This variable increased when selecting the high levels of the µIM parameters. Being the most process sensitive among the candidates, it was selected as best process fingerprint.

- $I_p/\Delta t$ showed a significant correlation with three measurands. In particular, the size of both flash and gate mark could be effectively controlled by monitoring $I_p/\Delta t$ value for each moulding cycle. This discovery demonstrated that in-line process optimization in µIM can be carried out by means of a robust monitoring strategy to control the dimensional quality of all manufactured parts.

6 Development of product/process fingerprints for nano scale surface replication

The present chapter describes the application of the product/process fingerprint framework to a micro moulded component featuring a nano-structured surface texture. The goal was, as for the previous study, the development of a strategy for fast in-line quality assurance based on process monitoring.

The surface replication performance of the µIM process at the nano scale was investigated for two polymers, one amorphous and one semi-crystalline, having similar viscosities. Areal surface texture parameters were selected in order to fully characterize the nano features of the surface. As process monitoring technique, flow visualization was employed as it provided an in-cavity measurement of the polymer melt conditions. An in-line quality assurance strategy for the replicated nano-structured parts based on in-cavity temperature profiles was finally proposed.

The results presented in this chapter has been submitted to publication [130].

6.1 Introduction

Micro- and nano-structured surfaces have attracted great attention in many fields such as microfluidics [81] and optics [131]. The most efficient and cost-effective way to manufacture components featuring this type of surfaces is to replicate a master geometry using a polymeric material. µIM stands out as the preferred solution because of its extremely high replication accuracy and short cycle time.

The replication of nano-structured surfaces is challenging and fundamentally differs from the replication of geometries having micrometre to sub-millimetre dimensions as those addressed in chapter 5. This is particularly true when high aspect-ratio features are the target because of the hesitation effect (see subsection 3.1.2). Moreover, being the size of the replicated features particularly small, the size effects of µIM become even more important. Adopting a state-of-the-art µIM machine can substantially improve the capability of the moulding process, but the complete replication of nano features is still difficult to achieve.

In literature, mould temperature and injection speed are widely reported as the process parameters that govern surface replication: high levels of both are typically needed to maximize replication because of their beneficial effects in contrasting the growth of the frozen layer, keeping the viscosity at the polymer-mould interface at a low value and widening the process window by postponing the freezing of the gate [42, 80].

Since the effects of µIM process parameters on the replication fidelity are very significant, the process optimization phase becomes central for obtaining a product that complies with the design specifications. This optimization relies on the accurate measurement of the surface texture of the moulded parts. For this task, optical instruments represent the preferred solution for their contact-less nature, nanometric resolution and versatility. However, the high throughput rate of µIM does not allow the quality assessment of all the manufactured polymeric parts using an in-line approach, being the measuring time of typical optical instruments, which is in the order of 2 to 10 minutes, much longer than a single moulding cycle. The most promising solution for in-line characterization of injection moulded samples having structured surfaces is nowadays scatterometry [132], which however is best suited for well-defined micro and nano structures such as gratings and therefore cannot be successfully applied to more complex and less deterministic surfaces such as laser textured ones.

In this chapter, a solution for in-line quality assessment of nano-structured moulded parts manufactured by replicating a laser-machined surface is investigated. This method is based on the combination of product and process fingerprints (see section 1.2).

The applied method is slightly different from that employed in chapter 5. In fact, the identification of the product fingerprint was, in this study, related to the definition of the areal texture parameters that allowed the best characterization of the surface replication. Therefore, the product fingerprint was represented by a set of roughness parameters, since no other geometrical feature of the part was linked to the functionality and therefore no other dimensional target was taken into account. As for the process fingerprint, the same procedure applied in chapter 5 was carried out (see Figure 6.1). The monitoring technique applied in this investigation was flow visualization with an infrared camera. Its applicability to in-line monitoring of nano-scaled surface replication had never been investigated before in µIM literature, even though its use is very promising since the temperature distribution within the cavity has a huge impact on how the mould surface is replicated.

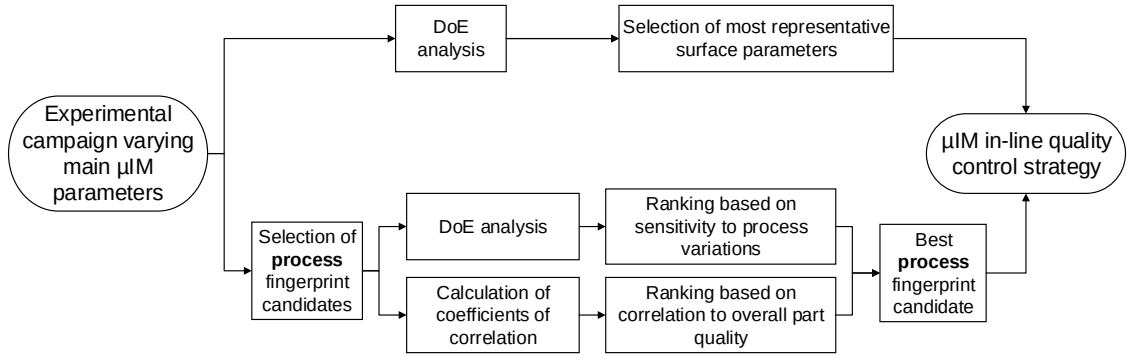

Figure 6.1: Flowchart representing the experimental work for the nano-structured part. The upper branch ends with the determination of the most representative surface texture parameters. The lower one is dedicated to the identification of the process fingerprint yielding the best performance in terms of in-line quality assurance control.

6.2 Case study and mould design

The moulded part was a disc with diameter 17.0 mm and thickness 0.6 mm (total volume of circa 135 mm^3) featuring a circular nano-structured area of diameter 10.0 mm that serves for antibacterial purposes. This area was manufactured by replicating a laser-structured insert made of tool steel integrated into a Hasco-K standard modular system with a single cavity (see Figure 6.2).

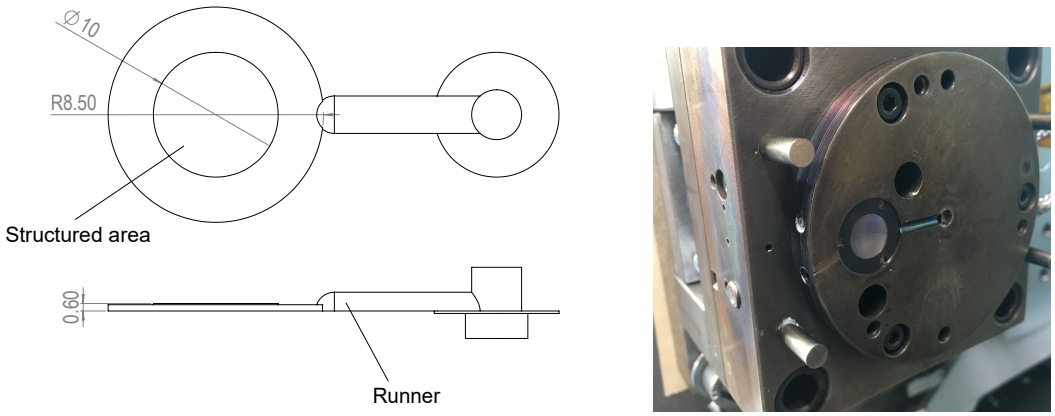

(a) **(b)**

Figure 6.2: (a) Geometry and nominal dimensions in mm of the moulded part. (b) Movable side of the mould with nano-structured insert.

A Yb-doped sub-pico 5 W laser source by Amplitude Systemes (Pessac, France) operating on a wavelength of 1030 nm was used. An average laser power of 0.55 W,

a scanning speed of 2 m/s and a frequency of 500 kHz were the parameters selected to generate the surface. The resulting texture presented a single-lay periodic pattern. The average height of the ripples generated on the insert was 50 nm while the pitch 900 nm (see Figure 6.3).

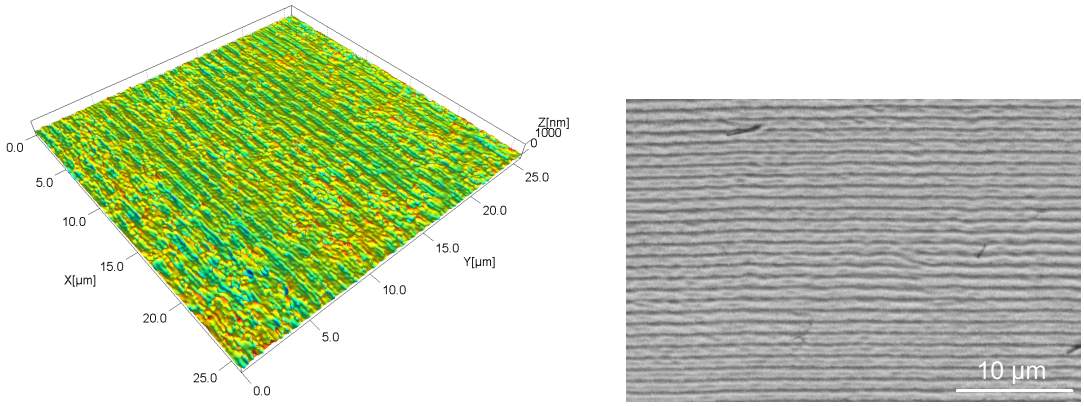

(a) **(b)**

Figure 6.3: Appearance of the laser-textured surface of the insert: (a) 3D acquisition with the confocal microscope and (b) SEM image.

The mould was modified to integrate a 45° tilted mirror and a sapphire window in the movable plate to allow the visualization of the cavity during moulding (see Figure 6.4 (a)). A high-speed infrared camera (FLIR X6540 SC, FLIR Systems, Wilsonville, OR, USA) was aligned to the mirror to image the cavity by means of the sapphire window (see Figure 6.4 (b)). The camera, which had been previously calibrated over a range of temperatures varying from 5 to 300 °C, has a cooled indium antimonide (InSb) focal plane array detector with a spectral range of 1.5 to 5.0 µm. It was operated with a frame-rate of 100 Hz and a field of view of 9 mm × 7 mm, which was set to the maximum possible value and allowed to cover most of the nano-structured cavity. The distance between the camera objective and the mould lateral opening was set in order to image the nano-structured cavity, thus monitoring the temperature at the mould-polymer interface, which plays a central role in the replication. Each acquisition was triggered manually at the start of the injection cycle. The temperature information for each pixel, at each recorded time step, was then extracted using a dedicated software coupled with the infrared camera.

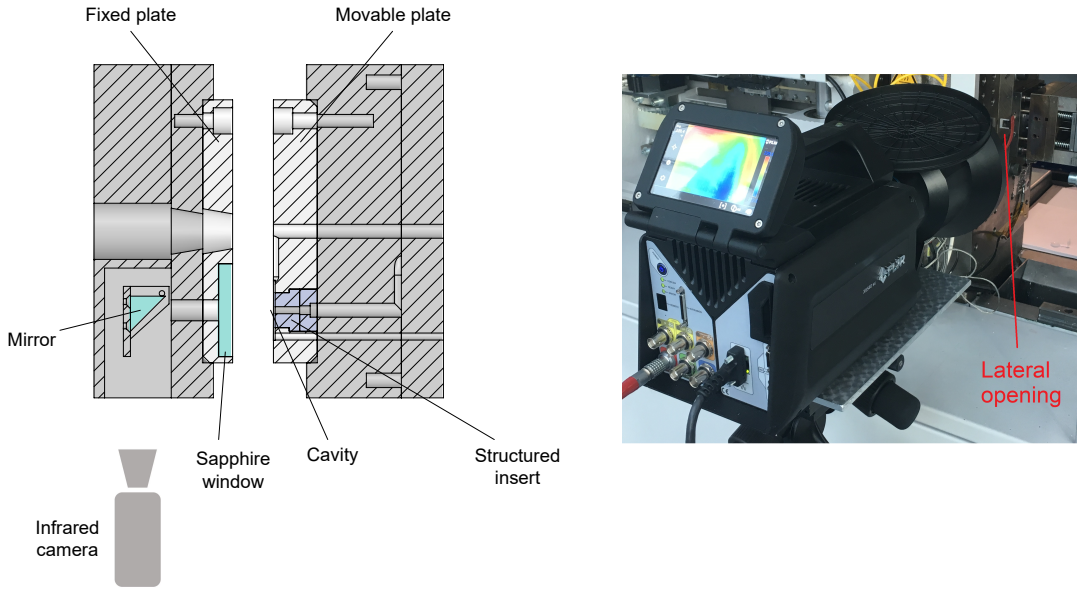

(a) **(b)**

Figure 6.4: (a) Scheme of the mould system with the flow visualization apparatus. (b) Infrared camera imaging the structured surface.

6.3 Experimental

6.3.1 Experimental design

A state-of-the-art µIM machine (Wittmann Battenfeld MicroPower 15) was used for the moulding experiments (see Figure 2.5 (a) for details). Two different polymers were moulded: unfilled Polyoxymethylene (Hostaform® C27021, manufactured by Celanese, Irving, TX, USA) and Polycarbonate (Makrolon® AL2447, manufactured by Covestro, Leverkusen, Germany). Table 6.1 reports the main characteristics of the two polymer grades and Figure 6.5 shows their viscosity and pvT data.

Table 6.1: Main properties of the two moulded materials. MVR data were gathered at a temperature of 190 °C and a load of 2.16 kg for POM and at a temperature of 300 °C and a load of 1.2 kg for PC.

Polymer	Density/(g/cm^3)	MVR/(cm^3/10min)
POM	1.41	24.0
PC	1.20	19.0

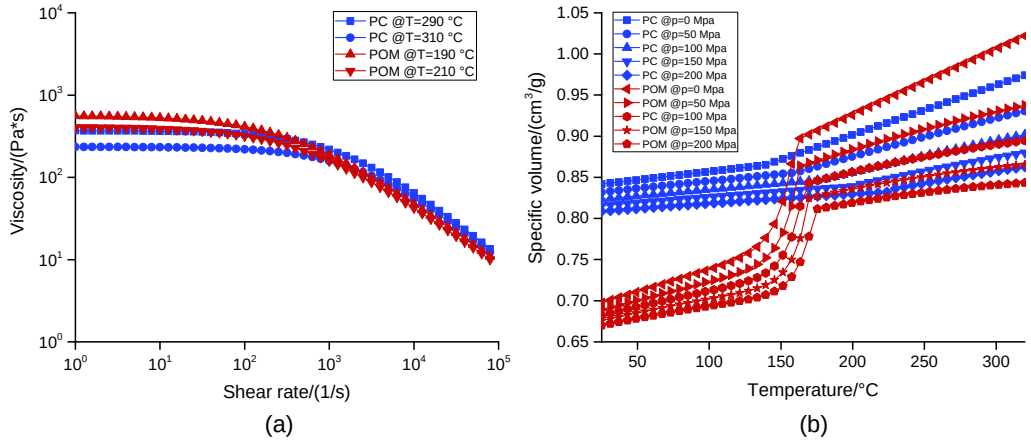

Figure 6.5: (a) Viscosity plot at the experimented melt temperatures for the two polymers. (b) pvT data at different pressures for the two polymers [129].

The two materials have high flowability as indicated by their very high MVR values and thus are suitable for filling small cavity details. The two polymers were selected since they exhibit very similar viscosity values at the experimented conditions (see Figure 6.5 (a)) even though their molecular structure is different, being POM semi-crystalline and PC amorphous. Therefore, comparing the behaviours of the two materials with respect to the variation of the processing conditions allowed to evaluate the influence of the different molecular structure on the replication.

A DoE approach was adopted to study the effects of the variation of µIM process parameters on the replication performance and identify the most suitable process fingerprint. Four process parameters were varied, namely holding pressure, injection speed, mould temperature and melt temperature. A two-level full factorial 2^4 experimental design was carried out. For each experimental run, the first ten moulded parts were discarded and the following five kept for evaluation. Therefore, 80 moulded parts were characterized for each material. Table 6.2 shows the levels of the process parameters, which were identified for both materials in a preliminary experimentation that aimed at obtaining consistent filling and minimized warpage of the moulded disc. To evaluate the difference between the two materials in terms of replication performance, they were processed in similar conditions: the same levels of mould temperature and injection speed were selected and the same range of variation was kept for holding pressure and melt temperature.

Table 6.2: DoE process settings for the two materials.

			POM		PC	
Process parameter	Symbol	Unit	Low	High	Low	High
Holding pressure	p_{hold}	bar	250	750	750	1250
Injection speed	v_{inj}	mm/s	50	150	50	150
Mould temperature	T_{mould}	°C	100	120	100	120
Melt temperature	T_{melt}	°C	190	210	290	310

6.3.2 Surface topography measurement and uncertainty evaluation

The insert and the replicated polymer surfaces were characterized using a laser scanning confocal microscope (Olympus Lext OLS4100) with a 100× magnification objective lens (see Table 2.4 for the characteristics). This measurement instrument was particularly suitable for the task since it is capable of acquiring transparent samples such as those moulded with PC. Moreover, a very high lateral resolution was necessary to characterize the finely-spaced ripples of the laser-structured surface.

Different areas were acquired on metal insert and moulded parts to evaluate the homogeneity of replication. In fact, it was of primary importance to ensure that the mould nano features were replicated at the same level over the entire structured area. In particular, five measurement areas were defined: one correspondent to the centre of the circular area, two along the flow direction and two on its perpendicular. The distance between the central area and the others was 2 mm. By measuring over these areas, the influence of the distance from the gate on the replication accuracy and the symmetry of replication could be evaluated. Figure 6.6 shows the scheme of the measurement areas, which were named according to the Cartesian coordinates of a plane centred on the centre of the disc. Each acquisition was repeated three times.

The raw surface acquisitions were post-processed using an image processing software (SPIP 6.7.3, Image Metrology A/S, Hørsholm, Denmark) before extracting quantitative information on the surface texture. Firstly, the 3D acquisitions were flattened by subtracting the first order plane fitted on the point cloud, thus eliminating any influence of a possible tilt. After that, a spatial filter was applied in order to filter the waviness out and consequently evaluate the capability of the µIM process when replicating only the laser-machined ripples, which provide the functionality to the part. Being the pitch of the ripples circa 900 nm, a linear areal Gaussian high-pass filter [133] at 1.0 µm was applied. By doing this, the overall waviness of the surface was effectively eliminated (see Figure 6.7). This procedure was necessary because the calculation of surface roughness parameters on the unfiltered surfaces would

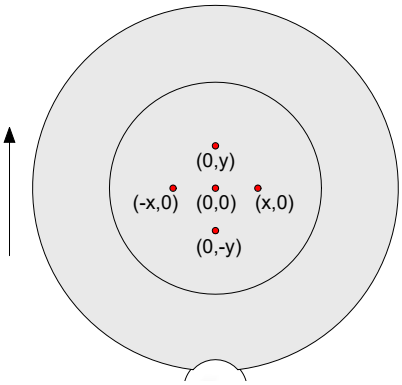

Figure 6.6: Measurement areas and their nomenclature. The black arrow represents the flow direction.

have been more sensitive to the low-frequency waviness rather than to the texture generated by the nano structures.

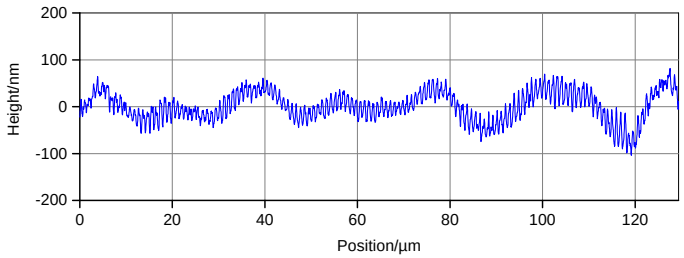

(a)

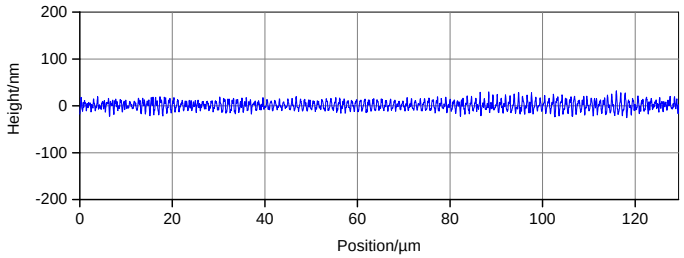

(b)

Figure 6.7: Average profile of the (0,0) insert surface in the direction perpendicular to the ripples: (a) as acquired and (b) after filtering with a Gaussian high-pass 1.0 µm filter.

After levelling and filtering, the surface topography was evaluated with areal texture parameters, which were then used to assess the replication by comparing master and moulded samples. In particular, the root mean square of the height Sq and the root mean square gradient Sdq of the surface were computed [134]. Sq is defined as:

$$Sq = \sqrt{\frac{1}{A}\iint_A z^2(x,y)\mathrm{d}x\mathrm{d}y} \tag{6.1}$$

where A represents the finite measured area upon which the height function $z(x,y)$ is defined. This parameter provides information on the average areal surface roughness of the surface, thus being a useful indicator for the replication of the height of the laser-machined ripples of the insert. It carries very similar information to the arithmetical mean height *Sa*, which is widely used to characterize antibacterial surfaces [135–137], but is more sensitive to local spikes or defects due to its quadratic nature and therefore usable to detect local defects.

Sdq is defined as:

$$Sdq = \sqrt{\frac{1}{A}\iint_A \left[\left(\frac{\partial z(x,y)}{\partial x}\right)^2 + \left(\frac{\partial z(x,y)}{\partial y}\right)^2\right]\mathrm{d}x\mathrm{d}y} \tag{6.2}$$

and is sensitive to the local slope of the surface. It can be used to determine whether local surface slopes have been replicated accurately. Therefore, by calculating *Sq* and *Sdq*, both the height and the slope of the ripples were characterized. Starting from *Sq* and *Sdq* values, two replication indicators were calculated for each of the 80 moulded samples. The indicators were defined as:

$$\Delta_S = \frac{S_{\mathrm{part}} - S_{\mathrm{mould}}}{S_{\mathrm{mould}}} \tag{6.3}$$

where S_{part} and S_{mould} are *Sq* or *Sdq* calculated for a moulded part and the mould respectively in correspondent measurement areas.

The uncertainty of the roughness measurements was also characterized. This was necessary since variations in replication accuracy due to processing conditions are typically in the order of nanometres when considering surface roughness. Therefore, the precision of the measurement results must be characterized in order to make the right conclusions on the significance of the effect of a particular process parameter. In this study, the uncertainty U was calculated once again following ISO 15530-3 [119]. A calibrated injection moulded roughness standard introduced by Tosello et al. [138] and having nominal *Ra* roughness of 100 nm was used. Three uncertainty contributions were taken into account for both *Sq* and *Sdq* measurements: u_{cal}, as the uncertainty of reference AFM measurements on the calibrated artefact [138]; u_{p}, introduced by the measurement procedure and calculated as standard deviation of 20 repeated measurements of the artefact; and u_{w}, associated with material and manufacturing variations of the actual measurand. The contribution due to the instrument resolution was not considered since the vertical resolution value declared by the microscope manufacturer cannot be verified. u_{w} was calculated as:

$$u_{\mathrm{w}} = \frac{\max(\boldsymbol{S}) - \min(\boldsymbol{S})}{2\sqrt{3}} \tag{6.4}$$

where $\boldsymbol{S}$ is the vector listing the three repeated *Sq* or *Sdq* measurements per part. The three contributions were then combined using the law of propagation of uncertainty to determine the expanded uncertainty U [95]:

$$U = k \times \sqrt{u_{\mathrm{cal}}^2 + u_{\mathrm{p}}^2 + u_{\mathrm{w}}^2} \tag{6.5}$$

where k is the coverage factor of 2 selected to achieve a 95 % approximated confidence interval. Table 6.3 and Table 6.4 report the uncertainty budgets for POM and PC respectively. The uncertainty results were very similar for the two materials, proving that there was no significant interaction between the selected microscope and the two different polymers.

Table 6.3: Average uncertainty contributions and expanded uncertainty U of the measurements of the POM moulded samples.

Uncertainty contribution	*Sq*/nm	*Sdq*
u_{cal}	2.10	0.009
u_{p}	0.30	0.009
u_{w}	0.55	0.009
$U(k = 2)$	4.4	0.032

Table 6.4: Average uncertainty contributions and expanded uncertainty U of the measurements of the PC moulded samples.

Uncertainty contribution	*Sq*/nm	*Sdq*
u_{cal}	2.10	0.009
u_{p}	0.30	0.009
u_{w}	0.26	0.009
$U(k = 2)$	4.3	0.032

6.3.3 Process monitoring

The temperature distribution inside the mould cavity was obtained by processing the videos recorded by the infrared camera using a dedicated software. In particular, for PC, the data were gathered only for the first half of the experimental plan due to feasibility reasons. Therefore, process fingerprint data were analysed according to

a 2^3 plan performed at low melt temperature (290 °C) for this material. Conversely, monitoring data derived from the whole 2^4 design were available for POM.

By looking at the recorded infrared images, the behaviour of the polymer melt inside the cavity could be clearly observed. The polymer melt entered the thin cavity and then proceeded to fill it progressively (see Figure 6.8 and Figure 6.9). Once the filling was complete, the polymer melt started to cool down and the part eventually detached from the sapphire window wall due to volumetric shrinkage. A great influence of the mould temperature could be observed: by comparing Figure 6.8 and Figure 6.9, it can be seen that when the high level of this parameter was used, the polymer melt not only had a generally higher temperature but also a larger hotter area, indicating that a better adhesion to the sapphire window was also promoted.

The curve of the maximum temperature among all the pixels over time was selected as the output of the process monitoring. In fact, the maximum temperature $T_{\max}$ carries valuable information on the polymer melt conditions as the filling progresses. Therefore, a time-profile of the maximum temperature was extracted for each experimental run.

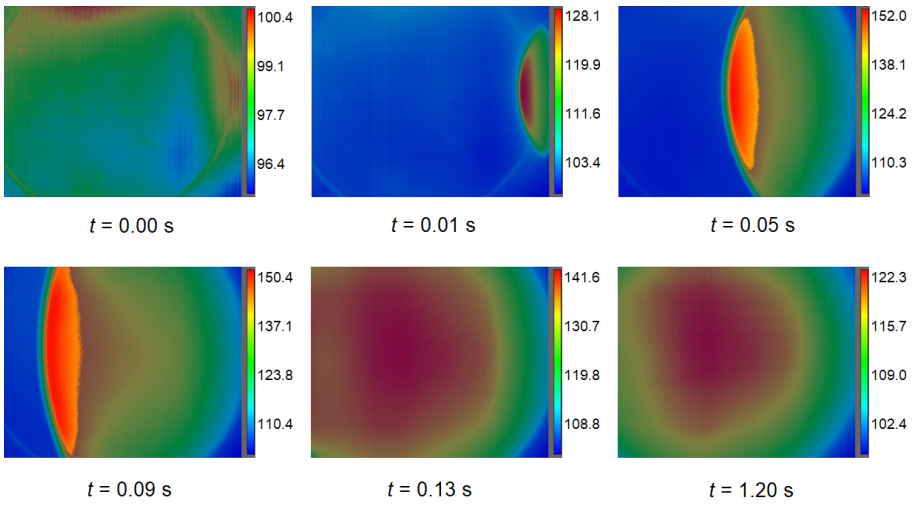

Figure 6.8: Infrared images captured at different filling stages during an experiment with POM using low T_{mould}. The circle visible on the background represents the perimeter of the structured area. The contour bars represent the temperature scale in °C. Flow direction is right to left in each image.

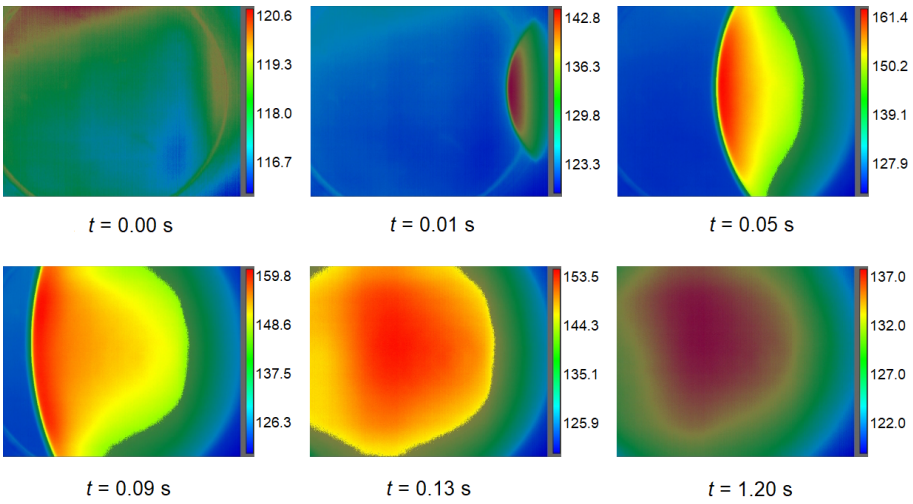

Figure 6.9: Infrared images captured at different filling stages during an experiment with POM using high T_{mould}. The circle visible on the background represents the perimeter of the structured area. The contour bars represent the temperature scale in °C. Flow direction is right to left in each image.

Figure 6.10 shows the shape of five $T_{\max}$ profiles correspondent to DoE repetitions. The very high repeatability of the process was reflected by five almost overlapped curves. After the initial phase in which the temperature equals T_{mould}, a sharp linear increase signalling the start of the filling was observed. Two temperature peaks are distinguishable: the first (T_{peak1}) is related to the burn effect caused by the rapid compression of the air due to the flow front advancement, while the second one (T_{peak2}) represents the maximum flow front temperature within the cycle [108]. It can be seen that T_{peak2} was lower than the melt temperature: this has been already reported in the literature when using an infrared camera [106] and was caused by the infrared absorption characteristics of POM and PC, which are both quite transparent to IR radiation. After the two peaks, the temperature declined rapidly as the polymer melt touched the colder mould surface during the packing and cooling phases of the moulding cycle.

Once the $T_{\max}$ profile was extracted for each moulded part, indicators that well characterized the shape and main features of the curves were calculated and then considered as process fingerprint candidates. Therefore, these variables were investigated with respect to their dependence on process settings variation and to the correlation with the replication quality expressed by Δ_{Sq} and Δ_{Sdq}. In particular, five candidates were identified::

- T_{peak1}: the first temperature peak (see Figure 6.10). This quantity relates to the temperature reached at the start of filling due to the burning effect.

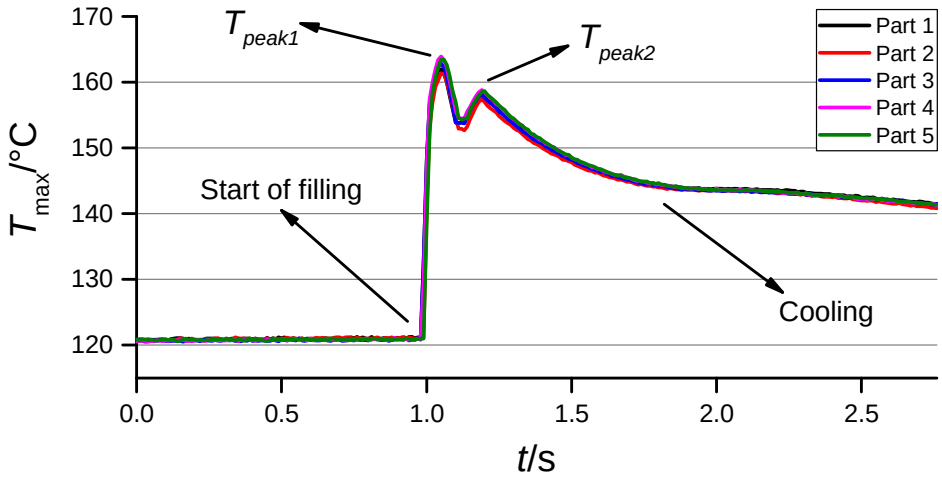

Figure 6.10: Maximum temperature profiles during five repeated moulding cycle with POM ($T_{\mathrm{mould}} = 120$ °C, $T_{\mathrm{melt}} = 190$ °C). The moulding phases, as well as the temperature peaks, are indicated.

- T_{peak2}: the second temperature peak (see Figure 6.10), which is related to the maximum flow front temperature reached inside the cavity in the moulding cycle. This variable provides information on the thermal conditions experienced by the polymer melt.
- T_{mean1}: the average temperature in the time interval between point A and C in Figure 6.11. It provides an average information on the abrupt temperature increase at the beginning of the moulding cycle.
- T_{mean2}: the average temperature in the time interval between point A and D in Figure 6.11, which spans from the start of the filling and second peak. It is related to the average thermal energy of the polymer during the filling of the cavity.
- $\mathrm{d}T/\mathrm{d}t$: the slope of T_{max} profile at the start of the filling. This indicator quantifies the heating rate in the cavity and was calculated as:

$$\frac{\mathrm{d}T}{\mathrm{d}t} = \frac{T_{\mathrm{B}} - T_{\mathrm{A}}}{t_{\mathrm{B}} - t_{\mathrm{A}}} \tag{6.6}$$

  where T_{A}, T_{B}, t_{A} and t_{B} are temperature and time values corresponding to the start and the end of the linear rise of temperature at the beginning of the filling (see Figure 6.11).

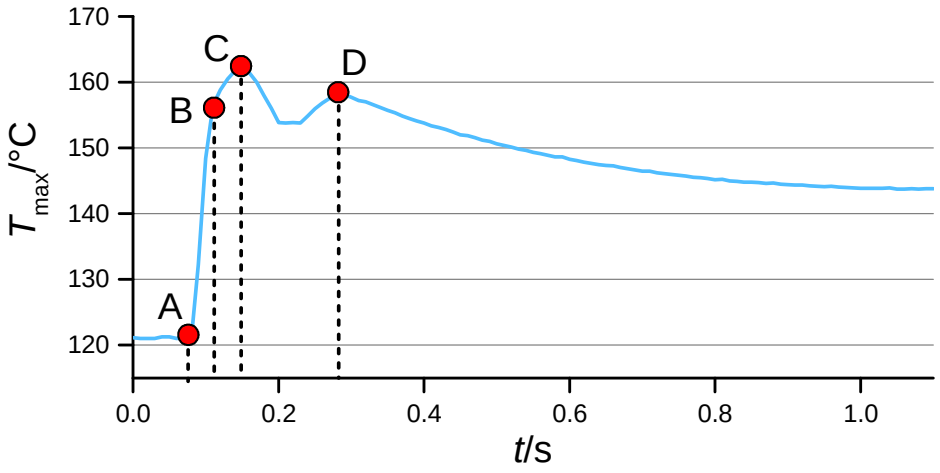

Figure 6.11: Maximum temperature curve with points indicating the intervals used for the calculation of the process fingerprint candidates. The points were identified by tracking first-order derivative values.

6.4 Results and discussion

6.4.1 Surface replication analysis

The homogeneity of replication among the entire structured area was evaluated by comparing Δ_{Sq} and Δ_{Sdq} values of the five measurement areas. Figure 6.12 reports the results for each of the 16 DoE runs. For both POM and PC, the replication quality in the five areas was congruent throughout the experimental campaign. In fact, no difference was notable between the results of the measurements among the five different positions due to overlapping uncertainty intervals. Moreover, the data dispersion for each DoE run was almost constant, proving that also the same level of precision was achieved throughout the various experiments. Because of this, the results of the five areas were considered as replicates of the DoE plan, thus making 25 replicates available considering also the five consecutively moulded part per process settings combination. What also stands out in Figure 6.12 is the correlation between Δ_{Sq} and Δ_{Sdq} for both materials.

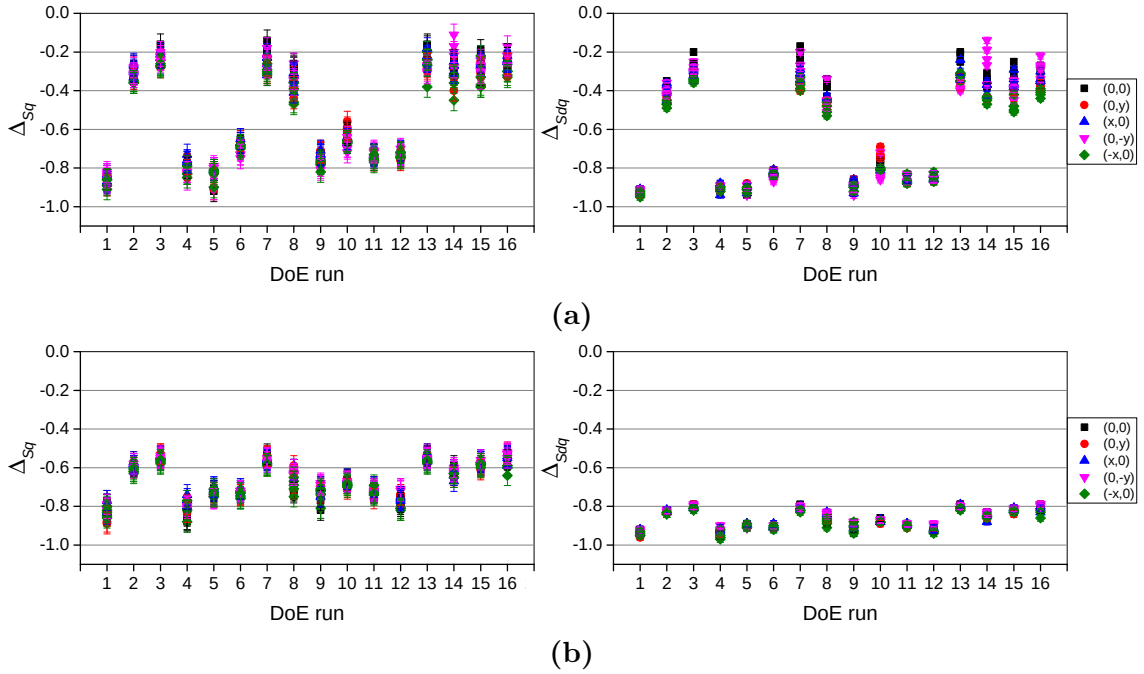

Figure 6.12: Replication results for *Sq* and *Sdq* on the five different measurement areas plotted against the 16 DoE runs for (a) POM and (b) PC. Interval bars represent the expanded measurement uncertainty.

Figure 6.13 shows the results of the DoE analysis for POM. Main effects plot and Pareto chart of effects are shown. In the first, the expanded measurement uncertainty U is shown to verify whether the measurement precision covered the effect of the process parameters. In the second, the interval bars are built as in chapter 5, thus they represent the standard deviation of the effects obtained by running five separate analyses correspondent to the the five DoE replicates.

The replication of both *Sq* and *Sdq* was dominated by the effect of the mould temperature: setting high T_{mould} resulted in an average increase of circa 0.5 for Δ_{Sq} and Δ_{Sdq}. The positive effect the mould temperature on replication has been already reported in the literature and is related to a decrease of viscosity and delayed solidification that in turn facilitates the filling of the surface nano structures. In particular, when using mould temperature of 100 °C, the nano ripples were only partially replicated (see Figure 6.15 and Figure 6.16) as the polymer melt did not fill completely the valleys of the topography of the master surface. This imperfect replication was mirrored in a decay of both *Sq* and *Sdq* since the moulded surface had lower nano structures (i.e. lower *Sq*) and with a generally lower slope (i.e. lower *Sdq*). Conversely, when setting the mould temperature at 120 °C, the replicated features resembled the ones of the insert much more because the local rise of temperature significantly reduced the viscosity of the melt within the nano-structured cavity. The second more relevant process parameter was T_{melt}, whose increase led to a better

replication of the master surface. However, considering the measurement uncertainty, this setting could not be considered as significant since the interval bars of the two levels overlap. The effects of p_{hold} and v_{inj} were negligible. The Pareto charts confirmed the predominance of T_{mould}, which had by far the largest effect on the replication indicators. The second biggest effect was the interaction between p_{hold} and T_{mould}: it was observed that moulding with the high level of T_{mould} increased the effect of p_{hold}, making the setting of 750 bar more significant for achieving a better replication. The interaction between p_{hold} and v_{inj} was also significant: only when using the high level of injection speed, was the increase of holding pressure beneficial for the replication. This happened because a more efficient packing phase was performed thanks to the faster injection and consequently postponed freezing of the gate.

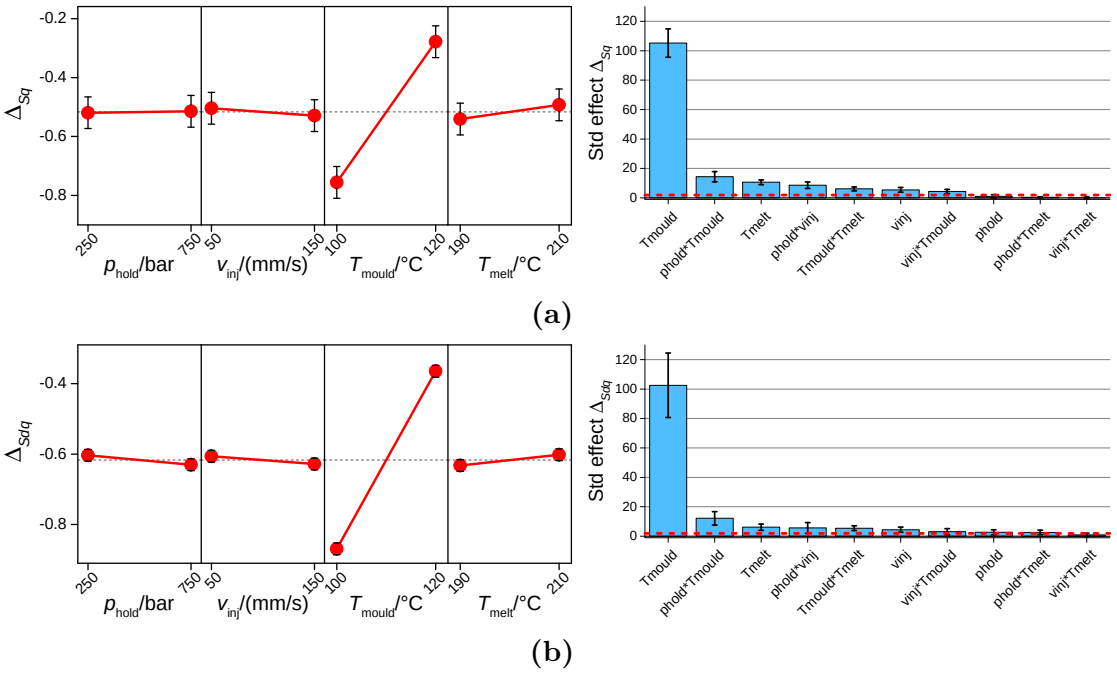

Figure 6.13: Main effects plot (left) and Pareto chart of effects (right) for replication indicators (a) Δ_{Sq} and (b) Δ_{Sdq} for POM.

Figure 6.14 shows the results for PC. Similarly to the other material, the mould temperature had the biggest impact on replication: setting T_{mould} at 120 °C increased Δ_{Sq} and Δ_{Sdq} of 0.2 and 0.1 respectively, resulting in better-replicated nano ripples (see Figure 6.15). The effects of the other process parameters were negligible for the analysis. The Pareto charts show that, as for POM, the interactions between p_{hold} and T_{mould} and between p_{hold} and v_{inj} were significant.

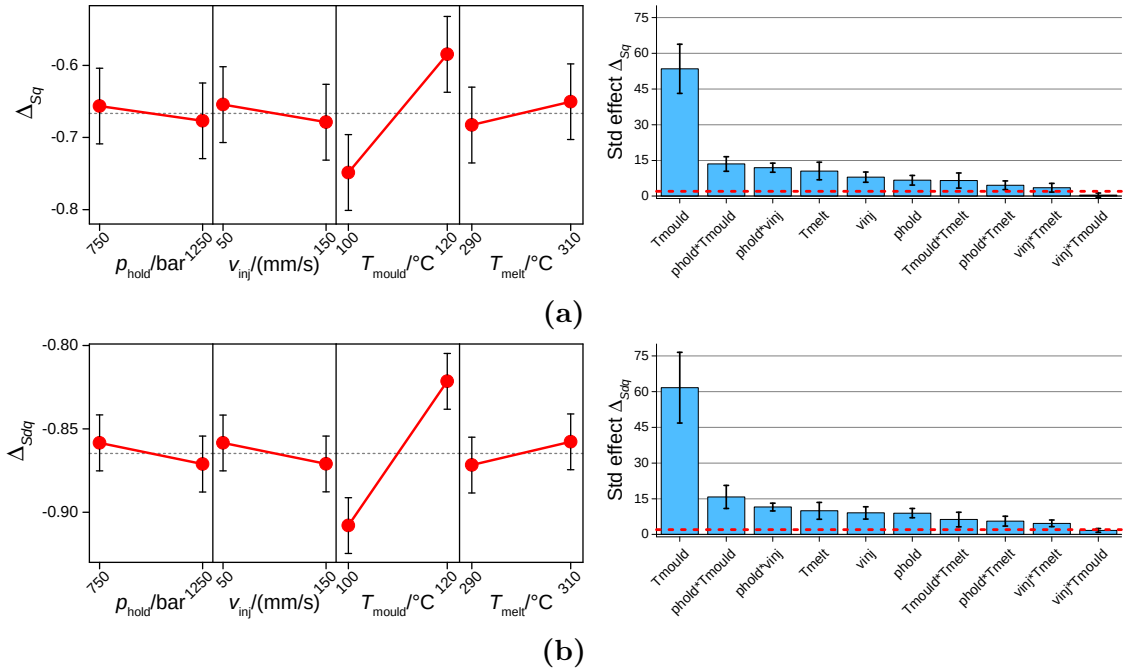

Figure 6.14: Main effects plot (left) and Pareto chart of effects (right) for replication indicators (a) Δ_{Sq} and (b) Δ_{Sdq} for PC.

By comparing the results for the two materials, it can be observed that the slopes of the main effects plots were the same for the four process variables considering both Δ_{Sq} and Δ_{Sdq}. This proved that, even though the molecular structure of the two polymers was different, µIM settings had the same impact on the replication of the nano ripples. However, the replication fidelity achieved with POM was higher than that obtained with PC. This was particularly true when using the high level of mould temperature (see Figure 6.15 and Figure 6.16): if, on one side, POM replicated the nano structures well when setting T_{mould} at 120 °C, on the other, PC only showed a slight improvement with respect to the low setting condition. Since the difference in viscosity between the two polymers was very small (see Figure 6.5 (a)), such an important difference can hardly be explained by this characteristic. Other properties of the polymer melt may have played a role in yielding this discrepancy. In particular, PC has a much higher molecular weight of repeat unit (254 g/mol) if compared to POM (30 g/mol). Since this property is known to have an influence on the molecular chain stiffness [139], it is possible that POM chains, being more flexible, were capable of replicating the nano ripples more accurately.

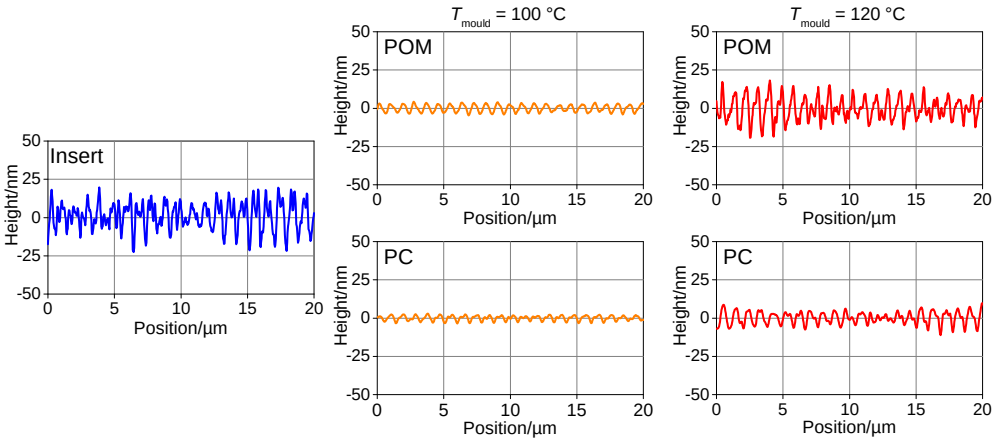

Figure 6.15: Surface replication when moulding at low (orange) and high (red) mould temperature for POM and PC in the same area. The correspondent insert surface is also shown in blue.

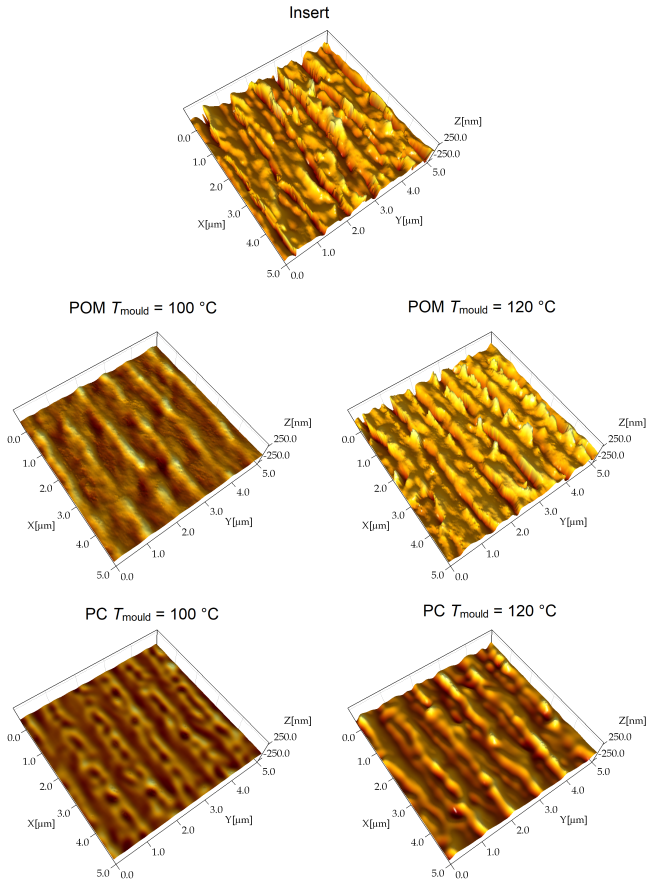

Figure 6.16: 3D detail of the insert and replicated surfaces.

For both materials, Δ_{Sq} and Δ_{Sdq} values were correlated, as shown by the similar main effects plots and Pareto charts. The connection between the two indicators was due to the link between *Sq* and *Sdq*: when considering surfaces having similar features, as those obtained replicating the same master geometry, an increase of average height comes with an increase of average slope and vice versa. This is clearly shown in Figure 6.15: surfaces replicated with high T_{mould} have both increased height and slope with respect to those moulded with low T_{mould}. However, the correlation between Δ_{Sq} and Δ_{Sdq} was different for POM and PC.

Figure 6.17 shows the relationship between Δ_{Sq} and Δ_{Sdq} for the two materials. Firstly, what stands out is that the replication of *Sq* and *Sdq* parameters was linked by a linear relationship, meaning that the two areal texture parameters can be controlled just by assessing only one of the two. This feature turns particularly useful in an in-line quality assurance framework since the calculation of one topography indicator yields a double relevant outcome. It can also be observed from the graph that the slope of the line fitting POM data is much higher than that of PC, meaning that an increase of Δ_{Sq} resulted in a smaller variation of Δ_{Sdq} for the latter. The reason for this must be searched in the peculiar morphology of the nano ripples, which have a complex shape on their upper part, with two peaks appearing in the majority of the cases (see Figure 6.18 (a)). This morphology was generated by the laser structuring process and was partially replicated only on the parts moulded with POM at high mould temperature (see Figure 6.18 (b)). In fact, PC was not fully able to develop the double-peaked structure of the master, even when setting high T_{mould} (see Figure 6.18 (c)). Having the two peaks a high slope, their presence in the profile influenced more the value of *Sdq* than that of *Sq*. Therefore, while Δ_{Sq} was related to the capability of replicating the master surface with respect to the height, Δ_{Sdq} was linked to how well the peculiar morphology of the master nano ripples was reproduced on the replica. The increase of T_{mould} from 100 °C to 120 °C allowed POM to increase the replication of both height (mirrored by an increase of Δ_{Sq}) and morphology (mirrored by an increase of Δ_{Sdq}) of the master surface. Conversely, for PC, only the replication of the height was improved significantly when setting high T_{mould}, since Δ_{Sdq} did not show a relevant increase, proving the double-peaked shape of the nano ripples was still not replicated.

This analysis demonstrated that the combined use of *Sq* and *Sdq* was necessary to quantitatively characterize the difference between the different types of replication obtained with the two materials.

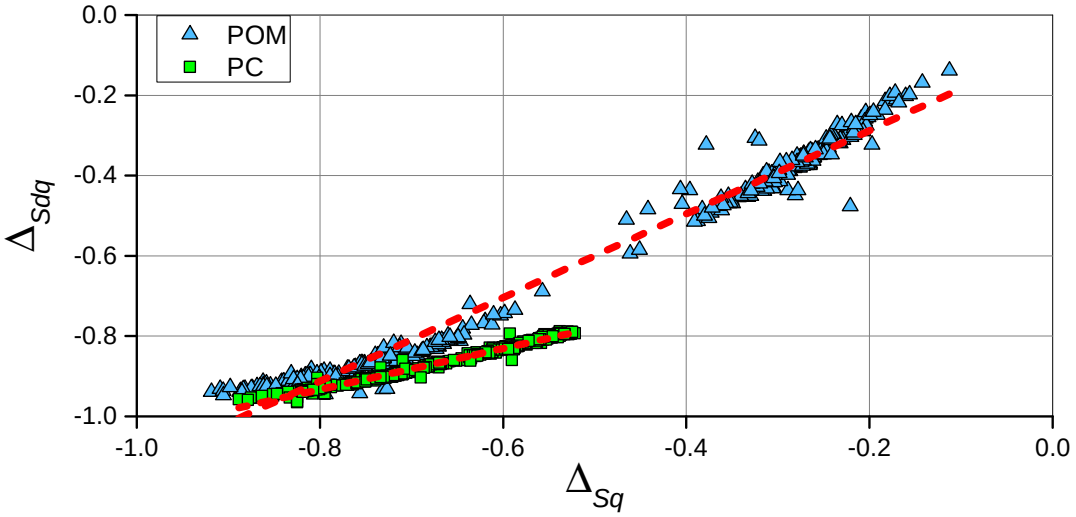

Figure 6.17: Relationship between Δ_{Sq} and Δ_{Sdq} for the two moulded materials. Red dashed lines represent fitted linear trends.

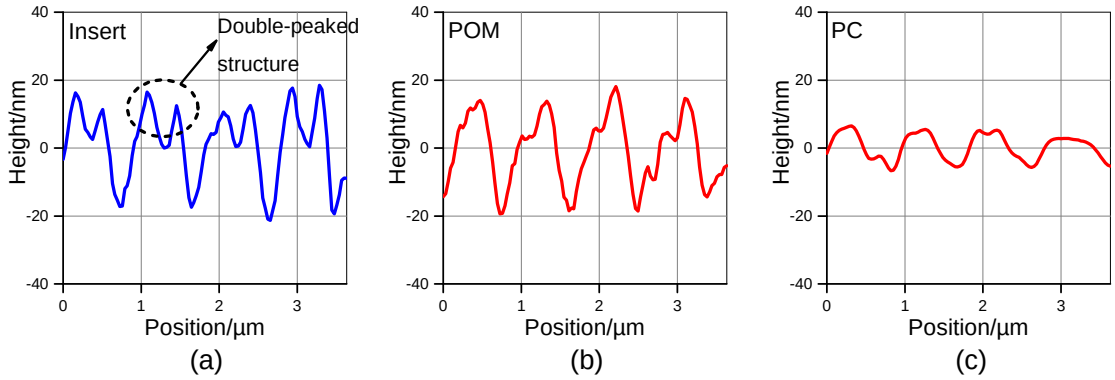

Figure 6.18: Detail of replicated structures at high T_{mould}. Nano ripples: (a) of the insert, (b) of the replicated POM and (c) of the replicated PC.

6.4.2 Analysis of flow visualization data

Effect of holding pressure, injection speed and mould temperature

The effects of p_{hold}, v_{inj} and T_{mould} on the five variables extracted from the monitored temperature curves were investigated. The effect of T_{melt} was analysed separately since the monitoring data gathered at high T_{melt} were only available for POM.

Figure 6.19 shows the results for POM. T_{peak1} was positively influenced by v_{inj} and T_{mould}, while p_{hold} effect was negligible (see Figure 6.19 (a)). This behaviour was strongly linked to the burning phenomenon that generated the first temperature peak. In particular, a polymer melt having higher speed generates a higher compression

of the air in the cavity, thus enhancing T_{peak1}. A similar effect, but greater in magnitude, was caused by an increase of mould temperature, meaning that a hotter cavity also favoured the burning effect.

T_{peak2}, which is related to the maximum flow front temperature, also increased when setting the high levels of v_{inj} and T_{mould} (see Figure 6.19 (b)). In this case, also the impact of the holding pressure was significant, as well as two interactions. A higher injection speed generated higher shear rates in the polymer melt and therefore a higher temperature due to shear heating. The effect of the mould temperature can be explained by considering that a larger amount of heat provided by the mould walls contributed to increasing melt flow temperature. Finally, the effect of p_{hold} was unexpected since the value of this variable is usually not supposed to play a role during the filling phase. This strongly suggests that the cavity was filled during the holding phase of the process, as often happens when very small volumes are injected and thus the final stage of the moulding cycle actually provides the melt to complete the filling [96]. For this reason, a higher p_{hold} favoured the entrance of more material inside the cavity and thus increased the value of T_{peak2}.

The two average temperatures T_{mean1} and T_{mean2}, which were calculated in different time intervals of the moulding cycle, showed similar dependences on the process parameters (see Figure 6.19 (c) and (d)). In particular, T_{mould} had the most important impact, yielding an increase of both indicators when its high level was selected. This happened because selecting the high mould temperature both increased the initial plateau, which was correlated to T_{mean1}, and the second peak of temperature, which had a positive influence on the magnitude of T_{mean2}. The injection speed was significant only for T_{mean2}, because of what mentioned for T_{peak2}, while the holding pressure was negligible for both average temperatures.

Finally, the last candidate $\mathrm{d}T/\mathrm{d}t$ showed a predominant dependence on v_{inj}: setting a higher injection speed determined a more drastic increase of temperature in the cavity due to a faster flow rate. The dependence on T_{mould} was less relevant and caused by the fact that starting the cycle with a higher mould temperature directly lowered the value of $\mathrm{d}T/\mathrm{d}t$ as defined in Equation 6.6. p_{hold} effect was, on the other hand, negligible.

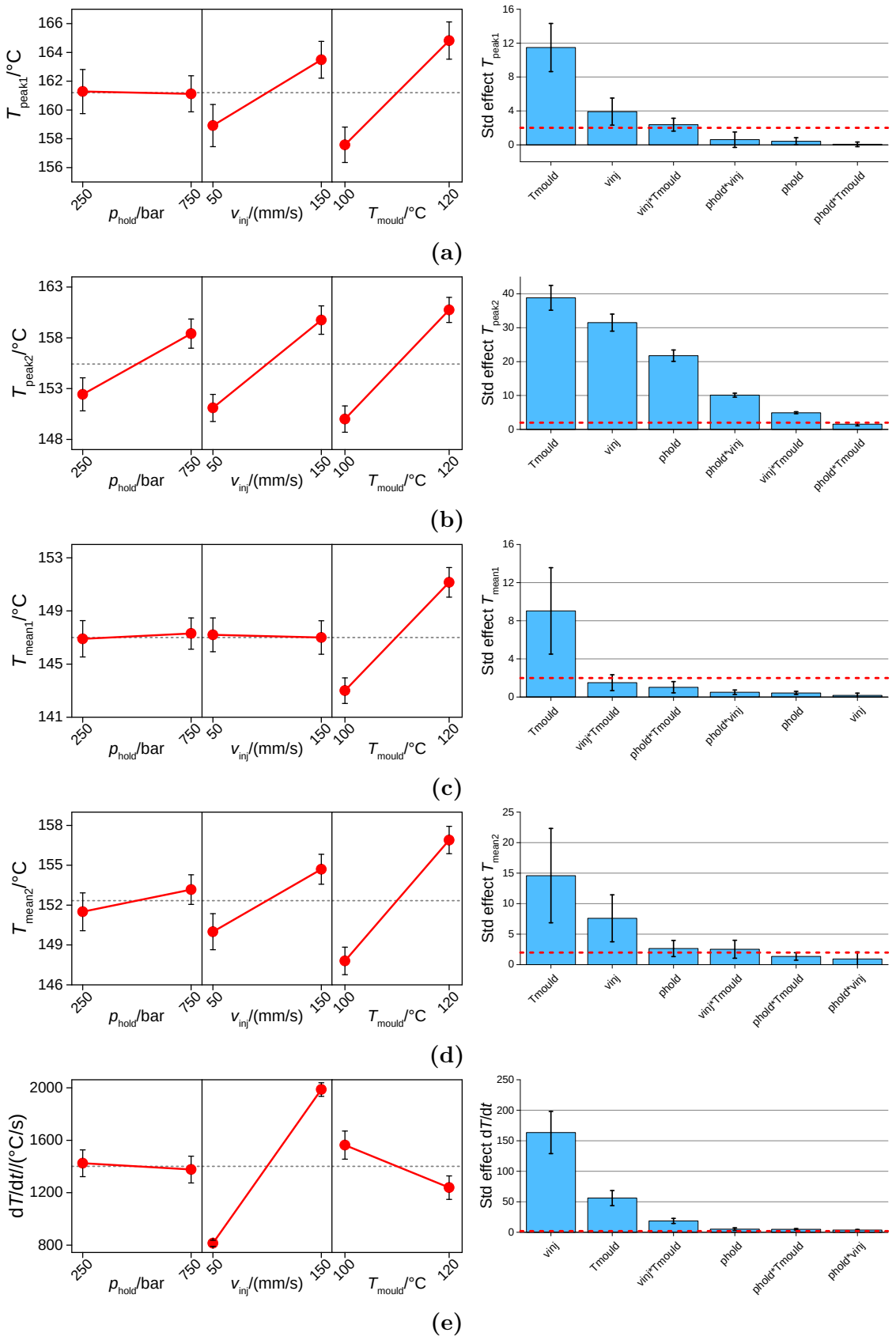

Figure 6.19: Influence of µIM on (a) T_{peak1}, (b) T_{peak2}, (c) T_{mean1}, (d) T_{mean2} and (e) $\mathrm{d}T/\mathrm{d}t$ for POM.

Figure 6.20 shows the effects of the process parameters on PC. Firstly, it can be observed that the signs of the slopes are very similar to those observed for POM, thus confirming the physical explanations behind the effects and highlighting the fact that there existed similarities between the two polymers. However, there was a major difference in terms of the significance of the µIM process parameters on the fingerprint candidates. In fact, the injection speed had a much larger impact on T_{peak1}, T_{peak2} and T_{mean2} for PC if compared to POM, where the mould temperature played the most important role. This might have been caused by the different molecular structure of the two polymers: the predominance of v_{inj} for PC suggests that the thermal history of this material was governed by the shear rate, which is mainly influenced by the injection speed setting. On the other hand, for POM, the temperature to which the melt was exposed in the cavity was the most important characteristics, being the mould temperature the parameter having the largest impact on most of the indicators extracted from the monitored curves. The only indicator that was mostly dependent on T_{mould} for POM and PC was T_{mean1} because of the fact that the initial plateau was equal to the mould temperature for both polymers.

$\mathrm{d}T/\mathrm{d}t$ behaved in a very similar way for the two materials. The injection speed was, in fact, the most significant µIM variable, confirming that the initial rise of temperature was mainly influenced by the flow rate.

It can be concluded that T_{peak1}, T_{peak2}, T_{mean1} and T_{mean2} were all generally sensible to the variation of µIM process settings for both materials. In particular, they all showed a degree of dependence on T_{mould}, which was the parameter having the most relevant impact on the replication of the laser-machined nano ripples (see Figure 6.13 and Figure 6.14), even though this dependence was greater for POM. On the other hand, the heating rate parameter $\mathrm{d}T/\mathrm{d}t$ was mainly influenced by the injection speed, whose effect was negligible when considering the replication quality. Thus, this indicator was not a suitable process fingerprint candidate, lacking the characteristic of sensitivity to the variation of quality-related µIM process parameters, which is essential to carry out an optimization based on in-line monitored variables.

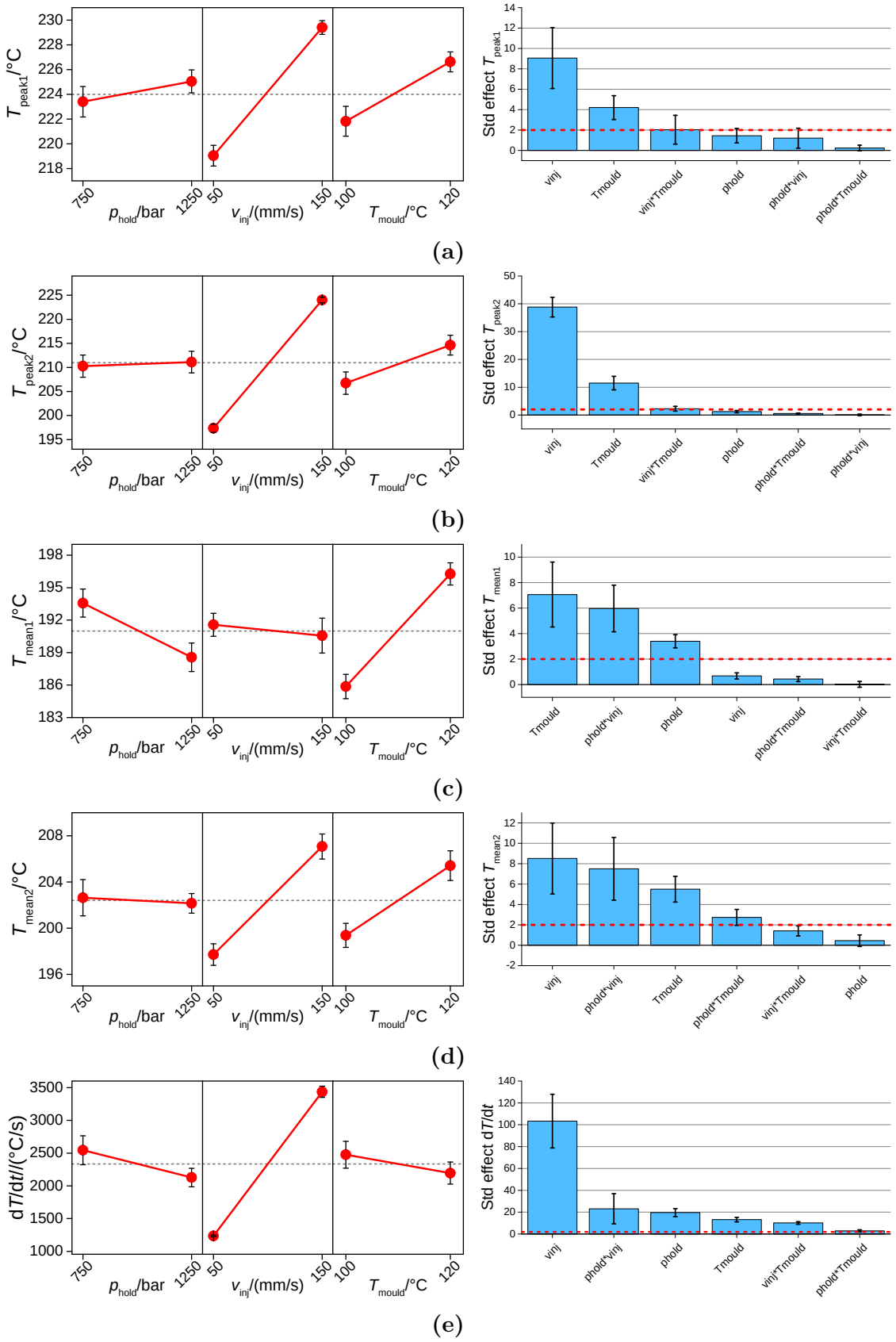

Figure 6.20: Influence of µIM on (a) T_{peak1}, (b) T_{peak2}, (c) T_{mean1}, (d) T_{mean2} and (e) $\mathrm{d}T/\mathrm{d}t$ for PC.

Effect of melt temperature

Figure 6.21 graphically shows the effect of the melt temperature variation on the temperature profile of POM and, as a consequence, on the value of the process fingerprint candidates. It can be observed that increasing T_{melt} shifted the profile upwards, resulting in an overall higher temperature due to the fact that a polymer melt having higher thermal energy entered the cavity. As regards the process fingerprint candidates, both T_{peak1} and T_{peak2} increased when setting the high T_{melt} value. In particular, the first temperature peak increased more than the second one, meaning that the burning effect was highly influenced by the initial polymer melt temperature. In addition, T_{mean1} and T_{mean2} were also positively dependent on the melt temperature value because of the general rise of the T_{max} profile. Finally, the T_{melt} setting did not influence $\mathrm{d}T/\mathrm{d}t$: the slope at the start of the filling did not change when selecting the high melt temperature level. Therefore, it can be concluded that all the process fingerprint candidates based on temperatures had a positive dependence on T_{melt}, whereas $\mathrm{d}T/\mathrm{d}t$ only depended on the injection speed.

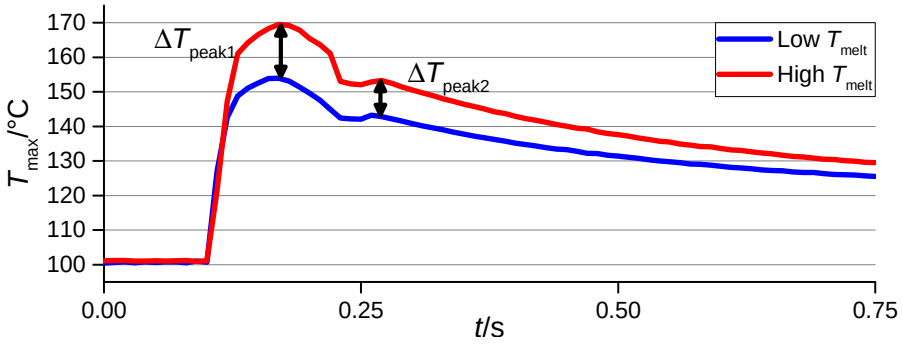

Figure 6.21: Maximum temperature profiles when setting low (blue) and high (red) melt temperature with POM. The other process parameters were kept as fixed.

6.4.3 Process fingerprint identification

In order to identify the best process fingerprint, a correlation analysis was performed between replication quality and the five candidates extracted from cavity temperature profiles. In particular, the coefficient of correlation ρ was selected as the indicator of the level of correlation and calculated according to Equation 5.6. For this analysis, only the product (i.e. Δ_{Sq} and Δ_{Sdq}) and process data (i.e. the process fingerprint candidates) gathered at the low level of melt temperature were considered in order to compare the correlation performance of the two materials.

Figure 6.22 shows the coefficients of correlation calculated between the two replication indicators Δ_{Sq} and Δ_{Sdq} and the five process fingerprint candidates for both the

moulded materials. In general, it can be seen that Δ_{Sq} and Δ_{Sdq} were very similarly correlated with the candidates, confirming the link between the two replication indicators (see Figure 6.17). This is important since it proved that the replication in height and morphology of the nano ripples can be controlled using the same monitored variable.

As regards POM, values of ρ close to 0.8 were observed for T_{peak1}, T_{mean1} and T_{mean2}, meaning that an increase of these variables happened with an improvement of the replication. The large correlation can also be noticed by comparing the effects of µIM process parameters (see Figure 6.13 and Figure 6.19): for both replication indicators and these three fingerprint candidates, the mould temperature was the most relevant process setting. T_{peak2} showed a slightly lower correlation (ρ equal to circa 0.6), while $\mathrm{d}T/\mathrm{d}t$ was not significantly correlated to Δ_{Sq} and Δ_{Sdq}. This was confirmed by the very different main effects plots, since they were influenced in a dissimilar way by the variation of µIM process parameters, being injection speed the preponderant parameter for $\mathrm{d}T/\mathrm{d}t$.

The correlation pattern was different for PC. In general, an inferior level of correlation was observed, since, for all process fingerprint candidates, lower ρ values were calculated. In particular, only T_{mean1} showed a significant level of correlation (ρ equal to 0.75) with Δ_{Sq} and Δ_{Sdq}. The different behaviour of PC was caused by the fact that, for this material, T_{mean1} was the only candidate for which the mould temperature played the most relevant role. In fact, the injection speed was the most impactful process parameter for T_{peak1}, T_{peak2} and T_{mean2} (see Figure 6.20). As for POM, $\mathrm{d}T/\mathrm{d}t$ did not show a meaningful correlation.

In conclusion, the correlation analysis on the two materials proved that T_{mean1} was the best process fingerprint candidate, being both process sensitive and the most correlated to the replication of the nano-structured surface. These finding demonstrated how the initial rise of temperature during the filling of the cavity due to the burning effect played a primary role in determining the outcome of the moulding process in terms of replication accuracy.

6.4.4 In-line quality assurance strategy

Figure 6.23 shows the replication indicators plotted against the selected process fingerprint T_{mean1} for the two materials.

For POM, two distinct subgroups of data are visible, corresponding to the parts moulded at low and high mould temperature. T_{mean1} is capable of describing this behaviour for both Δ_{Sq} and Δ_{Sdq}, which, as shown before, are highly correlated and appear as just shifted along the y-axis. In particular, the relationship between the variables is positive, since a higher value of the fingerprint came with an increase in the replication performance. This agrees with the slopes of the main effects plots (see Figure 6.13 and Figure 6.19) and the correlation coefficients that were, in fact,

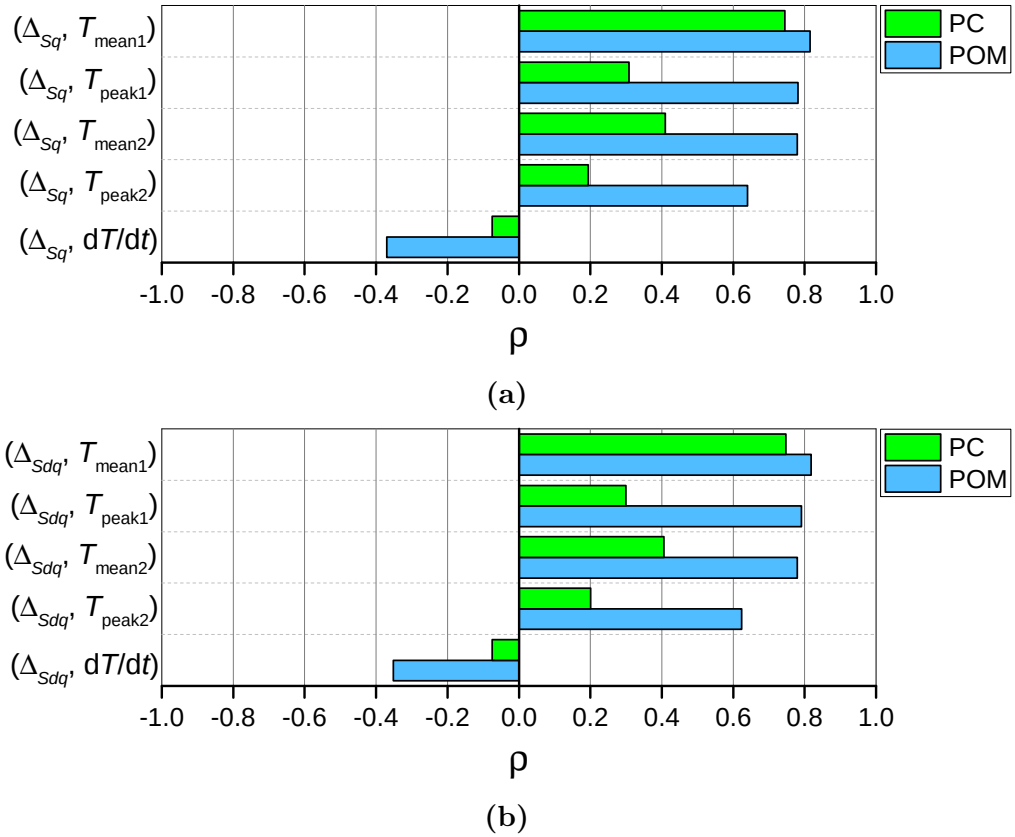

Figure 6.22: Values of coefficients of correlation calculated between the process fingerprint candidates and the replication indicators (a) Δ_{Sq} and (b) Δ_{Sdq}.

positive (see Figure 6.20). Although there exists some dispersion around the depicted linear trend, it is clear that a T_{mean1} higher of 148 °C was of primary importance to maximize the replication of the nano-structured ripples, leading to a circa 60 % increase of Δ_{Sq} and Δ_{Sdq}.

For PC, the performance of T_{mean1} in predicting the quality of the moulded surfaces was similar, since a clear positive trend existed among the data. In this case, however, there was not a distinct differentiation of Δ_{Sq} and Δ_{Sdq} in two subgroups. This was due to the fact that the improvement in replication generated by increasing T_{mould} was less significant, as discussed before (see Figure 6.15 and Figure 6.16). Therefore, direct recommendation on the value of the process fingerprint cannot be made as for POM. The plot also shows that the discrepancy between Δ_{Sq} and Δ_{Sdq} was higher for PC, particularly at their maxima, confirming that POM acted better in replicating both height and morphology of the nano structures.

It can be concluded that, for both materials, controlling the value of T_{mean1} in-line allows an accurate control of the nano-structured surface replication. Moreover, since T_{mean1} was calculated based on the first part of the maximum temperature profile,

only the initial phase of the moulding cycle has to be recorded and processed, thus lowering the computational burden. This could turn very beneficial in an industrial in-line quality assurance process.

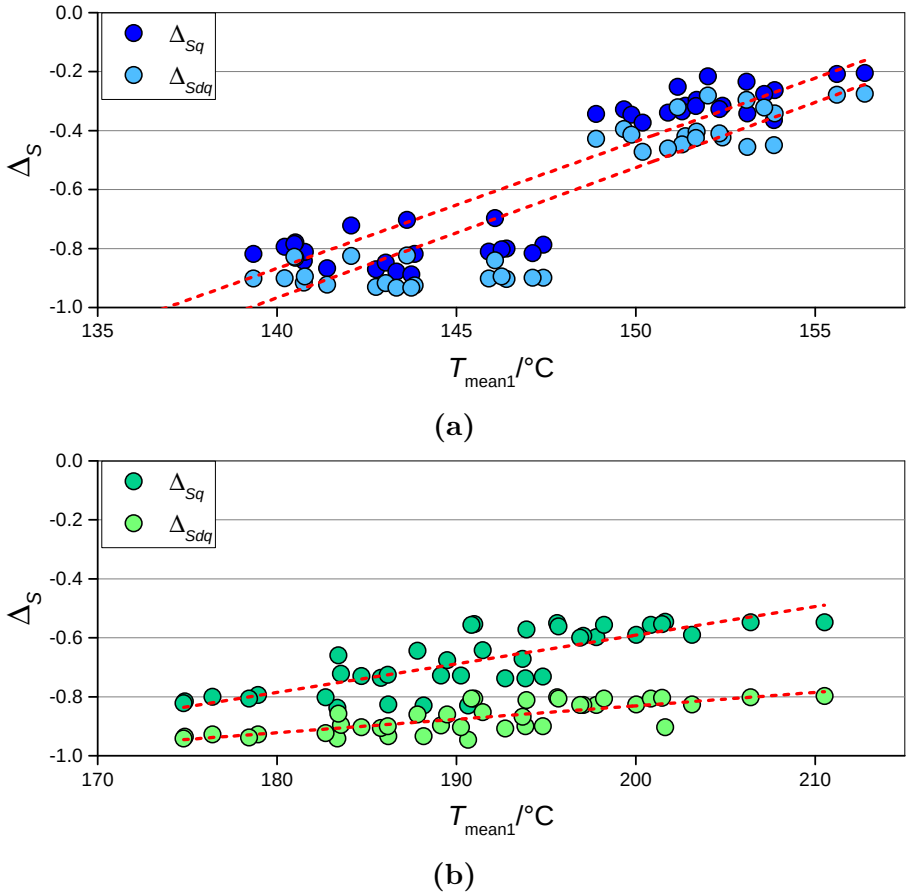

Figure 6.23: Replication indicators versus T_{mean1} for (a) POM and (b) PC. Red dashed lines represent the linear trends.

6.5 Summary and conclusions

The product/process fingerprint framework was applied to a moulded component featuring a nano-structured surface, with the aim of defining an in-line procedure for quality assurance based on flow visualization data for two different materials having similar viscosity (a POM and a PC grade).

The replication performance of the process was thoroughly characterized using two areal surface texture parameters, *Sq* and *Sdq*, which allowed to quantify the level of replication in terms of both height and morphology of the laser-machine ripples. The process fingerprint candidates were defined based on in-cavity temperature recordings

performed with a flow visualization apparatus featuring an infrared high-speed camera. The best candidates were then selected by considering two characteristics: sensitivity to process variations and correlation to replication quality.

The following conclusions can be drawn from the study:

- The use of the infrared camera allowed a useful visualization of the melt flow inside the cavity as well as the extraction of the thermal history of the polymer. This type of data is particularly significant with respect to surface replication, which is strongly dependent on the temperature at the mould-polymer interface.
- For both materials, the effects of the variations of the investigated µIM process parameters on the replication quality were similar, making the observed trend more general given the different molecular structure of POM and PC. Moreover, this demonstrated that a similar optimization procedure could be defined for both, making the selected strategy fairly general.
- The mould temperature was the most impactful process parameter for the replication of the nano ripples. In particular, setting its high level significantly improved the replicated features using both POM and PC because of the reduced viscosity at the mould-polymer interface and the delayed solidification of the melt.
- The combined use of replication indicators based on the areal roughness parameters *Sq* and *Sdq* allowed characterizing the main differences between the two materials. If, on one hand, POM was capable of well reproducing the nano ripples in terms of both height and morphology, on the other, PC was not accurate in replicating the morphology of the nano structures, since the double-peaked structure of the ripples was not present in PC moulded samples.
- The indicators extracted from the temperature profiles acquired with the infrared camera were mostly dependent on the mould temperature and the injection speed. In particular, T_{mould} was the most significant parameter for POM, while v_{inj} had a bigger impact on PC. This may have been caused by the fact that the thermal history of PC was more dependent on the shear rate, whereas that of POM was mostly influenced by the thermal condition of the polymer melt.
- The correlation analysis revealed that the mean temperature during the initial rise T_{mean1} was the candidate that was mostly correlated to the replication quality, demonstrating that the initial phase of the filling played a primary role with respect to the output of the µIM process.
- Using T_{mean1} as a process fingerprint seemed very promising since this variable showed a clear relationship with the replication quality for both the moulded materials, proving that the process can be effectively controlled by means of the value of a variable monitored during the moulding cycle. For POM, in

particular, a threshold value to obtain high-quality parts could be set at circa 148 °C, thus allowing the definition of a clear in-line control strategy based on T_{mean1} value.

7 Micro injection moulding simulations

In this chapter, the part of the thesis related to µIM process simulations is presented.

The main aim was to build and validate simulation models capable of predicting the quality of micro moulded parts. By using these validated models, further process optimization could be carried out in the virtual domain, thus saving the time needed to perform experiments and following characterizations. Two case studies are treated, the first related to the TPE micro rings and the second to the 3D micro part. The experimental work, which was needed to validate the numerical results, was presented in chapter 4 and chapter 5.

The research presented in this chapter was published in [140] and [141] and partially taken from these papers.

7.1 Introduction

Computer simulations represent a powerful tool in the current engineering scenario, which is taking a rapid turn towards digital. They provide a numerical computation of the solutions of complex equations and their related boundary conditions. There are several reasons that justify the importance of this tool. Firstly, they can be used to investigate systems that are not yet existent and thus can be helpful in the pre-selection of materials, geometrical configurations, constraints, etc. Simulations also allow the user to investigate the problem in detail. In fact, engineering phenomena are very often not directly observable due to their high speed, reduced scale dimensions or inaccessibility (that is also often the case of injection moulding). Finally, computer simulations can be employed to study how an output variable changes in response to a variation of the inputs. To implement a change in the real production is in fact often too costly, laborious or simply impossible.

The use of simulations comes of course with some limitations, too. First, it must be kept in mind that most mathematical models rely on idealizations and approximations that may be quite strong. Moreover, the numerical methods used to solve these models present a certain degree of approximation that is necessary to discretize complex continuous problems. It is also crucial to provide experimental evidence of

the simulations results. The validation phase is therefore of paramount importance to verify that the model that was built is capable of mirroring real phenomena.

For the aforementioned reasons, numerical simulations are often applied to the injection moulding process. The typical goals are [104, 126, 142–146]:

- shortening of development and time-to-market times,
- reduction of physical prototyping,
- assistance to part design, mould design and material selection,
- visualization of the filling steps and weld line formation,
- determination of a suitable process window,
- prediction of final part properties as well as defects.

In the field of conventional injection moulding, process simulations are well-established and widespread in the industrial world. The same cannot be said for µIM, due to the major differences between the macro and micro processes described in chapter 2.

7.2 Mathematical background

For both IM and µIM, the mathematical background behind process simulations is the same and can be divided into three parts: modelling of viscosity, flow and thermodynamics.

7.2.1 Viscosity

Viscosity is defined as the resistance to flow and plays a central role during the filling of the cavity in injection moulding technologies. Its value has a huge impact on the process settings, in particular on the values of pressure and speed needed to flow the polymer melt inside the cavity and attain a complete filling.

The viscosity is mathematically defined as the linear link between the shear stress and the shear rate. Given in tensor notation, the relationship is [147]:

$$\boldsymbol{\tau} = \eta \, \dot{\boldsymbol{\gamma}} \tag{7.1}$$

where $\boldsymbol{\tau}$ represents the shear stress, η the viscosity and $\dot{\boldsymbol{\gamma}}$ the shear rate.

For Newtonian fluids, such as water, the value of η can be considered as constant. Therefore, the shear stress is linearly linked to the shear rate for these materials. Polymer melts, however, are not Newtonian due primarily to their shear thinning

behaviour (see also subsection 3.1.2). As the shear rate increases, in fact, the viscosity of polymers decreases because of the disentanglement of the molecules, which facilitates the flow. Conversely, at low values of $\dot{\gamma}$, η is constant, generating the so-called Newtonian plateau (see Figure 7.1) It is thus necessary to define a function $\eta(\dot{\gamma})$ in order to model the behaviour of polymers in the injection moulding framework.

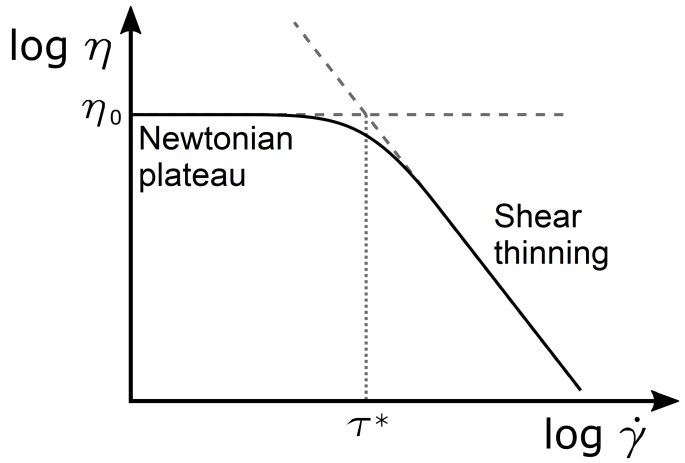

Figure 7.1: Typical shape of a viscosity curve of a polymer melt [148]. The zero shear rate viscosity η_0 and the shear rate at the transition to shear thinning τ^* are shown.

The most common viscosity model used in polymer processing simulations is the Cross model [147] since it is capable of describing the behaviour of polymer melts over a wide range of shear rates by combining a Newtonian region at low shear rates with a shear thinning region at high shear rates. According to this model [149], the viscosity is mathematically defined as:

$$\eta(\dot{\gamma}) = \frac{\eta_0}{1 + \left(\frac{\eta_0 \dot{\gamma}}{\tau^*}\right)^{1-n}} \tag{7.2}$$

where η_0 is the zero shear rate viscosity, τ^* is a constant related to the shear stress at the transition to shear thinning and n is the power law index, which describes the decreasing viscosity in the shear thinning region.

As previously mentioned in subsection 3.1.2, the temperature of the polymer melt also plays a central role in determining the viscosity value. Increasing temperature yields a decrease of viscosity, due to a lowering of the intra-molecular friction [66]. To take this effect into account, the Cross model can be modified using the Williams-Landel-Ferry (WLF) model based on the time-temperature superposition [150]. This modification yields to the Cross-WLF model and is carried out by mathematically defining η_0 as [147]:

$$\eta_0(T) = D_1 \exp\left[-\frac{C_1^0 (T - T_0)}{C_2^0 + T - T_0}\right] \tag{7.3}$$

where D_1, C_1^0 and C_2^0 are constants, T denotes the temperature and T_0 is the reference temperature, which can assume any value but is often chosen as the glass transition temperature T_g.

Finally, the viscosity also exhibits a dependence with respect to the pressure of the melt. In particular, a higher pressure leads to a higher viscosity, having this variable the opposite effect to temperature. This dependence is, in most cases, neglected in injection moulding simulations, being less relevant than the other effects [142].

7.2.2 Flow

Modelling the flow of the polymer melt is of primary importance to predict flow rate, pressure, filling time and all the other quantities related to the progressing of the melt inside the cavity. The Navier-Stokes equations, which are a system of non-linear partial differential equations, are commonly used to mathematically describe the flow in injection moulding [147]. In particular, they consist of:

- the continuity equation, which is derived from the conservation of mass,
- the momentum equation, which is derived from the conservation of momentum,
- the energy equation, which is derived from the conservation of energy.

The continuity equation is formulated as [147]:

$$\frac{D\rho}{Dt} = -\rho \boldsymbol{\nabla} \cdot \boldsymbol{v} \tag{7.4}$$

where the operator D/Dt indicates the material derivative, ρ is the density and $\boldsymbol{v}$ is the velocity vector.

The momentum equation is written as [147]:

$$\rho \frac{D\boldsymbol{v}}{Dt} = \rho \boldsymbol{g} + \boldsymbol{\nabla} \cdot \boldsymbol{\sigma} \tag{7.5}$$

where $\boldsymbol{g}$ is the gravity vector and $\boldsymbol{\sigma}$ is the stress tensor.

The energy equation is defined as [147]:

$$\rho c_p \frac{DT}{Dt} = \beta T \frac{Dp}{Dt} + p \boldsymbol{\nabla} \cdot \boldsymbol{v} + \boldsymbol{\sigma} : \boldsymbol{\nabla} \boldsymbol{v} + \boldsymbol{\nabla} \cdot (k \boldsymbol{\nabla} T) \tag{7.6}$$

where c_p denotes the specific heat capacity at constant pressure, β the coefficient of volumetric expansion, T the temperature, p the pressure and k the thermal conductivity.

7.2.3 Thermodynamics

Along with the viscosity, information on the thermodynamic characteristics of the polymer are also needed to perform injection moulding simulations. This information is contained in the equation state, also referred to as pvT data, which links pressure, density and temperature of a given material [147]. This type of data has a relevant importance in injection moulding simulations since it determines shrinkage and warpage of the moulded component.

For thermoplastic polymers, the Tait equation [151] is commonly used in simulation software tools. It is given as:

$$V(p,T) = V_0(T) \cdot \left[1 - C \, \ln\left(1 + \frac{p}{B(T)}\right)\right] + V_\mathrm{t}(p,T) \tag{7.7}$$

where V is the specific volume, $V_0(T)$, $B(T)$ and $V_\mathrm{t}(p,T)$ are temperature-dependent functions and C is a constant equal to 0.0894. These functions have different definitions depending on the two possible domains of the polymer, which are the solid and molten phase. In the solid phase, i.e. when the temperature is lower than the transition temperature T_t, they are equal to:

$$\begin{aligned} V_0(T) &= b_{1\mathrm{s}} + b_{2\mathrm{s}}\,(T - b_5) \\ B(T) &= b_{3\mathrm{s}}\,\exp\left[-b_{4\mathrm{s}}\,(T - b_5)\right] \\ V_\mathrm{t}(p,T) &= \begin{cases} b_7\,\exp\left[b_8\,(T - b_5) - b_9\,p\right] & \text{if semi-crystalline} \\ 0 & \text{if amorphous} \end{cases} \end{aligned} \tag{7.8}$$

Vice versa, in the molten phase:

$$\begin{aligned} V_0(T) &= b_{1\mathrm{m}} + b_{2\mathrm{m}}\,(T - b_5) \\ B(T) &= b_{3\mathrm{m}}\,\exp\left[-b_{4\mathrm{m}}\,(T - b_5)\right] \\ V_\mathrm{t}(p,T) &= 0 \end{aligned} \tag{7.9}$$

The transition temperature is assumed to be a linear function of pressure:

$$T_\mathrm{t} = b_5 + b_6\,p. \tag{7.10}$$

where $b_{1\mathrm{s}}$, $b_{2\mathrm{s}}$, $b_{3\mathrm{s}}$, $b_{4\mathrm{s}}$, $b_{1\mathrm{m}}$, $b_{2\mathrm{m}}$, $b_{3\mathrm{m}}$, $b_{4\mathrm{m}}$, b_5, b_6, b_7, b_8 and b_9 are coefficients fitted on experimental data.

7.3 Simulation software tools and meshing

Different software simulations packages are currently available on the market for injection moulding. The most common ones are Autodesk Simulation Moldflow® (Autodesk, San Rafael, CA, USA), Moldex3D® (CoreTech System, Chupei City, Taiwan) and SigmaSoft® (SIGMA Engineering, Aachen, Germany). All of them employ the aforementioned equations to model viscosity, flow and thermodynamics, which are numerically solved using finite element analysis (FEA).

In particular, the finite element method (FEM) is used to discretize the model, which is typically either 2D or 3D, into small elements of finite size by means of a meshing algorithm. This step has a huge impact on the accuracy of the results of the simulations: the element size is directly related to the capability of the numerical model to capture the real trends of the variables of interest.

There are two main meshing strategies that can be adopted [148]:

- Homogeneous meshing: a fixed element size is applied to the entire geometry of the model. The main disadvantage of this approach is that, when details that are small compared to the overall model size are the target, a very large number of elements is needed, often leading to very long computational times. Therefore, this strategy is well suited only for systems having features of comparable size.
- Multi-scale meshing: in this case, the mesh density changes within the geometry of the model. Even though the implementation of this strategy is more complex than the previous one, it is the best solution when features of different sizes are involved. In IM and µIM, this is very often the case: gate areas, surface features, ribs, etc., are typical areas where a finer mesh is needed to obtain truthful results.

7.4 Challenges of micro injection moulding simulations

The aforementioned commercial software packages are developed for macro moulded parts. Therefore, their use is nowadays state-of-the-art for the plastic industry dealing with conventional components. However, their application to µIM is not as straightforward because of the peculiar phenomena that happen only at the micro scale, which are usually neglected in commercial packages and thus lead to a decrease of the accuracy of the simulation results. The major discrepancies between IM and µIM in terms of process modelling are [31, 33, 143, 152–158]:

- The rheological data at very high shear rates ($>10^5$ s^{-1}), which are typical for µIM, are usually not available. This lack of information is caused by the fact that it is extremely difficult to measure the viscosity of a melt flowing in these conditions. Therefore, material data extrapolated by common rheometers such as rotational and capillary ones might be insufficient to describe the behaviour of a polymer inside a micro cavity.
- A 3D model is usually required to obtain truthful results. The 2.5D Hele-Shaw approximation, widely employed in conventional simulations [147], is not valid for the micro scale since variations of pressure along the thickness of micro components are normally not negligible.
- Microscopic phenomena such as micro scale viscosity, surface tension or wall-slip can become relevant in µIM whereas they are negligible in IM (see subsection 2.2.3).
- The commercial software packages are not designed to take into account the effects of surface roughness, which is particularly difficult to implement because of the extremely small size of the features that generate the surface topography. Although this is a reasonable approximation for the macro scale, a difference in surface roughness inside a micro cavity can generate a flow unbalance that becomes relevant if micro channels are filled. This limitation also applies to the prediction of the filling of surface nano structures.
- The elasticity of the polymer melt is usually neglected in IM software tools since the prevalent viscous effects dampen it. However, elongational viscosity plays a more important role in the micro scale, where the shear viscosity is decreased to a very low value because of the high shear rate and temperature.

To tackle these issues, two main strategies can be adopted. The first is the development of an in-house software specifically designed for µIM simulations that includes all the peculiar aspects of the flow at the micro scale [159]. This approach allows a more comprehensive implementation when compared to commercial tools but, at the same time, lacks repeatability and industrial interest.

The second strategy is based on the use of a commercial software with the aim of improving its prediction performances. With this intent, Costa et al. [154] studied the best strategies to carry out an accurate simulation of injection moulding of a flat thin cavity and of a miniaturized dog-bone shaped part using Autodesk Moldflow 2010® by optimizing mesh size and model definition. Their results showed that the modelling strategy for the nozzle tip strongly influenced the accuracy of the simulations, demonstrating that including the machine geometry into the model is beneficial with respect to the accuracy of the results. Tosello et al. [104] used Moldflow Plastics Insight® 6.1 to predict the outcome of µIM of a flat part with micro structures. The results clearly showed that appropriate implementation of material models and boundary conditions is essential if the accurate prediction of

the flow front development is the target. Marhöfer et al. [160] used a multi-scale mesh for modelling µIM of a microfluidic device using Autodesk Moldflow 2013®. By including mould blocks and barrel in the model, the authors showed that simulations results were largely improved. Marhöfer et al. [144] also successfully used process simulations to design the gate of two microfluidic components. The validation phase was based on SEM images of short shots that were compared to the correspondent simulated filling steps.

A further critical aspect of µIM simulations is related to the validation of the numerical results, which is of primary importance to assess the accuracy of the model. A common validation procedure is based on the comparison of simulated and experimental pressure curves, where the latter are monitored using sensors. When micro parts are moulded, the very small size of the cavity can make this option unusable. Moreover, a validation based on a comparison between real short-shots and filling steps cannot be always applied due to the small injected volume, which may not be controllable through short-shots given the limited resolution of the injection plunger stroke. This is particularly true when very small parts such as those considered in chapter 4 and chapter 5 are manufactured.

The current state-of-the-art still lacks examples of µIM simulations used to predict the outcome of the process in terms of dimensional accuracy of the final parts. The studies presented in this chapter aim at achieving this by validating suitable numerical models with respect to the dimensions of final functional geometries of the part within a range of experimented process parameters. The ideal application of these validated models is the virtual optimization of the process, which would be extremely beneficial to minimize the experimental time needed to tune µIM in the initial optimization phase of a new production.

7.5 Simulations of micro injection moulding of TPE micro rings

Process simulations were applied to the case study presented in chapter 4. Therefore, the target was a TPE micro ring having a 3D internal shape (see Figure 4.2). The experimental data used for the validation consisted of the outputs of the DoE outlined in Table 4.3, whose results were presented in subsection 4.1.7. Process simulations were compared with experimental results based on the prediction of the main defects and the dimensions of the outer diameter (OD) and inner diameter (ID) of the moulded micro rings.

7.5.1 Simulation set-up

The commercially available software Autodesk Simulation Moldflow Insight (ASMI) 2016® was used for the numerical analysis. The simulation model comprised the four parts and the feed system (see Figure 7.2). A 3D meshing was applied to this geometry. The commonly used 2.5 D Hele-Shaw approximation is in fact not suitable for µIM simulations, as mentioned before. To reduce the computational effort and, at the same time, achieve accurate results, a multi-scale mesh was used. In particular, an element size ranging from 50 to 500 µm was set: to increase the accuracy of the results, the regions of interest (i.e. ring geometry and the gate) were more finely discretized than the sprue, where the polymer flow followed a relatively simple pattern. The meshed model contained a total of 1.4×10^6 tetrahedrons. Table 7.1 shows the mesh settings in detail.

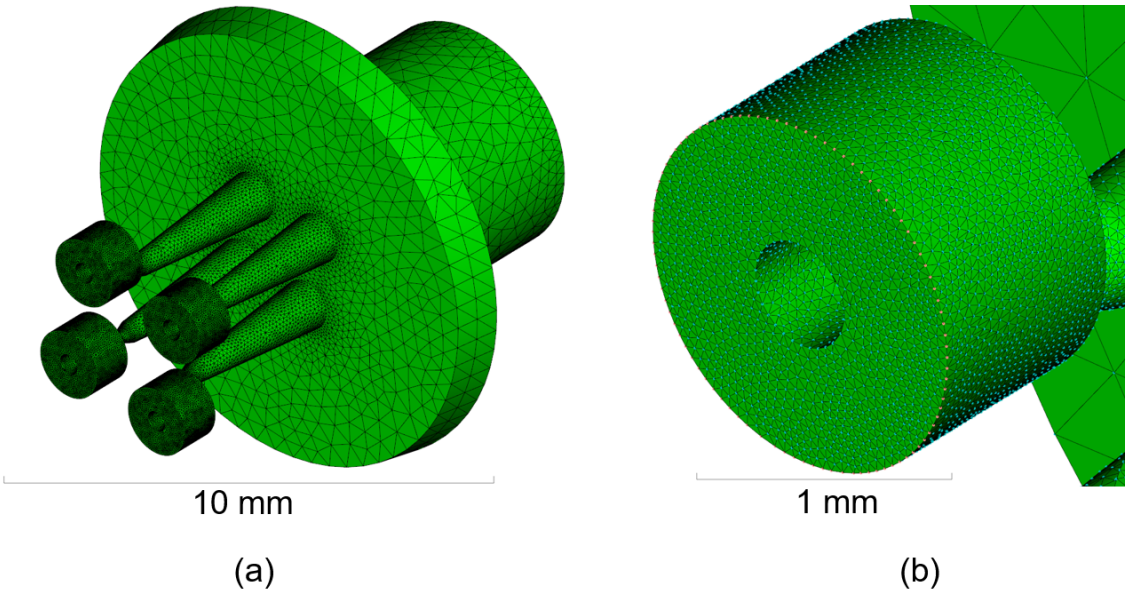

Figure 7.2: (a) Entire meshed model and (b) detail of the meshed micro ring.

Table 7.1: Mesh settings for the micro ring simulations.

Meshing parameter	Setting
Edge length/mm	0.05 - 0.50
Merge tolerance/mm	0.8
Minimum number of elements through thickness	10
Bias ratio	1.2
3D mesher	Advancing front
Total number of elements	1400000

In ASMI, the flow was modelled by Navier-Stokes equations in 3D as presented in subsection 7.2.2. As regards the material data, Cross-WLF and Tait models were used to describe the rheological and thermodynamic behaviours respectively. Material data provided by the material supplier were used to fit the two models, which were then imported in ASMI (see Figure 7.3). A "Fill+Pack+Warp" analysis sequence was run in order to obtain the final dimensions of the parts after the end of the moulding cycle, thus considering also the post-moulding shrinkage induced by the cooling of the polymer. As boundary conditions, the process settings employed in the experiments, i.e. melt temperature, mould temperature, injection speed and holding pressure, were selected to reproduce the real process conditions. 36 simulations were run in order to replicate the experimental DoE design, whose detail are reported in Table 4.3.

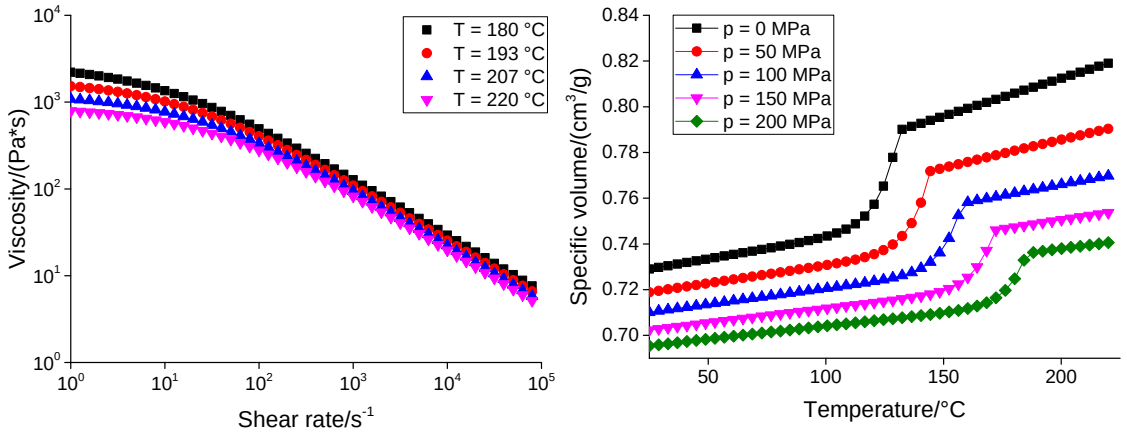

Figure 7.3: Material models employed in the micro ring simulations. (a) Viscosity plot at different temperatures and (b) pvT data at different pressures for the TPE material [129].

7.5.2 Prediction of defects

The simulation results indicated the presence of five air traps on both the outer and inner surface of the ring on the opposite side of the gate position (see Figure 7.4). This output can be easily derived from Moldflow results panel and is based on the filling development and presence of venting, which was not implemented in the model. The reason for the formation of the air trap was the filling pattern: being the gate asymmetrical with respect to the ring axis, the polymer flow separated and then converged on the other side of the ring, sealing the cavity (see Figure 7.5). Another defect caused by the asymmetrical gate was the presence of weld lines (see Figure 7.6) on the top and bottom ring surfaces. SEM images of real parts were taken and directly compared to simulation results. The process simulations accurately

predicted both air traps and weld line position, proving to be a powerful tool for defects prediction in micro moulded parts.

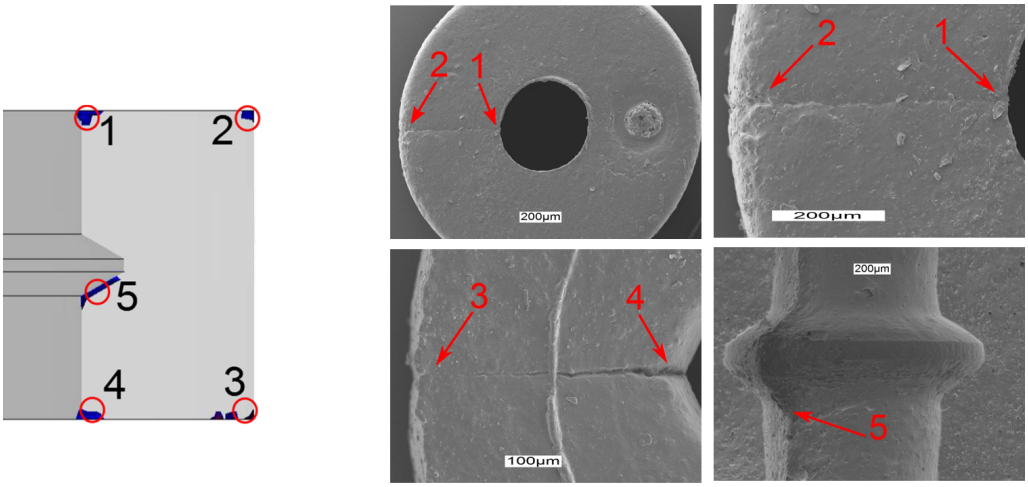

Figure 7.4: Air traps as predicted by process simulations (left) and SEM images showing the correspondent defects on real parts (right) [114].

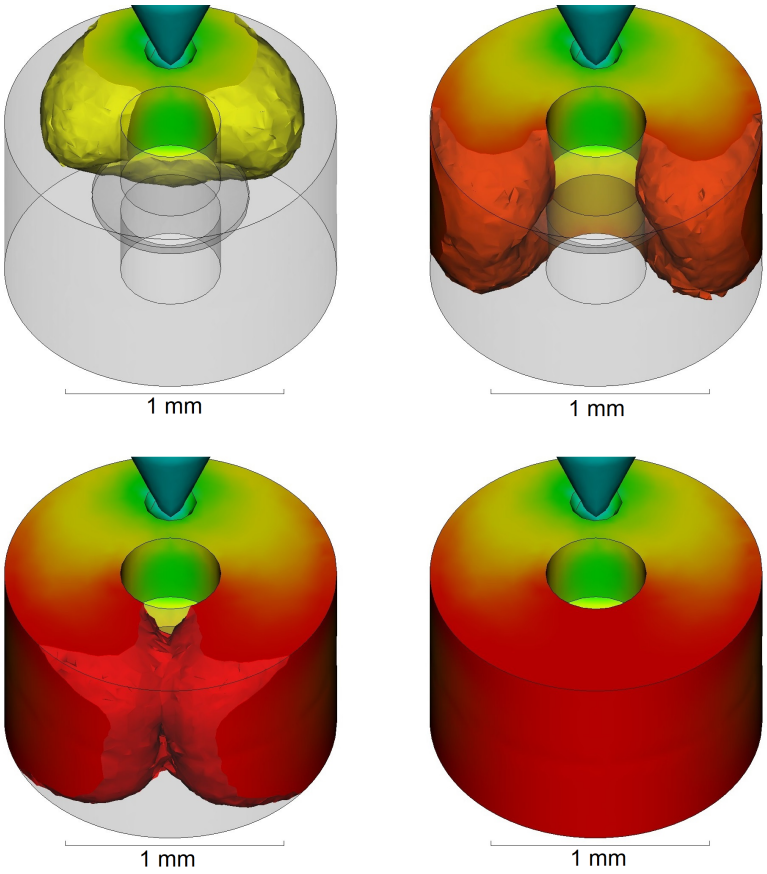

Figure 7.5: Sequential filling steps for a micro ring.

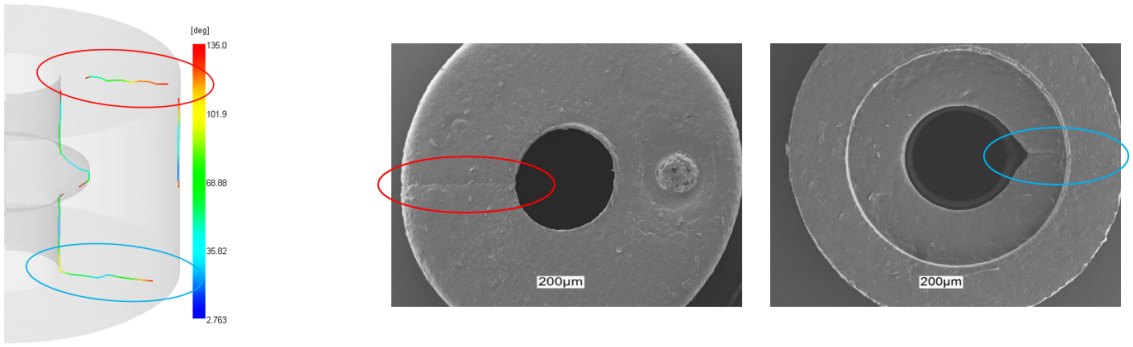

Figure 7.6: Weld lines as predicted by process simulations (left) and on real parts (right) [114]. The weld line on the upper surface is indicated in red, while the one on the lower surface in light blue.

7.5.3 OD prediction

After the analyses were completed, the spatial coordinates of the nodes standing on the outer diameter of the meshed rings were extracted and a circle was mathematically fitted to calculate the OD value (see Figure 7.7), which was then compared to the real measurements carried out with the focus variation microscope (see subsection 4.1.4 for details). For each process condition, the four OD values corresponding to the four cavities were averaged in order to eliminate any deviation introduced by possible non-perfect mesh symmetry.

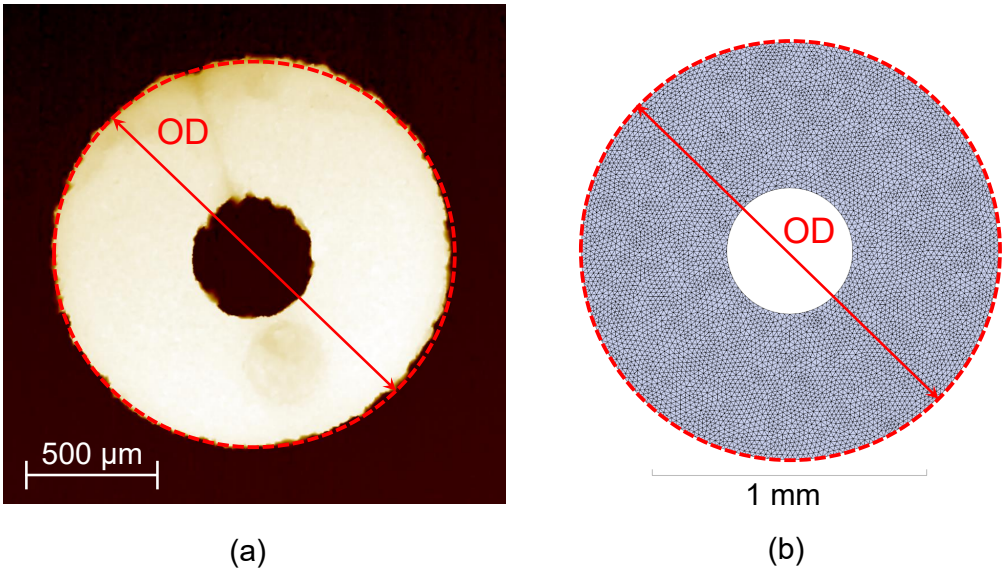

Figure 7.7: (a) Measurements of real moulded micro rings and (b) extraction of OD from the meshed model.

The measured mould dimensions were initially assigned to the CAD model that was successively meshed in ASMI. Particularly, the outer diameter of the cavity OD_{mould} was equal, on average, to 1.55 mm (see Figure 4.9). By assigning this dimension to the model, the numerical results overestimated the experimental observations. This was probably due to the fact that the models used in ASMI are specifically designed for macro parts, as described in section 7.4. In this case, the real polymer melt underwent a larger amount of shrinkage than predicted by the pvT model. In order to overcome this discrepancy, a calibration procedure aiming at optimizing the model dimension OD_{model} with respect to the experimental measurements was carried out. Figure 7.8 shows the flowchart of the calibration procedure: OD_{model} was progressively decremented of a 5 µm step until the numerical results fitted the experimental observations. 36 process simulations corresponding to the 36 DoE combinations were run for each of the calibration steps. The calibration procedure was ended when the average of the results provided by the numerical model for all DoE combinations OD_{num} fell inside the uncertainty interval built around the average of the experimental results OD_{exp}.

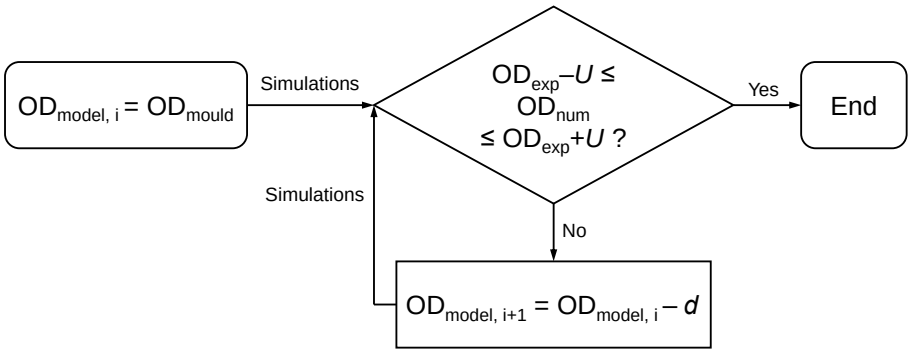

Figure 7.8: Flowchart of the model calibration procedure. d was equal to 5 µm.

Figure 7.9 shows the results of model calibration. Starting from a value of OD_{model} equal to OD_{mould}, six steps, correspondent to a reduction of 30 µm, were necessary to fit the experimental data according to the selected procedure: a final dimension of 1.520 mm was thus chosen for the model. The trend of OD_{num} against OD_{model} was very close to linear. This demonstrates that the amount of shrinkage of the part was linear with respect to the mould dimension, i.e. the percentage shrinkage of OD was constant in the numerical model.

The calibrated model was then used to validate the simulations with respect to the effects of the four process parameters on the outer diameter of the produced micro rings.

Figure 7.10 shows the comparison of moulding experiments and simulations in terms of main effects plots. Firstly, it is worth observing that OD averages were always lower than the design target of 1.5 mm (see Figure 4.2): the level of shrinkage had to be decreased to meet the specifications. The deviation between experiments and

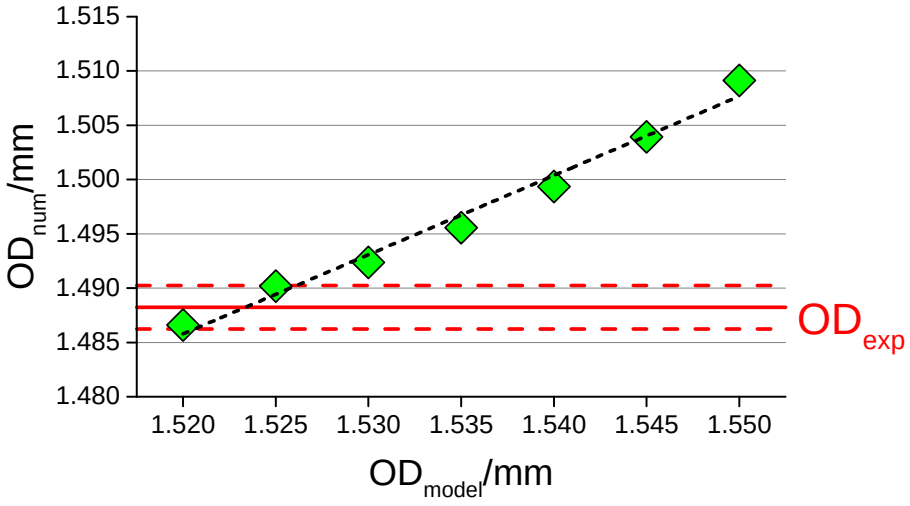

Figure 7.9: OD_{num} as function of OD_{model}. OD_{exp} is indicated by a red line. The red dashed lines indicate the interval identified by the expanded uncertainty U, whereas the black one denotes the linear fit of the data.

simulation results was, on average, equal to 1.6 µm. This value was completely covered by the uncertainty U of OD (see Table 4.4), and therefore the simulations were generally able to predict the outer diameter of the micro moulded rings at a level of accuracy equal to the precision of the measurements. As regards the effects of the process parameters on OD, a good agreement was also observed. The use of the high level of mould temperature provided an increase of OD for both simulations and real parts. This happened because, by increasing T_{mould}, a premature cooling of the polymer melt inside the cavity was hindered. The magnitude of this effect in the real process, which is indicated by the slope of the line in main effects plot, was larger than the simulated one. An increase of melt temperature resulted in a reduction of OD, as also predicted by simulations. As for T_{mould}, the effect of T_{melt} was underestimated by the numerical model. The effect of the injection speed was non-linear since the central level produced higher results than the low and high ones. This behaviour, which was due to larger residual stresses originated at high injection speed because of the more drastic cooling rate, was also predicted by the simulations. However, the effect of the real process was once again underestimated by the numerical analysis results. The effect of the holding pressure was the one that was best predicted by simulations. The direct relation between OD and p_{hold} was caused by the fact that a higher holding pressure allowed more material inside the cavity and consequently resulted in a better OD replication. The tendency towards compression of TPE might have helped this phenomenon. The numerical model accurately predicted the trend: the deviations of experimental and numerical results ranged between 0.0 µm and 2.6 µm among the three p_{hold} levels.

It is possible to conclude that the calibrated model was capable of accurately predicting the effects of the four process parameters. In fact, the signs of the slopes

of the main effects plots for real and simulated results were the same in all the investigated ranges. Therefore, the numerical model was considered as validated with respect to the prediction of the effects of the µIM parameters on the OD value.

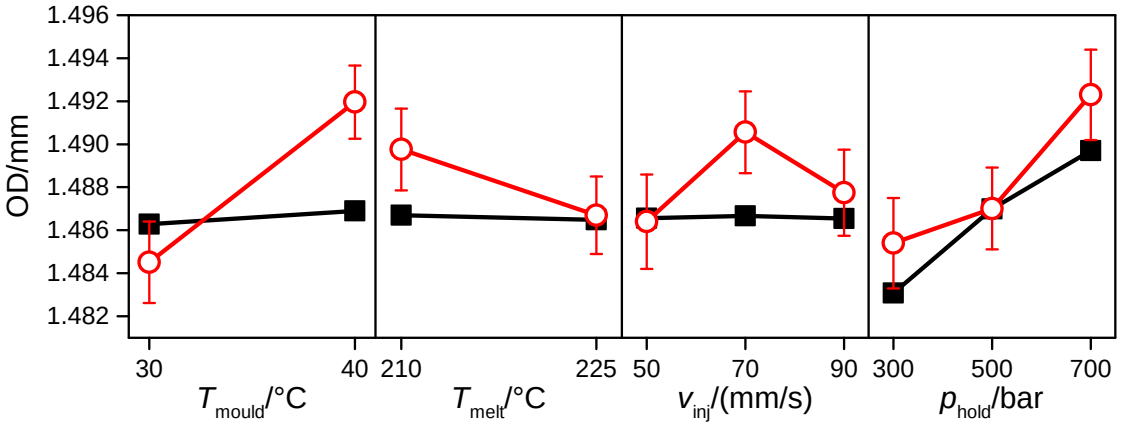

Figure 7.10: Main effects plots for OD. The measurement (red) and simulations (black) results are shown. The errors bars indicate the expanded measurement uncertainty U.

The calibrated and validated model was used to virtually optimize the process with respect to the OD target of 1.5 mm. To do this, a further virtual campaign was carried out. Table 7.2 shows the selected conditions. A two-level full factorial experimental plane was designed and simulated. In particular, only p_{hold}, T_{mould} and T_{melt} were varied as they were the most significant factors for the simulations results of the previous DoE analysis. The levels of the parameters for the optimization plane were selected according to the previous trends with the aim of increasing OD towards the target of 1.5 mm. In particular, the levels of melt temperature were selected as lower than the one investigated before since OD increased at decreasing T_{melt}. Conversely, higher levels of p_{hold} and T_{mould} were chosen since they had a positive impact on OD. The level of injection speed was kept at 70 mm/s.

Table 7.2: Settings for virtual optimization.

Process parameter	Levels
Melt temperature, T_{melt}/°C	180, 195
Mould temperature, T_{mould}/°C	50, 60
Holding pressure, p_{hold}/bar	900, 1000

Figure 7.11 shows the results of the virtual optimization. As for the previous experimental campaign, a clear effect of the holding pressure is evident: increasing p_{hold} determined an increase of OD. In particular, considering the target, selecting a holding pressure of 1100 bar was strongly suggested by the simulations results. As for the effect of mould temperature, its increase was important to achieve the desired

dimensional output for the micro rings and therefore the setting of a T_{mould} of 60 °C was necessary to get as close as possible to the specification target. The effect of T_{melt} was less important, particularly when setting high levels of p_{hold} and T_{mould}.

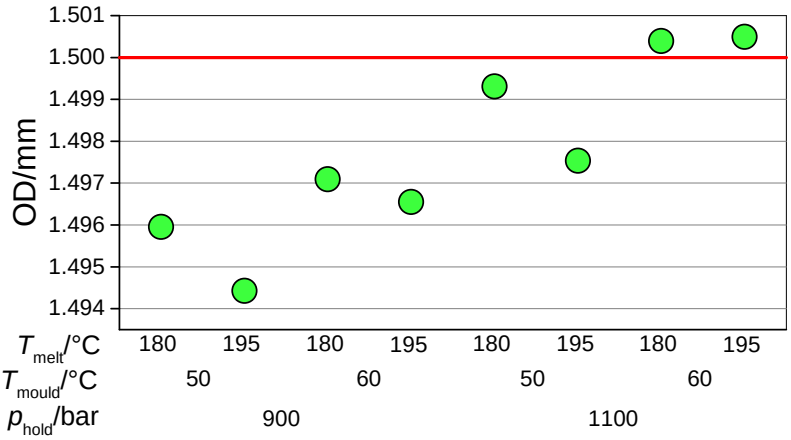

Figure 7.11: Individual value plot for the results of the virtual optimization plane. The red line represents the OD design target of 1.5 mm.

7.5.4 ID prediction

The same calibrated model was used to validate the effects of the four process parameters on the inner diameter ID of the micro rings. Figure 7.12 shows the results. What stands out is that the prediction performance of the model was worse than for OD. In particular, the average deviation between simulations results and experimental data was equal to 50 µm, which is higher than the values of both tolerance and uncertainty. This discrepancy could be reduced by a further calibration procedure. However, this would also worsen the overall performance in the OD prediction. As regards the magnitude of the effects, the numerical model always predicted effects which were not as significant as the real ones for all the four involved process parameters. This leads to the conclusion that the numerical model was not validated with respect to the effects of the process variations on ID, whereas it was for OD. In particular, the simulations were not capable of reproducing the opposite impact that the four parameters had on OD and ID (see Figure 4.13). This different prediction performance between the two geometries could have been caused by the incorrect or incomplete implementation of residual stresses in the model, which it was hypothesized to be the reason for the enhanced shrinkage of ID. The mathematical determination of the residual stresses caused by constrained shrinkage is indeed not reported in the examined injection moulding literature and therefore not comprised in the ASMI software. Moreover, a complete characterization of the thermo-mechanical properties of the polymer material based on experimental shrinkage data, which are typically gathered using a tag die with etched grid lines, is needed to solve residual

stresses problems [161]. These data were not available for the used TPE, being this material produced by a small manufacturer that does not perform this type of tests. Therefore, the lack of a proper shrinkage model was most probably the cause for the inaccurate prediction of ID.

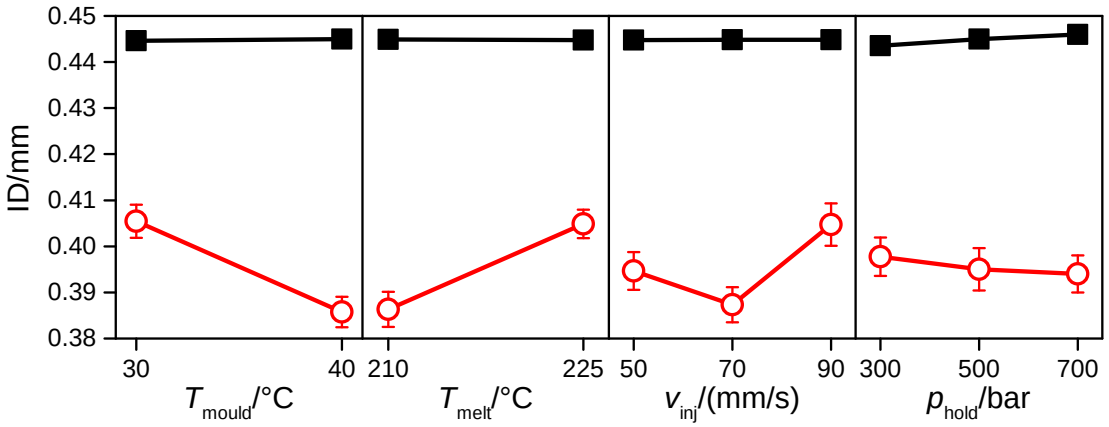

Figure 7.12: Main effects plots for ID. The measurement (red) and simulations (black) results are shown. The errors bars indicate the expanded measurement uncertainty U.

7.6 Simulations of the flash formation of a 3D micro part

Process simulations were also applied to the case study presented in chapter 5. The target was a 3D micro part with a through hole (see Figure 5.2). The focus was on the prediction of the flash size affecting the quality of the micro part. The flash area A_{flash} was in fact shown to be the best product fingerprint for this component, thus carrying valuable information on the overall part quality (see subsection 5.4.1). The experimental data used for the validation consisted of A_{flash} results, which were the outputs of the DoE outlined in Table 5.3. Process simulations were run to investigate their performance in the prediction of the flash size against the variations of µIM settings.

7.6.1 Simulation set-up

Injection moulding simulations were run with Autodesk Moldflow Insight 2017®. The model comprised the part and the feed system (see Figure 7.13). The venting channel was modelled as a continuation of the part geometry: the flash was then visualized as a virtual short-shot in the software. A multi-scale 3D mesh was used:

the element size ranged from 20 to 300 µm, generating circa 10^6 elements. In particular, the finest mesh density was assigned to the venting channel area, being of maximum interest for the analysis. To reproduce the 2^4 factorial DoE, 16 simulations were run. The velocity and pressure curves recorded via the machine interface (see subsection 5.3.4) were implemented as boundary conditions of the numerical model in order to reproduce the experimental conditions as best as possible as prescribed by Tosello et al. [104]. The POM material properties were modelled according to Autodesk Moldflow database (see Figure 5.6 for viscosity and pvT plots). Table 7.3 shows the mesh settings in detail.

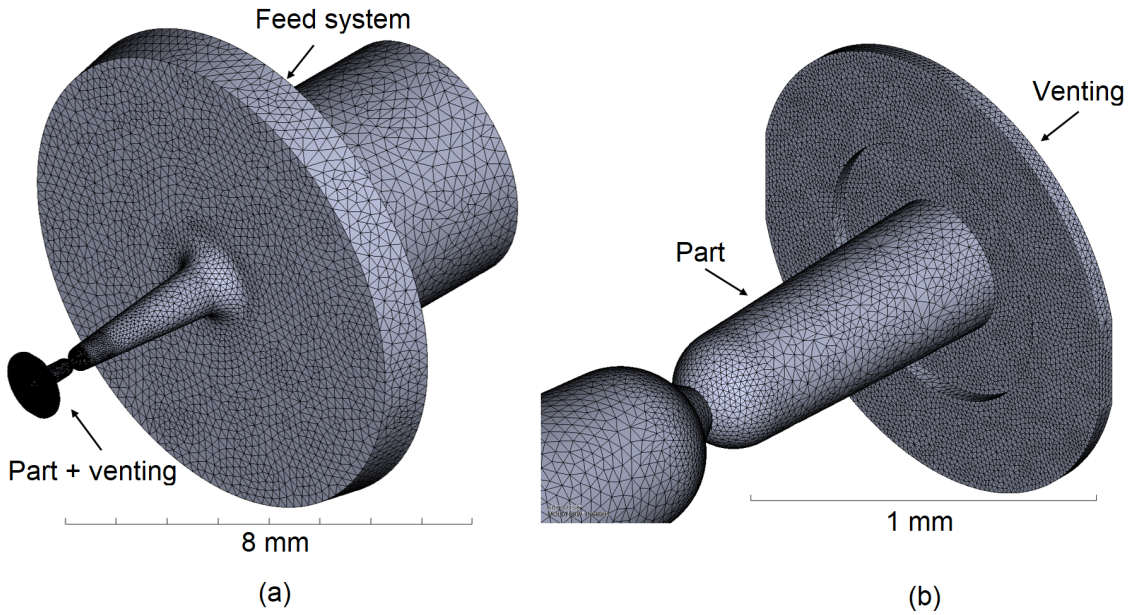

Figure 7.13: (a) Entire meshed model and (b) close-up of the part.

Table 7.3: Mesh settings for flash size simulations.

Meshing parameter	Setting
Edge length/mm	0.02 - 0.30
Merge tolerance/mm	0.8
Minimum number of elements through thickness	10
Bias ratio	1.2
3D mesher	Advancing front
Total number of elements	1000000

7.6.2 Prediction of flash size

The simulations results allowed the observation of the flash formation that, as expected, was caused by the polymer melt flowing inside the venting channels (see Figure 7.14).

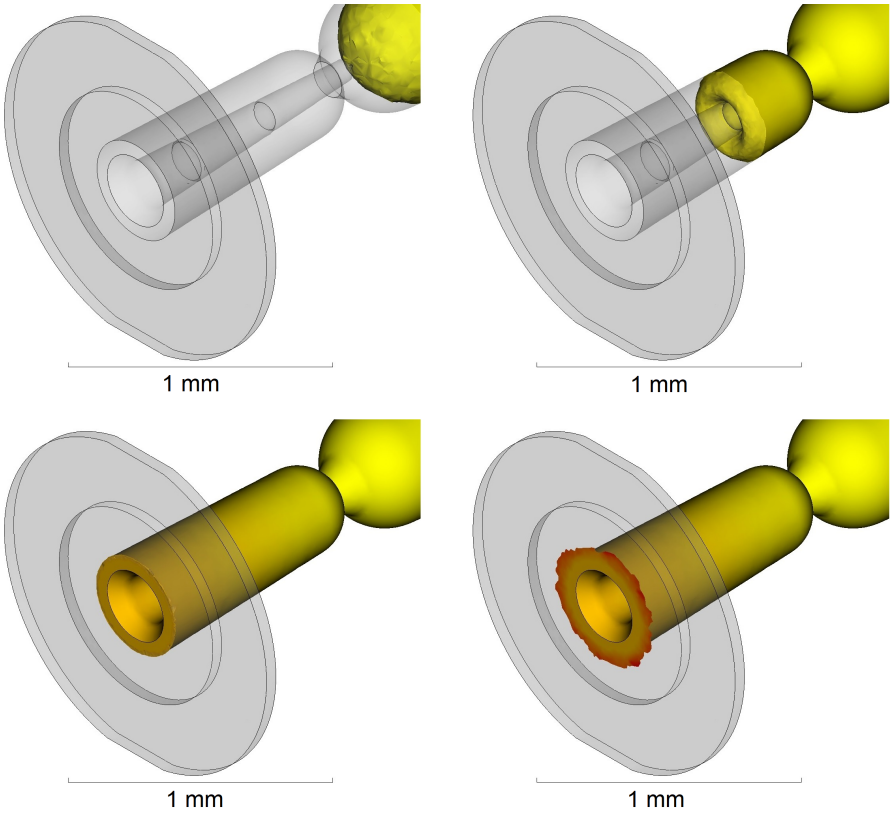

Figure 7.14: Sequential filling steps for the 3D micro part. The flash formed at the end of the flow path can be seen in the last image.

The flash in the software was measured by counting the pixels of the flash area formed at the end of the filling. It was then compared to real parts measurements performed with a focus variation microscope (see subsection 5.3.3 for details).

Figure 7.15 shows an example of a real flash and a simulated one with the same combination of process parameters. It is clear that the flash affecting the real part was smaller than the one predicted by the numerical model. This means that, in the virtual domain, the polymer flow was able to proceed further inside the venting channel before freezing. This deviation could be due to various reasons, most of them related to the underlying simplifications introduced by the numerical model, as for example the neglection of the cavity surface roughness that, for polymer melts flowing in micro channels, can be decisive in determining the filling history. This could be particularly important in the case of the 3D micro part under analysis because of the

extremely small injection volume and consequently very high surface-to-volume ratio. In fact, the roughness of the cavity might have increased the actual surface at the polymer-mould interface, thus resulting in a better heat evacuation, which caused, in turn, a decrease of flow length with respect to the numerical model, in which the cavity is considered as perfectly smooth. Other reasons for this discrepancy could be unrealistic heat transfer coefficient, due to the impossibility of modelling the real surface texture of the cavity, and venting boundary conditions.

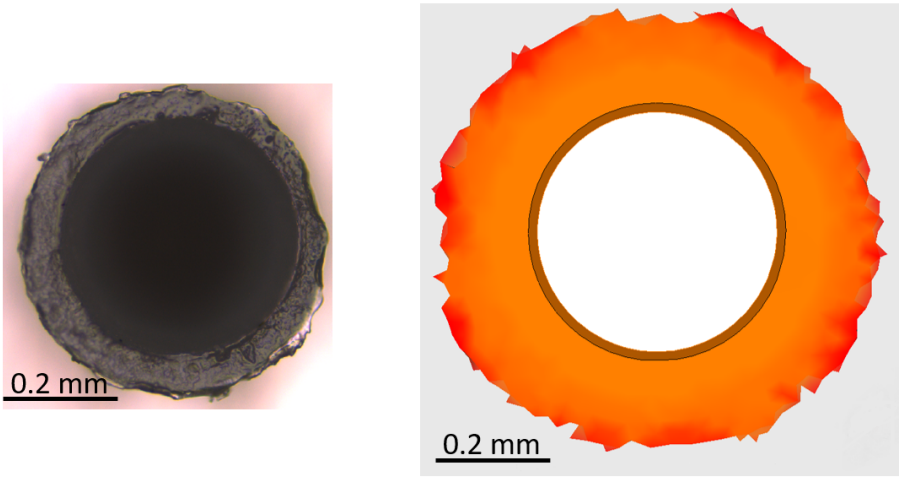

Figure 7.15: Real flash on the part (left) and simulated flash (right). The dimensional scale is equal in both images.

Figure 7.16 shows the main effects plot of the results. It can be seen that the simulations provided a flash area equal to circa twice the real one (the experimental flash area $A_{\text{flash-exp}}$ and the simulated one $A_{\text{flash-num}}$ were, on average, equal to 0.064 mm^2 and 0.137 mm^2 respectively). However, the slope signs of the two plots are equivalent in all the experimented process parameter ranges. In particular, the increase of the four variables led to an increase of both the measured and simulated flash area, as explained in subsection 5.4.1. Both experiments and simulations agreed on the sign of the four effects, whose magnitude, which is indicated by the value of the slopes, was very similar for the two sets of results. This was particularly true for T_{mould} and v_{inj}, for which experiments and simulations provided an almost identical influence on flash size variation. As for p_{hold}, the numerical model overestimated the real effect, being the variation introduced by this process parameters bigger than the real one. On the other hand, the effect of the T_{melt} was larger for experimental results and therefore underestimated by the numerical analysis.

From the comparison based on the flash measurements, it can be concluded that the implemented numerical model was validated with respect to the signs of the effects induced by µIM process parameters variation, but not with respect to the absolute value. The model can thus be used as a tool for process optimization, even though the real size of the flash cannot be predicted accurately.

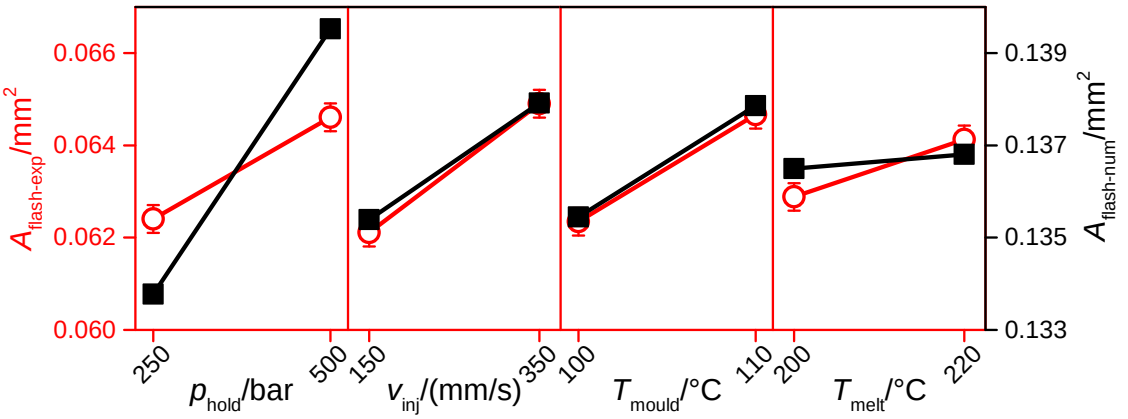

Figure 7.16: Main effects plot of flash area for experiments $A_{\text{flash-exp}}$ (in red) and simulations $A_{\text{flash-num}}$ (in black). Note that the scales for the two sets of results are different but the shown range, equal to 0.007 mm^2, is equal. The errors bars indicate the uncertainty U of the flash area measurements.

7.7 Conclusions

In this chapter, µIM process simulations were applied to the case studies of chapter 4 and chapter 5 with the aim of predicting the quality of the micro moulded parts as a function of the investigated process parameters. A commercial software, ASMI in the 2016 and 2017 versions, was used.

As regard the simulations of TPE micro rings, simulations were specifically employed to assess the performance of the numerical model in the prediction of the main defects and dimensions of the part. A 3D multi-scale mesh comprising the feed system and the four cavities and having 1.4×10^6 elements was used. The conclusions are:

- Simulations results matched the real defects very accurately. Both air traps and weld lines indicated by the software appeared in the same locations in real parts, thus proving that the implemented model can serve as a tool for predicting these defects.
- The OD shrinkage of the real parts was larger than that resulted from simulations. A calibration procedure was then designed to fit the simulated OD to experimental data.
- The calibrated model was capable of accurately predicting the OD value in terms of absolute value (average deviation of 1.6 µm, lower than the measurement uncertainty). Moreover, the model was also validated with respect to the effects of µIM parameters: the signs of the slopes induced by the variation of process settings were equal for experimental and numerical results in all the experimented ranges.

- The calibrated and validated model was used as a virtual optimization tool. This procedure allowed defining optimal values of holding pressure and mould temperature to achieve the target OD value.
- The model was not capable of well predicting ID experimental results. In particular, the average deviation between simulations and experiments was equal to 50 µm. Moreover, the simulated effects were not as significant as the real ones. This difference in prediction performance between OD and ID might have been caused by an incomplete residual stresses implementation in the model. Residual stresses were, in fact, the main reason that generated a higher level of shrinkage for ID with respect to OD for the moulded parts.

For the simulations of the 3D micro part, ASMI 2017 was used to predict the size of the flash that affected the part quality. This defect was particularly important, since its size was demonstrated to be a suitable product fingerprint candidate and, as such, correlated to the overall part quality. Therefore, if process simulations were validated as a tool for predicting the flash size, virtual optimization experiments could be effectively run in order to improve not only the defect size but also the dimensional quality of the part in general. A 3D mesh with 10^6 elements was used. In particular, the model comprised feed system, part and venting channel in order to simulate the flash size as a virtual short-shot. The conclusions of this study are:

- Numerical results overestimated the experimental flash area by a factor of circa 2. Therefore, the simulated flow length was larger than the real one. This discrepancy was most probably caused by micro-scale phenomena that are not implemented in ASMI, such as the effect of the cavity surface roughness on the flow length.
- The effects of the process parameters on the flash size were well predicted by the implemented model. In fact, the slopes of the main effects plots were equal in all ranges. The magnitude of the variations was also very similar, confirming the applicability of the model as a virtual optimization tool when flash minimization is the objective.

8 Replica technology for the indirect measurement of micro moulds

The present chapter is dedicated to the study of the performance of the replica technology applied to the indirect measurement of micro mould features machined by micro milling. The process consists of the replication by means of a fast and easy-to-apply replication media that is then used to measure the initial object in an indirect way. This investigation is of primary importance for the verification of µIM process chains since in many cases micro moulds have surfaces and geometries that are not directly measurable with common instruments due to their inaccessibility.

The replica technology using a two-part silicone media was applied to texture and geometrical features produced by micro milling, as this machining process is one of the preferable technology to manufacture micro moulds. Two specifically designed micro milled benchmark samples, which had multiple surfaces and pockets, were used to assess the replication by comparing indirect and direct measurements.

The results presented in this chapter were published in [162] and [163] and partially taken from these papers.

8.1 Introduction

Micro milling is the miniaturized adaptation of the conventional milling process. The capability of manufacturing 3D micro components with relatively high material removal rate makes this technology suitable for producing moulds and inserts employed in replication techniques such as µIM [20]. When evaluating the quality of a machined mould, two main characteristics must be assessed: the geometrical accuracy and the surface topography. This is firstly because dimensional features and surface topographies of the mould are directly transferred to the replicated products. Secondly, the mould surface has an impact on the replication process itself since it affects demoulding forces [21], which in turn have to be optimized in order to obtain products with the desired characteristics.

In micro milling, numerous phenomena, which are negligible for conventional milling, become significant for the surface generation. The main one is the minimum chip thickness effect [164]: when machining with chip thickness values comparable to the

tool edge radius, effects such as ploughing and elastic recovery become dominant, causing a decrease of dimensional accuracy and an increase of surface roughness, particularly for soft metallic alloys [165]. Therefore, producing a defect-less surface texture by micro milling becomes even more challenging than in the macro scale, making the surface topography assessment more important.

As already mentioned in this thesis, optical instruments are strongly emerging as the preferable measurement solution for assessing micro components of all kinds, including micro milled ones. However, certain features, as for instance micro holes or micro cavities, are inaccessible for optical lenses since an insufficient amount of light is reflected back to the measuring objective. In these cases, also instruments based on probes such as profilometers and CMMs are not effectively usable. In other cases, samples may not physically fit under the microscope. Inaccessible features are typical of micro moulds used in µIM, where high aspect ratio features are often the target [166–168]. Therefore, new solutions must be employed to perform dimensional and surface measurements without adopting destructive inspections. A possible one is the use of computed tomography (CT) [51], which is, however, not yet fully applicable to assess surface topography at the nanometric scale. Another one is the replica moulding technology, which is based on the fast replication of inaccessible features by casting a soft polymeric media such as polydimethylsiloxane (PDMS) or two-component silicone polymers [15].

When using the replica moulding, the common procedure consists of casting the media over the component to measure. After the curing is completed, the replica is carefully detached from the sample and then measured, providing indirect information of the actual geometry and surface of the object. The use of this method is well-established in medical and dental fields [169, 170] where specimens cannot be normally placed under a measuring instrument. It is also widely employed in non-destructive metallographic analyses of mechanical components [171, 172]. For dimensional and surface metrology tasks, replication kits based on a two-component polymer are nowadays the most common media [173, 174], since they ensure almost no shrinkage over a wide range of curing temperature and short curing times in the order of 5 to 20 minutes [174]. When using these kits, the polymer and the curing agent are mixed in a disposable nozzle before casting. A dispensing gun is used for directing the replication media onto the target object.

In recent decades, few studies were dedicated to the study of the performance of fast replication media used in indirect metrology tasks. Tosello et al. [175] successfully employed this method to monitor the tool wear of a mould for Fresnel lenses production presenting micro structures with a height of 23 µm. Madsen et al. [176] studied the shrinkage of a PDMS material used to measure nanometric geometries indirectly. The authors tested several mixing ratios and curing temperature levels and investigated the repeatability of the process by means of repeated replicas. They concluded that the utilized PDMS shrank linearly between 1 and 3 %, leading to dimensions that were smaller than the ones of the master. Goodall et al. [177]

used seven different silicone based replication media for quantitative surface texture characterization. Two masters, one smooth and one rough lower jaw tooth, were replicated. It was demonstrated that low viscosity media generally achieve higher accuracy and precision. The authors also highlighted the need for standardization for the technology, since the results of different impression media were not comparable. Finally, Gasparin et al. [178] investigated the surface texture replication performance of three replication media applied to two calibrated roughness artefacts. The measurements were performed with both optical and tactile instruments. A replication degree up to 96 % was attained and the measured deviations fell inside the uncertainty range. However, since the nominal *Ra* roughness value of the measured standard was 500 nm, the authors' considerations cannot be directly extended to micro milled surfaces, which are usually smoother. In fact, in most micro milling applications, *Ra* ranges between 50 and 250 nm on both flat and free-form components [179–181].

Although several approaches have been proposed in the literature [182, 183], the use of surface topography prediction models in industrial micro milling applications is still extremely limited because of the lack of robustness that the models show with respect to the variability of the material characteristics, tool micro geometry and wear. Thus, the measurement of micro milled components after machining represents the standard practice that machinists still adopt for verifying the cutting process results. The replication and the following indirect measurement are therefore the preferable solution for characterizing the surface topography of inaccessible micromilled features.

The aim of this chapter is to evaluate the performance of a commercial silicone replication media (RepliSet [174], Struers®, Ballerup, Denmark) in the indirect measurement of micro milled surfaces and geometries typical of micro moulds, thus providing useful insights on how to accurately assess inaccessible micro features that are often involved in µIM processes.

8.2 Experimental

Two different micro milled samples were designed to assess the replication performance of the replica technology. The first one was used to investigate indirect surface topography measurements, whereas the second to study the replication capability in indirect geometrical measurements. Two materials were milled for both samples: AISI 440 hardened (AISI 440 H, hardness equal to 60 HRC) and AISI 440 annealed (AISI 440 A, hardness equal to 18 HRC). These two stainless steel materials represent a suitable choice for mould manufacturing and were expected to produce different surface topographies in relation to the specific material characteristics, such as grain size and specific cutting force. Being AISI 440 A softer, the risk of ploughing was certainly higher than for AISI 440 H.

8.2.1 Micro milled surfaces

Three types of micro milled surfaces were produced on both materials. A coated WC Round End Mill (Mitsubishi Materials Corporation, Tokyo, Japan) (2 flutes, diameter D_C = 1 mm, corner radius = 0.1 mm and cutting edge radius = 6 µm) was used for the tests on an ultra-high precision KERN Evo micro milling machine. Table 8.1 shows the cutting parameters for the three machined surfaces, which were named S1, S2 and S3.

Table 8.1: Cutting parameters for the three micro milled surfaces. a_e and a_p are the radial and axial depth of cut respectively. v_c is the cutting speed. f_z is the feed per tooth.

Cutting parameter	S1	S2	S3
a_e/D_C	100 % (full slot)	30 % (overlapped)	30 % (finished)
a_p/µm	50	50	50
v_c/(m/min)	100	100	100
f_z/µm	12.5	12.5	12.5

S1 was machined in full slot (i.e. with a radial depth of cut a_e equal to 100 % of the mill diameter). Conversely, S2 and S3 were obtained by imposing a 30 % radial depth of cut. S2 designates the overlapped surface area, generated by two subsequent tool passes, whereas S3 was generated by the last mill pass. Figure 8.1 shows a schematic of the surface design. These surfaces represent typical conditions of a mould manufacturing process: S1 conditions are distinctive of roughing operations, in which full slot milling is used to minimize the machining time. On the other hand, S2 and S3 are representative of finishing operations, where the final surface texture of the component is generated using a lower value of the radial depth of cut. As a consequence, S1 surface roughness was expected to be higher than that of S2 and S3. The other milling parameters were kept constant. In particular, the feed per tooth f_z was set at the lowest limit for the selected mill, while the axial depth of cut a_p was 50 µm in all the tests to avoid the onset of chatter conditions which could lead to uncontrolled and defective surface generation due to tool vibrations. The same tool was used to machine all the samples. Two replicates for each surface type, named Sample 1 and Sample 2, were generated on the same steel workpiece (see Figure 8.1 (a)), making six surfaces per material available.

8.2.2 Micro milled geometrical features

Five two-stepped pockets were produced on the two materials to assess the performance of the replication applied to micro milled geometries. These pockets represent a generalization of 2D channels and cavities that often characterize micro moulds.

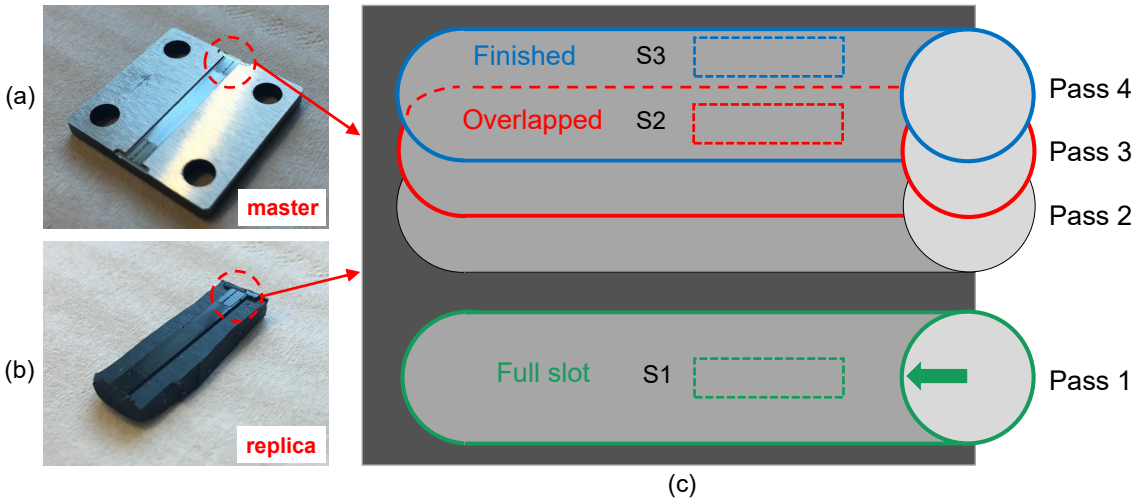

Figure 8.1: Micro milled surfaces and replicas. (a) AISI 440 H sample. (b) Silicone replica. (c) Scheme of the micro milled surfaces. The four mill passes are presented in their machining sequence. The three measured surfaces S1, S2 and S3 are indicated in green, red and blue with dashed lines. The green arrow represents the milling direction.

A WC flat end mill (Sandvik Coromant, Sandviken, Sweden) (2 flutes, diameter = 0.5 mm and cutting edge radius = 6 µm) was used to machine them on the same aforementioned micro milling machine. The cutting parameters (see Table 8.2) were kept constant for all the machined pockets. The same tool was used in all the machining operations.

Table 8.2: Cutting parameters for the five milled pockets.

Cutting parameter	Value
a_e/mm	200
a_p/µm	150
v_c/(m/min)	60
f_z/µm	10

Figure 8.2 shows the geometrical characteristics of the micro milled pockets, which were machined with a nominal constant width. The height of the two steps was instead varied to investigate the replication performance of the silicone media when penetrating geometrical features with different depths. To make the comparison between original and replicated specimens feasible, the depth values were set at a value that allowed the pockets to be measured directly on the metal samples. For the comparison, the width of the milled pockets was selected as the reference for the replication assessment. Therefore, the dimensions $W1$ and $W2$ (see Figure 8.2 (b)) were measured on both metal master and replicated samples and then compared.

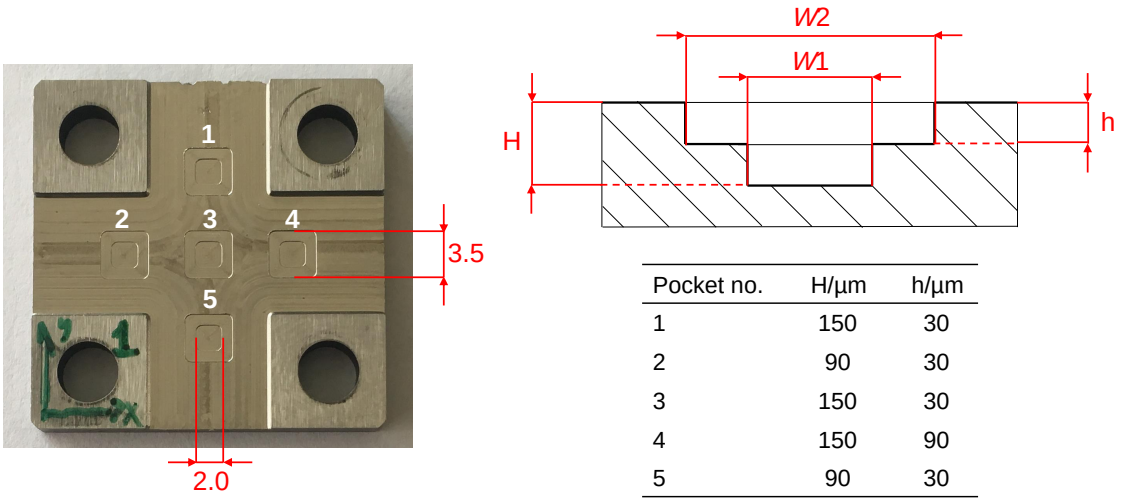

Pocket no.	H/µm	h/µm
1	150	30
2	90	30
3	150	30
4	150	90
5	90	30

(a) (b)

Figure 8.2: (a) Micro milled pockets with nominal width dimensions. (b) Pocket depths and the two measured widths $W1$ and $W2$.

8.2.3 Replication method

After the milling operations, the samples were cleaned from metal debris and dirt particles with ultrasonic cleaning and then blown with filtered air. The black two-component silicone rubber [174] was then poured on the steel masters by using the dedicated dispensing gun. The curing of the replication media was performed at room temperature. After complete solidification, the replicas were carefully removed from the master and prepared for the measurement. To assess the repeatability of the replication, the procedure was repeated three times for each steel sample, resulting in three silicone replicas for each micro milled surface and pocket.

8.2.4 Surface topography measurements and uncertainty evaluation

The surface topography measurements were carried out using a 3D confocal microscope (MarSurf CMW 100 from Mahr GmbH, Göttingen, Germany) with integrated white light interferometer employing a high-power 505 nm LED as light source. The instrument characteristics and selected settings are reported in Table 8.3.

A rectangular area of 1.0 mm × 0.2 mm was acquired for each steel and silicone surface to characterize a significant portion of the texture. To achieve this, a stitching operation of 9 images was performed to acquire the desired extension. The acquisition of a relatively large area allowed performing a more general comparison as well as decreasing the effect of potential relocation errors. The positions of S1, S2 and S3

Table 8.3: MarSurf CMW 100 confocal microscope characteristics.

Properties	Value
Magnification	100×
Field of view/µm	192 × 144
Digital lateral resolution/µm	0.25
Declared vertical resolution/nm	1.0

were uniquely identified by means of a fixed planar reference position defined on both steel and silicone samples. The raw surface acquisitions were post-processed with an image metrology software (MountainsMap®, Digital Surf, Besançon, France): the fitted first order plane was subtracted to ensure a correction for potential tilt. Figure 8.3 shows the appearance of the three different surfaces, which presented the typical characteristic of milled surfaces but with distinct patterns due to the different radial engagements of the tool.

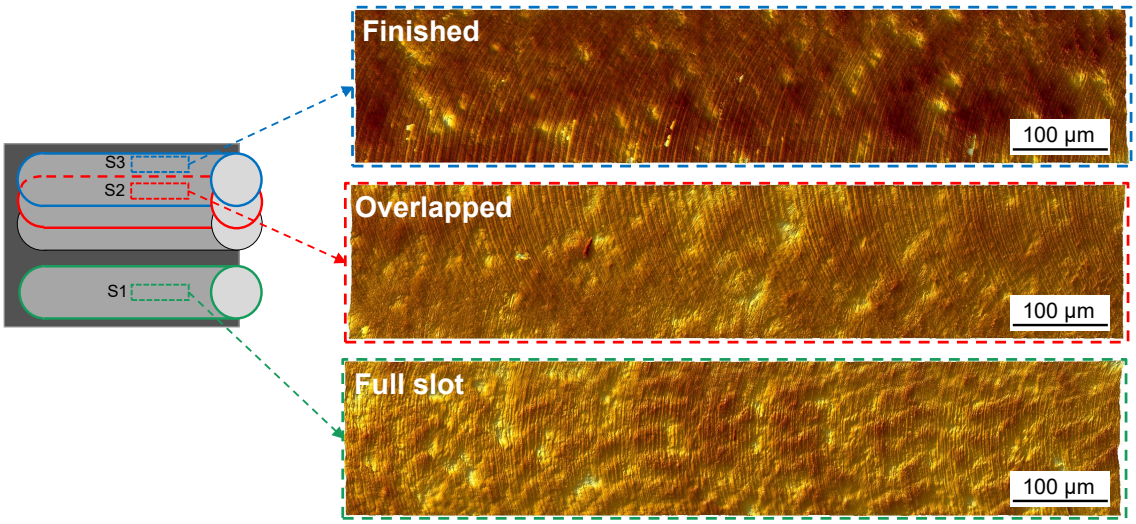

Figure 8.3: The surface texture of the three surfaces (AISI 440 H, Sample 2).

The performance verification of the replica technique was carried out by comparing masters and replicated surfaces using a surface parameter. In this case, the main objective was to assess the replication performance of the two-component silicone media with respect to the vertical profile development, since, given its nanometric variation, it is most critical to replicate. Thus, the arithmetical mean height *Sa* was computed for each surface and then used as the term of comparison. This areal parameter gives an indication about the average areal surface roughness of the surface, being analogous to *Ra* that is used to describe profile measurements [134]. It is defined as:

$$Sa = \frac{1}{A} \iint_A |z(x,y)| \, \mathrm{d}x\mathrm{d}y \tag{8.1}$$

where A represents the finite measured area upon which the height of the surface $z(x,y)$ is defined. Sa was chosen as an indicator since it is suitable for carrying out a general comparison between two surfaces based on their vertical height. No cut-off filter was applied before calculating Sa: the performance replication throughout the entire spatial frequency domain was therefore investigated.

The uncertainty evaluation of the surface roughness measurements was carried out following ISO 15530-3 [119]. In this particular case, a calibrated roughness artefact made of steel (nominal value: $Ra = 480$ nm) was used. The measurement uncertainty related to surface roughness measurements when using the confocal microscope, named u_{CONF}, was calculated as follows:

$$u_{\mathrm{CONF}} = \sqrt{u_{\mathrm{cal}}^2 + u_{\mathrm{p}}^2 + u_{\mathrm{res,CONF}}^2} \tag{8.2}$$

where u_{cal} is the standard calibration uncertainty of the roughness standard; u_{p} represents the standard uncertainty related to the measurement procedure and was calculated as the standard deviation of fifteen repeated measurements on the calibrated standard; and $u_{\mathrm{res,CONF}}$ is the resolution uncertainty related to the declared vertical resolution of the confocal microscope and calculated by assuming a rectangular distribution. To evaluate the uncertainty related to the measurements of the actual measurands, one more source of uncertainty was taken into account: $u_{Sa,\mathrm{mill}}$, the standard deviation of ten repeated Sa measurements on the micro milled samples and on their replicas. Therefore, the expanded uncertainty of surface roughness measurements was calculated as:

$$U_{Sa} = k \times \sqrt{u_{\mathrm{CONF}}^2 + u_{Sa,\mathrm{mill}}^2} \tag{8.3}$$

where k is the coverage factor, equal to 2, for a 95 % confidence interval. $u_{Sa,\mathrm{mill}}$ was calculated for the three materials involved in the study, i.e. AISI 440 H, AISI 440 A and silicone replica. Table 8.4 shows the uncertainty budget. What stands out is that the preponderant uncertainty contribution is the one related to the calibration certificate of the roughness standard artefact.

8.2.5 Geometrical measurements and uncertainty evaluation

The widths measurements of the micro milled pockets were carried out using the focus variation instrument Alicona Infinite Focus with a 10× magnification objective (see Table 2.5 for the detailed characteristics). The area corresponding to the whole pocket was acquired to measure $W1$ and $W2$. In particular, the two measurands were

Table 8.4: Uncertainty contributions for the *Sa* roughness measurements of the masters and replicated surfaces.

Uncertainty contribution	AISI 440 H	AISI 440 H	Silicone
u_{cal}/nm	11.0	11.0	11.0
u_{p}/nm	2.1	2.1	2.1
$u_{\mathrm{res,CONF}}$/nm	0.3	0.3	0.3
u_{CONF}/nm	11.2	11.2	11.2
$u_{Sa,\mathrm{mill}}$/nm	3.7	3.9	4.7
U_{Sa}/nm	24	24	24

assessed using cross-sectional profiles (see Figure 8.4): one thousand parallel profiles were extrapolated from the entire acquisition and averaged using the software SPIP 6.7.3 (Image Metrology A/S, Hørsholm, Denmark). The width was then measured as the horizontal distance between the two points corresponding to the upper edge of the vertical walls of the pocket.

The uncertainty was evaluated using the same method applied for surface roughness measurements. In this case, a calibrated gauge block of 1.5 mm was selected as calibrated artefact. The measurement uncertainty related to the width measurements using the focus variation instrument u_{FV} was calculated as:

$$u_{\mathrm{FV}} = \sqrt{u_{\mathrm{cal}}^2 + u_{\mathrm{p}}^2 + u_{\mathrm{res,FV}}^2} \tag{8.4}$$

where u_{cal} is the standard calibration uncertainty of the roughness standard and $u_{\mathrm{res,FV}}$ is the resolution uncertainty related to the 2.0 µm lateral resolution of the focus variation microscope. The expanded uncertainty was determined by adding the contributions of the micro milled samples:

$$U_W = k \times \sqrt{u_{\mathrm{FV}}^2 + u_{W,\mathrm{mill}}^2} \tag{8.5}$$

where k is the coverage factor, equal to 2, for a 95 % confidence interval and $u_{W,\mathrm{mill}}$ is the standard deviation of ten repeated width measurements on the micro milled metal and silicone samples. As for *Sa* measurements, this last contribution was determined for the three materials under investigation. U_W was applied to the measurements of both $W1$ and $W2$ since the standard deviations of their measurement results were equal for all the materials. Table 8.5 reports the uncertainty budget.

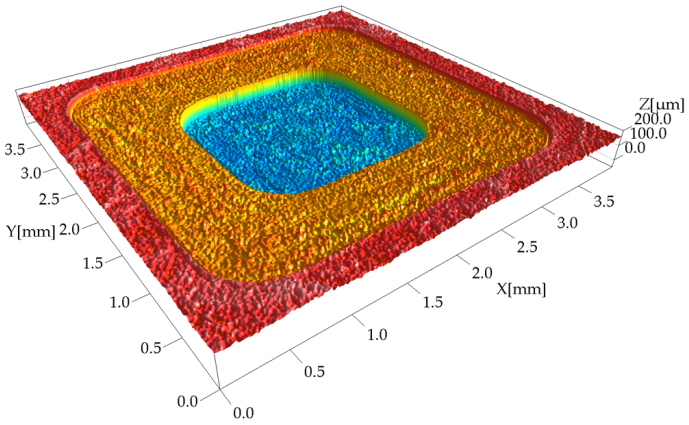

(a)

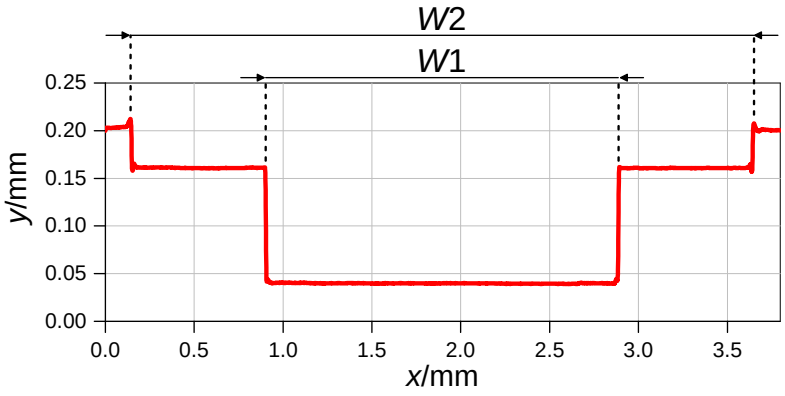

(b)

Figure 8.4: (a) Acquired 3D micro milled pocket (AISI 440 H, Pocket 3). (b) Average pocket profile and measurement of $W1$ and $W2$.

Table 8.5: Uncertainty contributions for $W1$ and $W2$ measurements of the masters and replicated pockets.

Uncertainty contribution	AISI 440 H	AISI 440 H	Silicone
$u_{\mathrm{cal}}/\mu\mathrm{m}$	0.5	0.5	0.5
$u_{\mathrm{p}}/\mu\mathrm{m}$	0.7	0.7	0.7
$u_{\mathrm{res,FV}}/\mu\mathrm{m}$	0.6	0.6	0.6
$u_{\mathrm{FV}}/\mu\mathrm{m}$	1.0	1.0	1.0
$u_{W,\mathrm{mill}}/\mu\mathrm{m}$	1.2	1.1	1.5
$U_W/\mu\mathrm{m}$	3.1	3.0	3.6

8.3 Results and discussion

8.3.1 Replication of surface topography

The replicated surfaces showed a good resemblance with the masters. The marks created by the micro tool passes were reproduced with fidelity in their finest details (see Figure 8.5), as for instance local discontinuities in the texture.

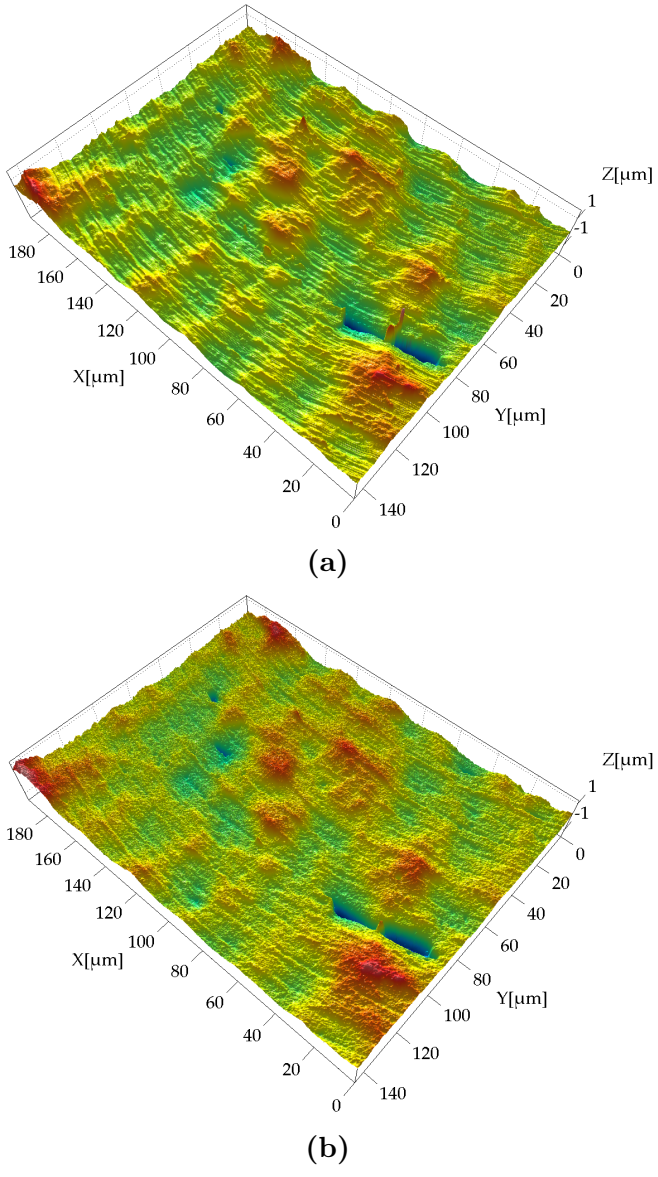

(a)

(b)

Figure 8.5: Detail of measured surface topography for AISI 440 H, surface S1, Sample 1: (a) metal master and (b) silicone replica. The original silicone acquisition was inverted with respect to the x- and z-axes to facilitate the visual comparison.

Figure 8.6 shows the surface roughness results for AISI 440 H. For both Sample 1 and Sample 2, the direct measurement showed a decreasing *Sa* when moving from the full slot surface (S1) to the other ones (S2 and S3). This is according to expectations, as S1 was machined in the cutting conditions that are typical of roughing operations. *Sa* measured on the master surfaces ranged between 55 and 96 nm. A certain variability was observed: Sample 1 had an 11 to 18 nm larger *Sa* compared to Sample 2. This was due to the repeatability of micro milling process since the surfaces were machined in the same cutting conditions on the two samples. The three replicas always had a larger *Sa* with respect to the original surface. However, taking the measurement uncertainty into account, direct and indirect measurements provided, in all the cases, the same *Sa* values. Indeed, the uncertainty intervals overlap, making the measurement outputs equal from a metrological point of view. The standard deviations among the three silicone replicas ranged between 3 and 11 nm, demonstrating that the replication procedure was very repeatable, being these values lower than the measurement uncertainty.

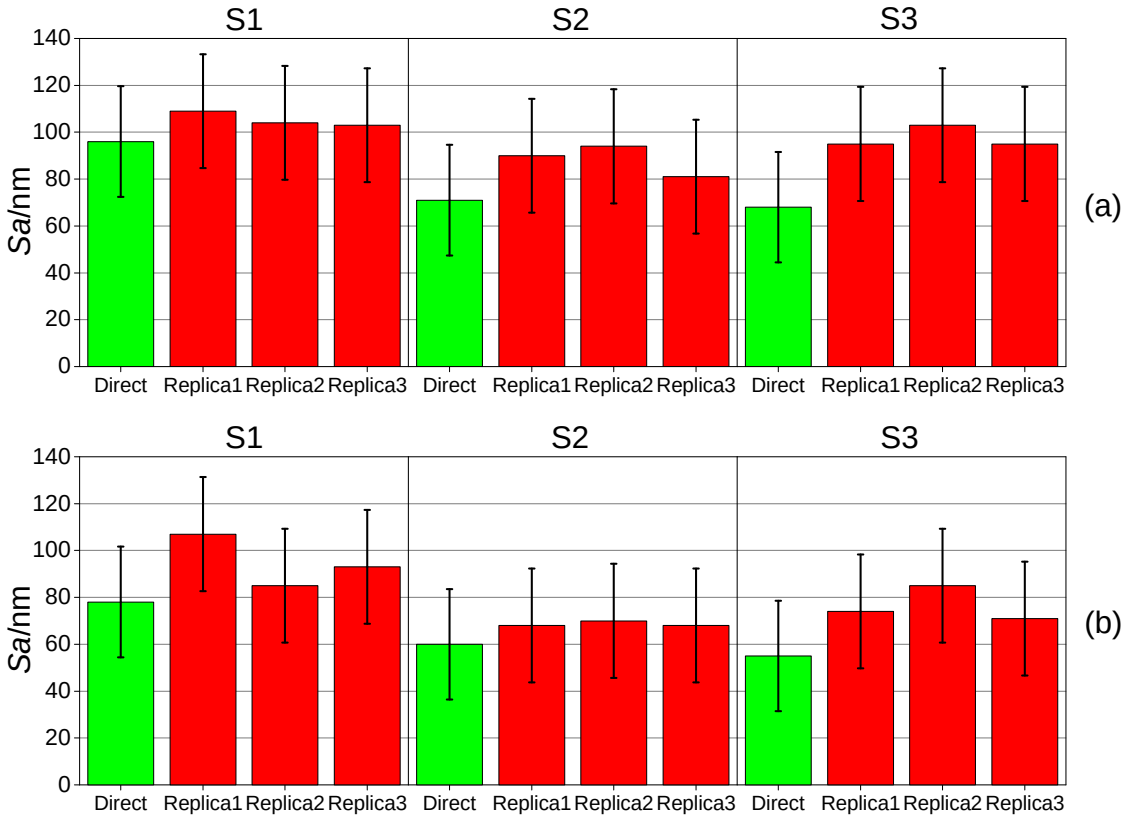

Figure 8.6: *Sa* values measured on master (green) and replicated (red) surfaces for AISI 440 H. The results for S1 (left), S2 (middle) and S3 (right) are shown. (a) Sample 1. (b) Sample 2. The error bars indicate the expanded uncertainty U_{Sa}.

Figure 8.7 shows the results of the *Sa* measurements for AISI 440 A. S1 and S2 were produced with similar *Sa* (ranging between 61 and 74 nm for the two samples), while S3 had a significantly higher *Sa* roughness of around 200 nm. This happened because of the presence of ploughing on the surface, which decreased the surface quality (see Figure 8.8). This event was observed only for S3 because of the material accumulated on the tool during the first three passes. The softness of the annealed material was the factor that enabled the onset of this phenomenon, since no evidence of ploughing was observed for the hardened steel. A certain variability due to the repeatability of the micro milling process was observed again between Sample 1 and Sample 2. When comparing direct and indirect measurements, it stands out that the replication process introduced, as in the previous case, an average overestimation of the surface roughness of the master. However, as for AISI 440 H, the uncertainty intervals of direct and indirect measurements overlap in most cases, except for Replica 2 of S3, Sample 1 and Replica 3 of S1, Sample 2. The replication process was again very repeatable: the three different replicas always provided the same measurement output, being the standard deviations among the three indirect measurements in the range 7 to 15 nm and thus lower than U_{Sa} .

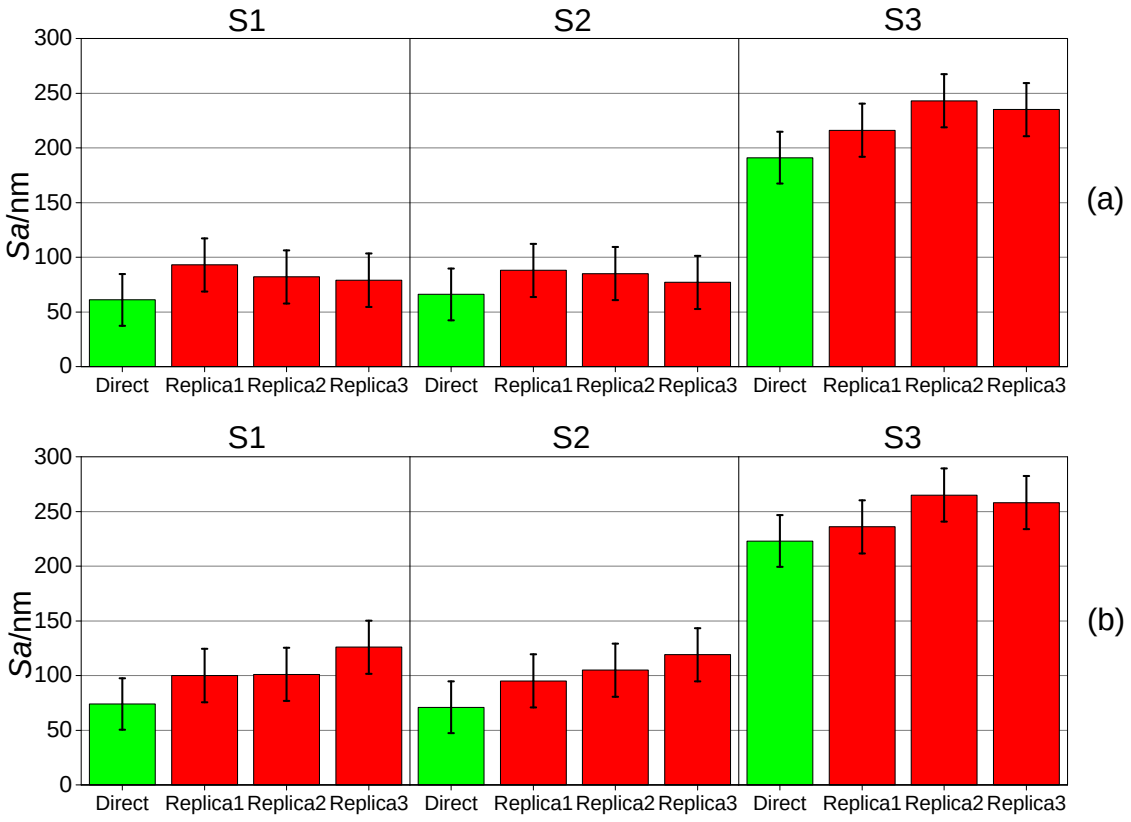

Figure 8.7: *Sa* values measured on master (green) and replicated (red) surfaces for AISI 440 A. The results for S1 (left), S2 (middle) and S3 (right) are shown. (a) Sample 1. (b) Sample 2. The error bars indicate the expanded uncertainty U_{Sa}.

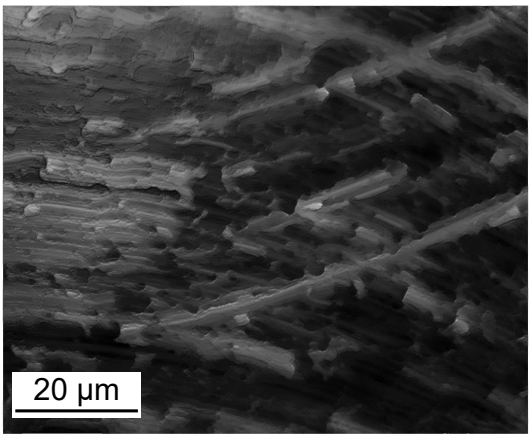

Figure 8.8: Ploughed marks on surface S3 of AISI 440 A, Sample 2.

The replication procedure introduced, in all replication experiments, an overestimation of the master roughness for both the hardened and annealed steel. The deviation Δ_{Sa}, defined as the difference between average *Sa* of the three replicas and *Sa* of the master, did not show any dependence on the master roughness (see Figure 8.9). In fact, Δ_{Sa} remained mostly constant around the value of 24 nm. This fact proves that there was not a dependence of the replication performance with respect to the two samples, the two materials and the three surface types, as also shown by the ANOVA results in Table 8.6. The *p*-values are in fact much larger than 5 % for both single factors and two-way interactions, demonstrating that Δ_{Sa} was not significantly affected by the analysed experimental variables.

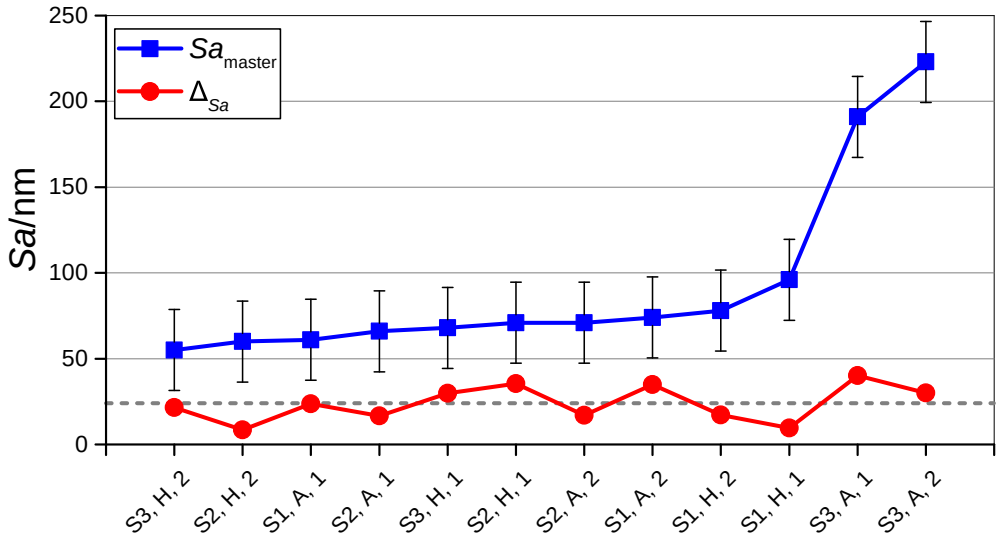

Figure 8.9: *Sa* values for master surfaces and deviations $\Delta_{Sa} = Sa_{\text{replica}} - Sa_{\text{master}}$. The dashed grey line represents the average overestimation that was equal to 24 nm. The *x*-axis shows the surface type (S1, S2 or S3), material (H or A) and Sample (1 or 2).

Table 8.6: ANOVA table of Δ_{Sa}.

Factor	Adj. MS	F-value	p-Value
Material	136.5	2.2	0.27
Surface type	137.7	2.3	0.31
Sample	57.7	1.0	0.43
Material × Surface type	115.8	1.9	0.34
Material × Sample	71.2	1.2	0.39
Surface type × Sample	145.2	2.4	0.30
Error	60.8		

Other areal parameters were taken into account to understand which roughness component caused the *Sa* overestimation. In particular, the functional parameters *Svk*, *Spk* and *Sk* were calculated and compared for masters and replicas. *Svk* is defined as the reduced dale height, and it provides an average indication of the depth of the valleys below the core roughness [134]. *Spk* is the reduced peak height and represents the mean height of peaks above the core surface [134]. *Sk* is used to characterize the core surface roughness [134]. To analyse how the silicone media replicated the valleys of the micro milled surfaces, the value of *Svk* calculated for the masters was compared to the *Spk* value of the corresponding replicas since a valley on the master corresponds to a peak on the replica and vice versa. The core roughness parameter *Sk* was also used as a parameter of comparison to determine whether the overestimation of the indirect *Sa* measurements was also due to its increase.

Figure 8.10 shows the results of the comparison. What stands out is that the *Svk* values of the master were systematically lower than the *Spk* values of the correspondent replicated surfaces. In particular, the *Spk* of the replicas was on average 60 % higher than the *Svk* of the masters. This proves that the replication procedure generated surfaces having peaks that were higher than the valleys of the master. The same happened for *Sk*: the indirect measurements provided an average 63 % higher level of *Sk* for all the produced surfaces, demonstrating that the core roughness was also increased through the replication procedure. Thus, the *Sa* overestimation of the indirect measurements was caused by two distinct phenomena: the increase of the height of the peaks with respect to depths of the valleys and the increase of the core roughness. These phenomena were most probably generated during the demoulding phase of the replica, in which the silicone material was detached from the milled sample. At first, during solidification, the replication media penetrated into the master surface valleys. When the solidified replica was manually removed, the silicone stuck to the deepest points of the valleys because of their extremely small width, making its removal more difficult than in other areas. Thus, the manual removal caused a nanometric stretch perpendicular to the average plane of the surface, which resulted in the observed increase of both dale height and core roughness. This also explains why the overestimation was almost constant (see Figure 8.9): the manual removal acted as an external factor, and, as such, was

not influenced by any of the experimented variables. Another evidence is given by the Kurtosis parameter *Sku* [134], which provides a quantitative evaluation of the sharpness of the surface roughness profile. The replicated surfaces had an average 23 % higher *Sku* value, demonstrating that they were characterized by a sharper profile than that of the masters, as a consequence of the stretch induced by the manual removal.

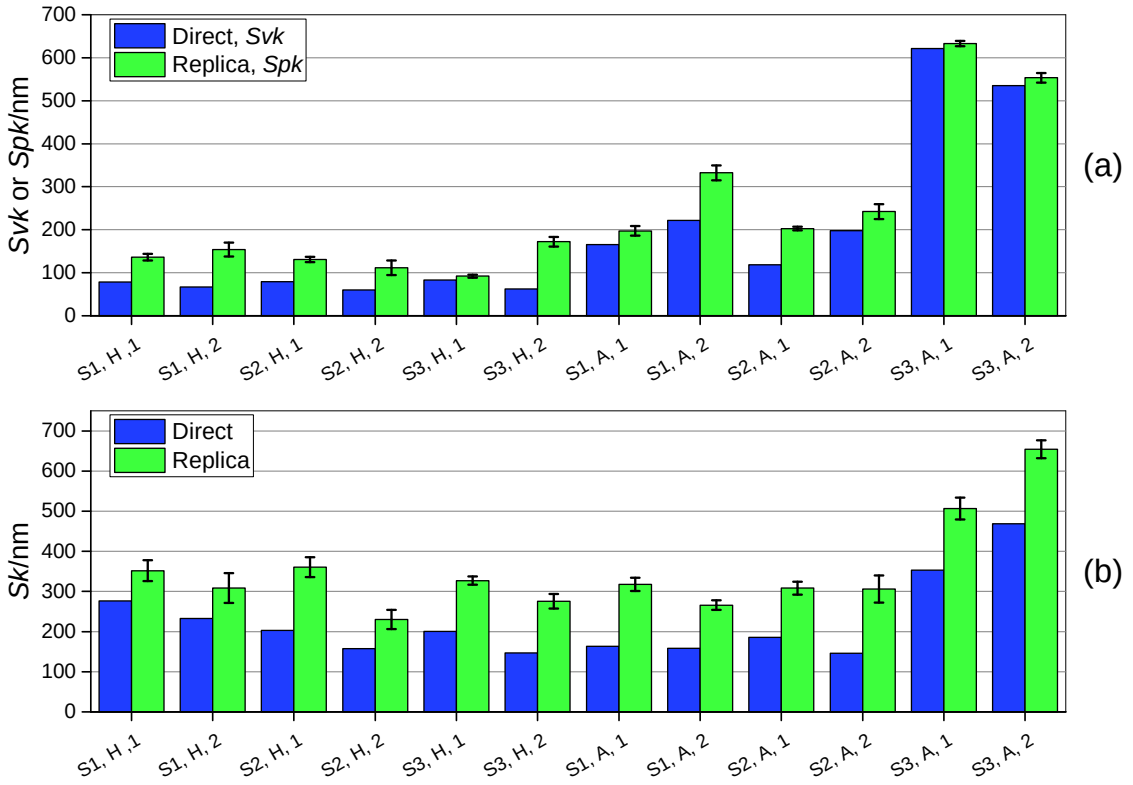

Figure 8.10: Functional roughness parameters calculated on master (blue) and replicated (green) samples. (a) *Svk* and *Spk* values for masters and replicas respectively. (b) *Sk* values. The interval bars indicate the standard deviations calculated among the three produced replicas. The x-axis indicates the surface type (S1, S2 or S3), material (H or A) and Sample (1 or 2).

8.3.2 Replication of geometries

The micro milled pockets and their silicone replicas had a very similar shape. In particular, the silicone material was capable of replicating the geometry of the vertical walls accurately, since no trace of any tilt, which could have been introduced by differential shrinkage, was observed (see Figure 8.11).

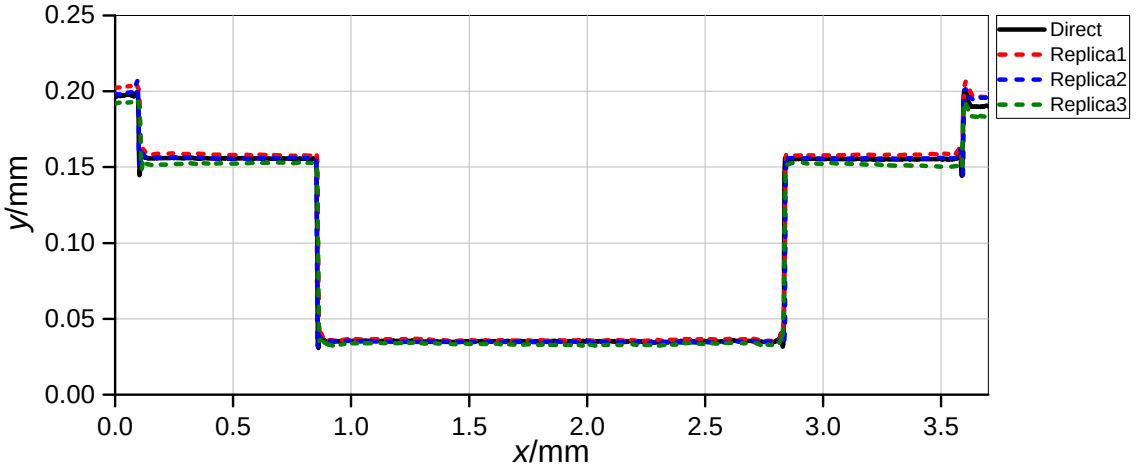

Figure 8.11: Profiles of master and replicated micro milled pockets. Original silicone acquisitions were inverted with respect to the y-axis in order to facilitate the visual comparison.

Figure 8.12 shows the results of the width measurements made on the AISI 440 H sample. The five steel micro milled pockets had an almost constant $W1$, while $W2$ results were more variable. It can be seen that the indirect measurement generally provided a lower value for both the measurands, as in only 10 % of the cases the indirect evaluation generated an overestimation of $W1$ and $W2$. Direct and indirect measurements provided the same output (i.e. the uncertainty intervals overlap) in 53 % of the comparisons for $W1$ and in 40 % for $W2$, demonstrating that the replication performance was better for the measurement of the inner geometry of the pockets. The average standard deviation, calculated among the three replicas and for the five pockets, was equal to 5 µm for $W1$ and to 9 µm for $W2$. Thus, it can be concluded that $W1$ was replicated more accurately and precisely than $W2$.

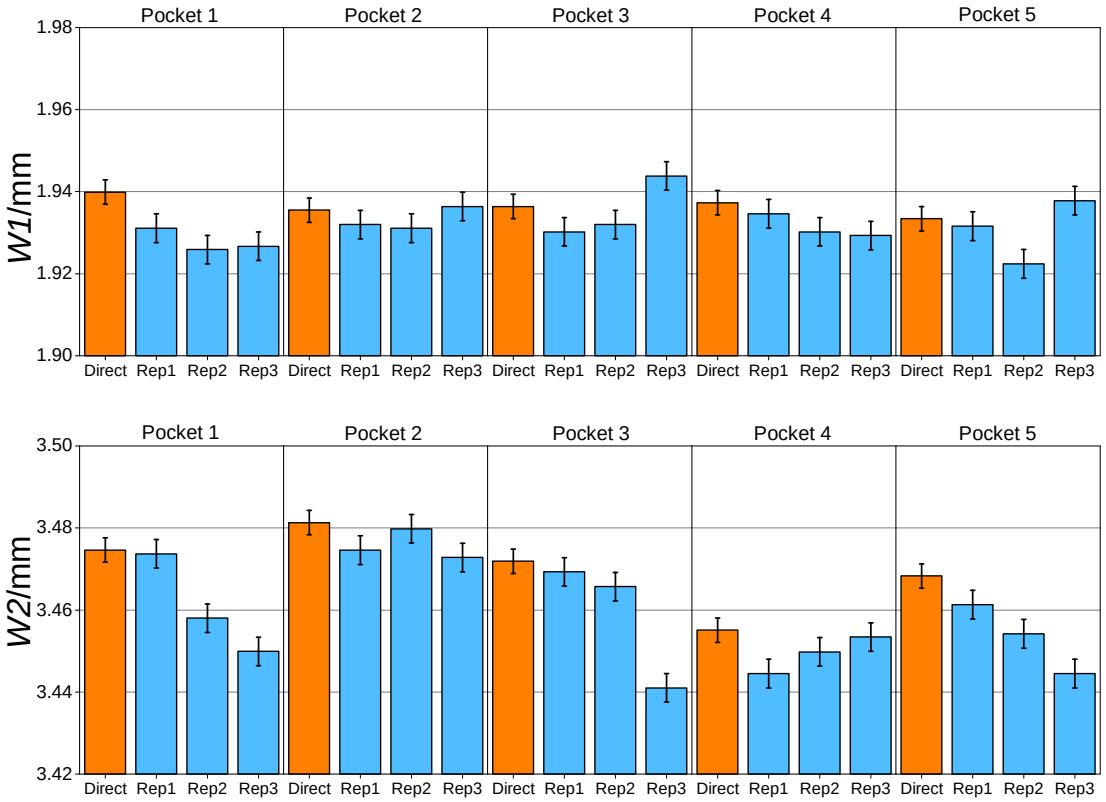

Figure 8.12: $W1$ and $W2$ measured on master (orange) and replicated (blue) pockets for AISI 440 H. The error bars represent the uncertainty U_W.

Figure 8.13 shows the results for the AISI 440 A sample. As for the hardened material, the replication generally introduced an underestimation of the original micro milled geometry: only in one case out of 30 the width of the replicated specimen was larger than that of the master. The uncertainty intervals of direct and indirect measurements overlap in 67 % of the cases for $W1$ and in 47 % of the cases for $W2$. Average standard deviations of 3 µm and 8 µm were observed for $W1$ and $W2$ respectively. Therefore, the replication performance was similar for the two steels and, once again, a better replication was achieved for the internal width of the pockets.

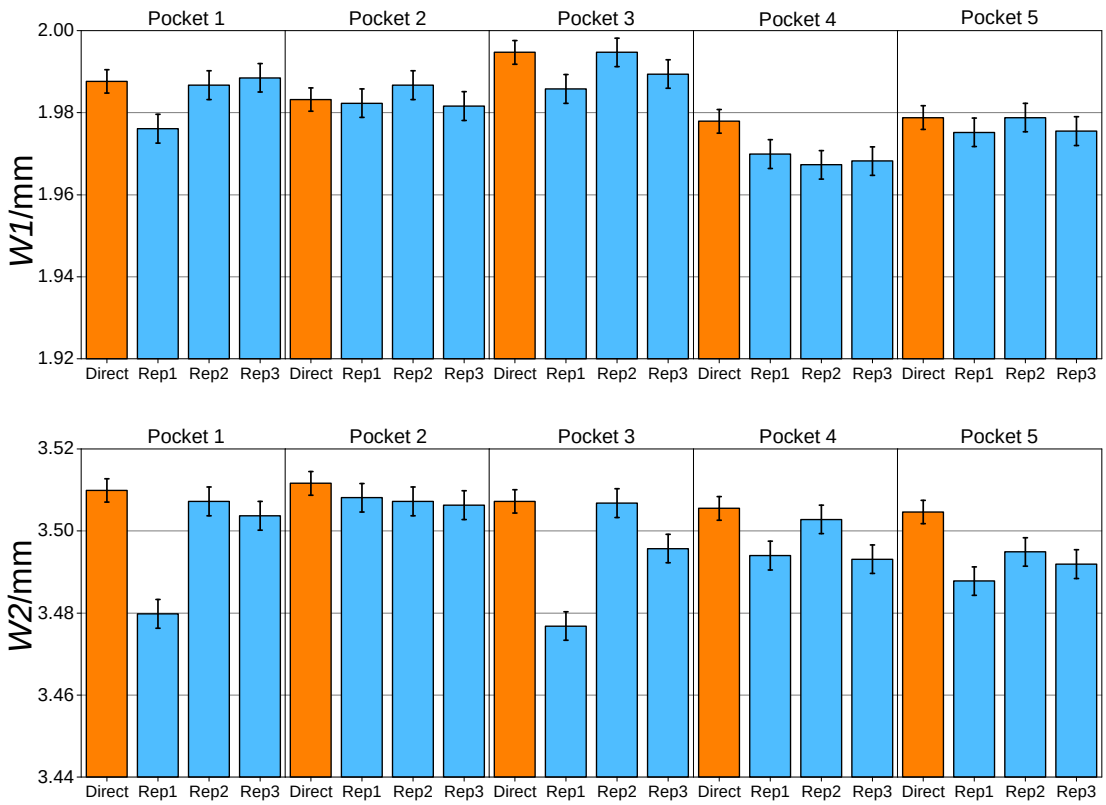

Figure 8.13: $W1$ and $W2$ measured on master (orange) and replicated (blue) pockets for AISI 440 A. The error bars represent the uncertainty U_W.

Figure 8.14 shows the results in terms of deviation Δ_W, calculated as the difference between direct and indirect measurement outputs, while Table 8.7 presents the ANOVA results. The replication performance did not depend on the material of the master, as the p-value was larger than 5 % for this experimental factor. The same conclusion can be drawn for the five pockets: the replication performance was unaffected by the different depth of the micro milled geometries, proving that the penetration of the silicone media was not hindered by a larger depth of the inner step of the investigated pocket. Conversely, the fidelity of the replicas was greatly affected by the type of measurand. When measuring $W2$, the deviation was on average 8 µm larger than when measuring $W1$. This strongly suggests that the silicone media better replicates geometries that are more internal with respect to the outer surface on which it is casted. This observation could also be explained by hypothesizing a linear shrinkage of the silicone material with respect to the replicated micro milled dimensions, being $W1$ smaller than $W2$.

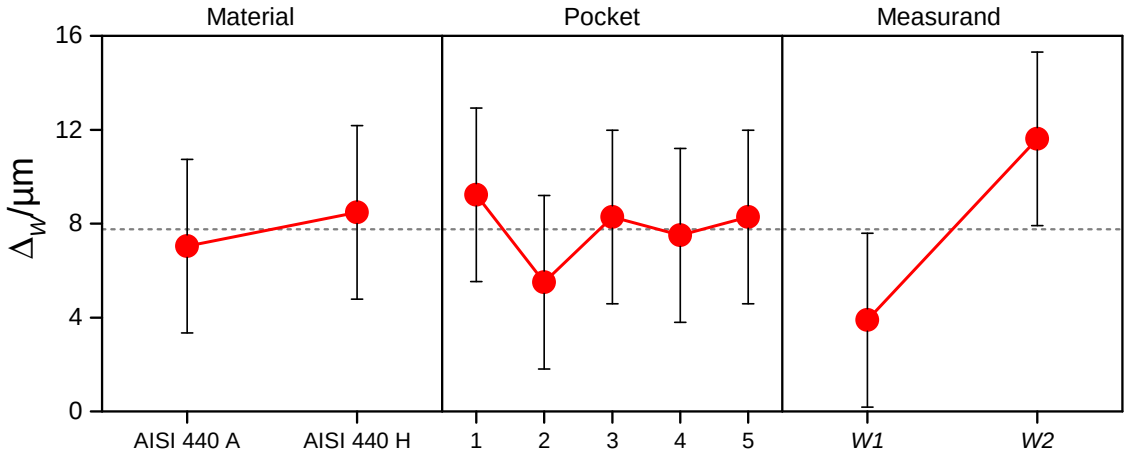

Figure 8.14: Main effects plot for the deviation $\Delta_W = W_{\text{master}} - W_{\text{replica}}$. The error bars indicate the measurement uncertainty of Δ_W.

Table 8.7: ANOVA table of Δ_W.

Factor	Adj. MS	F-value	p-Value
Material	32.2	0.6	0.46
Pocket	42.2	0.8	0.57
Measurand	800.2	14.1	0.00
Material × Pocket	56.9	1.0	0.42
Material × Measurand	5.6	0.1	0.76
Pocket × Measurand	69.8	1.2	0.31
Error	56.7		

To characterize the behaviour of the silicone when replicating geometrical features and verify the hypothesis of linear shrinkage, the shrinkage parameter s_W was calculated as:

$$s_W = \frac{W_{\text{master}} - W_{\text{replica}}}{W_{\text{master}}} \tag{8.6}$$

where W_{master} and W_{replica} are the width measurements of master and replica respectively. For both $W1$ and $W2$, the average s_W was equal to 0.27 % ± 0.03 %, where the last value represents the expanded uncertainty value calculated by means of the law of propagation of errors. Being s_W equal for both the measurand, it can be concluded that the shrinkage behaviour of the silicone was indeed linear with respect to the master dimensions. This parameter is particularly useful since it gives clear indication on what is the relative underestimation introduced by the replication procedure when measuring micro milled geometries. It can be used to determine the

dimension of the master when only an indirect measurement is available, provided that the uncertainty value of the shrinkage is taken into account.

8.4 Summary and conclusions

The replication performance of a commercial silicone replica media applied as an indirect measurement tool for micro milled components was investigated. Particular interest was paid to the applicability of this method to the measurement of inaccessible features that are often present in micro moulds used in µIM.

The replication capabilities related to surface texture and geometries were assessed separately with two micro milled samples for two different mould steels. The samples were designed in order to allow a comparison between direct and indirect measurements.

The comparison based on surface topography measurements revealed that:

- The silicone replication media was capable of accurately reproducing the appearance and features of the micro milled surface texture, even in the finest details such as mill passes and local discontinuities.
- The indirect *Sa* measurements always overestimated the surface roughness of the replicated master for both steel materials (average overestimation equal to 24 nm), even though the measurement uncertainty was larger than the deviation in 34 cases out of 36.
- The analysis based on the functional areal parameters *Svk*, *Spk* and *Sk* demonstrated that the overestimation introduced by the replication procedure was due to an increase of both core roughness and average peak height.
- Being the overestimation unaffected by the varied experimental conditions, it was concluded that it was caused by an external factor such as the manual detachment of the silicone replicas from the master surface. In particular, the removal generated a stretch of the peaks of the replica, which in turn provided an overall higher surface roughness at the nanometric level.

The comparison based on the measurements of micro milled pockets revealed that:

- The replicated widths of the two-stepped micro milled pockets were generally smaller than the metal masters because of the shrinkage of the silicone media during the curing phase.
- This underestimation was dependent on the type of measurand: the error was 8 µm larger for geometries that were less exposed to the pouring of the replication media, proving that more internal widths were replicated with higher fidelity by the silicone.

- Considering the measurement uncertainty, the direct and indirect width measurements provided the same result in 31 cases out of 60, showing that the replication performance did not allow meeting the target consistently at the micrometric level.
- The shrinkage of the replication media was calibrated and equal to 0.27 % ± 0.03 % for both the measured widths, proving that the silicone shrunk linearly with respect to the dimension of the master pocket.
- The value of the shrinkage and its uncertainty can be used to obtain the dimensions of the object when only indirect measurements are available.

9 Conclusions and outlook

9.1 Conclusions

Micro injection moulding is nowadays the preferable technology for micro plastic parts manufacturing. It is assuming more and more significance as the new digital era requires the development of novel and smaller industrial components.

This thesis was dedicated to expanding the state-of-the-art of µIM by studying thoroughly the impact of process variations on the accuracy and precision of the manufactured components and implementing new data-based strategies to achieve in-line quality assurance. In order to eliminate the quality control time based on off-line inspections, which acts as a bottleneck in process chains built around fast replication technologies such as µIM, a novel framework based on product and process fingerprints was defined and applied to two different typologies of micro moulded components, namely a 3D and a nano-structured one. Micro/nano optical metrology and process monitoring were key elements in these studies. The knowledge of µIM was also expanded by characterizing the process when moulding thermoplastic elastomers. µIM simulations models were tested and validated as tools for quality prediction and virtual process optimization. Finally, the applicability of the replica technology to the indirect measurement of micro milled moulds was investigated, thus providing an indication on how to assess surface texture and dimensions of inaccessible features of master inserts.

The achievements of the thesis satisfied the objectives of the project and can be summarized in the answers to the research questions presented in section 1.3.

What is the precision and accuracy of µIM when micro moulding TPE? What are the effects of the main process parameters on the part geometry?

µIM was successfully applied to manufacture TPE micro rings used in high-performance phono-cartridges. A preliminary study based on weld line depth measurements showed that low values of clamping force and injection speed were needed to reduce the defects caused by air entrapments. This finding was taken into account in a DoE investigation, where the effects of main µIM process parameters on the ring diameters were quantified. The process was characterized, demonstrating that a level of precision in the single micrometric digit was attained within the selected

process window along with a consistent multi-cavity production. The outer diameter was influenced mostly by mould temperature and holding pressure, whereas the inner one by mould temperature and melt temperature. A novel behaviour was observed: the two diameters showed an opposite dependence on the investigated parameters, therefore making the simultaneous increase of both geometrical output impossible in the experimented range. Moreover, the inner diameter suffered a larger shrinkage, most probably due to the presence of residual stresses caused by constrained shrinkage at the ring-pin interface. The moulded micro rings were also functionally tested with a specific apparatus: most of the rings passed the tests, apart from some samples having a large inner diameter and small outer diameter, providing useful insights on the impact of µIM parameters on the functionality of the final product. The same technology was also applied in an insert-moulding configuration. This process had the main advantage of reducing the assembly burden by moulding the TPE micro ring onto the metal substrate, thus greatly reducing the production time. Dimensional measurements of diameter and roundness of the overmoulded rings showed that it was not possible to maximize the diameter and minimize its deviation at the same time. The alignment of the overmoulded parts was demonstrated to be very good (alignment angles of circa 0.5° were measured).

How can the product/process fingerprint framework be effectively applied to a 3D micro component?

The product/process fingerprint framework, which aimed at defining an in-line quality assurance strategy, was applied to a 3D micro medical component in POM. DoE and correlation analyses allowed to define the best product fingerprint in the flash area, i.e. the dimensional indicator related to the flash size. Six process fingerprint candidates extracted from in-line monitored injection pressure and velocity curves were selected. No external sensor was employed, as the recordings were extracted from the µIM machine computer. The best one was the mean integral of the pressure during filling, which was influenced by 3 out of the 4 varied µIM parameters. This process fingerprint was also highly correlated to the product fingerprint and to the other main defect affecting the part quality, i.e. the gate mark length.

Is it possible to define a clear in-line quality assurance strategy for this component based on the combination of product and process fingerprints?

Since a correlation among product and process fingerprints was demonstrated, in-line µIM process optimization could be carried out by monitoring the selected indicators, thus setting up an effective quality monitoring strategy based on injection pressure recordings. In particular, the results showed that the mean integral of pressure must be maximized and kept at values of circa 500 bar to mould parts having minimum gate mark size, while the flash size was minimized when moulding in the opposite condition, i.e. with values of the process fingerprint of around 300 bar.

How can the product/process fingerprint framework be applied to the replication of a nano-structured surface?

The product/process fingerprint framework was applied also to a moulded disk in POM and PC featuring a nano-structured surface generated by replicating a laser-structured insert that presented a singe-lay texture made of nano-ripples. The nano scale replication performance of µIM was studied with a DoE campaign and characterized by using *Sq* and *Sdq* areal texture parameters, which acted as product fingerprints. In fact, the calculation of both was proved to be necessary to characterize replication of height and morphology of the nano-ripples, which was dominated by the value of the mould temperature. The in-line monitored data consisted of in-cavity temperature profiles collected using an infrared high-speed camera that imaged the cavity through a lateral opening and a sapphire window. Among five indicators extracted from these curves, the mean temperature during the initial part of the moulding cycle was the mostly correlated to the replication quality, showing that the initial phase of the filling played a primary role with respect to the µIM output. Thus, this variable was selected as process fingerprint, as it was capable of controlling the replication quality for both the moulded materials.

Is it possible to define a clear in-line quality assurance strategy for nano-structured surfaces?

The selected process fingerprint showed a clear relationship with the replication fidelity for both POM and PC, allowing to define a control strategy. In particular, moulding POM with fingerprint values higher than 148 °C was necessary to maximize the replication of the mould nano ripples in both height and morphology.

How can process simulations turn into a useful tool when dealing with the optimization phase of µIM?

µIM process simulations were applied to the case studies of TPE micro rings and 3D micro medical components with the aim of building models capable of predicting the quality of the parts against the variation of multiple process parameters. The software Autodesk Simulation Moldflow Insight was used in both cases to build the models and run the simulations. As regards the micro rings, a 3D model comprising the feed system and the four cavities was used. A calibration procedure was needed to fit the numerical results on the experimental observations. The calibrated model was validated against the effect of the variation of four process parameters on the outer diameter of the rings, being the average deviation between simulation results and real measurements equal to 1.6 µm, a value lower than the measurement uncertainty. This proved that the model can be effectively used to optimize the process in a virtual environment, thus providing significant cost savings. The prediction of the dimensions of the inner diameter was less accurate, most probably due to the lack of a general model capable of taking into account the residual stresses induced by

constrained shrinkage. As regards the 3D medical component, a 3D model was built in order to predict the size of the flash affecting the part quality as well as its dependence on the variation of µIM parameters. The numerical flash overestimated the experimental one by a factor of circa 2. This discrepancy was caused by the underlying simplified assumptions of the numerical finite element model such as neglecting of the mould surface roughness. The model was, on the other hand, validated with respect to the effects of the four µIM parameters, having the slopes of the main effects plot the same sign and very similar magnitude. Thus, the model can be applied to virtually tune the process with the aim of minimizing the size of the main part defect.

What is the accuracy of the replica moulding technology applied to micro milled mould features?

The replication capability of a fast silicone replica media applied to micro milled mould features was studied. Two micro milled samples having features typical of moulds for µIM applications were used: the first was used to assess the replication of surface texture, while the second the replication of width of pockets resembling mould channels. The comparison based on surface texture measurements demonstrated that the silicone was capable of accurately replicating the appearance of the master surface. However, the replicas introduced an overestimation of the surface roughness in the order of tenths of nanometres of *Sa*. This was caused by the manual detachment of the silicone from the replicated specimen. The comparison based on the width of the micro milled pockets showed that the replicated parts were generally smaller than the master. This phenomenon was caused by the shrinkage of the silicone, which shrunk linearly with respect to the master dimension. The level of shrinkage of the media was calibrated in order to provide a reference value that can be used to obtain the original dimension when only the indirect measurement is available.

9.2 Outlook

The results of the investigations carried out throughout the present project provided new knowledge and significant advancements in the field of µIM technology, with a particular focus on dimensional quality control and process optimization. The wide use of machine data perfectly fits the current industrial manufacturing scenario, which is rapidly moving towards a digital framework where sensor data become essential to control and predict the production outputs. Based on the achievements of the work, a variety of new research areas can be now explored:

- As the investigations carried out on µIM of TPE highlighted peculiar phenomena such as substantial shrinkage enhancement due to residual stresses, new research efforts could be dedicated to examining this behaviour in depth. Since it was

also demonstrated, for the first time in literature, the applicability of µIM to the manufacturing of soft high-accuracy micro TPE components, new part geometries have to be tested in order to make the know-how of these materials as developed as that of rigid thermoplastics. By doing so, µIM industrial applications could be substantially extended beyond the current state.

- The product/process fingerprint framework was proved to be a valuable resource for establishing an in-line quality control based on process monitoring. The studies presented in this work allowed defining the procedure of the method and determining the best control strategy for the specific cases studies under analysis. The next steps of the method will involve the actual implementation of the framework in a real µIM production scenario. The main challenge will be related to the in-line data extraction and analysis, as all the calculations must be performed within a single cycle time, which is usually in the order of tenths of seconds. If, on one hand, this issue is relatively easy to tackle for data such as those available from the machine computer (i.e. injection speed and velocity), on the other, the use of in-cavity temperature data is particularly challenging, as high-speed camera recordings need to be processed with a specific software in order to extract the temperature information. A possible solution would be the use of a processing computer with very high computational power that would allow the processing of the thermal images in a short time. Alternatively, the number of monitored shots could be reduced to allow the data processing, thus making the in-line quality assurance only partial.
- The proposed procedures to apply the product/process fingerprint framework were based on the use of machine data and high-speed imaging. Future research should focus on the applicability of different monitoring techniques, such as those based on in-cavity pressure and temperature sensors. When allowed by the part geometry and mould design, different sensor positions should be considered in order to identify the one providing data that are mostly correlated to part quality. The use of multiple sensors would also substantially enlarge the amount of data, thus making the approach more comprehensive and sensitive to process variations.
- In the study on the replication of nano-structured surfaces, two materials with similar viscosity but different molecular structure were tested. The experimental results clearly highlighted differences in replication performance, and it was hypothesized that the molecular weight played a role with this respect. The next step of this investigation should be dedicated to benchmark the replication fidelity of a wider pool of polymers in order to define the physical characteristics that mostly affect the outcome of the µIM process at the nano scale. The results of this study would provide a clear indication on the best typology of polymer to mould when extremely high levels of replication are needed to meet the part functionality.

- The potential of µIM simulations as a tool for virtual quality optimization will require more research. As shown in this thesis, a calibrated model can be used to successfully predict the effect of process variations on a target geometry. However, the model may not be validated with respect to multiple geometries, making the use of multiple specifically calibrated and uncoupled models the possible solution to assess the whole part quality in the virtual domain. As in this project only the size of micrometric dimensions was simulated, new research should be devoted to the prediction of nano structures as well as surface texture. The main challenge related to this task is the level of discretization needed to model the mould surface, which must be measured beforehand and then implemented in the simulation software. Mesh sizes in the order of nanometres should be used, consequently making the computational effort extremely burdensome even with multi-scale meshing approaches.
- The applicability of the replica technology to the indirect measurement of moulds was thoroughly assessed and verified. In this work, only micro milled features were considered. Future research should focus on different micro tooling processes such as µEDM and micro laser machining. The different surface topographies generated by these techniques could, in fact, yield to different conclusions. Therefore, the field in which this method works best could be defined. Multiple replication media should also be tested to define the most suitable tooling-replica combination to use in indirect measurements of inaccessible features.

Bibliography

[1] L. Alting, F. Kimura, H. N. Hansen, and G. Bissacco. "Micro Engineering". In: *CIRP annals* 52.2 (2003), pp. 635–657. DOI: 10.1016/S0007-8506(07)60208-X.

[2] E. B. Brousseau, S. S. Dimov, and D. T. Pham. "Some recent advances in multi-material micro- and nano-manufacturing". In: *International Journal of Advanced Manufacturing Technology* 47.1-4 (2010), pp. 161–180. ISSN: 02683768. DOI: 10.1007/s00170-009-2214-5.

[3] G. Tosello and H. N. Hansen. "Micro-injection-molding". In: *Micro-Manufacturing Engineering and Technology* (2010), pp. 90–113. DOI: 10.1016/B978-0-8155-1545-6.00006-5.

[4] J. Giboz, T. Copponnex, and P. Mélé. "Microinjection molding of thermoplastic polymers: a review". In: *Journal of Micromechanics and Microengineering* 17.6 (2007), R96–R109. ISSN: 0960-1317. DOI: 10.1088/0960-1317/17/6/R02.

[5] G. Tosello. "Precision moulding of polymer micro components". PhD thesis. Technical University of Denmark (DTU), 2008.

[6] H. N. Hansen, K. Carneiro, H. Haitjema, and L. De Chiffre. "Dimensional micro and nano metrology". In: *CIRP Annals - Manufacturing Technology* 55.2 (2006), pp. 721–743. ISSN: 00078506. DOI: 10.1016/j.cirp.2006.10.005.

[7] Microsystems Ltd. *https://microsystems.uk.com/project/lab-on-a-chip-component-with-hologram/*. URL: https://microsystems.uk.com/project/lab-on-a-chip-component-with-hologram/ (visited on 10/08/2018).

[8] *http://www.microman.mek.dtu.dk/*. URL: http://www.microman.mek.dtu.dk/ (visited on 10/09/2018).

[9] V. Goodship. *Pratical guide to injection moulding*. Shawbury, UK: Rapra Technology Limited, 2004. ISBN: 1859574440.

[10] W. Michaeli, H. Greif, G. Kretzschmar, and F. Ehring. *Training in Injection Molding: A Text- and Workbook*. Hanser, 2001. ISBN: 9783446214187.

[11] H. Zhou. *Computer modeling for injection molding : simulation, optimization, and control*. Wiley, 2013. ISBN: 9780470602997.

[12] D. O. Kazmer. *Injection Mold Design Engineering*. München: Carl Hanser Verlag GmbH & Co. KG, 2007. ISBN: 978-3-446-41266-8. DOI: 10.3139/9783446434196.

[13] T. V. Zhiltsova, M. S. A. Oliveira, and J. A. Ferreira. "Integral approach for production of thermoplastics microparts by injection moulding". In: *Journal of Materials Science* 48.1 (2012), pp. 81–94. ISSN: 0022-2461. DOI: 10.1007/s10853-012-6669-7.

[14] B. Whiteside, M. T. Martyn, P. D. Coates, G. Greenway, P. S. Allen, and P. Hornsby. "Micromoulding: process measurements, product morphology and properties". In: *Plastics, Rubber and Composites* 33.1 (2004), pp. 11–17. ISSN: 14658011. DOI: 10.1179/146580104225018346.

[15] H. N. Hansen, R. J. Hocken, and G. Tosello. "Replication of micro and nano surface geometries". In: *CIRP Annals - Manufacturing Technology* 60.2 (2011), pp. 695–714. ISSN: 00078506. DOI: 10.1016/j.cirp.2011.05.008.

[16] Grand View Research. *Polymer Microinjection Molding Market Analysis And Segment Forecasts to 2020*. Tech. rep. San Francisco, CA, USA, 2014. URL: https://www.grandviewresearch.com/industry-analysis/polymer-microinjection-molding-industry.

[17] U. M. Attia and J. R. Alcock. "A review of micro-powder injection moulding as a microfabrication technique". In: *Journal of Micromechanics and Microengineering* 21.4 (2011), pp. 1–22. ISSN: 0960-1317. DOI: 10.1088/0960-1317/21/4/043001.

[18] M. Philipp-Pichler. "MicroPower". In: *ATV-SEMAPP: Miro-Nano Moulding Technologies and Applications*. Odense, Denmark: ATV-SEMAPP, 2015.

[19] P. Bangert, P. Cajaraville, B. Dormann, M. Köhler, P. Imgrund, J. Haack, J. Volkert, O. Lopez, P. Rodriguez, L. Martinez, and N. Salk. "Real-Time Quality Control of Injection Molding". In: *XIX Conference on Machine Tools and Manufacturing Technologies*. San Sebastian, Spain, 2012.

[20] G. Bissacco, H. N. Hansen, and L. De Chiffre. "Micromilling of hardened tool steel for mould making applications". In: *Journal of Materials Processing Technology* 167.2-3 (2005), pp. 201–207. ISSN: 09240136. DOI: 10.1016/j.jmatprotec.2005.05.029.

[21] P. Parenti, D. Masato, M. Sorgato, G. Lucchetta, and M. Annoni. "Surface footprint in molds micromilling and effect on part demoldability in micro injection molding". In: *Journal of Manufacturing Processes* 29 (2017), pp. 160–174. ISSN: 15266125. DOI: 10.1016/j.jmapro.2017.05.024.

[22] Q. Su and M. D. Gilchrist. "Demolding forces for micron sized features during micro-injection molding". In: *Polymer Engineering & Science* 56.7 (2016), pp. 810–816. ISSN: 00323888. DOI: 10.1002/pen.24309.

[23] F. Regi, J. B. Nielsen, D. Li, Y. Zhang, J. R. Frisvad, H. Aanæs, and G. Tosello. "A method for the characterization of the reflectance of anisotropic functional surfaces". In: *Surface Topography: Metrology and Properties* 6.3 (2018), p. 034005. ISSN: 2051-672X. DOI: 10.1088/2051-672X/aac373.

[24] J. Valentinčič, G. Bissacco, and S. Bigot. "Snapshot of micro EDM technology for industry". In: *International Conferences on Multi-material Micro Manufacture, 4m/international Conferences on Micro Manufacturing, Icomm*. 2009. DOI: 10.1243/17547164C0012009088.

[25] Q. Su, N. Zhang, and M. D. Gilchrist. "The use of variotherm systems for microinjection molding". In: *Journal of Applied Polymer Science* 133.9 (2016). ISSN: 00218995. DOI: 10.1002/app.42962.

[26] B. Saha, W. Q. Toh, E. Liu, S. B. Tor, D. E. Hardt, and J. Lee. "A review on the importance of surface coating of micro/nano-mold in micro/nano-molding processes". In: *Journal of Micromechanics and Microengineering* 26.1 (2016), p. 013002. ISSN: 0960-1317. DOI: 10.1088/0960-1317/26/1/013002.

[27] G. Lucchetta, D. Masato, M. Sorgato, L. Crema, and E. Savio. "Effects of different mould coatings on polymer filling flow in thin-wall injection moulding". In: *CIRP Annals - Manufacturing Technology* 65.1 (2016), pp. 537–540. ISSN: 17260604. DOI: 10.1016/j.cirp.2016.04.006.

[28] K. Awati, Y. Park, E. Weisser, and M. Mackay. "Wall slip and shear stresses of polymer melts at high shear rates without pressure and viscous heating effects". In: *Journal of Non-Newtonian Fluid Mechanics* 89.1-2 (2000), pp. 117–131. ISSN: 03770257. DOI: 10.1016/S0377-0257(99)00037-3.

[29] N. Zhang and M. Gilchrist. "Characterization of thermo-rheological behavior of polymer melts during the micro injection moulding process". In: *Polymer Testing* 31.6 (2012), pp. 748–758. ISSN: 01429418. DOI: 10.1016/j.polymertesting.2012.04.012.

[30] S. G. Hatzikiriakos. "Wall slip of molten polymers". In: *Progress in Polymer Science* 37.4 (2012), pp. 624–643. ISSN: 00796700. DOI: 10.1016/j.progpolymsci.2011.09.004.

[31] C. Yang, X.-H. Yin, and G.-M. Cheng. "Microinjection molding of microsystem components: new aspects in improving performance". In: *Journal of Micromechanics and Microengineering* 23.9 (2013), pp. 1–21. ISSN: 0960-1317. DOI: 10.1088/0960-1317/23/9/093001.

[32] M. Sorgato, D. Masato, G. Lucchetta, and L. Orazi. "Effect of different laser-induced periodic surface structures on polymer slip in PET injection moulding". In: *CIRP Annals* 67.1 (2018), pp. 575–578. ISSN: 17260604. DOI: 10.1016/j.cirp.2018.04.102.

[33] D. Yao and B. Kim. "Scaling Issues in Miniaturization of Injection Molded Parts". In: *Journal of Manufacturing Science and Engineering* 126.November (2004), p. 733. ISSN: 10871357. DOI: 10.1115/1.1813479.

[34] C. S. Chen, S. C. Chen, W. L. Liaw, and R. D. Chien. "Rheological behavior of POM polymer melt flowing through micro-channels". In: *European Polymer Journal* 44.6 (2008), pp. 1891–1898. ISSN: 00143057. DOI: 10.1016/j.eurpolymj.2008.03.007.

[35] J. Giboz, T. Copponnex, and P. Mélé. "Microinjection molding of thermoplastic polymers: morphological comparison with conventional injection molding". In: *Journal of Micromechanics and Microengineering* 19.2 (2009), p. 025023. ISSN: 0960-1317. DOI: 10.1088/0960-1317/19/2/025023.

[36] F. Liu, C. Guo, X. Wu, X. Qian, H. Liu, and J. Zhang. "Morphological comparison of isotactic polypropylene parts prepared by micro-injection molding and conventional injection molding". In: *Polymers for Advanced Technologies* 23.3 (2012), pp. 686–694. ISSN: 10427147. DOI: 10.1002/pat.1946.

[37] F. Baruffi, A. Charalambis, M. Calaon, R. Elsborg, and G. Tosello. "Comparison of micro and conventional injection moulding based on process precision and accuracy". In: *Procedia CIRP* 75 (2018), pp. 149–154. ISSN: 22128271. DOI: 10.1016/j.procir.2018.04.046.

[38] F. Baruffi, A. Charalambis, K. Vellaiappan, and K. Venetis. "Comparison of conventional and micro injection moulding technologies for the manufacturing of a micro TPE component for sensor applications". Report for the course "Experimental Plastics Technologies - 41972". Technical University of Denmark, 2017.

[39] X. J. Jiang and D. J. Whitehouse. "Technological shifts in surface metrology". In: *CIRP Annals - Manufacturing Technology* 61.2 (2012), pp. 815–836. ISSN: 00078506. DOI: 10.1016/j.cirp.2012.05.009.

[40] Y. Yang, B. Yang, S. Zhu, and X. Chen. "Online quality optimization of the injection molding process via digital image processing and model-free optimization". In: *Journal of Materials Processing Technology* 226 (2015), pp. 85–98. ISSN: 09240136. DOI: 10.1016/j.jmatprotec.2015.07.001.

[41] D. Masato, M. Sorgato, and G. Lucchetta. "Analysis of the influence of part thickness on the replication of micro-structured surfaces by injection molding". In: *Materials & Design* 95 (2016), pp. 219–224. ISSN: 02641275. DOI: 10.1016/j.matdes.2016.01.115.

[42] G. Lucchetta, M. Sorgato, S. Carmignato, and E. Savio. "Investigating the technological limits of micro-injection molding in replicating high aspect ratio micro-structured surfaces". In: *CIRP Annals - Manufacturing Technology* 63.1 (2014), pp. 521–524. ISSN: 00078506. DOI: 10.1016/j.cirp.2014.03.049.

[43] D. Masato, M. Sorgato, P. Parenti, M. Annoni, and G. Lucchetta. "Impact of deep cores surface topography generated by micro milling on the demolding force in micro injection molding". In: *Journal of Materials Processing Tech.* 246 (2017), pp. 211–223. ISSN: 09240136. DOI: 10.3850/978-981-11-0749-8.

[44] G. Tosello, H. N. Hansen, and S. Gasparin. "Applications of dimensional micro metrology to the product and process quality control in manufacturing of precision polymer micro components". In: *CIRP Annals - Manufacturing Technology* 58.1 (2009), pp. 467–472. ISSN: 00078506. DOI: 10.1016/j.cirp.2009.03.027.

[45] R. Surace, V. Bellantone, G. Trotta, V. Basile, F. Modica, and I. Fassi. "Design and Fabrication of a Polymeric Microfilter for Medical Applications". In: *Journal of Micro and Nano-Manufacturing* 4.1 (2015), p. 011006. ISSN: 2166-0468. DOI: 10.1115/1.4032035.

[46] X. Mendibil, I. Llanos, H. Urreta, and I. Quintana. "In process quality control on micro-injection moulding: the role of sensor location". In: *The International Journal of Advanced Manufacturing Technology* (2016). ISSN: 0268-3768. DOI: 10.1007/s00170-016-9300-2.

[47] J. M. Stormonth-Darling, R. H. Pedersen, C. How, and N. Gadegaard. "Injection moulding of ultra high aspect ratio nanostructures using coated polymer tooling". In: *Journal of Micromechanics and Microengineering* 24.7 (2014), p. 075019. ISSN: 0960-1317. DOI: 10.1088/0960-1317/24/7/075019.

[48] V. Speranza, S. Liparoti, M. Calaon, G. Tosello, R. Pantani, and G. Titomanlio. "Replication of micro and nano-features on iPP by injection molding with fast cavity surface temperature evolution". In: *Materials and Design* 133 (2017), pp. 559–569. ISSN: 18734197. DOI: 10.1016/j.matdes.2017.08.016.

[49] F. B. Hasnaes, G. Tosello, M. Calaon, R. Elsborg, and H. N. Hansen. "Investigation of air entrapment and weld line defects in micro injection mouded thermoplastic elastomer micro rings". In: *4M/Iccom 2015*. Milan, Italy, 2015, pp. 978–981. ISBN: 9789810946098. DOI: 10.3850/978-981-09-4609-8.

[50] G. Tosello, A. Gava, H. N. Hansen, and G. Lucchetta. "Study of process parameters effect on the filling phase of micro-injection moulding using weld lines as flow markers". In: *International Journal of Advanced Manufacturing Technology* 47.1-4 (2010), pp. 81–97. ISSN: 02683768. DOI: 10.1007/s00170-009-2100-1.

[51] S. Ontiveros, J. A. Yagüe-Fabra, R. Jiménez, G. Tosello, S. Gasparin, A. Pierobon, S. Carmignato, and H. N. Hansen. "Dimensional measurement of micro-moulded parts by computed tomography". In: *Measurement Science and Technology* 23.12 (2012), p. 125401. ISSN: 0957-0233. DOI: 10.1088/0957-0233/23/12/125401.

[52] M. La, J. G. Lee, and S. J. Park. "Numerical and experimental investigation of plastic injection molding of micro-engineered surfaces". In: *Polymer Engineering & Science* 51.S1 (2017), E73–E81. ISSN: 00323888. DOI: 10.1002/pen.24652.

[53] J. Peters, J. Bryan, W. Estler, C. Evans, H. Kunzmann, D. Lucca, S. Sartori, H. Sato, E. Thwaite, P. Vanherck, R. Hocken, J. Peklenik, T. Pfeifer, H. Trumpold, and T. Vorburger. "Contribution of CIRP to the Development of Metrology and Surface Quality Evaluation during the last fifty years". In: *CIRP Annals* 50.2 (2001), pp. 471–488. ISSN: 00078506. DOI: 10.1016/S0007-8506(07)62996-5.

[54] R. Leach. *Optical measurement of surface topography*. Berlin: Springer-Verlag, 2011.

[55] R. Hocken, N. Chakraborty, and C. Brown. "Optical Metrology of Surfaces". In: *CIRP Annals - Manufacturing Technology* 54.2 (2005), pp. 169–183. ISSN: 00078506. DOI: 10.1016/S0007-8506(07)60025-0.

[56] *https://www.azom.com/equipment-details.aspx?EquipID=3508*. URL: https://www.azom.com/equipment-details.aspx?EquipID=3508 (visited on 10/29/2018).

[57] R. Danzl and F. Helmli. "Form measurement of engineering parts using an optical measurement system based on focus variation". In: *Proceedings of the 7th International Conference & Exhibition of the European Society for Precision Engineering and Nanotechnology (euspen)*. Bremen, DE: euspen, 2007.

[58] F. Hiersemenzel, J. N. Petzing, R. Leach, F. Helmli, and J. Singh. "Areal texture and angle measurements of tilted surfaces using focus variation methods". In: *Proceedings of the 3rd International Conference on Surface Metrology*. 2012.

[59] D. Quagliotti, F. Baruffi, G. Tosello, S. Gasparin, M. Annoni, P. Parenti, R. Sobiecki, and H. N. Hansen. "Performance verification of focus variation and confocal microscopes measuring tilted ultra-fine surfaces". In: *Proceedings of the 16th International Conference & Exhibition of the European Society for Precision Engineering and Nanotechnology (euspen)*. Nottingham, UK: euspen, 2016, pp. 169–170.

[60] *https://www.ctemag.com/news/articles/measuring-real-edge-contour*. URL: https://www.ctemag.com/news/articles/measuring-real-edge-contour (visited on 10/29/2018).

[61] J. Zhao, R. Mayes, and G. Chen. "Effects of process parameters on the micro molding process". In: *Polymer Engineering and Science* 43.9 (2003), pp. 1542–1554.

[62] J. Zhao, R. H. Mayes, G. Chen, P. S. Chan, and Z. J. Xiong. "Polymer micromould design and micromoulding process". In: *Plastics, Rubber and Composites* 32.6 (2003), pp. 240–247. ISSN: 1465-8011. DOI: 10.1179/146580103225002614.

[63] Z. Shayfull, S. Sharif, A. M. Zain, M. F. Ghazali, and R. M. Saad. "Potential of conformal cooling channels in rapid heat cycle molding: A review". In: *Advances in Polymer Technology* 33.1 (2014). ISSN: 07306679. DOI: 10.1002/adv.21381.

[64] D. O. Kazmer, S. Velusamy, S. Westerdale, S. Johnston, and R. X. Gao. "A comparison of seven filling to packing switchover methods for injection molding". In: *Polymer Engineering & Science* 50.10 (2010), pp. 2031–2043. ISSN: 00323888. DOI: 10.1002/pen.21731.

[65] J. M. Dealy and J. Wang. *Melt Rheology and its Applications in the Plastics Industry*. Engineering Materials and Processes. Dordrecht, NE: Springer Netherlands, 2013. ISBN: 978-94-007-6394-4. DOI: 10.1007/978-94-007-6395-1.

[66] T. Osswald and N. Rudolph. *Polymer Rheology: Fundamentals and Applications*. München, DE: Carl Hanser Verlag GmbH & Co., 2014. ISBN: 978-1-56990-523-4.

[67] B. Sha, S. Dimov, C. Griffiths, and M. S. Packianather. "Investigation of micro-injection moulding: Factors affecting the replication quality". In: *Journal of Materials Processing Technology* 183.2-3 (2007), pp. 284–296. ISSN: 09240136. DOI: 10.1016/j.jmatprotec.2006.10.019.

[68] V. Bellantone, R. Surace, G. Trotta, and I. Fassi. "Replication capability of micro injection moulding process for polymeric parts manufacturing". In: *The International Journal of Advanced Manufacturing Technology* 67.5-8 (2012), pp. 1407–1421. ISSN: 0268-3768. DOI: 10.1007/s00170-012-4577-2.

[69] D. Annicchiarico, U. M. Attia, and J. R. Alcock. "Part mass and shrinkage in micro injection moulding: Statistical based optimisation using multiple quality criteria". In: *Polymer Testing* 32.6 (2013), pp. 1079–1087. ISSN: 01429418. DOI: 10.1016/j.polymertesting.2013.06.009.

[70] A. Eladl, R. Mostafa, A. Islam, D. Loaldi, H. Soltan, H. Hansen, and G. Tosello. "Effect of Process Parameters on Flow Length and Flash Formation in Injection Moulding of High Aspect Ratio Polymeric Micro Features". In: *Micromachines* 9.2 (2018), p. 58. ISSN: 2072-666X. DOI: 10.3390/mi9020058.

[71] M. Sorgato, D. Masato, and G. Lucchetta. "Effect of vacuum venting and mold wettability on the replication of micro-structured surfaces". In: *Microsystem Technologies* 23.7 (2016), pp. 2543–2552. ISSN: 09467076. DOI: 10.1007/s00542-016-3038-5.

[72] M. Calaon, G. Tosello, J. Garnaes, and H. N. Hansen. "Injection and injection-compression moulding replication capability for the production of polymer lab-on-a-chip with nano structures". In: *Journal of Micromechanics and Microengineering* 27.10 (2017). ISSN: 13616439. DOI: 10.1088/1361-6439/aa853f.

[73] D. Yao and B. Kim. "Injection molding high aspect ratio microfeatures". In: *Journal of Injection Molding Technology* 6.1 (2002), pp. 11–17. ISSN: 1533905x.

[74] S. Yuan, N. P. Hung, B. K. A. Ngoi, and M. Y. Ali. "Development of Microreplication Process—Micromolding". In: *Materials and Manufacturing Processes* 18.5 (2003), pp. 731–751. ISSN: 1042-6914. DOI: 10.1081/AMP-120024972.

[75] C. Huang, S. Chen, and C. Yang. "Accuracy and mechanical properties of multiparts produced in one mold in microinjection molding". In: *Polymer Engineering & Science* 45.11 (2005), pp. 1471–1478. ISSN: 0032-3888. DOI: 10.1002/pen.20408.

[76] A. W. McFarland, M. A. Poggi, L. A. Bottomley, and J. S. Colton. "Injection moulding of high aspect ratio micron-scale thickness polymeric microcantilevers". In: *Nanotechnology* 15.11 (2004), pp. 1628–1632. ISSN: 0957-4484. DOI: 10.1088/0957-4484/15/11/044.

[77] Y.-C. Su, J. Shah, and L. Lin. "Implementation and analysis of polymeric microstructure replication by micro injection molding". In: *Journal of Micromechanics and Microengineering* 14.3 (2004), pp. 415–422. ISSN: 0960-1317. DOI: 10.1088/0960-1317/14/3/015.

[78] R. Surace, V. Bellantone, G. Trotta, and I. Fassi. "Replicating capability investigation of micro features in injection moulding process". In: *Journal of Manufacturing Processes* 28 (2017), pp. 351–361. ISSN: 15266125. DOI: 10.1016/j.jmapro.2017.07.004.

[79] G. Tosello, A. Gava, H. N. Hansen, and G. Lucchetta. "Study of process parameters effect on the filling phase of micro-injection moulding using weld lines as flow markers". In: *International Journal of Advanced Manufacturing Technology* 47.1-4 (2010), pp. 81–97. ISSN: 02683768. DOI: 10.1007/s00170-009-2100-1.

[80] J. Vera, A.-C. Brulez, E. Contraires, M. Larochette, N. Trannoy-Orban, M. Pignon, C. Mauclair, S. Valette, and S. Benayoun. "Factors influencing microinjection molding replication quality". In: *Journal of Micromechanics and Microengineering* 28.1 (2018), p. 015004. ISSN: 0960-1317. DOI: 10.1088/1361-6439/aa9a4e.

[81] U. M. Attia, S. Marson, and J. R. Alcock. "Micro-injection moulding of polymer microfluidic devices". In: *Microfluidics and Nanofluidics* 7.1 (2009), pp. 1–28. ISSN: 16134982. DOI: 10.1007/s10404-009-0421-x.

[82] U. M. Attia and J. R. Alcock. "Optimising process conditions for multiple quality criteria in micro-injection moulding". In: *International Journal of Advanced Manufacturing Technology* 50.5-8 (2010), pp. 533–542. ISSN: 02683768. DOI: 10.1007/s00170-010-2547-0.

[83] M. T. Martyn, B. R. Whiteside, P. D. Coates, P. S. Allan, G. Greenway, and P. Hornsby. "Micromoulding: consideration of processing effects on medical materials". In: *Proceedings of the 61st Annual Technical Conference of the Society of Plastics Engineers 2003 (ANTEC 2003)*. 2003, pp. 2582–2586.

[84] D. Masato, J. Rathore, M. Sorgato, S. Carmignato, and G. Lucchetta. "Analysis of the shrinkage of injection-molded fiber-reinforced thin-wall parts". In: *Materials and Design* 132 (2017), pp. 496–504. ISSN: 18734197. DOI: 10.1016/j.matdes.2017.07.032.

[85] D. Annicchiarico, U. M. Attia, and J. R. Alcock. "A methodology for shrinkage measurement in micro-injection moulding". In: *Polymer Testing* 32.4 (2013), pp. 769–777. ISSN: 01429418. DOI: 10.1016/j.polymertesting.2013.03.021.

[86] S. H. Yoon, P. Padmanabha, N. G. Cha, J. L. Mead, and C. M. F. Barry. "Evaluation of vacuum venting for micro-injection molding". In: *International Polymer Processing* 26.4 (2011), pp. 346–353. ISSN: 0930777X. DOI: 10.3139/217.2308.

[87] C. A. Griffiths, S. S. Dimov, S. G. Scholz, G. Tosello, and A. Rees. "Influence of Injection and Cavity Pressure on the Demoulding Force in Micro-Injection Moulding". In: *Journal of Manufacturing Science and Engineering* 136.3 (2014), p. 031014. ISSN: 1087-1357. DOI: 10.1115/1.4026983.

[88] Z. Chen and L. S. Turng. "A review of current developments in process and quality control for injection molding". In: *Advances in Polymer Technology* 24.3 (2005), pp. 165–182. ISSN: 07306679. DOI: 10.1002/adv.20046.

[89] M. Azaman, S. Sapuan, S. Sulaiman, E. Zainudin, and A. Khalina. "Optimization and numerical simulation analysis for molded thin-walled parts fabricated using wood-filled polypropylene composites via plastic injection molding". In: *Polymer Engineering & Science* 55.5 (2015), pp. 1082–1095. ISSN: 00323888. DOI: 10.1002/pen.23979.

[90] U. M. Attia and J. R. Alcock. "Evaluating and controlling process variability in micro-injection moulding". In: *International Journal of Advanced Manufacturing Technology* 52.1-4 (2011), pp. 183–194. ISSN: 02683768. DOI: 10.1007/s00170-010-2724-1.

[91] D. Masato, M. Sorgato, and G. Lucchetta. "Effect of ultrasound vibration on the ejection friction in microinjection molding". In: *International Journal of Advanced Manufacturing Technology* 96.1-4 (2018), pp. 345–358. ISSN: 14333015. DOI: 10.1007/s00170-018-1652-3.

[92] C. A. Griffiths, S. Dimov, S. G. Scholz, H. Hirshy, and G. Tosello. "Process Factors Influence on Cavity Pressure Behavior in Microinjection Moulding". In: *Journal of Manufacturing Science and Engineering* 133.3 (2011), p. 031007. ISSN: 10871357. DOI: 10.1115/1.4003953.

[93] D. C. Montgomery. *Design and Analysis of Experiments*. New York, USA: Wiley, 2012.

[94] Minitab. *http://www.minitab.com/en-us/*. (Visited on 10/30/2018).

[95] Joint Committee for Guides in Metrology (JCGM). *Evaluation of measurement data: Guide to the expression of uncertainty in measurement*. Paris, FR: JCGM, 2008.

[96] B. Whiteside, M. Babenko, and E. Brown. "Micro Molding Process Monitoring and Control". In: *Micro Injection Molding*. München, DE: Carl Hanser Verlag GmbH & Co., 2018, pp. 31–55. ISBN: 978-1-56990-653-8.

[97] B. Whiteside, C. Tuinea-Bobe, and P. D. Coates. "Characterising the Injection Kinetics of a Microinjection Moulding Machine". In: *Proceedings of the 9th International Conference on Multi-Material Micro Manufacture*. Vienna, AT, 2012, pp. 262–265. ISBN: 978-981-07-3354-4. DOI: 10.3850/978-981-07-3353-7_330.

[98] C. A. Griffiths, S. S. Dimov, and E. B. Brousseau. "Microinjection moulding: The influence of runner systems on flow behaviour and melt fill of multiple microcavities". In: *Proceedings of the Institution of Mechanical Engineers, Part B: Journal of Engineering Manufacture* 222.9 (2008), pp. 1119–1130. ISSN: 09544054. DOI: 10.1243/09544054JEM1084.

[99] A. Bendada, A. Derdouri, M. Lamontagne, and Y. Simard. "Analysis of thermal contact resistance between polymer and mold in injection molding". In: *Applied Thermal Engineering* 24.14-15 (2004), pp. 2029–2040. ISSN: 13594311. DOI: 10.1016/j.applthermaleng.2003.12.027.

[100] C. Abeykoon, P. J. Martin, A. L. Kelly, and E. C. Brown. "A review and evaluation of melt temperature sensors for polymer extrusion". In: *Sensors and Actuators A: Physical* 182 (2012), pp. 16–27. ISSN: 09244247. DOI: 10.1016/j.sna.2012.04.026.

[101] K.-M. Tsai and J.-K. Lan. "Correlation between runner pressure and cavity pressure within injection mold". In: *The International Journal of Advanced Manufacturing Technology* 79.1-4 (2015), pp. 273–284. ISSN: 0268-3768. DOI: 10.1007/s00170-014-6776-5.

[102] N. Zhang, Q. Su, S. Y. Choi, and M. D. Gilchrist. "Effects of gate design and cavity thickness on filling, morphology and mechanical properties of microinjection mouldings". In: *Materials & Design* 83 (2015), pp. 835–847. ISSN: 02641275. DOI: 10.1016/j.matdes.2015.06.012.

[103] D. Masato, M. Sorgato, and G. Lucchetta. "Effect of ultrasound vibration on the ejection friction in microinjection molding". In: *The International Journal of Advanced Manufacturing Technology* 96.1-4 (2018), pp. 345–358. ISSN: 0268-3768. DOI: 10.1007/s00170-018-1652-3.

[104] G. Tosello, A. Gava, H. N. Hansen, H. Reinecke, G. Lucchetta, and A. Schoth. "Experimental validation of micro molding simulations using different process settings conditions". In: *Antec 2009*. Chicago, USA, 2009, pp. 1787–1793.

[105] B. Whiteside, R. Spares, and P. D. Coates. "Rheo-optical measurements in micromoulding". In: *67th Annual Technology Conference of the Society of Plastics Engineers 2009*. Chicago, USA: Society of Plastic Engineers, 2009, pp. 1803–1810. ISBN: 9781615673278.

[106] M. Babenko, J. Sweeney, P. Petkov, F. Lacan, S. Bigot, and B. Whiteside. "Evaluation of heat transfer at the cavity-polymer interface in microinjection moulding based on experimental and simulation study". In: *Applied Thermal Engineering* 130 (2018), pp. 865–876. ISSN: 13594311. DOI: 10.1016/j.applthermaleng.2017.11.022.

[107] X. Han and H. Yokoi. "Visualization analysis of the filling behavior of melt into microscale V-grooves during the filling stage of injection molding". In: *Polymer Engineering & Science* 46.11 (2006), pp. 1590–1597. ISSN: 00323888. DOI: 10.1002/pen.20615.

[108] M. Sorgato, M. Babenko, G. Lucchetta, and B. Whiteside. "Investigation of the influence of vacuum venting on mould surface temperature in micro injection moulding". In: *The International Journal of Advanced Manufacturing Technology* 88.1-4 (2017), pp. 547–555. ISSN: 0268-3768. DOI: 10.1007/s00170-016-8789-8.

[109] P. Guerrier, G. Tosello, K. K. Nielsen, and J. H. Hattel. "Three-dimensional numerical modeling of an induction heated injection molding tool with flow visualization". In: *International Journal of Advanced Manufacturing Technology* 85.1-4 (2016), pp. 643–660. ISSN: 14333015. DOI: 10.1007/s00170-015-7955-8.

[110] D. Masato, M. Sorgato, M. Babenko, B. Whiteside, and G. Lucchetta. "Thin-wall injection molding of polystyrene parts with coated and uncoated cavities". In: *Materials & Design* 141 (2018), pp. 286–295. ISSN: 02641275. DOI: 10.1016/j.matdes.2017.12.048.

[111] F. Baruffi, M. Calaon, and G. Tosello. "Effects of micro-injection moulding process parameters on accuracy and precision of thermoplastic elastomer micro rings". In: *Precision Engineering* 51 (2018), pp. 353–361. ISSN: 01416359. DOI: 10.1016/j.precisioneng.2017.09.006.

[112] F. Baruffi, M. Calaon, G. Tosello, and R. Elsborg. "Investigation on the micro injection molding process of an overmolded multi-material micro component". In: *Proceedings of the World Congress on Micro and Nano Manufacturing (WCMNM) 2017*. Kaohsiung, Taiwan, 2017, pp. 349–352.

[113] J. G. Drobny. *Handbook of thermoplastic elastomers*. Norwich, USA: William Andrew, 2007. ISBN: 9780815515494.

[114] F. B. Hasnæs. "Micro Injection Moulding Technology of Thermoplastic Elastomers". Master Thesis. Technical University of Denmark, 2014.

[115] R. Varma, D. Liu, and K. Venkataswamy. "TPE Overmolding Technology". In: *Annual Technical Conference - ANTEC, Conference Proceedings*. Vol. 3. Nashville, USA, 2003, pp. 3051–3058.

[116] M. W. Alabran, J. L. Mead, C. M. F. Barry, M. Lowell, D. J. Carter, T. Charles, and S. Draper. "Effects of Tooling and Injection Molding Conditions on Nanoscale Replication of Thermoplastic Elastomers". In: *Annual Technical Conference - ANTEC, Conference Proceedings*. Vol. 85. Cincinnati, USA, 2007, pp. 1990–1994.

[117] U. M. Attia and J. R. Alcock. "A process chain for integrating microfluidic interconnection elements by micro- overmoulding of thermoplastic elastomers". In: *Journal of Micromechanics and Microengineering* 20.5 (2010), p. 055017. ISSN: 0960-1317. DOI: 10.1088/0960-1317/20/5/055017.

[118] C. H. Wu and W. J. Liang. "Effects of geometry and injection-molding parameters on weld-line strength". In: *Polymer Engineering and Science* 45.7 (2005), pp. 1021–1030. ISSN: 00323888. DOI: 10.1002/pen.20369.

[119] *ISO 15530 -3: Geometrical product specifications (GPS) - Coordinate measuring machines (CMM): Technique for determining the uncertainty of measurement*. 2011.

[120] C. A. Griffiths, S. S. Dimov, S. Scholz, and G. Tosello. "Cavity Air Flow Behavior During Filling in Microinjection Molding". In: *Journal of Manufacturing Science and Engineering* 133.1 (2011), p. 11006. ISSN: 1087-1357. DOI: 10.1115/1.4003339.

[121] Ortofon A/S. *https://www.ortofon.com/*. URL: https://www.ortofon.com/ (visited on 11/06/2018).

[122] *http://www.hi-fiworld.co.uk/index.php/vinyl-lp/70-tests/103-cartridge-tests.html?start=2*. URL: http://www.hi-fiworld.co.uk/index.php/vinyl-lp/70-tests/103-cartridge-tests.html?start=2 (visited on 02/04/2019).

[123] *ISO 1101: Geometrical product specifications (GPS): Tolerances of form, orientation, location and run-out*. 2012.

[124] F. Baruffi, M. Calaon, and G. Tosello. "Micro-injection moulding in-line quality assurance based on product and process fingerprints". In: *Micromachines* 9.6 (2018). ISSN: 2072666X. DOI: 10.3390/mi9060293.

[125] F. Degli Esposti. "Micro Injection Moulding Process Simulation for Quality Assurance". Master Thesis. Technical University of Denmark, 2017.

[126] E. Hakimian and A. B. Sulong. "Analysis of warpage and shrinkage properties of injection-molded micro gears polymer composites using numerical simulations assisted by the Taguchi method". In: *Materials and Design* 42 (2012), pp. 62–71. ISSN: 02641275. DOI: 10.1016/j.matdes.2012.04.058.

[127] P. Mélé and J. Giboz. "Micro-injection molding of thermoplastic polymers: Proposal of a constitutive law as function of the aspect ratios". In: *Journal of Applied Polymer Science* 135.4 (2018), p. 45719. ISSN: 10974628. DOI: 10.1002/app.45719.

[128] P. C. Vella, S. S. Dimov, E. Brousseau, and B. R. Whiteside. "A new process chain for producing bulk metallic glass replication masters with micro- and nano-scale features". In: *International Journal of Advanced Manufacturing Technology* 76.1-4 (2014), pp. 523–543. ISSN: 14333015. DOI: 10.1007/s00170-014-6148-1.

[129] Autodesk Simulation Moldflow Insight ®. *Autodesk Moldflow database*. San Rafael, CA, USA, 2017.

[130] F. Baruffi, M. Gülçür, M. Calaon, J. M. Romano, P. Penchev, S. Dimov, B. Whiteside, and G. Tosello. "Correlating nano-scale surface replication accuracy and cavity temperature in micro-injection moulding using in-line process control and high-speed thermal imaging". In: *Journal of Manufacturing Processes* Submitted (2019).

[131] C. Huang, L. Li, and A. Y. Yi. "Design and fabrication of a micro Alvarez lens array with a variable focal length". In: *Microsystem Technologies* 15.4 (2009), pp. 559–563. ISSN: 09467076. DOI: 10.1007/s00542-008-0706-0.

[132] J. S. Madsen, L. H. Thamdrup, I. Czolkos, P. E. Hansen, A. Johansson, J. Garnaes, J. Nygård, and M. H. Madsen. "In-line characterization of nanostructured mass-produced polymer components using scatterometry". In: *Journal of Micromechanics and Microengineering* 27.8 (2017), p. 085004. ISSN: 0960-1317. DOI: 10.1088/1361-6439/aa7a3a.

[133] *ISO 16610-61: Geometrical product specification (GPS) - Filtration - Part 61: Linear areal filters - Gaussian filters*. 2015.

[134] *ISO 25178-2: Geometrical product specifications (GPS) - Surface texture: Areal - Part 2: Terms, definitions and surface texture parameters*. 2012.

[135] A. H. Lutey, L. Gemini, L. Romoli, G. Lazzini, F. Fuso, M. Faucon, and R. Kling. "Towards laser-textured antibacterial surfaces". In: *Scientific Reports* 8.1 (2018), pp. 1–10. ISSN: 20452322. DOI: 10.1038/s41598-018-28454-2.

[136] S. Bagherifard, D. J. Hickey, A. C. de Luca, V. N. Malheiro, A. E. Markaki, M. Guagliano, and T. J. Webster. "The influence of nanostructured features on bacterial adhesion and bone cell functions on severely shot peened 316L stainless steel". In: *Biomaterials* 73 (2015), pp. 185–197. ISSN: 18785905. DOI: 10.1016/j.biomaterials.2015.09.019.

[137] J. Hasan, R. J. Crawford, and E. P. Ivanova. "Antibacterial surfaces: The quest for a new generation of biomaterials". In: *Trends in Biotechnology* 31.5 (2013), pp. 295–304. ISSN: 01677799. DOI: 10.1016/j.tibtech.2013.01.017.

[138] G. Tosello, H. Haitjema, R. K. Leach, D. Quagliotti, S. Gasparin, and H. N. Hansen. "An international comparison of surface texture parameters quantification on polymer artefacts using optical instruments". In: *CIRP Annals - Manufacturing Technology* 65.1 (2016), pp. 529–532. ISSN: 17260604. DOI: 10.1016/j.cirp.2016.04.003.

[139] L. M. Nicholson, K. S. Whitley, T. S. Gates, and J. A. Hinkley. "How molecular structure affects mechanical properties of an advanced polymer". In: *International Sampe Symposium and Exhibition*. Vol. 44. 1999.

[140] F. Baruffi, M. Calaon, G. Tosello, and R. Elsborg. "On the applicability of micro-injection moulding simulations to multivariate integrated process/product optimization". In: *Proceedings of the World Congress on Micro and Nano Manufacturing (WCMNM) 2018*. Portorož , SI, 2018, pp. 171–174.

[141] F. Baruffi, M. Calaon, and G. Tosello. "Prediction of micro-sized flash using micro-injection moulding process simulations". In: *Proceedings of the 18th International Conference & Exhibition of the European Society for Precision Engineering and Nanotechnology (euspen)*. Venice, IT: euspen, 2018, pp. 263–264.

[142] U. Vietri, A. Sorrentino, V. Speranza, and R. Pantani. "Improving the predictions of injection molding simulation software". In: *Polymer Engineering & Science* 51.12 (2011), pp. 2542–2551. ISSN: 00323888. DOI: 10.1002/pen.22035.

[143] S. A. Khalilian, S. S. Park, and T. I. Freiheit. "The Application of Commercial Injection Molding Software to Micro-Component Design and Process Development". In: *Proceedings of the 8th Internation Conference on Micro Manufacturing (ICOMM 2013)* (2013), pp. 50–56.

[144] D. M. Marhöfer, G. Tosello, A. Islam, and H. N. Hansen. "Gate Design in Injection Molding of Microfluidic Components Using Process Simulations". In: *Journal of Micro and Nano-Manufacturing* 4.2 (2016), p. 025001. ISSN: 2166-0468. DOI: 10.1115/1.4032302.

[145] T. Nguyen-Chung, C. Loser, G. Juttner, T. Pham, M. Obadal, and M. Gehde. "Simulation of the micro-injection moulding process: effect of the thermorheological status on the morphology". In: *Proceedings of the Institution of Mechanical Engineers, Part E: Journal of Process Mechanical Engineering* 225.4 (2011), pp. 224–238. ISSN: 0954-4089. DOI: 10.1177/0954408911415940.

[146] V. Piotter, K. Mueller, K. Plewa, R. Ruprecht, and J. Hausselt. "Performance and simulation of thermoplastic micro injection molding". In: *Microsystem Technologies* 8.6 (2002), pp. 387–390. ISSN: 09467076. DOI: 10.1007/s00542-002-0178-6.

[147] P. Kennedy. *Flow analysis of injection molds: Second edition*. 2nd editio. München, DE: Carl Hanser Verlag GmbH & Co., 2013. ISBN: 9781569905128.

[148] D. M. Marhöfer. "Design and Manufacture of Molded Micro Product Using Cuncurrent Engineering". PhD thesis. Technical University of Denmark (DTU), 2016.

[149] M. M. Cross. "Rheology of non-Newtonian fluids: A new flow equation for pseudoplastic systems". In: *Journal of Colloid Science* 20.5 (1965), pp. 417–437. DOI: 10.1016/0095-8522(65)90022-X.

[150] M. L. Williams, R. F. Landel, and J. D. Ferry. "The Temperature Dependence of Relaxation Mechanisms in Amorphous Polymers and Other Glass-forming Liquids". In: *Journal of the American Chemical Society* 77.14 (1955), pp. 3701–3707. DOI: 10.1021/ja01619a008.

[151] D. W. van Krevelen. *Properties of Polymers: Their Estimation and Correlation with Chemical Structure*. Amsterdam, NE: Elsevier, 1976. ISBN: 0444414673.

[152] R. Chien, W. R. Jong, and S. Chen. "Study on rheological behavior of polymer melt flowing through micro-channels considering the wall-slip effect". In: *Journal of Micromechanics and Microengineering* 15 (2005), pp. 1389–1396. ISSN: 00323888. DOI: 10.1002/pen.23113.

[153] G. Tosello, F. Costa, and H. N. Hansen. "Micro Injection Moulding High Accuracy Three-Dimensional Simulations and Process Control". In: *Proceedings of Polymer Process Engineering 11* (2011).

[154] F. Costa, G. Tosello, and B. Whiteside. "Best practice strategies for validation of micro moulding process simulation". In: *Proceedings of Ppe'09* (2009), pp. 331–364.

[155] A. Haddout and G. Villoutreix. "Polymer melt rheology at high shear rates". In: *International Polymer Processing* 15.3 (2000), pp. 291–296.

[156] S. K. Kim, S.-J. Choi, K.-H. Lee, D.-J. Kim, and Y.-E. Yoo. "Observation of Instabilities in Flow Front During Micro Injection Molding Process". In: *Polymer Engineering and Science* 47 (2010), pp. 1377–1381. ISSN: 00323888. DOI: 10.1002/pen.

[157] A. L. Kelly, T. Gough, B. R. Whiteside, and P. D. Coates. "High shear strain rate rheometry of polymer melts". In: *Journal of Applied Polymer Science* 114.2 (2009), pp. 864–873. ISSN: 00218995. DOI: 10.1002/app.30552.

[158] A. Gava and G. Lucchetta. "On the performance of a viscoelastic constitutive model for micro injection moulding simulations". In: *Express Polymer Letters* 6.5 (2012), pp. 417–426. ISSN: 1788618X. DOI: 10.3144/expresspolymlett.2012.44.

[159] S. J. Choi and S. K. Kim. "Multi-scale filling simulation of micro-injection molding process". In: *Journal of Mechanical Science and Technology* 25.1 (2011), pp. 117–124. ISSN: 1738494X. DOI: 10.1007/s12206-010-1025-9.

[160] D. M. Marhöfer, G. Tosello, H. N. Hansen, and A. Islam. "Advancements on the simulation of the micro injection moulding process". In: *Proceedings of the 10th International Conference on Multi-material Micro Manufacture* (2013).

[161] Autodesk Simulation Moldflow Insight ®. *Advanced Cool and Warp - Theory and Concepts*. San Rafael, CA, USA: Autodesk Inc., 2017.

[162] F. Baruffi, P. Parenti, F. Cacciatore, M. Annoni, and G. Tosello. "On the Application of Replica Molding Technology for the Indirect Measurement of Surface and Geometry of Micromilled Components". In: *Micromachines* 8.6 (2017), p. 195. ISSN: 2072-666X. DOI: 10.3390/mi8060195.

[163] F. Baruffi, P. Parenti, F. Cacciatore, M. Annoni, and G. Tosello. "Investigation on the micromilled surface characterization through replica technology". In: *Proceedings of the 11th International Conference on Multi-Material Micro Manufacture (4M2016)*. Kgs. Lyngby, DK, 2016, pp. 277–280.

[164] X. Liu, R. E. DeVor, S. G. Kapoor, and K. F. Ehmann. "The Mechanics of Machining at the Microscale: Assessment of the Current State of the Science". In: *Journal of Manufacturing Science and Engineering* 126.4 (2004), pp. 666–678. ISSN: 10871357. DOI: 10.1115/1.1813469.

[165] H. Weule, V. Hüntrup, and H. Tritschler. "Micro-Cutting of Steel to Meet New Requirements in Miniaturization". In: *CIRP Annals - Manufacturing Technology* 50.1 (2001), pp. 61–64. ISSN: 00078506. DOI: 10.1016/S0007-8506(07)62071-X.

[166] D. Yao and B. Kim. "Injection molding high aspect ratio microfeatures". In: *The Journal of injection molding technology* 6.1 (2002), pp. 11–17.

[167] A. W. Mcfarland, M. A. Poggi, L. A. Bottomley, and J. S. Colton. "Injection moulding of high aspect ratio micron-scale thickness polymeric microcantilevers". In: *Nanotechnology* 15 (2004), pp. 1628–1632. ISSN: 0957-4484. DOI: 10.1088/0957-4484/15/11/044.

[168] A. C. Liou and R. H. Chen. "Injection molding of polymer micro- and sub-micron structures with high-aspect ratios". In: *International Journal of Advanced Manufacturing Technology* 28.11-12 (2006), pp. 1097–1103. ISSN: 02683768. DOI: 10.1007/s00170-004-2455-2.

[169] W. Bachmann, B. Jean, T. Bende, M. Wohlrab, and H. J. Thiel. "Silicone replica technique and automatic confocal topometry for determination of corneal surface roughness". In: *German Journal of Ophthalmology* 2.6 (1993), pp. 400–403.

[170] R. Scott, P. Ungar, T. Bergstrom, C. Brown, B. Childs, M. Teaford, and A. Walker. "Dental microwear texture analysis: technical considerations". In: *Journal of Human Evolution* 51 (2006), pp. 339–349.

[171] D. Zuljan and J. Grum. "Non-destructive metallographic analysis of surfaces and microstructures by means of replicas". In: *8th International Conference of the Slovenian Society for Non-Destructive Testing: Application of Contemporary Non-Destructive Testing in Engineering*. Portorož , SI, 2005, pp. 359–368. ISBN: 9619061055.

[172] J. B. Jordon, J. D. Bernard, and J. C. Newman. "Quantifying microstructurally small fatigue crack growth in an aluminum alloy using a silicon-rubber replica method". In: *International Journal of Fatigue* 36.1 (2012), pp. 206–210. ISSN: 01421123. DOI: 10.1016/j.ijfatigue.2011.07.016.

[173] *AccuTrans 2012 AccuTrans Brochure*. 2012. URL: http://www.accutrans.info/fileadmin/dam/DATEN/AccuTrans/downloads/others/30000992%7B%5C_%7D11-12%7B%5C_%7DIFU%7B%5C_%7DAccuTrans%7B%5C_%7DAM%7B%5C_%7D01.pdf (visited on 02/15/2017).

[174] *Struers 2008 RepliSet Brochure*. 2010. URL: http://www.struers.com/en-GB/Products/Materialographic-analysis/Materialographic-analysis-equipment/Replication-system (visited on 02/15/2017).

[175] G. Tosello, H. N. Hansen, S. Gasparin, J. A. Albajez, and J. I. Esmoris. "Surface wear of TiN coated nickel tool during the injection moulding of polymer micro Fresnel lenses". In: *CIRP Annals - Manufacturing Technology* 61.1 (2012), pp. 535–538. ISSN: 00078506. DOI: 10.1016/j.cirp.2012.03.016.

[176] M. H. Madsen, N. A. Feidenhans'l, P.-E. Hansen, J. Garnæs, and K. Dirscherl. "Accounting for PDMS shrinkage when replicating structures". In: *Journal of Micromechanics and Microengineering* 24.12 (2014), p. 127002. ISSN: 0960-1317. DOI: 10.1088/0960-1317/24/12/127002.

[177] R. H. Goodall, L. P. Darras, and M. A. Purnell. "Accuracy and precision of silicon based impression media for quantitative areal texture analysis." In: *Scientific reports* 5 (2015), p. 10800. ISSN: 2045-2322. DOI: 10.1038/srep10800.

[178] S. Gasparin, H. N. Hansen, and G. Tosello. "Traceable surface characterization using replica moulding technology". In: *13th International Conference on Metrology and Properties of Engineering Surfaces*. Kgs. Lyngby, DK, 2011, pp. 306–315.

[179] W. Jinsheng, Z. Dajian, and G. Yadong. "A Micromilling Experimental Study on AISI 4340 Steel". In: *Key Engineering Materials* 408.407-408 (Feb. 2009), pp. 335–338. ISSN: 1662-9795. DOI: 10.4028/www.scientific.net/KEM.407-408.335.

[180] G. Kiswanto, D. Zariatin, and T. Ko. "The effect of spindle speed, feed-rate and machining time to the surface roughness and burr formation of Aluminum Alloy 1100 in micro-milling operation". In: *Journal of Manufacturing Processes* 16.4 (Oct. 2014), pp. 435–450. ISSN: 15266125. DOI: 10.1016/j.jmapro.2014.05.003.

[181] J. Wang, Y. Gong, J. Shi, and G. Abba. "Surface Roughness Prediction in Micromilling using Neural Networks and Taguchi's Design of Experiments". In: *Proocedings of the IEEE International Conference on Industrial Engineering and Engineering Managament (IEEM)*. Gippsland, AU, 2009, pp. 1–6.

[182] X. Liu, R. E. DeVor, and S. G. Kapoor. "Model-Based Analysis of the Surface Generation in Microendmilling—Part I: Model Development". In: *Journal of Manufacturing Science and Engineering* 129.3 (2007), pp. 453–460. ISSN: 10871357. DOI: 10.1115/1.2716705.

[183] A. M. Abdelrahman Elkaseer, S. S. Dimov, K. B. Popov, M. Negm, and R. Minev. "Modeling the Material Microstructure Effects on the Surface Generation Process in Microendmilling of Dual-Phase Materials". In: *Journal of Manufacturing Science and Engineering* 134.4 (2012), p. 44501. ISSN: 1087-1357. DOI: 10.1115/1.4006851.

List of Publications

Peer-reviewed journal papers

- M. Calaon, **F. Baruffi**, G. Tosello, G. Fantoni, I. Cirri, M. Santochi, and H.N. Hansen. "Functional analysis validation of micro and conventional moulding machines performances based on process precision and accuracy for micro manufacturing". Ready for submission to International Journal of Machine Tools and Manufacture (2019).
- **F. Baruffi**, M. Gülçür, M. Calaon, J.M. Romano, P. Penchev, S. Dimov, B. Whiteside, and G. Tosello. "Correlating nano-scale surface replication accuracy and cavity temperature in micro injection moulding using in-line process control and high-speed thermal imaging". Submitted to Journal of Manufacturing Processes (2019).
- **F. Baruffi**, M. Calaon, and G. Tosello. "Micro-injection moulding in-line quality assurance based on product and process fingerprints". In: Micromachines 9.6 (2018). ISSN: 2072666X. doi: 10.3390/mi9060293
- Y. Zhang, D. B. Pedersen, M. Mischkot, M. Calaon, **F. Baruffi**, and G. Tosello. "A Soft Tooling Process Chain for Injection Molding of a 3D Component with Micro Pillars". In: Journal of Visualized Experiments 138 (2018), e57335–e57335. ISSN: 1940-087X. doi: 10.3791/57335
- **F. Baruffi**, M. Calaon, and G. Tosello. "Effects of micro-injection moulding process parameters on accuracy and precision of thermoplastic elastomer micro rings". In: Precision Engineering 51 (2018), pp. 353–361. ISSN: 01416359. doi: 10.1016/j.precisioneng.2017.09.006
- **F. Baruffi**, P. Parenti, F. Cacciatore, M. Annoni, and G. Tosello. "On the Application of Replica Molding Technology for the Indirect Measurement of Surface and Geometry of Micromilled Components". In: Micromachines 8.6 (2017), p. 195. ISSN: 2072-666X. doi: 10.3390/mi8060195

Peer-reviewed conference papers

- **F. Baruffi**, M. Gülçür, M. Calaon, B. Whiteside, and G. Tosello. "In-line monitoring of micro structured surface replication in micro-injection moulding". In: Proceedings of the euspen Special Interest Group Meeting on Structured and Freeform Surfaces. Paris, FR: euspen, 2018.
- **F. Baruffi**, M. Calaon, G. Tosello, and R. Elsborg. "On the applicability of micro-injection moulding simulations to multivariate integrated process/product optimization". In: Proceedings of the World Congress on Micro and Nano Manufacturing (WCMNM) 2018. Portorož, SI, 2018, pp. 171–174.
- **F. Baruffi**, M. Calaon, and G. Tosello. "Prediction of micro-sized flash using micro-injection moulding process simulations". In: Proceedings of the 18$^{\text{th}}$ International Conference & Exhibition of the European Society for Precision Engineering and Nanotechnology (euspen). Venice, IT: euspen, 2018, pp. 263–264.
- **F. Baruffi**, M. Calaon, and G. Tosello. "Micro injection moulding process optimization of an ultra-small POM three-dimensional component". In: Proceedings of the euspen Special Interest Group Meeting on Micro/Nano Manufacturing. Glasgow, UK: euspen, 2017.
- **F. Baruffi**, M. Calaon, and G. Tosello. "On the performance of micro injection moulding process simulations of TPE micro rings". In: Proceedings of the euspen Special Interest Group Meeting on Micro/Nano Manufacturing. Glasgow, UK: euspen, 2017.
- D. Loaldi, M. Calaon, D. Quagliotti, **F. Baruffi**, P. Parenti, G. Tosello, and M. Annoni. "Laser confocal microscope noise evaluation on injection compression moulded (ICM) transparent polymer Fresnel lenses". In: Proceedings of the 17$^{\text{th}}$ International Conference & Exhibition of the European Society for Precision Engineering and Nanotechnology (euspen). Hannover, DE: euspen, 2017, pp. 357–358.
- **F. Baruffi**, M. Calaon, G. Tosello, H. Hansen, M. Prantl, and N. Miller. "Replication quality assessment and uncertainty evaluation of a polymer precision injection moulded component". In: Proceedings of the 17$^{\text{th}}$ International Conference & Exhibition of the European Society for Precision Engineering and Nanotechnology (euspen). Hannover, DE: euspen, 2017, pp. 495–496.
- **F. Baruffi**, M. Calaon, G. Tosello, and R. Elsborg. "Investigation on the micro injection molding process of an overmolded multi-material micro component". In: Proceedings of the World Congress on Micro and Nano Manufacturing (WCMNM) 2017. Kaohsiung, Taiwan, 2017, pp. 349–352.

- **F. Baruffi**, P. Parenti, F. Cacciatore, M. Annoni, and G. Tosello. "Investigation on the micromilled surface characterization through replica technology". In: Proceedings of the 11th International Conference on Multi-Material Micro Manufacture (4M2016). Kgs. Lyngby, Denmark, 2016, pp. 277-280.
- D. Quagliotti, **F. Baruffi**, G. Tosello, S. Gasparin, M. Annoni, P. Parenti, R. Sobiecki, and H. N. Hansen. "Performance verification of focus variation and confocal microscopes measuring tilted ultra-fine surfaces". In: Proceedings of the 16th International Conference & Exhibition of the European Society for Precision Engineering and Nanotechnology (euspen). Nottingham, UK: euspen, 2016, pp. 169–170.

The present thesis is dedicated to the advancement of the current state-of-the-art of process/ product control of polymer micro components manufactured by micro injection moulding (μIM). The main focus was the achievement of in-line quality assurance and optimization in μIM by means of a combination of product micro/nano metrology and real-time process monitoring. To achieve this, the newest technologies available in the moulding scenario were employed. Multiple important aspects of μIM, as the use of unconventional materials, process simulations and indirect metrology for mould assessment were also investigated.

DTU Mechanical Engineering
Section of Manufacturing Engineering
Technical University of Denmark

Produktionstorvet, Bld. 425
DK-2800 Kgs. Lyngby
Denmark

Tlf.: +45 4525 4763
Fax: +45 4525 1961

www.mek.dtu.dk

February 2019

ISBN: 978-87-7475-567-8